

NON-EQUILIBRIUM TOPOLOGY
IN MAGNONIC SYSTEMS

PIETER M. GUNNINK

PhD thesis, Utrecht University, September 2023

Printed by: ProefschriftMaken

ISBN: 978-90-393-7569-3

DOI: 10.33540/1887

About the cover: Central in this Thesis are topological spin waves. The cover shows a numerical simulation of the propagation of such a topological edge state, starting on the bottom right of the back page. The individual spins are represented by the circles, with the arrow indicating their precession angle and the color their deviation from their equilibrium position.

NON-EQUILIBRIUM TOPOLOGY IN MAGNONIC SYSTEMS

NIET-EVENWICHTSTOPOLOGIE IN
MAGNONISCHE SYSTEMEN
(met een samenvatting in het Nederlands)

Proefschrift

ter verkrijging van de graad van doctor aan de Universiteit Utrecht op gezag
van de rector magnificus, prof. dr. H.R.B.M. Kummeling, ingevolge het besluit
van het college voor promoties in het openbaar te verdedigen op

woensdag 13 september 2023 des middags te 2.15 uur

door

Pieter Marco Gunnink

geboren op 1 oktober 1995
te Bellville, Zuid-Afrika

PROMOTOR:

Prof. dr. R.A. Duine

COPROMOTOR:

Dr. A. Mook

BEOORDELINGSCOMMISSIE:

Prof. dr. ir. A. Brinkman

Prof. dr. C. De Morais Smith

Prof. dr. A.P. Mosk

Prof. dr. ir. H.T.C. Stoof

Prof. dr. S. Viola Kusminskiy

Dit proefschrift werd mede mogelijk gemaakt met financiële steun van de
Nederlandse Organisatie voor Wetenschappelijk Onderzoek (NWO)

PUBLICATIONS

This Thesis is based on the following publications:

1. Chapter 2 is based on P. M. Gunnink, R. A. Duine, and A. Rückriegel, "Electrical detection of unconventional transverse spin currents in obliquely magnetized thin films," *Physical Review B* **101**, 220407(R) (2020);
2. Chapter 3 is based on P. M. Gunnink, R. A. Duine, and A. Rückriegel, "Theory for electrical detection of the magnon Hall effect induced by dipolar interactions," *Physical Review B* **103**, 214426 (2021);
3. Chapter 4 is based on P. M. Gunnink, J. S. Harms, R. A. Duine, and A. Mook, *Zero-frequency chiral magnonic edge states protected by non-equilibrium topology*, (Feb. 13, 2023) arXiv:2302.06597;
4. Chapter 5 is based on P. M. Gunnink, B. Flebus, H. M. Hurst, and R. A. Duine, "Nonlinear dynamics of the non-Hermitian Su-Schrieffer-Heeger model," *Physical Review B* **105**, 104433 (2022).

Other publications of this author (not included in this Thesis):

5. P. M. Gunnink, R. L. Bouwmeester, and A. Brinkman, "Artificial oxide heterostructures with non-trivial topology," *Journal of Physics: Condensed Matter* **33**, 085601 (2020).

CONTENTS

Motivation	1
1 Basics	5
1.1 Classical magnetization dynamics	5
1.2 Spin waves	9
1.3 Dipole-dipole interaction	10
1.4 Microwave antenna excitation	11
1.5 Wave packet dynamics	13
1.6 Dynamics of the magnon distribution function	15
1.7 Diffusion model	16
1.8 Electrical spin injection and detection	19
1.9 Bulk-boundary correspondence	22
1.10 Magnon Chern insulator	23
1.11 Further topological magnon phases	26
1.12 Outline	27
2 Electrical detection of unconventional transverse spin currents in obliquely magnetized thin films	29
2.1 Introduction	29
2.2 Method	30
2.3 Results	33
2.4 Conclusion and Discussion	38
3 Theory for electrical detection of the magnon Hall effect induced by dipolar interactions	45
3.1 Introduction	45
3.2 Setup	48
3.3 Method	49
3.4 Hall angle and diffusion length	53
3.5 Diffusion in the Hall bar	57
3.6 Conclusion and Discussion	58
4 Zero-frequency chiral magnonic edge states protected by non-equilibrium topology	71
4.1 Introduction	71
4.2 Model	72
4.3 Numerical verification of the edge modes	76
4.4 Propagating spin wave spectroscopy	77
4.5 Discussion and Conclusion	79
5 Nonlinear dynamics of the non-Hermitian Su-Schrieffer-Heeger model	93
5.1 Introduction	93

5.2	System	95
5.3	Simulations	98
5.4	Results	100
5.5	Comparison to photonic systems	106
5.6	Conclusion and discussion	107
6	Electrical control of chiral edge states in the non-Hermitian magnon Chern insulator	111
6.1	Introduction	111
6.2	Non-Hermitian magnon Chern insulator	113
6.3	Finite-size system	116
6.4	Numerical LLG simulations	119
6.5	Transport	119
6.6	Conclusion and discussion	122
7	Conclusion and outlook	127
	Samenvatting: <i>Topologische spingolven raken uit evenwicht</i>	131
	Acknowledgments	139
	Curriculum Vitae	141
	Bibliography	143

MOTIVATION

Chances are that while you are reading this Thesis, you have a phone in your pocket, while your laptop is probably not very far away. When you get home in your car, tens of computers will have cooperated to ensure that you get there safely, that the temperature of the air-conditioning was set correctly and that your windshield wipers came on as soon as it started raining. If you use your washing machine to do your laundry tonight, a computer is controlling the various pumps and motors that wash your clothes. All this would not be possible without the invention of the integrated circuit: a large number of miniaturized transistors placed on a single chip. This has allowed manufacturers to design computers that are increasingly smaller, faster and less expensive, driving productivity and growth in almost every economic area. But integrated circuits have a significant drawback: their power usage. The power used by computers, data centers and network equipment accounts for 5% of the global energy consumption [6] and 2% of annual greenhouse gas emissions [7]. And even though there is now significant effort devoted to improving the energy efficiency of integrated circuits, there is a fundamental problem that is hard to overcome: the passage of an electric current through a conductor—the main working principle behind integrated circuits—produces heat, an effect known as *Joule heating*.

Joule heating cannot be completely circumvented, only reduced, and therefore a major strategy to decrease the overall heat production is to increase the density of transistors in a single chip. Since the introduction of dense integrated circuits in the 1960s, the density of transistors has doubled roughly every two years, an observation which is known as Moore's law [8, 9]. However, all exponential trends must come to an end, which in the case of integrated circuits is ultimately determined by the physical limit of a transistor, set by the size of a single atom. We are rapidly approaching this limit [10], signaling an end to Moore's law, at least for conventional electronic integrated circuits. Therefore, new approaches are needed if we want to drive power consumption down, or equivalently, increase computational power for the same power consumption.

One of the candidates in the search for alternatives to electronic integrated circuits is the usage of spin waves as data carriers. Spin waves are local disturbances of the magnetic moment of a material, as depicted in Fig. 1. Magnetic moments (or colloquially speaking, spins) are aligned to each other through an effect known as the exchange interaction. Therefore, disturbing

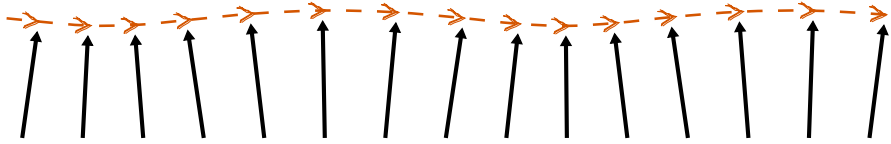


Figure 1: A spin wave propagating from left to right. The spin are schematically shown as arrows, and align to each other through the exchange interaction. The wave-like motion is indicated by the dashed line.

the left spin will cause the next spin to align to it, and the next spin, and so on forth, leading to wave-like behavior, hence the name “spin-wave”. A spin wave can thus propagate through a material, and carry with it information, making it suitable to design computing devices. Moreover, spin waves are fast enough to compete with modern electronic processors, since they have frequencies in the GHz-range, and couple easily to external magnetic fields, allowing for close experimental control.

Most importantly, there are no moving electrons associated with a spin wave, and therefore no Joule heating, leading to a drastically lower energy consumption. However, there is a catch: in actual computational devices spin waves would have to travel over relatively long distances, moving through a series of gates in order to perform computational operations. Even relatively simple numerical tasks can require many of such operations. For example, adding two one-bit integers can require up to 28 transistors [11], and the signal carried by the spin waves has to propagate through all these transistors. This is one of the major challenges associated with spin waves, since a spin wave is not necessarily conserved and thus cannot travel indefinitely, but decays after some time. This is the result of interactions with impurities, electrons, vibrations of the lattice, and other spin waves. It therefore seems likely that any real device will require the periodic amplification of spin waves, complicating the design of a real spin wave computer.

In this Thesis, we focus on a possible solution to this problem: making use of the topological protection that can be found in certain spin wave systems. Speaking generally, topological protection implies that a spin wave that is propagating through a material can only interact with other particles in such a way that its topological charge is conserved. In less technical terms: certain interactions that would normally lead to damping of the spin wave, are now forbidden. Importantly, this is a fundamental property of the spin waves, and is not (easily) violated. Therefore, spin waves can travel over longer distances, and there is less need for amplification. Besides their highly efficient transport of spin, topologically-protected spin waves are also of interest for fundamental reasons. The field of topological insulators—where topological protection

was pioneered—is principally concerned with electrons, which are fermions. For fermions, each energy state can only be occupied by one particle, which has profound implications on their transport properties. Spin waves, on the other hand, are bosons, which means that more than one spin wave can occupy an energy state. Topological insulators formed out of bosons are not as well-studied, since there are only a limited number of bosonic topological insulators available. Here spin waves could offer useful insights in how bosonic topological insulators differ from their fermionic counterparts. Specifically, to what limit the topological protection for nonconserved particles (such as spin waves) remains is still an open question. Moreover, there is a special class of topological insulators, the non-Hermitian topological insulators, which are much easier realized in bosonic systems, since they require the absorption or emission of particles to and from the environment. Spin waves couple quite naturally to the environment—in fact, this is what causes the damping of a spin wave in the first place—and are therefore a good choice to realize non-Hermitian topological phases.

At this point it is natural to wonder: if spin waves are such a natural fit to realize bosonic topology, why has this not been experimentally realized yet? In fact, topological spin waves were first theoretically proposed in 2010 [12], but experimental verification has turned out to be a real challenge. This is in part due to the fact that, in contrast to their fermionic counterparts, spin waves must appear at finite energies. Since in most proposed topological spin wave systems this corresponds to frequencies in the THz-range, one cannot straightforwardly excite and detect the topologically-protected spin waves.

This Thesis is therefore primarily concerned with this question: *What are the observable consequences of topological magnetic excitations and how can they be used for applications on the long term?* Since direct detection is not feasible, we study here a series of alternative approaches to access the effects of topology in magnetic systems, with a focus on the effect of topology on the transport properties of spin wave systems.

BASICS

In this Thesis we are primarily concerned with magnetic insulators, where finite magnetic moments \mathbf{S}_i are arranged in a lattice, but which do not support electrical currents. The finite magnetic moments arise due to ionic shells with nonzero angular momentum [13], which primarily interact with each other through the quantum-mechanical exchange interaction, as described by the Hamiltonian

$$\hat{H}_{\text{ex}} = -\frac{1}{2} \sum_{ij} J_{ij} \hat{\mathbf{S}}_i \cdot \hat{\mathbf{S}}_j, \quad (1.1)$$

where J_{ij} is the exchange interaction parameter and $\hat{\mathbf{S}}_i$ is the spin angular momentum operator with quantum number S at site i . The exchange interaction follows from the Pauli exclusion principle, and is thus a purely quantum-mechanical effect. It is important to note that Eq. (1.1) is only an approximation, valid in the limit of small overlap between the orbitals forming the magnetic moments. However, it is applicable for a wide range of materials, with varying sources of magnetism.

The sign of the exchange parameter J_{ij} determines if it is energetically favorable for the spins i and j to align (ferromagnetism) or anti-align (antiferromagnetism). In this Thesis we will only be concerned with ferromagnetism, and throughout the exchange parameter will be positive. Furthermore, the exchange interaction falls off rapidly as a function of distance, and it is usually sufficient to only consider exchange interactions between neighboring magnetic moments.

1.1 CLASSICAL MAGNETIZATION DYNAMICS

In order to further illustrate the dynamics of a ferromagnet, we consider a simple Hamiltonian,

$$\hat{H} = -\frac{1}{2} \sum_{ij} J_{ij} \hat{\mathbf{S}}_i \cdot \hat{\mathbf{S}}_j - \frac{g\mu_B}{\hbar} \mathbf{H} \cdot \sum_i \hat{\mathbf{S}}_i, \quad (1.2)$$

considering the exchange interaction and an external magnetic field \mathbf{H} .¹ Here g is the gyromagnetic ratio, μ_B is the Bohr magneton and \hbar is the reduced Planck constant. The dynamics then follow from the equation of motion in the Heisenberg picture,

$$\hbar \partial_t \hat{\mathbf{S}}_i = i[\hat{H}, \hat{\mathbf{S}}_i] \quad (1.3)$$

$$= -\hat{\mathbf{S}}_i \times \left(\frac{g\mu_B}{\hbar} \mathbf{H} + \frac{1}{2} \sum_j J_{ij} \hat{\mathbf{S}}_j \right). \quad (1.4)$$

In general, we can write this as

$$\partial_t \hat{\mathbf{S}}_i = -\hat{\mathbf{S}}_i \times \hat{\mathbf{H}}_{\text{eff}}; \quad \hat{\mathbf{H}}_{\text{eff}} = -\frac{\delta \hat{H}}{\hbar \delta \hat{\mathbf{S}}_i}, \quad (1.5)$$

where $\hat{\mathbf{H}}_{\text{eff}}$ is an effective magnetic field operator. Our main goal here is to find a classical limit within which we can treat this equation of motion, Eq. (1.5). We therefore write the equation of motion for the expectation value

$$\partial_t \langle \hat{\mathbf{S}}_i \rangle = -\langle \hat{\mathbf{S}}_i \times \hat{\mathbf{H}}_{\text{eff}} \rangle \quad (1.6)$$

and want to find the classical limit, i.e., where $\langle \hat{\mathbf{S}}_i \times \hat{\mathbf{H}}_{\text{eff}} \rangle = \langle \hat{\mathbf{S}}_i \rangle \times \langle \hat{\mathbf{H}}_{\text{eff}} \rangle$ holds.

To this end, we will make use of spin coherent states [14] in the Euler-angle representation, which are defined as rotating the z -axis towards the direction of the spin at site i ,

$$|g\rangle \equiv e^{i \sum_i \phi_i \hat{S}_i^z} e^{i \sum_i \theta_i \hat{S}_i^y} |S_z\rangle, \quad (1.7)$$

where ϕ_i, θ_i are spherical coordinates of the rotation of spin at site i . The spin coherent states form a complete set, and thus have the resolution of identity²

$$\hat{1} = \int d[g] |g\rangle \langle g|. \quad (1.8)$$

We will continue to work in the classical limit where $S \rightarrow \infty$, whilst $\hbar \rightarrow 0$, such that the product of $\hbar S$ remains finite. Now within this limit we have that

$$\lim_{\substack{S \rightarrow \infty \\ \hbar \rightarrow 0}} \langle h | \hat{\mathbf{S}}_i | f \rangle = \hbar S \hat{\mathbf{h}}_i \delta(\hat{\mathbf{h}}_i - \hat{\mathbf{f}}_i) \quad (1.9)$$

where $\hat{\mathbf{h}}_i, \hat{\mathbf{f}}_i$ are the two unit vectors corresponding to the rotation of the coherent states $|h, f\rangle$ on site i .

¹ In accordance with the (sadly) commonly used practice in magnetism, we will employ CGS units throughout this Thesis.

² We have absorbed a normalization constant in the integration measure, because it does not have an effect on the final result.

We prepare the system in some coherent state $|g_0\rangle$ and find as the equation of motion

$$\partial_t \langle g_0 | \hat{S}_i | g_0 \rangle = - \int d[g] \langle g_0 | \hat{S}_i | g \rangle \times \sum_j \mathbf{H}_{\text{eff},j} \langle g | \hat{S}_j | g_0 \rangle, \quad (1.10)$$

where we have assumed that the effective magnetic field operator can be written as $\hat{\mathbf{H}}_{\text{eff}} = \sum_j \mathbf{H}_{\text{eff},j} \hat{S}_j$ and have inserted the resolution of identity, Eq. (1.8). It is not essential here that the effective magnetic field operator is first order in spin operators, since for higher order spin operators one can repeat the procedure outlined here, again inserting the resolution of identity. We proceed in the classical limit and find

$$\hbar S \partial_t \hat{g}_{0,i} = - \hbar S \hat{g}_{0,i} \times \hbar S \sum_j \mathbf{H}_{\text{eff},j} \hat{g}_{0,j}, \quad (1.11)$$

where we have made use of Eq. (1.9).

Identifying the classical spin as a vector with length $\hbar S$, i.e., $\mathbf{S}_i = \hbar S \hat{g}_{0,i}$, we arrive at the central result:

$$\partial_t \mathbf{S}_i = - \mathbf{S}_i \times \mathbf{H}_{\text{eff},i} \quad \mathbf{H}_{\text{eff},i} \equiv - \frac{\delta H}{\hbar \delta \mathbf{S}_i}, \quad (1.12)$$

which is commonly known as the *Landau-Lifshitz* equation [15], and $\mathbf{H}_{\text{eff},i}$ is called the effective magnetic field. As we have shown here, it is valid only in the classical limit of large spin. It can also be directly obtained from Eq. (1.5) by replacing the quantum-mechanical spin operators with classical spins. Note that some authors prefer to work with the magnetic moment of the spins, $\mathbf{m}_i = g\mu_B \mathbf{S}_i$, such that the Landau-Lifshitz equation becomes

$$\partial_t \mathbf{m}_i = - \gamma \mathbf{m}_i \times \frac{\delta H}{\delta \mathbf{m}_i}, \quad (1.13)$$

where $\gamma \equiv g\mu_B/\hbar$ is the gyromagnetic ratio. This approach has the added benefit that the effective magnetic field, $\delta H/\delta \mathbf{m}_i$, actually has the units of a magnetic field, which is not the case in Eq. (1.12). In this Thesis we work with the classical spins \mathbf{S}_i and thus Eq. (1.12) throughout, but both approaches are of course equivalent.

The Landau-Lifshitz equation (1.12) thus describes the classical dynamics of a magnet. Here an important observation can already be made: the spins precess around an effective magnetic field, and their length is conserved. As was noted before, it is only valid for large spin S . This is typically the case, since many forms of magnetism originate from some combination of orbital and spin angular momentum and thus $S \gg 1$. Moreover, for ferromagnets the Landau-Lifshitz equation is only valid for temperatures well below the Curie temperature, such that thermal fluctuations can be disregarded [16].

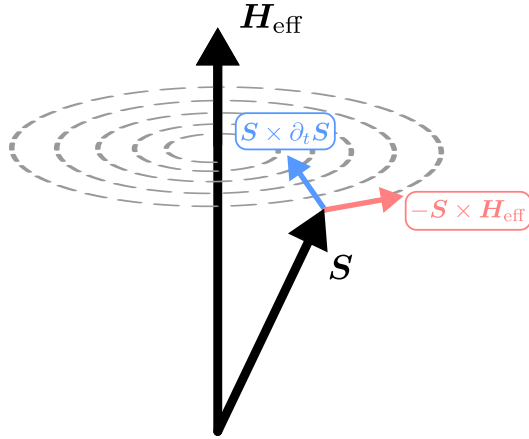


Figure 1.1: The precession of a single spin around an effective magnetic field \mathbf{H}_{eff} , with the direction of the Gilbert damping torque indicated. The dotted lines indicate the precession, which relaxes the spin to its equilibrium position along the effective magnetic field.

The Curie temperature is set by the exchange energy scale, which for many magnetic materials of interest is much larger than $k_B T$ at room temperature, making the Landau-Lifshitz equation of use in a wide range of temperatures.

The Landau-Lifshitz equation does not yet explain the simple experimental observation that applying an external magnetic field realigns the orientation of the spins. One therefore expects that there is a damping contribution which aligns the spins to the direction of the (effective) magnetic field. On basis of simple phenomenological arguments, Gilbert [17] proposed a damping that is proportional to the first order time derivative. Inserting this in Eq. (1.12) results in the celebrated *Landau-Lifshitz-Gilbert* (LLG) equation

$$\partial_t \mathbf{S}_i = -\mathbf{S}_i \times \mathbf{H}_{\text{eff},i} + \alpha \mathbf{S}_i \times \partial_t \mathbf{S}_i, \quad (1.14)$$

where α is the dimensionless Gilbert damping parameter. The LLG equation describes classical spin dynamics, including the effects of damping, and has been experimentally verified in a wide range of systems. It is of central importance in this Thesis, and will be the starting point to describe the spin dynamics in every chapter.

In Fig. 1.1 we illustrate the precession described by the LLG equation (1.14) for a single spin. The spin starts in a deviation from the direction of the effective magnetic field \mathbf{H}_{eff} and starts to precess around the effective magnetic field. However, the Gilbert damping will drive the spin towards the effective magnetic field, eventually relaxing the spin to its equilibrium direction. Typically, precession frequencies are of the order of GHz in ferromagnets, whilst in

high-quality magnetic materials, such as the ferromagnetic workhorse Yttrium Iron Garnet (YIG), $\alpha \approx 10^{-4}$ [18]. The relaxation towards equilibrium happens on a timescale Q/ω , where $Q = 1/\alpha$ is the quality factor. This is $Q/\omega \approx 10 \mu\text{s}$ for YIG and therefore the excitations are relatively long-lived, proving their usefulness for applications.

1.2 SPIN WAVES

With the LLG equation (1.14) in hand the classical dynamics of the magnetization are fully determined. But, in many real systems the dynamics resulting from the LLG equation are complex and cannot be fully solved analytically. Looking at the typical behavior of a ferromagnet, we notice however that all the spins are aligned and we can therefore expect that the dynamics are dominated by small deviations from this uniform state. The resulting excitations are called spin waves, as was also explained in the Motivation and Fig. 1 therein.

We will now derive the spin waves explicitly, by performing the following linearization procedure. We start from a simple Heisenberg Hamiltonian of N localized spins forming a one-dimensional chain, aligned to an external magnetic field $\mathbf{H}_e = H_0 \hat{z}$, applied along the z -direction,

$$\mathcal{H} = -\frac{1}{2} \sum_{ij} J_{ij} \hat{\mathbf{S}}_i \cdot \hat{\mathbf{S}}_j - \mu \mathbf{H}_e \cdot \sum_i \hat{\mathbf{S}}_i, \quad (1.15)$$

where $J_{ij} = J > 0$ for neighboring spins, and zero otherwise, and $\mu = g\mu_B/\hbar$. As was shown in Section 1.1, the classical dynamics are then described by the LLG equation (1.14). Since in the ground state, all the spins will be aligned to the external magnetic field, we introduce small deviations from this uniform state $\mathbf{S}_i = S \hat{z}$ as $m_i = (S_x^i + iS_y^i)/\sqrt{2S}$. Inserting this in the LLG equation (1.14), the magnetization dynamics are given by

$$i\hbar \partial_t m_i = \sum_j H_{ij} m_j; \quad H_{ij} = (h + 2JS)\delta_{ij} - JS\delta_{i,i\pm 1}, \quad (1.16)$$

where H_{ij} is the linear spin-wave Hamiltonian, with the Zeeman energy $h \equiv \mu H_0$. We introduce the Fourier transform as

$$m_i = \frac{1}{\sqrt{N}} \sum_{\mathbf{k}} e^{i\mathbf{k} \cdot \mathbf{r}_i} m_{\mathbf{k}}, \quad (1.17)$$

and obtain the final equation of motion for the spin waves

$$i\hbar \partial_t m_{\mathbf{k}} = H_{\mathbf{k}} m_{\mathbf{k}}; \quad H_{\mathbf{k}} = h + 2JS - 2JS \cos(ka), \quad (1.18)$$

where a is the lattice spacing, i. e., the distance between neighboring spins and $H_{\mathbf{k}}$ is the linear spin-wave Hamiltonian in momentum space. Written in this

form, it is clear that the spin waves are truly waves, with a dispersion given by $2JS + h - 2JS \cos(ka) \approx h + J_s k^2$, where we have expanded in small wave number ka and have defined the spin stiffness, $J_s \equiv JSa^2$.

The spin waves as derived here are classical, but can also be quantized, resulting in magnons. This can be done by simply invoking the canonical quantization

$$\left[m_i, m_j^\dagger \right] = \delta_{ij}, \quad (1.19)$$

or more formally, by performing the Holstein-Primakoff transformation [19]. The magnons obey the same dispersion relation as the spin waves, but it is important to note that the magnon creation (m^\dagger) and annihilation (m) operators act on a bosonic Fock space. Therefore, magnons obey Bose-Einstein statistics, and magnons and spin waves are not equal in all regards. The two descriptions are however equivalent when the uncertainty Δn of the magnon number n vanishes, which is given by [20]

$$\frac{\Delta n}{\bar{n}} = \frac{1}{\sqrt{\bar{n}}}, \quad (1.20)$$

where \bar{n} is the mean magnon number. Therefore, in the limit of large mean magnon number \bar{n} the uncertainty in the magnon number goes to zero, and the quantum statistics of the magnons no longer plays a role. Importantly, this implies that for sufficiently strong driving—such that many magnons with the same quantum number are excited—the magnons will obey a classical behavior well described by the Landau-Lifshitz-Gilbert equation. Furthermore, in thermal equilibrium the mean magnon number is large for magnons with energies smaller than $k_B T$, where k_B is the Boltzmann constant. For these energies the mean magnon number is therefore given by the Rayleigh-Jeans distribution which follows from classical equipartition. For high energies compared to $k_B T$ there are however relatively fewer magnons and their Bose-Einstein statistics play a significant role. In this Thesis we will be interested in the classical limit, such that the quantum character of the magnons does not play a role, although we will at times use the fact that in thermal equilibrium the magnons are well described by the Bose-Einstein distribution function. We therefore also use the terms *spin wave* and *magnon* interchangeably, both referring to the same magnetic excitation.

1.3 DIPOLE-DIPOLE INTERACTION

Since the spins we consider here are magnetic dipoles, they also interact with each other through the dipole-dipole interaction,

$$\mathcal{H}_{\text{dip}} = -\frac{1}{2} \sum_{ij, i \neq j} \frac{\mu^2}{|\mathbf{R}_{ij}|^3} [3 (\mathbf{S}_i \cdot \hat{\mathbf{R}}_{ij}) (\mathbf{S}_j \cdot \hat{\mathbf{R}}_{ij}) - \mathbf{S}_i \cdot \mathbf{S}_j], \quad (1.21)$$

where \mathbf{R}_{ij} is the vector connecting the two spins i, j and $\hat{\mathbf{R}}_{ij} = \mathbf{R}_{ij}/|\mathbf{R}_{ij}|$. Since the dipole-dipole interaction is long ranged and dependent on the relative orientation of the spins, thus also taking into account the boundary, its implications are also dimension- and shape-dependent. Most prominently, it will lead to a demagnetization field, which favors configurations such that the magnetization runs parallel to the surface of the sample. Further specifics of the dipole-dipole interaction depend on the geometry of the magnetic sample considered, and we therefore only make a few general comments regarding its nature here.

Most importantly, the dipole-dipole interaction couples the spin dynamics to the lattice degree of freedom, as can be seen from the fact that the interaction depends on the positions \mathbf{R}_{ij} of the spins. This implies the existence of a magnetic anisotropy, where the spins will tend to align with a specific axis, which is in general dependent on the specific sample geometry. This has two important implications for the spin waves: the anisotropy will open a gap in the spin wave spectrum and because of the coupling to the lattice there will be non-spinconserving processes, which will give rise to an elliptical precession, where the S_z -component varies during the precession.

Since the dipole-dipole interaction is a long-range interaction, coupling all spins in the system, the summation in Eq. (1.21) is difficult to perform. However, the short-range exchange interaction primarily affects the short-wavelength spin waves, while the dipole-dipole interaction mainly affects the low-energy long-wavelength spin waves [21–23], and thus at sufficiently high temperatures it can usually be ignored. In the Chapters 2 and 3 we are interested in the symmetry breaking that follows from the dipole-dipole interaction, and therefore have to consider its effects in full.

1.4 MICROWAVE ANTENNA EXCITATION

One of the main reasons why spin waves have attracted much attention is the fact that they easily couple to external magnetic fields, offering a readily available handle for control. To show this explicitly, we consider the excitation of spin waves with a local microwave antenna, which generates a local oscillating Øersted magnetic field by passing an alternating current through a wire, as shown in Fig. 1.2. This magnetic field extends into the ferromagnet, where it couples to the spin waves. Here it is important to note that spin waves typically have frequencies in the GHz-range, which are easily accessible with modern signal generators.

To describe the microwave antenna we add a local magnetic field \mathbf{h}_i to the LLG Eq. (1.14), such that

$$\partial_t \mathbf{S}_i = -\mathbf{S}_i \times [\mathbf{H}_{\text{eff},i} + \mathbf{h}_i] + \alpha \mathbf{S}_i \times \partial_t \mathbf{S}_i, \quad (1.22)$$

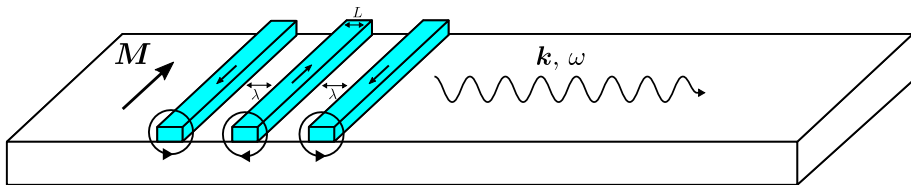


Figure 1.2: A coplanar waveguide, exciting spin waves with frequency ω and wave number $k = 2\pi/\lambda$ through an oscillating transverse magnetic field, induced by passing a current through the microwave antennas. In the limit of $\lambda \rightarrow \infty$, i.e., if only one of the microwave antennas is used, all spin waves up to $2\pi/L$ are excited.

where the spins are aligned to an external magnetic field, and the field \mathbf{h}_i induced by a microwave antenna is oscillating transverse to the external magnetic field. After performing the linear spin-wave expansion as in Section 1.2, we obtain the equation of motion in frequency and momentum space,

$$m_{\mathbf{k}}(\omega) = G_{\mathbf{k}}(\omega)h_{\mathbf{k}}(\omega), \quad (1.23)$$

where $h_{\mathbf{k}}(\omega)$ is the Fourier transform of the transverse components $h_{\mathbf{k}} = h_{\mathbf{k}}^x + ih_{\mathbf{k}}^y$ and we have introduced the retarded magnon Green's function—sometimes also referred to as the spin susceptibility—defined by

$$G_{\mathbf{k}}^{-1}(\omega) = -(1 + i\alpha)\omega + H_{\mathbf{k}}. \quad (1.24)$$

Written in this form, it is clear that a transversely oscillating magnetic field will excite a magnon wave-packet with frequency ω , the propagation of which is described by $G_{\mathbf{k}}(\omega)$. The opposite effect also exists, where a microwave antenna converts the magnetic field generated by spin waves traveling in the magnet to an alternating current, thus allowing both the excitation and detection of spin waves.

Furthermore, the spatial Fourier transform of the antenna will determine the shape in k -space of the wave packet. Usually, either one of two approaches is employed. The first is simply an antenna of width L , which will excite all modes approximately up to a wave number $2\pi/L$. This is what is used to theoretically describe the excitation of magnons in Chapter 4. Alternatively, by designing an antenna with a spacing λ , as shown in Fig. 1.2, the antenna only excites modes with approximately the wave number $k = 2\pi/\lambda$ [24]. This approach is considered in Chapter 2 in order to distinguish the effects of long- and short-wavelength spin waves.

1.5 WAVE PACKET DYNAMICS

In this Thesis we are predominantly interested in the dynamics of spins on a lattice. On a lattice, the eigenstates, $|\psi_{n\mathbf{k}}\rangle$, of the spin wave Hamiltonian $H_{\mathbf{k}}$ obey Bloch's theorem,

$$\langle \hat{\mathbf{r}} | \psi_{n\mathbf{k}} \rangle = \frac{1}{\sqrt{N}} e^{i\mathbf{k} \cdot \mathbf{r}} u_{n\mathbf{k}}(\mathbf{r}), \quad (1.25)$$

where $u_{n\mathbf{k}}$ is a periodic function with the same periodicity as the lattice. Here the label n refers to the band index.

The dynamics of the Bloch spin waves then follow from considering a spin-wave wavepacket in band n , well localized around $(\mathbf{r}_c, \mathbf{k}_c)$ in phase space,

$$|\Psi_n\rangle = \frac{1}{\sqrt{N}} \sum_{\mathbf{k}} e^{-i\mathbf{k} \cdot \mathbf{r}_c} w_{n\mathbf{k}} |\phi_{n\mathbf{k}}\rangle, \quad (1.26)$$

where

$$w_{n\mathbf{k}} = |w_{n\mathbf{k}}| e^{i(\mathbf{k} - \mathbf{k}_c) \cdot \mathcal{A}_{\mathbf{k}_c}} \quad (1.27)$$

is a periodic weighing function. The amplitude determines the range of wave numbers involved, $\Delta\mathbf{k}$, which has to be sharply peaked around \mathbf{k}_c for the wave packet to be well defined [25]. The phase factor $i(\mathbf{k} - \mathbf{k}_c) \cdot \mathcal{A}_{\mathbf{k}_c}$ carries information about the spatial location of the wave packet and has to be carefully chosen in order for the wave packet to be localized in space.¹ Furthermore, since the wavepacket has to be normalized, $\langle \Psi_n | \Psi_n \rangle = 1$, we have that $\sum_{\mathbf{k}} |w_{n\mathbf{k}}|^2 = 1$.

We will derive the phase $\mathcal{A}_{\mathbf{k}}$ by requiring that

$$\langle \Psi_n | \mathbf{r} - \mathbf{r}_c | \Psi_n \rangle = 0, \quad (1.28)$$

which becomes

$$\begin{aligned} & \langle \Psi_n | \mathbf{r} - \mathbf{r}_c | \Psi_n \rangle \\ &= \int \frac{d\mathbf{r}}{N} \sum_{\mathbf{k}\mathbf{k}'} w_{n\mathbf{k}'} w_{n\mathbf{k}}^* u_{n\mathbf{k}'} u_{n\mathbf{k}}^* \frac{\partial}{\partial i\mathbf{k}'} e^{i(\mathbf{k}' - \mathbf{k}) \cdot (\mathbf{r} - \mathbf{r}_c)} \end{aligned} \quad (1.29)$$

$$= - \int_{\Omega} d\mathbf{r} \sum_{\mathbf{k}\mathbf{k}'} \delta_{\mathbf{k}\mathbf{k}'} w_{n\mathbf{k}} w_{n\mathbf{k}}^* u_{n\mathbf{k}}^* \frac{\partial}{\partial i\mathbf{k}'} [w_{n\mathbf{k}'} u_{n\mathbf{k}'}] \quad (1.30)$$

$$= - \int_{\Omega} d\mathbf{r} \sum_{\mathbf{k}} |w_{n\mathbf{k}}|^2 u_{n\mathbf{k}}^* \frac{\partial u_{n\mathbf{k}}}{\partial i\mathbf{k}} + |u_{n\mathbf{k}}|^2 w_{n\mathbf{k}}^* \frac{\partial w_{n\mathbf{k}}}{\partial i\mathbf{k}}, \quad (1.31)$$

where we have used Bloch's theorem, Eq. (1.25), to replace the eigenfunction with the periodic functions $u_{n\mathbf{k}}$ and performed integration by parts² over \mathbf{k}' ,

¹ Here one might worry that we have already constrained the phase factor to the form $i(\mathbf{k} - \mathbf{k}_c) \cdot \mathcal{A}_{\mathbf{k}_c}$, but this is of course no accident, as will be clear later on.
² In order to perform the integration by parts, we convert between sums and integrals in the thermodynamic limit using the relation $\frac{1}{N} \sum_{\mathbf{k}} \leftrightarrow \left(\frac{a}{2\pi}\right)^d \int d^d k$, where d is the dimension.

and finally performing the integral over all space. Here \int_{Ω} refers to integration over the first Brillouin zone. We now make use of that fact that: (1) $|w_{n\mathbf{k}}|^2$ is sharply peaked around \mathbf{k}_c , allowing us to replace $\mathbf{k} \rightarrow \mathbf{k}_c$, and sums to 1; (2) $|u_{n\mathbf{k}}|^2$ integrates to 1 over the Brillouin zone and (3) from Eq. (1.27) we have that $\partial_{\mathbf{k}_c} w_{n\mathbf{k}_c} = iw_{n\mathbf{k}_c} \hat{\mathbf{k}}_c \cdot \partial_{\mathbf{k}_c} \mathcal{A}_{\mathbf{k}_c}$ (since $|w_{n\mathbf{k}}|$ has a maximum at \mathbf{k}_c and thus its derivative vanishes). We therefore obtain that

$$\langle \Psi_n | \mathbf{r} - \mathbf{r}_c | \Psi_n \rangle = i \left[\int_{\Omega} d\mathbf{r} u_{n\mathbf{k}_c}^* \frac{\partial u_{n\mathbf{k}_c}}{\partial \mathbf{k}_c} \right] - \mathcal{A}_{\mathbf{k}_c} \quad (1.32)$$

and thus, in order to have the wave packet well localized at \mathbf{r}_c , we require that

$$\mathcal{A}_{\mathbf{k}_c} = i \int_{\Omega} d\mathbf{r} u_{n\mathbf{k}_c}^* \frac{\partial u_{n\mathbf{k}_c}}{\partial \mathbf{k}_c}, \quad (1.33)$$

which is a quantity known as the Berry connection. It contains information about the geometric phase of the eigenfunctions, and it will play an important role in the wave packet dynamics.

The dynamics can be found from the Lagrangian,

$$\mathcal{L} = \langle \Psi_{n\mathbf{k}} | i\hbar \frac{\partial}{\partial t} | \Psi_{n\mathbf{k}} \rangle - \langle \Psi_{n\mathbf{k}} | \hat{H} + U(\mathbf{r}) | \Psi_{n\mathbf{k}} \rangle, \quad (1.34)$$

$$= \hbar \mathbf{k} \cdot \dot{\mathbf{r}} + \hbar \dot{\mathbf{k}} \cdot \mathcal{A}_{\mathbf{k}} - \varepsilon_{n\mathbf{k}} - U(\mathbf{r}), \quad (1.35)$$

where \hat{H} is a periodic spin wave Hamiltonian with eigenvalues $\varepsilon_{n\mathbf{k}}$ and we have included a potential $U(\mathbf{r})$. Since the Lagrangian only depends on $\mathbf{k}_c, \mathbf{r}_c$, we have dropped the c subscript, and we furthermore assume there are no interband transitions and thus drop the subscript n .¹

We then obtain from the Euler-Lagrange equations the following equations of motion [26]

$$\dot{\mathbf{r}} = \frac{1}{\hbar} \frac{\partial \varepsilon_{\mathbf{k}}}{\partial \mathbf{k}} - \dot{\mathbf{k}} \times \mathbf{\Omega}_{\mathbf{k}}, \quad (1.36)$$

$$\hbar \dot{\mathbf{k}} = -\nabla_{\mathbf{r}} U(\mathbf{r}), \quad (1.37)$$

where $\mathbf{\Omega}_{\mathbf{k}} = \nabla_{\mathbf{k}} \times \mathcal{A}_{\mathbf{k}}$ is a vector called the Berry curvature. From the equations of motion one can readily see that a non-zero Berry curvature will induce an anomalous velocity

$$\mathbf{v}_{\mathbf{k}}^a = -\frac{1}{\hbar} \mathbf{F} \times \mathbf{\Omega}_{\mathbf{k}} \quad (1.38)$$

¹ Here it might seem that the Berry connection $\mathcal{A}_{\mathbf{k}}$ is the property of a single magnon band, but it is actually intimately related to interband transitions and will be zero in the presence of a single band in the system. It can however be conveniently written in this form, where it will affect the dynamics of a single band.

due to a force $\mathbf{F} \equiv -\nabla U(\mathbf{r})$. Here one might question the existence of such a force in the magnon case, but as was shown by Xiao *et al.* [27], this force need not be microscopic, but could also be a statistical force, i.e., the presence of a temperature or chemical potential gradient. In Chapter 3 we will show in more detail how this can be derived.

The Berry curvature has to be calculated from the eigenfunctions of the specific spin wave Hamiltonian, and is generally non-zero. However, under simultaneous inversion and time-reversal symmetry it vanishes. This can be seen from the fact that under time reversal \mathbf{k} flips sign, but $\mathcal{A}_{\mathbf{k}}$ is unchanged, see Eq. (1.33), and thus $\Omega_{\mathbf{k}} = -\Omega_{-\mathbf{k}}$. However, under inversion symmetry both \mathbf{k} and \mathbf{r} and thus $\mathcal{A}_{\mathbf{k}}$ change sign, implying $\Omega_{\mathbf{k}} = \Omega_{-\mathbf{k}}$. Therefore, under simultaneous inversion and time-reversal symmetry the Berry curvature must be zero.

1.6 DYNAMICS OF THE MAGNON DISTRIBUTION FUNCTION

It might seem that the magnon dynamics are fully described by the equations of motion as derived in Eqs. (1.36) and (1.37), but this situation is misleading. In any magnetic system there will be higher order interactions between the spin waves, the spin waves will couple to other (quasi)-particles, such as phonons and electrons, and will also scatter off impurities. These interactions are challenging to incorporate in an Hamiltonian formalism, let alone make progress towards solving it.

It turns out that a precise knowledge of these processes is often not necessary if all one is interested in are the collective transport properties of a large number of spin waves. In this case, we can make further progress within a more phenomenological approach. We consider N spin waves living in the phase space defined by (\mathbf{r}, \mathbf{k}) , which are distributed as

$$dN = f(\mathbf{r}, \mathbf{k}, t) d\mathbf{r}d\mathbf{k}, \quad (1.39)$$

where $f(\mathbf{r}, \mathbf{k}, t)$ is a probability density function describing the number of spin waves, dN , within a phase space volume element $d\mathbf{r}d\mathbf{k}$. In the absence of collisions, the phase space volume element $d\mathbf{r}d\mathbf{k}$ is constant, and thus after a time Δt we have that

$$f(\mathbf{r} + \dot{\mathbf{r}} \Delta t, \mathbf{k} + \dot{\mathbf{k}} \Delta t, t + \Delta t) d\mathbf{r}d\mathbf{k} = f(\mathbf{r}, \mathbf{k}, t) d\mathbf{r}d\mathbf{k}, \quad (1.40)$$

where $\dot{\mathbf{r}}, \dot{\mathbf{k}}$ are given by Eqs. (1.36) and (1.37). We now turn to the collisions, which change the total number of particles over a time Δt in a space volume element by

$$dN_{\text{coll}} = (\Gamma[f(\mathbf{r}, \mathbf{k}, t)]_{\text{in}} - \Gamma[f(\mathbf{r}, \mathbf{k}, t)]_{\text{out}}) \Delta t d\mathbf{r}d\mathbf{k}, \quad (1.41)$$

where $\Gamma[f(\mathbf{r}, \mathbf{k}, t)]_{\text{in,out}}$ are the total rates scattering into and out of spin wave state (\mathbf{r}, \mathbf{k}) . Here it is important that this approach is only valid if the collisions are weak, such that the dynamics of the spin waves in between collisions are still given by the wave packet equations of motion.

Combining Eqs. (1.39) to (1.41) and taking the limit $\Delta t \rightarrow 0$ we obtain

$$\frac{\partial f}{\partial t} + \dot{\mathbf{r}} \cdot \nabla_{\mathbf{r}} f + \dot{\mathbf{k}} \cdot \nabla_{\mathbf{k}} f = \Gamma[f]_{\text{in}} - \Gamma[f]_{\text{out}}, \quad (1.42)$$

which is known as the *Boltzmann equation*. It describes the complete evolution of the probability density of particles, including collisions.

Equation (1.42) might seem relatively simple, but this is deceptive, since the $\Gamma[f]_{\text{in,out}}$ collision terms are not yet specified. Generally speaking they are non-local and nonlinear operators in $f(\mathbf{r}, \mathbf{k}, t)$ [28], and thus closed solutions to the Boltzmann equation are often not available. However, there are certain assumptions one can make about the collision terms, which make the problem tractable. Most importantly, one expects the collision terms to relax the distribution function f toward thermal equilibrium. Since the equilibrium distribution for spin waves is the Bose-Einstein distribution, we can write down a simple form, known as the *relaxation time approximation*, for the collision term

$$\Gamma[f] = \frac{1}{\tau} (f - n_B), \quad (1.43)$$

where τ is the relaxation time and

$$n_B = \frac{1}{e^{(\epsilon_{\mathbf{k}} - \mu(\mathbf{r}))/k_B T(\mathbf{r})} - 1} \quad (1.44)$$

is the Bose-Einstein distribution with some temperature $T(\mathbf{r})$ and chemical potential $\mu(\mathbf{r})$, which we have allowed to be position dependent in order to incorporate non-equilibrium setups, such as a temperature gradient. Since spin waves are not conserved, the chemical potential in equilibrium is zero. However, out of equilibrium the chemical potential can be non-zero, describing a long-lived non-equilibrium magnon state.

1.7 DIFFUSION MODEL

We will next apply the relaxation time approximation to an isotropic magnetic insulator at room temperature, following in large the derivation by Cornelissen *et al.* [29], but incorporating the anomalous velocity. In this system, there are a number of collision sources that need to be taken into account: (1) The magnon relaxation into the phonon bath, parametrized by τ_{mr} , which is approximated by the Gilbert damping at low energies. This will drive the magnon distribution function to the phonon distribution function, parametrized by a temperature T_p . (2) The elastic scattering of magnons off defects,

parametrized by τ_{el} and (3) from each other through magnon-magnon interactions, parametrized by τ_{mm} . Both of these processes conserves magnon number, and therefore on the timescale set by τ_{mc} the magnon distribution function will be driven to a Bose-Einstein function with magnon chemical potential μ_m and a magnon temperature T_m , where $1/\tau_{mc} = 1/\tau_{el} + 1/\tau_{mm}$. (4) There are also magnon-phonon processes that conserve magnon number, parameterized by τ_{mp} , driving the magnon distribution function to the phonon distribution function with temperature T_p but with a chemical potential μ_m , since the magnon number is conserved in this process.

Therefore, allowing for a finite Berry curvature and thus an anomalous velocity, we find the Boltzmann equation

$$\begin{aligned} \frac{\partial f}{\partial t} + \left(\frac{1}{\hbar} \frac{\partial \varepsilon_{\mathbf{k}}}{\partial \mathbf{k}} + \mathbf{F} \times \boldsymbol{\Omega}_{\mathbf{k}} \right) \cdot \nabla_{\mathbf{r}} f = & \frac{1}{\tau_{mc}} \left[f - n_B \left(\frac{\varepsilon_{\mathbf{k}} - \mu_m}{k_B T_m} \right) \right] \\ & + \frac{1}{\tau_{mr}} \left[f - n_B \left(\frac{\varepsilon_{\mathbf{k}}}{k_B T_p} \right) \right] \\ & + \frac{1}{\tau_{mp}} \left[f - n_B \left(\frac{\varepsilon_{\mathbf{k}} - \mu_m}{k_B T_p} \right) \right] \end{aligned} \quad (1.45)$$

where we have left the force \mathbf{F} unspecified for now. Here the distributions functions are chosen to represent the fact that the elastic, magnon-magnon and magnon-phonon scattering processes conserve magnon number and thus the scattering processes stop when f approaches a Bose-Einstein distribution with a finite chemical potential μ_m . Similarly, the temperatures T_m and T_p are chosen to express the fact that energy is exchanged with the phonon bath in the magnon relaxation and magnon-phonon scattering processes. We will allow the magnon chemical potential to be position dependent, in order to model the deviations from the equilibrium. In principle, the magnon temperature could also be position dependent, but for simplicity we will disregard this.

At room temperature in Yttrium Iron Garnet (YIG), a typical ferromagnetic insulator, $\tau_{mc} \ll \tau_{\eta}$ for $\eta \in \{mr, mp\}$. Therefore, on the fastest time scale the system will be driven towards the Bose-Einstein distribution with a magnon chemical potential μ_m and magnon temperature T_m , as can also be seen from Eq. (1.45). We can thus approximate the local distribution as the sum of a drift term δf and a local Bose-Einstein distribution

$$f(\mathbf{r}, \mathbf{k}, t) = n_B \left(\frac{\varepsilon_{\mathbf{k}} - \mu_m(\mathbf{r})}{k_B T_m} \right) + \delta f(\mathbf{r}, \mathbf{k}). \quad (1.46)$$

From the Boltzmann Eq. (1.45) we can then solve for the local drift term and find

$$\delta f(\mathbf{r}, \mathbf{k}) = \tau \frac{\partial n_B \left(\frac{\varepsilon_{\mathbf{k}}}{k_B T_p} \right)}{\partial \varepsilon_{\mathbf{k}}} \left(\frac{1}{\hbar} \frac{\partial \varepsilon_{\mathbf{k}}}{\partial \mathbf{k}} \right) \cdot \nabla_{\mathbf{r}} \mu_m(\mathbf{r}), \quad (1.47)$$

where $1/\tau = 1/\tau_{\text{mr}} + 1/\tau_{\text{mp}}$.

Finally, after expanding the collision terms up to first order in magnon chemical potential and inserting the drift term back in the Boltzmann equation we obtain

$$\partial_t f + \nabla_{\mathbf{r}} \cdot \mathbf{j}_m = -\frac{1}{\tau_{\text{mr}}} \frac{\partial n_B \left(\frac{\varepsilon_{\mathbf{k}}}{k_B T_p} \right)}{\partial \varepsilon_{\mathbf{k}}} \mu_m, \quad (1.48)$$

where $\mathbf{j}_m = \frac{1}{\hbar} \frac{\partial \varepsilon_{\mathbf{k}}}{\partial \mathbf{k}} \delta f$ is the magnon current. Here only the drift term δf contributes to the non-equilibrium transport, since by construction the left and right hand side of Eq. (1.45) cancel for the equilibrium distribution $n_B \left(\frac{\varepsilon_{\mathbf{k}} - \mu_m(\mathbf{r})}{k_B T_m} \right)$. Furthermore, we can observe that the Berry curvature does not (yet) play role in transport. In order to derive its contribution one has to explicitly consider interband transitions, as we will show in Chapter 3. Alternatively, one can use the fact that a chemical potential gradient results in a statistical force, thus replacing $\mathbf{F} \rightarrow \nabla_{\mathbf{r}} \mu_m$ and adding this to the current, such that [27]

$$\mathbf{j}_m = \frac{1}{\hbar} \frac{\partial \varepsilon_{\mathbf{k}}}{\partial \mathbf{k}} \delta f + n_B \left(\frac{\varepsilon_{\mathbf{k}}}{k_B T_p} \right) (\nabla \mu_m \times \mathbf{\Omega}_{\mathbf{k}}). \quad (1.49)$$

This procedure might seem ad-hoc here, but we will show in Chapter 3 that it matches (up to some constants) the results of a more rigorous derivation.

Equation (1.48) describes the out of equilibrium response of the magnetic insulator in terms of a locally varying magnon chemical potential. To be explicit, we now consider a two-dimensional thin film with a finite Berry curvature (the same setup as considered in Chapter 3) such that $\mathbf{\Omega}_{\mathbf{k}} = \Omega_{\mathbf{k}} \hat{z}$.¹ Ultimately, the observable we are interested in is the magnon spin density,

$$\rho(\mathbf{r}, t) = \hbar \int \frac{d^2 k}{(2\pi)^2} f(\mathbf{k}), \quad (1.50)$$

which, following Eq. (1.48), obeys the continuity equation

$$\partial_t \rho + \sum_{\alpha} \partial_{r_{\alpha}} J_m^{\alpha} = \frac{1}{\tau_{\text{mr}}} \frac{\partial \rho}{\partial \mu_m} \mu_m, \quad (1.51)$$

where $\alpha \in \{x, y\}$, the magnon spin current is

$$J_m^{\alpha} = \sigma_s \partial_{r_{\alpha}} \mu_m + \sigma_s^a \sum_{\beta} \varepsilon^{\alpha\beta} \partial_{r_{\beta}} \mu_m, \quad (1.52)$$

with $\varepsilon^{\alpha\beta}$ the two-dimensional Levi-Civita symbol,

$$\sigma_s = \hbar \tau \int \frac{d^2 k}{(2\pi)^2} \frac{\partial n_B \left(\frac{\varepsilon_{\mathbf{k}}}{k_B T_p} \right)}{\partial \varepsilon_{\mathbf{k}}} \left(\frac{1}{\hbar} \frac{\partial \varepsilon_{\mathbf{k}}}{\partial \mathbf{k}} \right)^2 \quad (1.53)$$

¹ Note that a finite Berry curvature requires at least two bands, and therefore sums over the bands are also implied here.

is the magnon spin conductivity and

$$\sigma_s^a = \hbar \int \frac{d^2k}{(2\pi)^2} n_B \left(\frac{\varepsilon_{\mathbf{k}}}{k_B T_p} \right) \Omega_{\mathbf{k}} \quad (1.54)$$

is the anomalous conductivity. The quantities follow from integrating Eq. (1.48) over momentum space and multiplying by \hbar , analogous to the definition of the magnon spin density, Eq. (1.50). We can now conclude that a magnon chemical potential gradient will lead to an anomalous current perpendicular to the propagation direction induced by the Berry curvature, as can be seen from the Levi-Civita symbol in the anomalous spin current. However, from the anomalous conductivity, Eq. (1.54), it is also clear that this description is not complete, since the anomalous conductivity is independent of τ and therefore does not include the magnon relaxation processes. The more complete derivation in Chapter 3 takes these effects properly into account.

From the combined Eqs. (1.51) and (1.52) we obtain a diffusion equation

$$\nabla_{\mathbf{r}}^2 \mu_m(\mathbf{r}) = \mu_m / l_m^2, \quad (1.55)$$

which shows that the magnon chemical potential diffuses over a characteristic length scale

$$l_m = \sqrt{\frac{\tau_{mr} \sigma_s}{\partial \rho / \partial \mu_m}}. \quad (1.56)$$

The diffusion equation (1.55) is isotropic, since $\partial_{\beta} J_m^{\alpha} = -\partial_{\alpha} J_m^{\beta}$ for $\alpha \neq \beta$, and therefore does not contain an anomalous current contribution. This is not an accident, and is related to the fact that the anomalous current is a boundary effect. To see this, we have to consider the boundary conditions, requiring at the boundary that the current perpendicular to the sample vanishes, $\mathbf{J}_m \cdot \hat{\mathbf{n}} = 0$, such that (considering a boundary along the \hat{x} direction and thus requiring that $J_m^y = 0$)

$$\left(\sigma_s \partial_{r_y} + \sigma_s^a \partial_{r_x} \right) \mu_m = 0, \quad (1.57)$$

which makes it clear that there is an anomalous current at the boundary, induced by the non-zero Berry curvature of the bands.

1.8 ELECTRICAL SPIN INJECTION AND DETECTION

We have now described the magnon diffusion within a ferromagnet, but in order to accurately measure this effect, one also needs to a way to inject and detect spin, i.e., raise and detect the magnon chemical potential. To this end, a normal metal (NM) can be employed, where a charge current, j_c , will generate a transverse spin current, j_s , due to the spin Hall effect [30]. The opposite effect, the inverse spin Hall effect, will induce a charge current from a spin

current. These two effects therefore offer a convenient tool to generate and detect spin currents. The spin Hall effect is related to the anomalous Hall effect, since it also generates a transverse spin current from an unpolarized charge current.¹ Furthermore, the origin for both effects is the spin-orbit coupling, which generates an asymmetric deflection of the charge carriers. However, the spin Hall effect does not require a finite magnetization and is thus present also in normal metals. Since the spin Hall effect results from the spin-orbit coupling, heavy metals, such as Platinum, are often employed in order to obtain large transverse spin currents.

We consider a ferromagnetic insulator interfaced with two normal metals [31], as indicated in Fig. 1.3. We focus first on the left interface, where there exists an interfacial exchange coupling between the localized spins in the magnetic insulator and the itinerant spins in the normal metal, which is phenomenologically described by

$$V_{\text{int}} = \int dx dx' V(x, x') \hat{\mathbf{S}}(x) \cdot \hat{\mathbf{s}}(x'), \quad (1.58)$$

where we have assumed the coupling to be isotropic and local to the interface. Here $\hat{\mathbf{S}}(x)$ is the spin density in the ferromagnet and $\hat{\mathbf{s}}(x)$ is the spin density of the electrons in the metal, given by

$$\hat{\mathbf{s}}(x) = \frac{\hbar}{2} \sum_{\sigma\sigma'} \psi_{\sigma'}^{\dagger}(x) \boldsymbol{\sigma}_{\sigma\sigma'} \psi_{\sigma'}(x), \quad (1.59)$$

where $\psi_{\sigma}^{\dagger}(x)$ and $\psi_{\sigma}(x)$ are the electron creation and annihilation operators respectively and $\boldsymbol{\sigma}$ are the Pauli matrices. We assume the spin density in the magnetic insulator to be classical and the temperature to be small, such that $\hat{\mathbf{S}}(x) = \hbar s \mathbf{s}$, where $s = S/a^3$ is the spin density per unit cell with volume a^3 and \mathbf{s} is a unit vector. We can then obtain an interfacial spin current [32]

$$\mathbf{I}_s^{\text{int}} = -\hbar \frac{g^{\uparrow\downarrow}}{4\pi} \mathbf{S} \times \frac{d\mathbf{S}}{dt}, \quad (1.60)$$

where $g^{\uparrow\downarrow}$ is the spin-mixing conductance. Therefore, a precessing magnetization in the ferromagnetic insulator will pump spins into an adjacent metal, leading to a spin accumulation in the metal. Furthermore, Onsager reciprocity implies that the opposite effect is also present, where a spin accumulation in the metal will lead to a spin pumping over the interface into the ferromagnet. Since by conservation of angular momentum, the spins ejected by $\mathbf{I}_s^{\text{int}}$ correspond to a torque $-\mathbf{I}_s^{\text{int}}$ on the ferromagnet, the LLG equation is modified to

$$\partial_t \mathbf{S} = -\mathbf{S} \times \mathbf{H}_{\text{eff}} + (\alpha + \alpha_{\text{sp}}) \mathbf{S} \times \partial_t \mathbf{S} + \alpha_{\text{sp}} \mathbf{S} \times (\boldsymbol{\mu} \times \mathbf{S}), \quad (1.61)$$

¹ An important difference is that the anomalous Hall effect generates a measurable polarized charge current, whilst in the spin Hall effect a pure spin current is generated, which does not result in a Hall voltage.

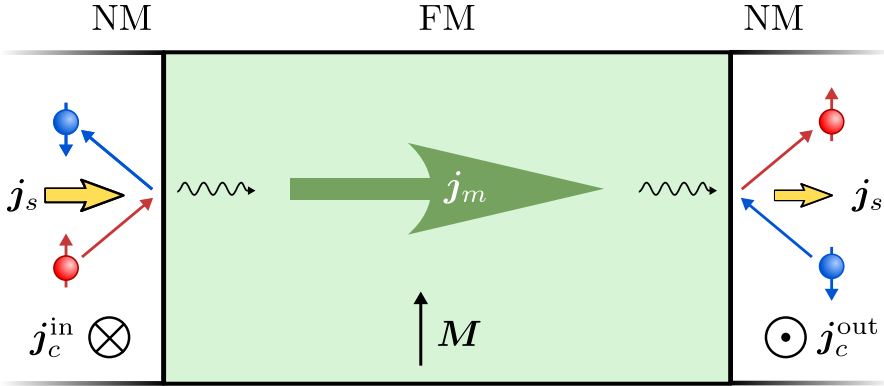


Figure 1.3: A charge current j_c in a normal metal generates a spin current j_s with polarization along \hat{z} , towards the NM|FM interface. Therefore a spin accumulation builds up at the interface, injecting magnons into the FM with the spin polarization parallel to the magnetization M . At the right interface, the opposite process occurs, driving a spin accumulation in the right normal metal and a spin current. Through the inverse spin Hall effect the spin current is converted to a charge current, which can subsequently be detected.

where $\alpha_{sp} = \hbar g^{\uparrow\downarrow}/4\pi$ and $\boldsymbol{\mu} = \mu_s \hat{z}$ is the vectorial spin accumulation [33]. Here we have conveniently incorporated the spin-pumping torque due to the precessing magnetization into an effective Gilbert damping enhancement α_{sp} [34].

Therefore, through interfacing a normal metal with a ferromagnet one can inject angular momentum, driving the spins in the ferromagnet, while the reciprocal process allows for detection of a precessing magnetization. This thus allows us to consider a setup where magnons are excited coherently using a microwave antenna, and detected electrically through a normal metal [35], as used in Chapter 2.

Linearizing the spin pumping across the interface and assuming the resulting magnons to follow the Bose-Einstein distribution, the spin pumping becomes

$$j_s^{\text{int}} = -\frac{\hbar g^{\uparrow\downarrow}}{2\pi e^2 s} \int d\epsilon D(\epsilon) (\epsilon - \mu_s) \left[n_B \left(\frac{\epsilon - \mu_m}{k_B T_m} \right) - n_B \left(\frac{\epsilon - \mu_s}{k_B T_e} \right) \right], \quad (1.62)$$

where $D(\epsilon)$ is the magnon density of states. A full derivation of this spin current is beyond the scope of this Thesis, but can be found in Refs. [31, 36, 37]. Intuitively, this process can be understood as the scattering of an electron with spin $+\hbar/2$ of the interface, flipping its spin to $-\hbar/2$ and transmitting \hbar into the ferromagnet, thus exciting a magnon, as indicated schematically

in Fig. 1.3. Expanding this up to linear order in the magnon and electron chemical potential we then find that

$$j_s^{\text{int}} = \frac{3\hbar g^{\uparrow\downarrow}}{4\pi e^2 s \Lambda^3} \zeta(3/2) (\mu_m - \mu_s), \quad (1.63)$$

where $\Lambda = \sqrt{4\pi J_s / (k_B T)}$ is the magnon thermal wavelength. Therefore, a spin accumulation μ_s in the normal metal will drive the magnons in the ferromagnetic insulator out of equilibrium. At the detector the inverse process occurs, and a chemical potential difference between the ferromagnet and the normal metal will transmit spin into the normal metal, leading to a spin accumulation and thus a spin current. This spin current will induce charge current via the inverse spin Hall, which can subsequently be electrically measured.

The electrical injection and detection is used in Chapter 3 to propose a completely electrical detection of the magnon Hall effect. Here it is important to note that electrical injection and detection is an incoherent effect, exciting all spin waves with a distribution given by the Bose-Einstein function, whereas the coherent excitation and detection via microwave antennas excites only spin waves with a specific frequency and wave number.

1.9 BULK-BOUNDARY CORRESPONDENCE

Upon close inspection, we notice that the anomalous conductivity, Eq. (1.54), depends on the integral of the Berry curvature over the Brillouin zone, weighed by the Bose-Einstein distribution function. Here there is an important topological connection, since the the integral of the Berry curvature, called the Chern number C_n , over a *closed* manifold is quantized in units of 2π , i.e., [38]

$$C_n \equiv \frac{1}{2\pi} \int_{\Omega} d^2k \Omega_n = \mathbb{Z}. \quad (1.64)$$

This implies that the Chern number of a single band n in the Brillouin zone is quantized, as long as the band is gapped. Furthermore, by adiabatically changing the Hamiltonian the Chern number cannot be changed without closing the energy gap. Therefore, we can classify all the Hamiltonians that can be adiabatically deformed into each other without closing the energy gap using the Chern number of the energy bands. This has important consequences when we consider the interface between two Hamiltonians where the bands have different Chern numbers.

To illustrate this, let us imagine a system where there is a boundary between a trivial Hamiltonian (all bands have Chern number zero) and a non-trivial Hamiltonian (the bands have non-zero Chern numbers). The system parameters are tuned in such a way that over the boundary there is continuous

transition between the two phases. Starting at the trivial side of the boundary, in order for the Chern number to change, the energy gap has to vanish, thus implying the existence of boundary modes with energies that cross the bulk band gap. This principle is known as the *bulk-boundary correspondence* and it is a topological effect, since it results from the topology of the bands. It is not only valid for two-dimensional systems with finite Berry curvature as considered here, but can be found in a wide myriad of systems [39–41]. These boundary states are unique in condensed matter, because they are required to form at an interface between topologically trivial—including the vacuum—and non-trivial systems. This implies that any perturbation which does not change the topology of the system cannot prevent the formation of the boundary states. Because of this topological property, the boundary states are remarkably robust against perturbations and are therefore often referred to as being *topologically protected*.

We note here that in the diffusive magnon systems as considered in Section 1.7 the bulk-boundary correspondence will lead to a finite anomalous conductivity. Because of the topological protection of the edge states, this anomalous conductivity is then robust against disorder and other perturbations.

1.10 MAGNON CHERN INSULATOR

We now consider the magnon Chern insulator using the Haldane model [42], which is a simple realization of a system where the bands have a non-zero Chern number and thus has the topological properties as discussed above. The Haldane model was first introduced for electrons with a staggered magnetic field, but for magnons the same model can be realized [43, 44]. The spins are placed on a honeycomb lattice as indicated in Fig. 1.4, and are described by the two-dimensional Hamiltonian

$$\mathcal{H} = -\frac{1}{2} \sum_{ij} [J_{ij} \hat{\mathbf{S}}_i \cdot \hat{\mathbf{S}}_j - D_{ij} \hat{\mathbf{z}} \cdot (\hat{\mathbf{S}}_i \times \hat{\mathbf{S}}_j)] - h \sum_i \hat{S}_i^z, \quad (1.65)$$

where \mathbf{S}_i are spins with quantum number S located on lattice sites \mathbf{R}_i of a honeycomb lattice. Nearest neighbors experience an exchange coupling, $J_{ij} = J$, and next-nearest neighbors are coupled through the Dzyaloshinskii-Moriya interaction, $D_{ij} = -D_{ji} = D$. The spins are aligned to an external magnetic field applied in the z direction, contributing a Zeeman energy h .

The classical dynamics are described by the Landau-Lifshitz-Gilbert equation (1.14) and we introduce the deviations $m_i = (S_i^x + iS_i^y)/\sqrt{2S}$ around the

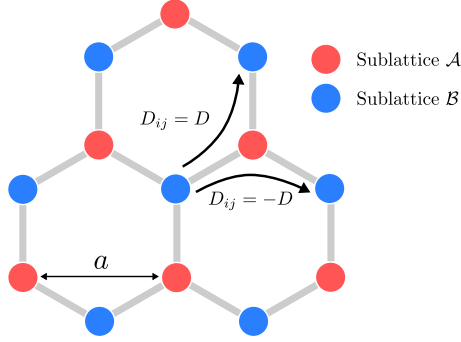


Figure 1.4: The honeycomb lattice of the Haldane model considered here. The relative sign of the Dzyaloshinskii-Moriya interaction is indicated. The nearest and next-nearest neighbor vectors are $\delta = [(0, -a/\sqrt{3}), (a/2, a/\sqrt{3}), (-a/2, a/\sqrt{3})]^T$, and $\rho = [(a, 0), (-a/2, \sqrt{3}a/2), (-a/2, -\sqrt{3}a/2)]^T$ respectively.

uniform state, $S_i = S\hat{z}$. We expand the Hamiltonian, Eq. (1.65), up to the first nontrivial order in m_i , and obtain the quadratic Hamiltonian

$$\mathcal{H}_2 = \sum_{ij} \left[\delta_{ij} \left(h + S \sum_n J_{in} \right) - S(J_{ij} + iD_{ij}) \right]. \quad (1.66)$$

We introduce the Fourier transform of the spin-wave operators, $m_{A/B,i} = \sqrt{2/N} \sum_{\mathbf{k}} e^{i\mathbf{k} \cdot \mathbf{R}_i} m_{A/B,\mathbf{k}}$ for the sublattices \mathcal{A}/\mathcal{B} , and obtain the Hamiltonian

$$\mathcal{H}_{\mathbf{k}} = \sum_{\mathbf{k}} \Psi_{\mathbf{k}}^\dagger [(H + 3JS)\sigma_0 + \mathbf{h}_{\mathbf{k}} \cdot \boldsymbol{\sigma}] \Psi_{\mathbf{k}}, \quad (1.67)$$

where $\Psi_{\mathbf{k}} = (m_{A,\mathbf{k}}, m_{B,\mathbf{k}})^T$ is the magnon state vector, σ_η are the Pauli matrices in the sublattice space, $\boldsymbol{\sigma}$ is a pseudovector of Pauli matrices and

$$\mathbf{h}_{\mathbf{k}} = S \sum_i \begin{pmatrix} -J \cos(\mathbf{k} \cdot \boldsymbol{\delta}_i) \\ J \sin(\mathbf{k} \cdot \boldsymbol{\delta}_i) \\ 2D \sin(\mathbf{k} \cdot \boldsymbol{\rho}_i) \end{pmatrix}, \quad (1.68)$$

where $\boldsymbol{\delta}_i$ and $\boldsymbol{\rho}_i$ are the vectors connecting nearest and next-nearest neighbors respectively. The magnon dispersion follows as $\omega_{\mathbf{k}}^\pm = H + 3SJ \pm |\mathbf{h}_{\mathbf{k}}|$, which we show in Fig. 1.5a. It is clear that we obtain two bands, separated by a band gap, which is opened up by the DMI. The Chern number of this model is quantized¹ and in Fig. 1.5a we have indicated the Chern numbers of the

¹ Calculating the Berry curvature requires a gauge where the Bloch wave-functions are continuous, but if only the Chern number is required, it can easily be calculated with the algorithm as suggested by Fukui *et al.* [45], which does not require a specific gauge choice.

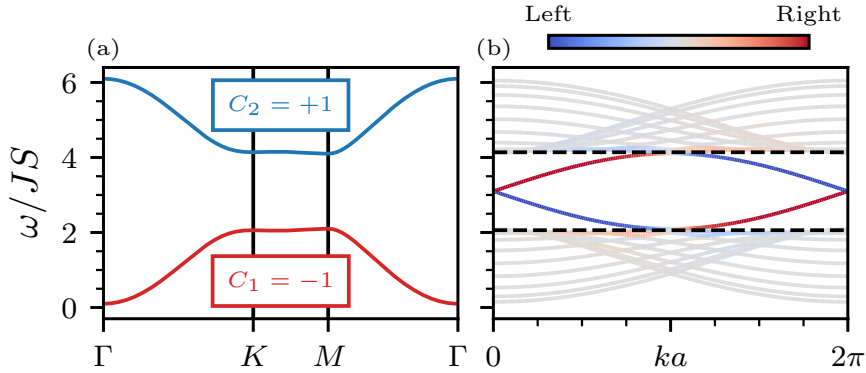


Figure 1.5: (a) The bulk spectrum of the magnon Haldane model, with the Chern numbers C_n indicated. (b) The spectrum of a nanoribbon with zigzag edges for the magnon Haldane model, with the localization indicated in the colorscale. $D/J = -0.2$.

bands. Since the Chern numbers are non-zero and the two bands are gapped, this system is said to be in a topologically non-trivial phase. From the bulk-boundary correspondence we thus expect edge modes connecting the two bands with opposite Chern number.

We show these edge modes explicitly in Fig. 1.5b, by considering the band-structure of a ribbon, with periodic boundary conditions along one direction and open boundary conditions along the other direction. The color scale indicates the localization of the eigenvectors associated with the frequencies.¹ We observe the existence of the bulk bands, which are not localized on one side of the ribbon, and are separated by a bulk band gap. Within the bulk band gap, there are edge modes connecting the two bulk bands, localized on opposite sides of the ribbon. There is one left- and one right-moving edge mode, where the doubling here is due the fact that we have two boundaries: one on the top and one on the bottom. There is therefore only one edge mode one each side of the sample, which move in opposite directions, and are therefore chiral.

The edge modes that exist at the boundaries of a Chern insulator are topologically protected, meaning that as long as the Chern number of the bands is unchanged the edge states remain. This implies that the edge states are stable against any perturbation that does not close the bulk energy gap, since the Chern number can only change through a band closing. Therefore, the edge states form at any boundary of the Chern insulator, independent of the specific shape of the edge. Furthermore, the chirality of the edge states

¹ The localization is defined as $\|\Psi_{\mathbf{k}}(r_t)\| - \|\Psi_{\mathbf{k}}(r_b)\|$, where $r_{t,b}$ is the top or bottom half of the ribbon.

implies that there are no other states to scatter into, thus increasing the lifetime of the state. In electronic systems this implies perfectly quantized conductance,¹ but in magnon systems this does not happen because of the existence of magnon-number non-conserving processes, as parameterized by Gilbert damping, and the Bose-Einstein statistics.

In most of the magnetic insulators that have been proposed to realize the magnon Chern insulator [12, 43, 44, 47–49], the energy of the first bulk band is set by the exchange interaction, and the corresponding frequencies are in the THz-range. Direct detection and excitation, for example by Brillouin Light Scattering or microwave excitation and detection is not possible at these frequencies. The high frequency of the edge modes is one of the main reasons why the magnon Chern insulator has not been experimentally verified, even though several candidate materials have been identified [50–52]. We address this problem further in Chapter 4, by showing that the edge states can be lowered to zero frequency in a non-equilibrium state.

1.11 FURTHER TOPOLOGICAL MAGNON PHASES

The bulk-boundary correspondence is not unique to the magnon Chern insulator, but can be found in a wide range of topological magnon phases [53–63]. Their defining feature is the existence of a topological invariant, that can be used to classify their topological phase [64]. The bulk-boundary correspondence then assures the existence of boundary states in the topologically non-trivial phase. For example, in the one-dimensional Su-Schrieffer-Heeger (SSH) model, alternating coupling strengths in a chain lead to a bulk band gap and edge modes within this gap, localized on the ends of the chain [65, 66]. Again, here one can define a topological invariant similar to the Chern number, which predicts the existence of the edge states, exemplifying the power of the bulk-boundary correspondence.

Furthermore, concepts of topological order can also be extended to include the wider class of non-Hermitian systems, which are open and out-of-equilibrium [67]. With this extension comes a number of striking effects, and the full implications have most certainly not been exhausted. Most notably, in specific non-Hermitian topological systems all the modes, not just the edge modes, can collect at a boundary, leading to a skin-effect which is hyper sensitive to the boundary [68, 69]. Another striking result of the non-Hermitian topology is the existence of lasing edge modes, where the edge modes are amplified or damped [70–73].

In the magnon systems that are of interest in this Thesis, non-Hermitian Hamiltonians are readily available. The ubiquitous Gilbert damping offers

¹ The quantization is remarkably exact: in quantum Hall systems, the Hall conductance is quantized to 1 parts in 10^9 [46].

dissipation, whilst the spin-transfer torque can be used to drive or damp the system, offering on-site control. Furthermore, different non-Hermitian couplings between sites can be engineered, such as non-reciprocal [74] and dissipative couplings [75]. In this Thesis we consider two non-Hermitian topological magnon insulators, in Chapters 5 and 6, where the non-Hermiticity stems from on-site gain and loss through the spin-transfer torque. Their central feature is the topological protection of the edge states, which become spontaneously lasing (Chapter 5) or have an enhanced lifetime (Chapter 6).

1.12 OUTLINE

The remainder of this Thesis is outlined as follows. The first two Chapters 2 and 3 are concerned with the topological effects rooted in the dipole-dipole interaction. We start in Chapter 2 with studying the propagation of spin waves in obliquely magnetized thin films. In this setup the inversion symmetry is broken due to the dipole-dipole interaction. We show that a single spin wave excited by a microwave antenna will induce a transverse spin current, which can be detected with a normal metal lead. In Chapter 3 we study how the magnon Hall effect can be detected through electrical injection and detection. If dipole-dipole interactions are taken into account, the magnons in a ferromagnetic thin film have a non-zero Berry curvature. We therefore set up a diffusion-relaxation model based on the quantum kinetic equations, rigorously deriving Eqs. (1.52) and (1.55), including the anomalous contribution. From this model we can calculate the Hall coefficient, which we show to be measurable.

In Chapters 4 to 6 we turn our attention to the topological magnon insulators. We start with the magnon Chern insulator in Chapter 4, where we address a major problem in the field of magnon topology: the high frequencies of the chiral edge modes in magnon Chern insulators. We propose a strategy to lower these chiral edge states to zero frequency, by considering a non-equilibrium setup. We show that the spin waves can be excited in the GHz-range, making them directly experimentally detectable. Next, we study two different non-Hermitian extensions of topological magnon insulators. We start with a non-Hermitian extension of a one-dimensional topological magnon insulator in Chapter 5, realized by coupling an array of spin-torque oscillators. We focus on the non-linearities inherent in any spin-wave system, and show that the edge excitations are robust. Furthermore, we incorporate stochastic fluctuations to model the finite-temperature dynamics in the presence of non-linearities, and show that the topological edge states exist up to relatively high temperatures. Finally, we consider in Chapter 6 a non-Hermitian extension of the magnon Chern insulator, and show that the chiral edge states can be topologically amplified or damped. This model also exhibits a novel non-

Hermitian hybrid skin effect, where the edge modes are localized on specific sides of the lattice, and we propose an experiment to detect this skin effect. We end with a conclusion and outlook in Chapter 7.

ELECTRICAL DETECTION OF UNCONVENTIONAL TRANSVERSE SPIN CURRENTS IN OBLIQUELY MAGNETIZED THIN FILMS

In a typical experiment in magnonics, thin films are magnetized in-plane and spin waves only carry angular momentum along their spatial propagation direction. Motivated by the experiments of Bozhko et al. [76], we show theoretically that for obliquely magnetized thin films, exchange-dipolar spin waves are accompanied by a transverse spin-current. We propose an experiment to electrically detect this transverse spin-current with Pt strips on top of a YIG film, by comparing the induced spin-current for spin waves with opposite momenta. We predict the relative difference to be of the order 10^{-4} , for magnetic fields tilted at least 30° out of plane. This transverse spin-current is the result of the long range dipole-dipole interaction and the inversion symmetry breaking of the interface.¹

2.1 INTRODUCTION.

Magnons, or spin waves, are able to transport angular momentum over long distances along their propagation direction [77, 78]. This has opened the way to novel signal processing devices which could replace conventional electronic devices [79–81]. In recent years, multiple applications have been explored, such as wave-based computing [82, 83], three-terminal transistors [84], logic gates [85, 86] and novel non-linear effects [87, 88].

The manipulation of spin waves is still an ongoing area of research and a full toolbox for controlling spin waves is yet to be developed [89]. In this work we consider an alternative approach to control the spin current in a magnetized thin film: by tilting the magnetic field out of plane. This breaks the inversion symmetry and allows a spin current to flow transverse to the propagation direction of the spin waves, transporting angular momentum along the film normal.

¹ This chapter is based on P. M. Gunnink, R. A. Duine, and A. Rückriegel, “Electrical detection of unconventional transverse spin currents in obliquely magnetized thin films,” *Physical Review B* **101**, 220407(R) (2020). R.A.D. and A.R. conceived the project, P.M.G. performed the calculations and prepared the manuscript, and A.R. derived the magnetostatic calculations. All authors contributed to the manuscript.

This mechanism for generating a transverse spin-current was first proposed by Bozhko *et al.* [76], who used a micromagnetic approach to calculate the exchange spin-current in a thin film of $\text{Y}_3\text{Fe}_2(\text{FeO}_4)_3$ (YIG), without considering spin absorption at the boundaries. They argued that this spin current is non-zero if the magnetic field is tilted out of plane. However, this transverse spin-current can only be detected with an attached spin sink, such as a heavy metal strip. The interaction with the spin sink influences the physics of the problem significantly. Moreover, only the transfer of angular momentum by the exchange interaction was considered. The dipole-dipole interaction is also capable of transporting angular momentum and therefore needs to be taken into account for a complete description of this system.

In this work we propose an experiment where the transverse spin-current in an obliquely magnetized thin film is detected electrically. We consider, within linear spin-wave theory, a thin ferromagnetic film with two leads attached, which pick up the transverse spin-current induced by left- and right-moving spin waves via the inverse spin-Hall effect (ISHE) [90]. A transverse spin-current would transport more angular momentum into the right spin sink than into the left spin sink, or vice versa. This is equivalent to the experimentally harder to realize system with leads attached to the top and bottom. We propose to compare the spin current picked up by the left and right lead, in order to exclude any usual spin pumping effects, which are also present for an in-plane magnetic field [34]. In order to further understand the origin of the transverse spin-current we show in Appendix 2.A with a magnetostatic calculation, that the symmetry breaking at the interface is carried by the dipole-dipole interaction.

2.2 METHOD.

The setup we consider is a thin film of ferromagnetic YIG, where coherent spin-waves are excited using a coplanar waveguide [24], as depicted in Fig. 2.1. The wavevector (k) of the excited magnons is controlled by the grating of the antenna and the frequency (ω) of the excited magnons by the frequency of the driving field. To the right and left of this antenna two platinum (Pt) leads are placed which function as spin sinks via the inverse spin-Hall effect and pick up the transverse spin-current induced by the spin waves with opposite momenta. The distance between the Pt leads and the coplanar waveguide is assumed to be such that the signal is strong enough to measure small variations. Structures with a separation distance of 3 mm are possible [35], but the magnon diffusion length of $\lambda = 9.4 \mu\text{m}$ in YIG [77] indicates that shorter distances would be preferable.

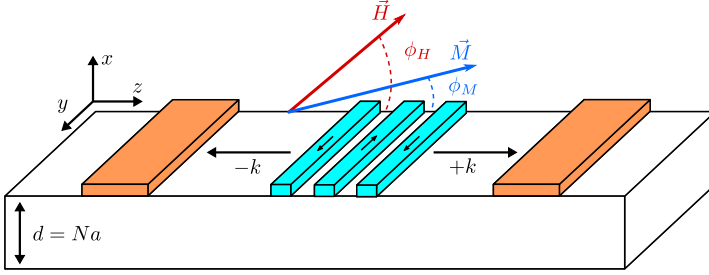


Figure 2.1: The setup considered in this chapter, with a coplanar waveguide in the middle, exciting spin waves in two opposite directions in a thin ferromagnetic film with thickness d . Two heavy-metal leads pick up the spin current induced by these left- and right-moving spin waves. The magnetic field is tilted out of plane at an angle ϕ_H with the plane and the magnetization has angle ϕ_M with the plane.

The spin dynamics are governed by the semi-classical Landau-Lifshitz-Gilbert (LLG) equation:

$$\partial_t \mathbf{S}_i = \mathbf{S}_i \times \left(-\frac{\partial \mathcal{H}}{\partial \mathbf{S}_i} + \mathbf{h}_i(t) - \frac{\alpha_i}{S} \partial_t \mathbf{S}_i \right), \quad (2.1)$$

where we describe YIG as a Heisenberg ferromagnet with effective spin S , on a cubic lattice. Including both the exchange and dipole-dipole interactions our effective Hamiltonian [91] is

$$\begin{aligned} \mathcal{H} = & -\frac{1}{2} \sum_{ij} J_{ij} \mathbf{S}_i \cdot \mathbf{S}_j - \mu \mathbf{H}_e \cdot \sum_i \mathbf{S}_i \\ & - \frac{1}{2} \sum_{ij, i \neq j} \frac{\mu^2}{|\mathbf{R}_{ij}|^3} [3 (\mathbf{S}_i \cdot \hat{\mathbf{R}}_{ij}) (\mathbf{S}_j \cdot \hat{\mathbf{R}}_{ij}) - \mathbf{S}_i \cdot \mathbf{S}_j], \quad (2.2) \end{aligned}$$

where the sums are over the lattice sites \mathbf{R}_i , with $\mathbf{R}_{ij} = \mathbf{R}_i - \mathbf{R}_j$ and $\hat{\mathbf{R}}_{ij} = \mathbf{R}_{ij} / |\mathbf{R}_{ij}|$. We only consider nearest neighbour exchange interactions, so $J_{ij} = J$ for nearest neighbours and 0 otherwise. Here $\mu = 2\mu_B$ is the magnetic moment of the spins, with $\mu_B = e\hbar / (2m_e c)$ the Bohr magneton. \mathbf{H}_e is the external magnetic field, which we take strong enough to fully saturate the ferromagnet.

To the top of the thin film we attach a spin sink to detect the spin waves, which introduces an interfacial Gilbert damping α_i^L , which is only non-zero for sites at the top interface of the ferromagnet [34]. The total Gilbert damping is then $\alpha_i = \alpha^B + \alpha_i^L$, where α^B is the bulk Gilbert damping. Furthermore, $\mathbf{h}_i(t)$ is the circularly polarized driving field, which we take to be uniform throughout the film. Within linear spin-wave theory, the LLG has been shown to be fully equivalent to the non-equilibrium Green's function formalism [92].

We consider a thin film, infinitely long in the y, z directions and with a thickness $d = Na$ in the x direction, where a is the lattice constant and N is the number of layers. The magnetic field is tilted at an angle ϕ_H with respect to the film, as shown in Fig. 2.1. The magnetization is tilted by an angle ϕ_M , as determined by minimizing the energy given by Eq. (2.2) for a classical, uniform spin configuration:

$$\frac{\partial}{\partial \phi_M} \left[-M_s H_e \cos(\phi_M - \phi_H) - 2\pi M_s^2 \cos^2 \phi_H \right] = 0, \quad (2.3)$$

where $M_s = \mu S/a^3$ is the saturation magnetization and $H_e = |\mathbf{H}_e|$.

We have two reference frames, one aligned with the thin film as described above and one where the z axis is aligned with the magnetization \mathbf{M} . We work in the reference frame of the lattice and rotate the spin operators, such that $\mathbf{S}_i \rightarrow \mathcal{R}_y^{-1}(\phi_M) \bar{\mathbf{S}}_i$, where $\mathcal{R}_y(\phi_M)$ is a rotation around the y -axis by angle ϕ_M and $\bar{\mathbf{S}}_i$ are the rotated spin operators, with the \bar{S}_i^z component pointing along the magnetization \mathbf{M} .

We linearize in the deviations from the ground state, $b_i = \frac{1}{2} \sqrt{2S} (\bar{S}_i^x + i\bar{S}_i^y)$ and assume translational invariance in the yz -plane. The equation of motion for b_i becomes in frequency space:

$$\mathbf{G}_{\mathbf{k}}^{-1}(\omega) \boldsymbol{\psi}_{\mathbf{k}}(\omega) = -\mathbf{h}_{\mathbf{k}}(\omega), \quad (2.4)$$

where $\mathbf{k} = (k_y, k_z)$ and we have introduced the driving field

$$\mathbf{h}_{\mathbf{k}}(\omega) = \underbrace{(h_{\mathbf{k}}(\omega), \dots, h_{\mathbf{k}}(\omega))}_{N \text{ elements}}, \underbrace{(h_{-\mathbf{k}}^*(\omega), \dots, h_{-\mathbf{k}}^*(\omega))}_{N \text{ elements}}^T, \quad (2.5)$$

where $h_{\mathbf{k}}(\omega) = \bar{h}_x + i\bar{h}_y$ is the Fourier transform of the rotated driving field. Furthermore, the magnon state vector is

$$\boldsymbol{\psi}_{\mathbf{k}}(\omega) = (b_{\mathbf{k}}(\omega, x_1), \dots, b_{\mathbf{k}}(\omega, x_N), b_{-\mathbf{k}}^*(\omega, x_1), \dots, b_{-\mathbf{k}}^*(\omega, x_N))^T \quad (2.6)$$

and the inverse Green's function is

$$\mathbf{G}_{\mathbf{k}}^{-1}(\omega) = \sigma_3 (1 + i\sigma_3 \alpha) \omega - \sigma_3 \mathcal{H}_{\mathbf{k}}, \quad (2.7)$$

where $\sigma_3 = \text{diag}(1, \dots, 1, -1, \dots, -1)$, $\alpha = \text{diag}(\alpha_1, \dots, \alpha_N, \alpha_1, \dots, \alpha_N)$ and

$$\mathcal{H}_{\mathbf{k}} = \begin{pmatrix} \mathbf{A}_{\mathbf{k}} & \mathbf{B}_{\mathbf{k}} \\ \mathbf{B}_{\mathbf{k}}^\dagger & \mathbf{A}_{\mathbf{k}} \end{pmatrix}, \quad (2.8)$$

is the Hamiltonian matrix within linear spin-wave theory, with the amplitude factors $[\mathbf{A}_{\mathbf{k}}]_{ij} = A_{\mathbf{k}}(x_i - x_j)$ and $[\mathbf{B}_{\mathbf{k}}]_{ij} = B_{\mathbf{k}}(x_i - x_j)$. The dispersion is obtained by diagonalizing the inverse Green's function (2.4) in the absence of

damping and spin pumping. The full expressions for the amplitude factors $A_{\mathbf{k}}, B_{\mathbf{k}}$ and the dispersions for different tilting angles of the magnetic field are given in Appendices 2.B and 2.C.

From the equation of motion, Eq. (2.4), the total spin-current injected into the lead is obtained from the continuity equation for the spin:

$$\partial_t \bar{S}_i^z + \sum_j I_{i \rightarrow j}^{\text{ex}} + \sum_j I_{i \rightarrow j}^{\text{dip-dip}} = I_i^\alpha + I_i^h. \quad (2.9)$$

The explicit form of the terms is given in Appendix 2.D. We find a source and sink term, providing angular momentum via the driving field (I_i^h) and dissipating angular momentum to the lattice and the lead via the Gilbert damping (I_i^α). There are two ways angular momentum can be transferred through the film. Firstly, there is a spin current transferring angular momentum between adjacent sites ($I_{i \rightarrow j}^{\text{ex}}$), which is driven by the exchange interaction.

The dipole-dipole interaction also transports angular momentum ($I_{i \rightarrow j}^{\text{dip-dip}}$), but because the dipole-dipole interaction is non-local, angular momentum is transferred from and to all other sites. It is therefore not possible to write this as a local divergence and thus as a current. Also note that the dipole-dipole interaction couples the magnons to the lattice, which means that a non-zero dipole-dipole contribution is accompanied by a transfer of angular momentum from and to the lattice.

The measurable quantity is the angular momentum absorbed by the spin sink in the attached lead, which is proportional to the voltage generated by the ISHE, and is given by

$$I_L^\alpha(\mathbf{k}, \omega) = 2\alpha^L \text{Im} [b_{\mathbf{k}}^*(x_1) \partial_t b_{\mathbf{k}}(x_1)]. \quad (2.10)$$

We are interested in the relative difference between the spin currents induced by the left- and right-moving spin waves in order to show a transverse spin transport, which we define as

$$\Delta(|\mathbf{k}|, \omega) = \frac{I_L^\alpha(\mathbf{k}, \omega) - I_L^\alpha(-\mathbf{k}, \omega)}{\max[|I_L^\alpha(\mathbf{k}, \omega)|, |I_L^\alpha(-\mathbf{k}, \omega)|]}. \quad (2.11)$$

In the next section we consider this quantity in detail.

2.3 RESULTS.

The parameters used throughout this work are summarized in Table. 2.1. In Fig. 2.2 we show the difference between the spin current induced by left- and right-moving spin waves for different tilting angles of the magnetic field. For a magnetic field either completely in- or out of plane there is no difference between the left and right lead (not shown). As we tilt the magnetic field out of

Table 2.1: Parameters for YIG used in the numerical calculations in this chapter. Note that S follows from $S = M_s a^3 / \mu$.

Quantity	Value
N	400
a	12.376 Å [93]
S	14.2
$4\pi M_s$	1750 G [94]
J	1.60 K [23]
α^B	7×10^{-4} [18]
α^L	7×10^{-3} [18]
H_e	2500 Oe
h_x, h_y	$0.01 H_e$

plane a small difference becomes visible, which peaks at $\Delta = 1.25 \times 10^{-4}$ for $\phi_H = 60^\circ$ and $2.5 < k < 12.5 \mu\text{m}^{-1}$. As the tilting angle is further increased the distribution of Δ shifts slightly, with the most notable change the movement of the maximum, which moves towards smaller wavevectors. We found that the relative difference Δ increases linearly with the bulk Gilbert damping constant. In order to measure this effect it might therefore be beneficial to use a YIG thin film with deliberately introduced impurities such as rare-earth ions, to increase the damping [95], or even use a different ferromagnetic material with a higher Gilbert damping.

Numerically, we found that the relative difference Δ is non-zero even when the exchange coupling is artificially turned off, which indicates that only the dipole-dipole interaction is responsible for this effect. In Appendix 2.A we show a full magnetostatic derivation of the eigenmodes for an obliquely magnetized thin film with only dipole-dipole interactions. Even though the energies are inversion-symmetric, we find that the eigenmodes explicitly depend on

$$k_z \sin(2\phi_M), \quad (2.12)$$

which introduces an asymmetry between left- and right-moving spin waves if the magnetic field is tilted out of plane. A complete description of this problem also requires the inclusion of the exchange coupling, as was done in our numerical calculations. However, ignoring the exchange coupling allows us to demonstrate that the origin of the asymmetry between left- and right-moving spin waves lies in the the long range dipole-dipole interaction carrying the inversion symmetry breaking of the interface.

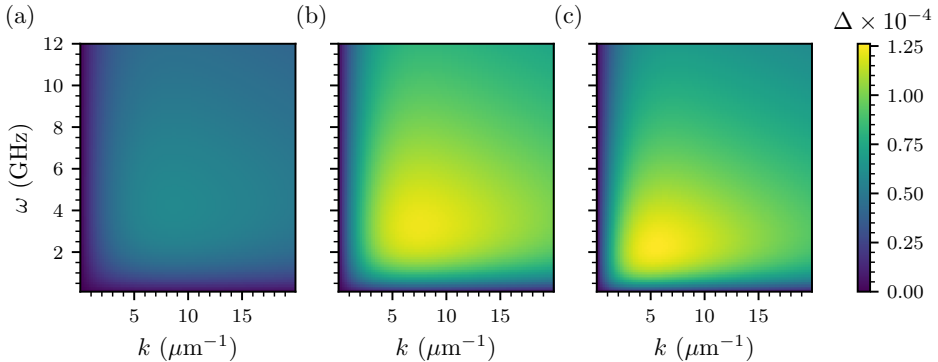


Figure 2.2: The relative difference Δ between the spin current induced by left- and right-moving spin waves, as defined in Eq. (2.11), as a function of k and ω , for three different tilting angles of the magnetic field. The spin waves travel parallel to the in-plane projection of the magnetic field, such that $\mathbf{k} = k\hat{z}$. (a) $\phi_H = 30^\circ, \phi_M = 18^\circ$, (b) $\phi_H = 60^\circ, \phi_M = 40^\circ$ and (c) $\phi_H = 80^\circ, \phi_M = 64^\circ$. The peak difference is $\Delta(k = 7.5 \mu\text{m}^{-1}, \omega = 4 \text{GHz}) = 1.25 \times 10^{-4}$, when the field is tilted at an angle $\phi_H = 60^\circ$. For a magnetic field completely in- or out of plane (not shown) there is no discernible difference.

Bozhko *et al.* [76] suggested a partial-wave picture to explain the transverse spin-current. They reason that the profile along the film normal is made up by two partial waves, which have opposite momenta $\pm k_x$ and equal frequency ω if the film is magnetized in-plane, thus cancelling any transfer of angular momentum or energy. As the magnetic field is tilted out of plane the two partial waves would, in this picture, no longer have opposite momenta, but still have the same frequencies. This would then allow for angular momentum transfer, but not energy transfer. With the magnetostatic calculation we are able to show that this picture is incomplete: the amplitudes of the two partial waves are asymmetric, not their momenta. This therefore allows both energy and angular momentum transfer, which we have confirmed numerically by evaluating $\langle \partial_t E \rangle$.

We found numerically that the region in k -space where the relative difference Δ is significant has a lower bound related to the thickness of the thin film. Decreasing the thickness shifts the distribution as seen in Fig. 2.2 towards larger wavevectors. This can be traced to the fact that the long-wavelength magnetostatic magnon modes are standing waves, with wavevectors $\pm k_x$, where k_x is proportional to k_z . The standing waves need to have a wavevector big enough to fit at least one wavelength into the system, thus requiring that $k_z \gtrsim k_L$, where $k_L = 2\pi/d$. The reason for this coupling of the in-plane and out of plane directions is the long-range nature of the dipole-dipole interaction, ensuring that within our system the divergence of the magnetic field is zero,

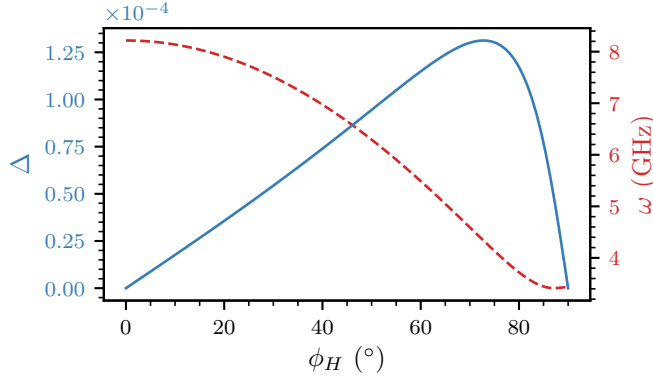


Figure 2.3: Relative difference between the spin current induced by left- and right-moving spin waves, Δ , as defined in Eq. (2.11), as a function of magnetic field tilt angle ϕ_H , for ω corresponding to the lowest mode in the spin-wave dispersion and fixed $k = 7.5 \mu\text{m}^{-1}$ (solid line). Also shown is the frequency of the lowest mode as a function of the tilt angle (dashed line).

i.e., $\nabla \cdot \mathbf{B} = 0$. The maximum value of Δ does not change depending on the thickness of the film, only the location of the maximum. We have confirmed this numerically for the range $60 \leq d \leq 480 \text{ nm}$. For even thinner films the maximum value of Δ becomes lower.

Excitation of magnons is only possible for values of ω determined by the spin-wave dispersion, with a minimum given by the lowest mode. We therefore show in Fig. 2.3 for fixed $k = 7.5 \mu\text{m}^{-1}$ the evolution of the relative spin-current difference Δ as the magnetic field is tilted out of plane, with a driving at frequency ω corresponding to the lowest mode in the spin-wave dispersion. Also shown is the frequency of the lowest mode as a function of magnetic field tilt angle. It is clear that up to some critical value of the magnetic field angle Δ increases linearly, after which it falls off rapidly. It is also clear that the lowest mode is capable of transferring angular momentum along the film normal. This is contrary to the statements made by Bozhko *et al.* [76], who predicted that the lowest mode, which has an uniform profile, would not induce a transverse spin-current. This is most likely due to the fact that in their work only the exchange current is considered, whereas we have taken all current contributions into account. Another possible explanation is their expansion in eigenfunctions of the second-order exchange operator, which might have failed to properly take the dipole-dipole interaction into account.

The different contributions to the transverse angular momentum transport, as defined in Eq. (2.9), are shown in Fig. 2.4 for left- and right-moving spin

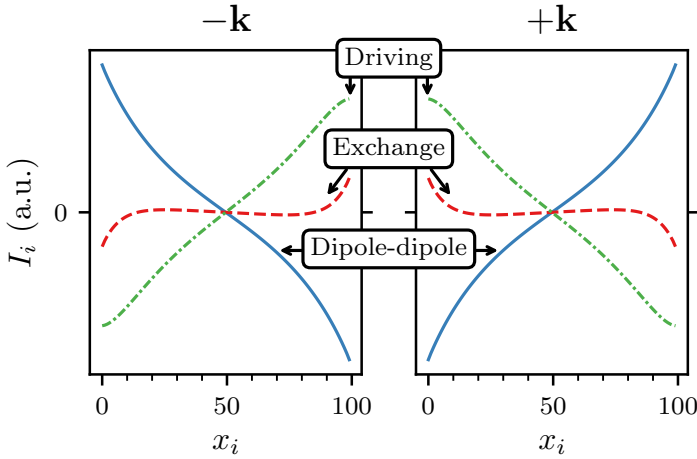


Figure 2.4: The different contributions to the transfer of angular momentum along the film normal, where $I_i = \sum_j I_{i \rightarrow j}$ for the exchange and dipole-dipole interaction. The damping plays a negligible role in the transport of angular momentum, so it is turned off to illustrate the effects of the other contributions. The thickness of the thin film is reduced to $N = 100$ in order to better illustrate the variation through the film. The magnetic field is tilted out of plane with angle $\phi_M = 60^\circ$ and the wavevector and driving frequency are fixed at $k = 30 \mu\text{m}^{-1}$, $\omega = 4 \text{ GHz}$.

waves. We have set the bulk and interface damping to zero in order to clearly show the exchange, dipole-dipole and driving contributions to the transfer of spins along the film normal. Firstly, we can see that there is a transport of angular momentum, even in the case of no spin absorption at the boundary, which agrees with the results by Bozhko *et al.* [76]. All contributions are zero in the case of an in-plane magnetic field (not shown)—if no spin sinks are attached. We can see that every contribution switches sign between left- and right-moving spin waves, as would be expected from symmetry. From this figure it is clear that the exchange spin current is not the only way the system transfers angular momentum. In fact, the contributions from the dipole-dipole interaction are larger than those of the exchange current. This shows that it is necessary to consider both interactions in order to gain a full understanding of the transport of angular momentum in the transverse direction. Also note that since the dipole-dipole contribution is non-zero there is a finite torque on the system, which could be measured in a cantilever experiment [96].

2.4 CONCLUSION AND DISCUSSION.

In this work we have shown, using microscopic linear spin-wave theory, that there is a flow of angular momentum, or spin current, along the film normal in obliquely magnetized thin films. This can be measured using an antenna-detector setup, where the spin current induced by the left- and right-moving spin waves will be different, proving the existence of a transverse spin-current. This effect can be used as a way to manipulate the spin current flowing along the film normal, for example by controlling the magnetic field angle. We have also demonstrated that this spin current is the result of the dipole-dipole interactions in the film, which carry the inversion breaking at the interface.

We have not considered explicitly the interactions of the spin waves with the lattice. The dipole-dipole interactions couple the magnons to the lattice and therefore angular momentum can be transferred from and to the phonons, which can also transport angular momentum [97–99]. A more complete description of the system should therefore include these phonon-magnon interactions, but this is beyond the scope of this article.

2.A MAGNETOSTATIC CALCULATIONS

Our goal is to derive the eigenfunctions for the thin film geometry as depicted in Fig. 2.1 in the main text. We know from the numerics that the dipole-dipole interaction alone is sufficient to give a transverse spin-current, so we ignore the exchange interaction in this derivation. This considerably simplifies the work needed and allows us to find a completely analytical expression for the eigenfunctions.

We start from the Landau-Lifshitz-Gilbert equation (LLG)

$$\partial_t \mathbf{S}(x, \mathbf{r}, t) = \mathbf{S}(x, \mathbf{r}, t) \times \left[\mathbf{H}_{eff} - \frac{\alpha}{S} \partial_t \mathbf{S}(x, \mathbf{r}, t) \right], \quad (2.13)$$

where $\mathbf{r} = (y, z)$. The classical ground state is

$$\hat{\mathbf{n}} = \frac{\langle \mathbf{S} \rangle}{S} = \sin \phi_M \hat{\mathbf{x}} + \cos \phi_M \hat{\mathbf{z}}, \quad (2.14)$$

with the angle ϕ_M is determined by Eq. (2.3) in the main text. We write the solution to the LLG as fluctuations on this ground state with

$$\psi = \frac{1}{\sqrt{2S}} (\hat{\mathbf{a}} + i\hat{\mathbf{b}}) \cdot \mathbf{S}(\mathbf{r}, t), \quad (2.15)$$

where $\hat{\mathbf{a}}, \hat{\mathbf{b}}$ are orthogonal unit vectors chosen such that by $\hat{\mathbf{a}} \times \hat{\mathbf{b}} = \hat{\mathbf{n}}$. The effective magnetic field is given by

$$\mathbf{H}_{eff} = \mathbf{H} + \mathbf{H}_D; \quad \mathbf{H}_D = \mathbf{H}_D^{(0)} + \nabla \chi, \quad (2.16)$$

where \mathbf{H}_D is the dipolar field with a static component $\mathbf{H}_D^{(0)}$ and a dynamic component, $\nabla\chi$. \mathbf{H} is the external field. We transform to Fourier space with the relations

$$\psi(x, \mathbf{r}, \omega) = \int \frac{d^2k}{(2\pi)^2} e^{i\mathbf{k}\cdot\mathbf{r}} \psi(x, \mathbf{k}, \omega), \quad (2.17)$$

$$\chi(x, \mathbf{r}, \omega) = \int \frac{d^2k}{(2\pi)^2} e^{i\mathbf{k}\cdot\mathbf{r}} \chi(x, \mathbf{k}, \omega). \quad (2.18)$$

We only consider the situation where $k_y = 0$, so $\mathbf{k} = k\hat{z}$. Outside the film the dynamics of the dipolar field are governed by

$$\left(-k^2 + \partial_x^2\right) \chi(x, \mathbf{k}, \omega) = 0, \quad x \geq \frac{d}{2} \quad (2.19)$$

which has solutions

$$\chi(x, \mathbf{k}, \omega) = \begin{cases} \chi\left(\frac{d}{2}, \mathbf{k}, \omega\right) e^{-|k|(x-d/2)}, & x \geq \frac{d}{2}; \\ \chi\left(-\frac{d}{2}, \mathbf{k}, \omega\right) e^{|k|(x+d/2)}, & x \leq \frac{d}{2}. \end{cases} \quad (2.20)$$

The boundary conditions for χ at the top and bottom of the thin film are

$$\begin{aligned} \partial_x \chi(x, \mathbf{k}, \omega) \Big|_{x=\pm\frac{d}{2}\mp 0^+} + 4\pi M_S \frac{1}{\sqrt{2}} \left[\hat{\mathbf{x}} \cdot (\hat{\mathbf{a}} - i\hat{\mathbf{b}}) \psi\left(\pm\frac{d}{2}, \mathbf{k}, \omega\right) \right. \\ \left. + \hat{\mathbf{x}} \cdot (\hat{\mathbf{a}} + i\hat{\mathbf{b}}) \psi^*\left(\pm\frac{d}{2}, -\mathbf{k}, -\omega\right) \right] = \mp |k| \chi\left(\pm\frac{d}{2}, \mathbf{k}, \omega\right) \end{aligned} \quad (2.21)$$

and the bulk equation of motion, for $|x| \leq \frac{d}{2}$ is

$$\begin{aligned} \left(k^2 - \partial_x^2\right) \chi(x, \mathbf{k}, \omega) = \frac{4\pi M_S}{\sqrt{2}} \left[(\hat{\mathbf{a}} - i\hat{\mathbf{b}}) \cdot (i\mathbf{k} + \hat{\mathbf{x}}\partial_x) \psi(x, \mathbf{k}, \omega) \right. \\ \left. + (\hat{\mathbf{a}} + i\hat{\mathbf{b}}) \cdot (i\mathbf{k} + \hat{\mathbf{x}}\partial_x) \psi^*(x, -\mathbf{k}, -\omega) \right]. \end{aligned} \quad (2.22)$$

For the magnon field we have the bulk equation of motion

$$\left[(1 + i\alpha)\omega - \mathbf{H} \cdot \hat{\mathbf{n}} - 4\pi M_S (\hat{\mathbf{x}} \cdot \hat{\mathbf{n}})^2\right] \psi(x, \mathbf{k}, \omega) + h_D(x, \mathbf{k}, \omega) = 0. \quad (2.23)$$

This gives the solution

$$\psi(x, \mathbf{k}, \omega) = G(\omega) h_D(x, \mathbf{k}, \omega), \quad (2.24)$$

where

$$G(\omega) = \left[-(1 + i\alpha)\omega + \mathbf{H} \cdot \hat{\mathbf{n}} + 4\pi M_S (\hat{\mathbf{x}} \cdot \hat{\mathbf{n}})^2\right]^{-1}. \quad (2.25)$$

For brevity we define

$$\Delta G(\omega) \equiv G(\omega) + G^*(-\omega). \quad (2.26)$$

From the bulk equation of motion the solution for the potential is

$$\chi(x, \mathbf{k}, \omega) = \chi_+ e^{qx} + \chi_- e^{-qx}, \quad (2.27)$$

where

$$q = |k_z| \sqrt{\frac{a(\mathbf{k}, \omega)}{b(\mathbf{k}, \omega)}}, \quad (2.28)$$

with

$$a(\mathbf{k}, \omega) = 1 + 2\pi M_s \Delta G(\omega) \sin^2 \phi_M, \quad (2.29)$$

$$b(\mathbf{k}, \omega) = 1 + 2\pi M_s \Delta G(\omega) \cos^2 \phi_M. \quad (2.30)$$

From the boundary conditions in Eq. (2.21) we then have the matrix equation

$$\begin{pmatrix} (F_+(\mathbf{k}, \omega) + |\mathbf{k}|) e^{q\frac{d}{2}} & (F_-(\mathbf{k}, \omega) + |\mathbf{k}|) e^{-q\frac{d}{2}} \\ (F_+(\mathbf{k}, \omega) - |\mathbf{k}|) e^{-q\frac{d}{2}} & (F_-(\mathbf{k}, \omega) - |\mathbf{k}|) e^{q\frac{d}{2}} \end{pmatrix} \begin{pmatrix} \chi_+ \\ \chi_- \end{pmatrix} = 0 \quad (2.31)$$

where

$$F_{\pm}(\mathbf{k}, \omega) = -i\pi M_s \Delta G(\omega) k_z \sin(2\phi_M) \pm q \left(2\pi M_s \Delta G(\omega) \cos^2 \phi_M + 1 \right). \quad (2.32)$$

The solutions for the potential are then

$$\chi_+ = -\chi_- \frac{(F_-(\mathbf{k}, \omega) + |\mathbf{k}|)}{(F_+(\mathbf{k}, \omega) + |\mathbf{k}|)} e^{-qd} \quad (2.33)$$

which gives for the magnon field

$$\begin{aligned} \psi(x, \mathbf{k}, \omega) = -G(\omega) & \left[q\chi_- \cos \phi_M \left(\frac{(F_-(\mathbf{k}, \omega) + |\mathbf{k}|)}{(F_+(\mathbf{k}, \omega) + |\mathbf{k}|)} e^{qx-qd} + e^{-qx} \right) \right. \\ & \left. + ik_z \chi_- \sin \phi_M \left(-\frac{(F_-(\mathbf{k}, \omega) + |\mathbf{k}|)}{(F_+(\mathbf{k}, \omega) + |\mathbf{k}|)} e^{qx-qd} + \chi_- e^{-qx} \right) \right]. \quad (2.34) \end{aligned}$$

Because $F_{\pm}(\mathbf{k}, \omega)$ depends linearly on $k_z \sin(2\phi_M)$, the eigenfunctions for magnons travelling in $\pm k_z$ directions differ whenever $\sin(2\phi_M) \neq 0$. This behaviour is in agreement with our numerics, which show that the difference between the transverse spin-current induced by left- and right-moving spin

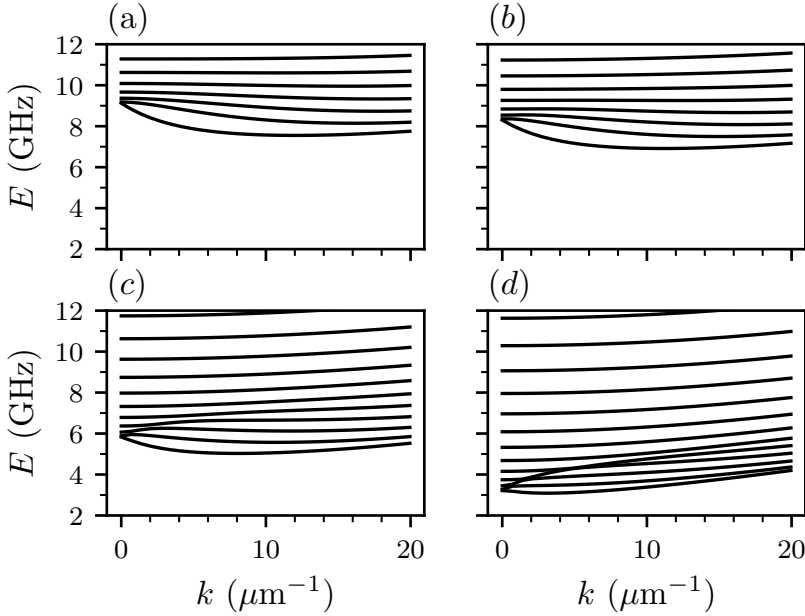


Figure 2.5: Spin wave dispersion of a YIG film with thickness $d = 400a \approx 0.48 \mu\text{m}$ for increasingly tilted magnetic field. The spin waves travel parallel to the in-plane projection of the magnetic field, such that $\mathbf{k} = k\hat{z}$. (a) $\phi_H = \phi_M = 0^\circ$, (b) $\phi_H = 30^\circ, \phi_M = 18^\circ$, (c) $\phi_H = 60^\circ, \phi_M = 40^\circ$ and (d) $\phi_H = 80^\circ, \phi_M = 64^\circ$.

waves vanishes if the magnetization is either completely in- or out of plane. Ultimately the source of the linear term is therefore the boundary conditions in Eq. (2.21). Because the dipole-dipole interaction is a long-range interaction the boundary conditions interact with all the spin-waves in the thin film, carrying the inversion breaking at the interface. This thus allows a transverse spin current to flow.

2.B DISPERSION

We diagonalize the Hamiltonian in Eq. (2.8) in the main text, in the absence of damping and spin pumping, from which we obtain the spin-wave energies [100]. The spin-wave spectra are shown in Fig. 2.5 for multiple tilt angles of the magnetic field, for spin waves propagating parallel to the in-plane projection of the magnetic field, along the k_z direction. The parameters used for these spectra are summarized in Table. 2.1 in the main text. We show the regime of wavevectors where both dipole-dipole interactions and the exchange inter-

action are of roughly equal magnitude. The exchange interaction dominates for large wavevectors and gives a quadratic wavevector dependence, curving the bands upwards. For small wavevector the dipole-dipole interaction is the dominant term in the Hamiltonian, which suppresses the quadratic behavior. Comparing these dispersion with both the numerical and experimental results [76] the general shape of the dispersions matches well, and the same shift down in energy is observed as the magnetic field is tilted.

2.C COMPLETE AMPLITUDE FACTORS

The amplitude factors in Eq. (2.8) in the main text are (making use of the fact that $D_{\mathbf{k}}^{xx} + D_{\mathbf{k}}^{yy} + D_{\mathbf{k}}^{zz} = 0$)

$$A_{\mathbf{k}}(x_{ij}) = \sum_{\mathbf{r}_{ij}} e^{-i\mathbf{k}\cdot\mathbf{r}} A(x_i - x_j, \mathbf{r}), \quad (2.35)$$

$$\begin{aligned} &= \delta_{ij} \left[S \sum_n (\sin^2 \phi_M D_0^{xx}(x_{in}) + \cos^2 \phi_M D_0^{zz}(x_{in})) \right. \\ &\quad \left. + \frac{1}{2} \sin 2\phi_M D_0^{xz}(x_{in}) + \cos(\phi_H - \phi_M) h \right] + S J_{\mathbf{k}}(x_{ij}) \\ &\quad + \frac{S}{2} \left[\sin^2 \phi_M D_{\mathbf{k}}^{xx}(x_{ij}) + \cos^2 \phi_M D_{\mathbf{k}}^{zz}(x_{ij}) + \sin 2\phi_M D_{\mathbf{k}}^{xz}(x_{ij}) \right], \end{aligned}$$

$$B_{\mathbf{k}}(x_{ij}) = \sum_{\mathbf{r}_{ij}} e^{-i\mathbf{k}\cdot\mathbf{r}} B(x_i - x_j, \mathbf{r}), \quad (2.36)$$

$$\begin{aligned} &= -\frac{S}{2} \left[(1 + \cos^2 \phi_M) D_{\mathbf{k}}^{xx}(x_{ij}) + (1 + \sin^2 \phi_M) D_{\mathbf{k}}^{zz}(x_{ij}) \right. \\ &\quad \left. - \frac{1}{2} \sin 2\phi_M D_{\mathbf{k}}^{xz}(x_{ij}) + i \sin \phi_M D_{\mathbf{k}}^{yz}(x_{ij}) - i \cos \phi_M D_{\mathbf{k}}^{xy}(x_{ij}) \right], \end{aligned}$$

where

$$J_{\mathbf{k}}(x_{ij}) = J [\delta_{ij} (6 - \delta_{j1} - \delta_{jN} - 2 \cos(k_y a) - 2 \cos(k_z a)) - \delta_{ij+1} - \delta_{ij-1}] \quad (2.37)$$

and $\mathbf{r}_{ij} = (y_{ij}, z_{ij})$.

The dipole-dipole interaction is written as a tensor

$$D_{\mathbf{k}}^{\alpha\beta}(x_{ij}) = \sum_{\mathbf{r}_{ij}} e^{-i\mathbf{k}\cdot\mathbf{r}_{ij}} D_{ij}^{\alpha\beta}, \quad (2.38)$$

where

$$D_{ij}^{\alpha\beta} = \mu^2 (1 - \delta_{ij}) \frac{\partial^2}{\partial R_{ij}^\alpha \partial R_{ij}^\beta} \frac{1}{|\mathbf{R}_{ij}|}. \quad (2.39)$$

For small wavevectors the sums in Eq. (2.38) are slowly converging, so we use the Ewald summation method as outlined by Kreisel *et al.* [23]. With this method the sums are split in two parts: one sum over real space and a one sum over reciprocal space. These sums are much faster to converge. We first write the sums as a derivative of

$$I_{\mathbf{k}}(x_{ij}) = \mu^2 \sum_{y_{ij}, z_{ij}} \frac{e^{-i(k_y y_{ij} + k_z z_{ij})}}{(x_{ij}^2 + y_{ij}^2 + z_{ij}^2)^{5/2}}, \quad (2.40)$$

such that we have

$$D_{\mathbf{k}}^{xx} = \left[\frac{\partial^2}{\partial k_z^2} + \frac{\partial^2}{\partial k_y^2} + 2x_{ij}^2 \right] I_{\mathbf{k}}(x_{ij}), \quad (2.41)$$

$$D_{\mathbf{k}}^{yy} = \left[\frac{\partial^2}{\partial k_z^2} - 2 \frac{\partial^2}{\partial k_y^2} - x_{ij}^2 \right] I_{\mathbf{k}}(x_{ij}), \quad (2.42)$$

$$D_{\mathbf{k}}^{zz} = \left[\frac{\partial^2}{\partial k_y^2} - 2 \frac{\partial^2}{\partial k_z^2} - x_{ij}^2 \right] I_{\mathbf{k}}(x_{ij}), \quad (2.43)$$

$$D_{\mathbf{k}}^{xy} = 3ix_{ij} \frac{\partial}{\partial k_y} I_{\mathbf{k}}(x_{ij}), \quad (2.44)$$

$$D_{\mathbf{k}}^{xz} = 3ix_{ij} \frac{\partial}{\partial k_z} I_{\mathbf{k}}(x_{ij}), \quad (2.45)$$

$$D_{\mathbf{k}}^{yz} = 3 \frac{\partial}{\partial k_z \partial k_y} I_{\mathbf{k}}(x_{ij}). \quad (2.46)$$

Note the symmetries $D_{\mathbf{k}}^{yy} = D_{\mathbf{k}}^{zz}(k_y \rightarrow k_z, k_z \rightarrow k_y)$ and $D_{\mathbf{k}}^{xz} = D_{\mathbf{k}}^{xy}(k_y \rightarrow k_z, k_z \rightarrow k_y)$, so we need not derive the full form of all dipolar sums. Then, after applying the Ewald summation, we have

$$D_{\mathbf{k}}^{xx} = \frac{\pi\mu^2}{a^2} \sum_{\mathbf{g}} \left(\frac{8\sqrt{\varepsilon}}{3\sqrt{\pi}} e^{-p^2 - q^2} - |\mathbf{k} + \mathbf{g}| f(p, q) \right) \quad (2.47)$$

$$- \frac{4\mu^2}{3} \sqrt{\frac{\varepsilon^5}{\pi}} \sum_{\mathbf{r}} (|\mathbf{r}_{ij}|^2 - 3x_{ij}^2) \cos(k_y y_{ij}) \cos(k_z z_{ij}) \varphi_{3/2}(|\mathbf{r}_{ij}|^2 \varepsilon),$$

$$D_{\mathbf{k}}^{yy} = \frac{\pi\mu^2}{a^2} \sum_{\mathbf{g}} \left(\frac{4\sqrt{\varepsilon}}{3\sqrt{\pi}} e^{-p^2 - q^2} - \frac{(k_y + g_y)^2}{|\mathbf{k} + \mathbf{g}|} f(p, q) \right) \quad (2.48)$$

$$- \frac{4\mu^2}{3} \sqrt{\frac{\varepsilon^5}{\pi}} \sum_{\mathbf{r}} (|\mathbf{r}_{ij}|^2 - 3y_{ij}^2) \cos(k_y y_{ij}) \cos(k_z z_{ij}) \varphi_{3/2}(|\mathbf{r}_{ij}|^2 \varepsilon),$$

$$D_{\mathbf{k}}^{xy} = i \frac{\pi\mu^2}{a^2} \text{sig}(x_{ij}) \sum_{\mathbf{g}} (k_y + g_y) f(p, q) \quad (2.49)$$

$$+ i \frac{4\varepsilon^{5/2}\mu^2}{\sqrt{\pi}} x_{ij} \sum_{\mathbf{r}} \sin(k_y y_{ij}) \cos(k_z z_{ij}) \varphi_{3/2}(|\mathbf{r}_{ij}|^2 \varepsilon),$$

$$D_{\mathbf{k}}^{yz} = -\frac{\pi\mu^2}{a^2} \sum_{\mathbf{g}} \frac{(k_y + g_y)(k_z + g_z)}{|\mathbf{k} + \mathbf{g}|} f(p, q) \quad (2.50)$$

$$+ 4 \frac{\varepsilon^{5/2}\mu^2}{\sqrt{\pi}} \sum_{\mathbf{r}} y_{ij} z_{ij} \sin(k_y y_{ij}) \sin(k_z z_{ij}) \varphi_{3/2}(|\mathbf{r}_{ij}|^2 \varepsilon),$$

where

$$\varphi_{3/2}(x) = e^{-x} \frac{3+2x}{2x^2} + \frac{3\sqrt{\pi} \operatorname{Erfc}(\sqrt{x})}{4x^{5/2}} \quad (2.51)$$

and $q = x_{ij}\sqrt{\varepsilon}$, $p = |\mathbf{k} + \mathbf{g}| / (2\sqrt{\varepsilon})$ and

$$f(p, q) = e^{-2pq} \operatorname{Erfc}(p - q) + e^{2pq} \operatorname{Erfc}(p + q).$$

The sums are either over the real space lattice or the reciprocal lattice, where the reciprocal lattice vectors are $g_y = 2\pi m$, $g_z = 2\pi n$, $\{m, n\} \in \mathbb{Z}$. ε determines the ratio between the reciprocal and real sums. We choose $\varepsilon = a^{-2}$, such that $2pq \approx 1$ and $\exp[\pm 2pq]$ converges quickly.

2.D CURRENT CONTRIBUTIONS

In the continuity equation for the angular momentum in the main text, Eq. (2.9), the explicit form of the terms is

$$I_i^\alpha(\mathbf{k}, \omega) = 2\alpha_i \operatorname{Im} [b_{\mathbf{k}}^*(x_i) \partial_t b_{\mathbf{k}}(x_i)], \quad (2.52)$$

$$I_i^h(\mathbf{k}, \omega) = -\sqrt{2S} \operatorname{Im} [h_i b_{\mathbf{k}}^*(x_i)], \quad (2.53)$$

$$I_{i \rightarrow j}^{\text{ex}}(\mathbf{k}, \omega) = i(1 - \delta_{ij}) S J_{\mathbf{k}}(x_{ij}) b_{\mathbf{k}}^*(x_i) b_{\mathbf{k}}(x_j), \quad (2.54)$$

$$I_{i \rightarrow j}^{\text{dip-dip}}(\mathbf{k}, \omega) = i \left[(1 - \delta_{ij}) A_{\mathbf{k}}^{\text{dip}}(x_{ij}) b_{\mathbf{k}}^*(x_i) b_{\mathbf{k}}(x_j) \right. \\ \left. - \frac{B_{\mathbf{k}}(x_{ij})}{2} b_{-\mathbf{k}}(x_i) b_{\mathbf{k}}(x_j) + \frac{B_{\mathbf{k}}^*(x_{ij})}{2} b_{\mathbf{k}}^*(x_i) b_{-\mathbf{k}}^*(x_j) \right], \quad (2.55)$$

where $A_{\mathbf{k}}^{\text{dip}}(x_{ij}) = A_{\mathbf{k}}^{h=J=0}(x_{ij})$, i.e., only the contributions from the dipole-dipole interaction. Note that $B_{\mathbf{k}}(x_{ij})$ already includes only dipole-dipole interactions.

3

THEORY FOR ELECTRICAL DETECTION OF THE MAGNON HALL EFFECT INDUCED BY DIPOLAR INTERACTIONS

We derive the anomalous Hall contributions arising from dipolar interactions to diffusive spin transport in magnetic insulators. Magnons, the carriers of angular momentum in these systems, are shown to have a non-zero Berry curvature, resulting in a measurable Hall effect. For yttrium iron garnet (YIG) thin films we calculate both the anomalous and magnon spin conductivities. We show that for a magnetic field perpendicular to the film the anomalous Hall conductivity is finite. This results in a non-zero Hall signal, which can be measured experimentally using Permalloy strips arranged like a Hall bar on top of the YIG thin film. We show that electrical detection and injection of spin is possible, by solving the resulting diffusion-relaxation equation for a Hall bar. We predict the experimentally measurable Hall coefficient for a range of temperatures and magnetic field strengths. Most strikingly, we show that there is a sign change of the Hall coefficient associated with increasing the thickness of the film.¹

3.1 INTRODUCTION

One of the earliest successes of the concepts of geometry and topology in condensed matter was the explanation of the anomalous Hall effect in terms of the Berry phase. The anomalous Hall effect was therefore a stepping stone for further understanding of geometrical and topological effects, such as the quantum Hall effect [101]. Since it is a geometrical effect, the anomalous Hall effect is not restricted to electronic systems. Indeed, it has also been observed for other types of carriers, such as phonons and photons [102–104]. Since spin waves, or magnons, are the carriers of angular momentum in ferromagnets, the question thus naturally arises if a magnon analogue of the anomalous Hall effect can also exist. Continuing the analogy with the anomalous Hall effect, the magnon Hall effect could lead to further understanding of topology in magnonic systems.

¹ This chapter is based on P. M. Gunnink, R. A. Duine, and A. Rückriegel, “Theory for electrical detection of the magnon Hall effect induced by dipolar interactions,” *Physical Review B* **103**, 214426 (2021). R.D. and A.R. conceived the project, P.M.G. performed the calculations and prepared the manuscript and A.R. derived the diffusion equations. All authors contributed to the manuscript.

Previously, a thermal magnon Hall effect has been proposed, where magnons are the heat carriers. First predicted for chiral quantum magnets [12], it was subsequently observed in $\text{Lu}_2\text{V}_2\text{O}_7$ [105, 106]. In these systems the chiral nature of the spin waves provides the time-reversal symmetry breaking that is necessary for a finite anomalous Hall response. For forward volume magneto-static spin waves in a thin-film ferromagnet a thermal magnon Hall effect has also been proposed [107, 108], where the dipole-dipole interaction provides the required symmetry breaking. A transverse thermal Hall conductivity has also been calculated for this system [109], but has not yet been measured experimentally. This is most likely due to the small transverse thermal conductivities predicted for the most commonly used insulating ferromagnet, yttrium iron garnet (YIG) [105]. Moreover, phonons also contribute to the thermal Hall effect, and it might therefore be hard to disentangle the contributions of the two heat carriers. An effort has been made by Tanabe *et al.* [110] to excite spin waves using a coplanar waveguide and measure the temperature gradient perpendicular to the propagation direction. However, they were only able to measure a transverse temperature gradient in the unsaturated regime, which can therefore not directly be attributed to magnons.

Recent advances have shown that it is possible to electrically inject and detect spin waves using metallic leads [77]. This has opened the way to electrically measure the magnon Hall effect. However, a complete picture of the interaction between the electrical detection and the Hall effect is still lacking. Electrical detection via metal strips can significantly modify magnon transport properties [111], and it is not clear if a finite magnon Hall response can still survive. In this chapter we therefore develop a theory for the electrical detection of the magnon Hall effect in order to determine if the magnon Hall effect can be measured electrically.

We numerically calculate the Hall response, using the diffusion-relaxation equation for magnons in a Hall bar geometry, as depicted in Fig. 3.1. In order to determine the magnitude of the expected Hall response two contributing factors need to be calculated: (1) the magnon spin and anomalous conductivities and (2) the boundary conditions which incorporate the electrical detection. We numerically calculate these using a microscopic description. Starting from the Keldysh quantum kinetic equations [112], we derive the equation of motion of the magnon distribution function to leading order in a semiclassical expansion in gradients. This allows us to separate the spin diffusion and anomalous Hall contributions to the spin current.

This chapter is ordered as follows. We first discuss the specific Hall geometry required to measure a finite magnon Hall effect in Sec. 3.2. Next, in order to determine the magnitude of the magnon Hall effect we derive the equations of motion for the spin density in Sec. 3.3. We also show how the equations of motion have to be modified if a metallic lead is interfaced with the system,

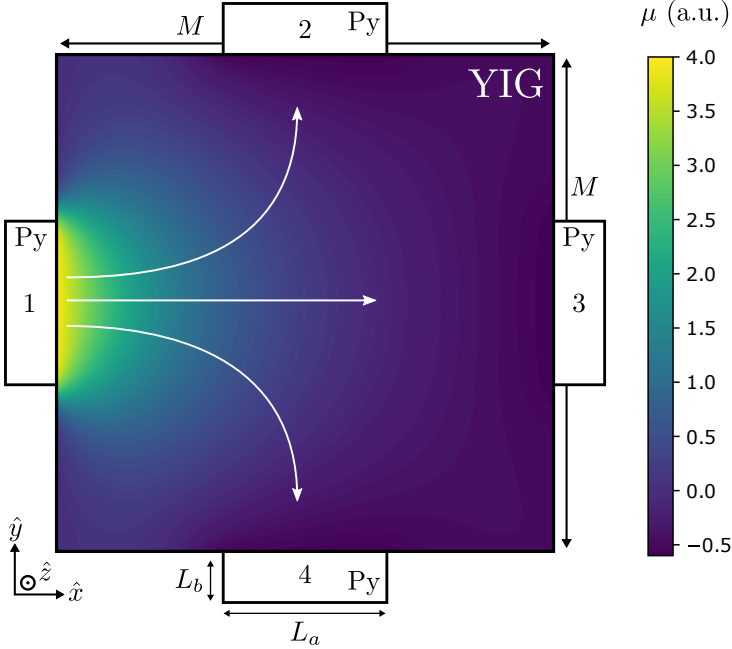


Figure 3.1: The Hall bar with electrical injection and detection of spin currents using Permalloy strips on top of YIG. Spin current is injected by the Py strip 1, and is detected by the strips 2, 3 and 4. The colorscale shows the diffusion of the magnon chemical potential throughout the film, obtained by solving the diffusion-relaxation equations as described in Sec. 3.3.2. The Hall bar has size $M \times M$, and the Py detectors and detectors have size $L_a \times L_b$, where $L_b \ll L_a$. The magnetic field is oriented out of plane, as shown in Fig. 3.2, where also the interface between the YIG and the Py is shown in more detail.

in order to detect or inject spins. From the equation of motion we derive a diffusion-relaxation equation, which fully describes the magnon diffusion and relaxation in the Hall bar geometry, including boundary conditions. In Sec. 3.4 we show how the conductivities and damping can be numerically evaluated and we discuss results for a typical thin film of YIG. In Sec. 3.5 we solve the diffusion-relaxation equation numerically and present our results for a YIG Hall bar, where spin waves are injected and detected electrically. A summary and conclusion are given in Sec. 3.6. In the appendices 3.A-3.E we give a more detailed derivation of the quantum kinetic equations for general bosonic systems, and more details regarding the diffusion-relaxation equation and the Hamiltonian.

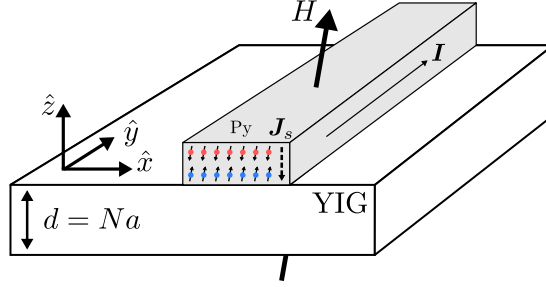


Figure 3.2: The considered geometry, with the magnetic field pointing slightly off the \hat{z} -axis, as explained in the main text. The Py strip on top of the YIG has a charge current I running parallel to the film, which induces a spin current J_s such that there is an accumulation of spin at the interface between the YIG and the Py.

3.2 SETUP

First, we discuss the experimental setup necessary to measure a magnon Hall effect electrically. We consider a Hall bar geometry, as shown in Fig. 3.1. There are four terminals, formed by metal strips on top of a YIG thin film. The strips act as injectors and detectors of spin currents. Magnons are injected at terminal 1 and diffuse through the film. They are then detected at terminals 2, 3 and 4. By comparing the detected currents at terminals 2 and 4 a Hall signal can be measured. Note that in electronic Hall experiments terminal 3 is necessary in order for a current to flow, but in our case we have only included it for completeness.

The Berry curvature is only non-zero if either time-reversal or inversion symmetry is broken [38]. Breaking these symmetries can be achieved by applying a magnetic field perpendicular to the plane, which leads to forward volume modes, as was previously suggested by Matsumoto and Murakami [107]. Conventionally, one would use the spin Hall effect (SHE) in the metal strips to excite magnons in the YIG film [77]. However, the polarization of the spin current induced by the SHE is always in-plane [113] and can therefore not excite forward-volume modes in the YIG film. Instead, we propose to use ferromagnetic Permalloy (Py) strips. If a charge current flows through the Py strip, the anomalous spin Hall effect (ASHE) induces a spin current polarized parallel to the magnetization of the Py strip, as shown in Fig. 3.2. For sufficiently large external magnetic fields the magnetization of the Py strips and the YIG will both be aligned to the external field. This spin current can therefore excite magnons in the YIG film. However, the spatial direction of the spin current is $J_s \sim I \times M$, where I and M are the charge current and magnetization respectively [114, 115]. Therefore, if the magnetic field

is oriented along the \hat{z} direction and the charge current flows along the \hat{y} direction the spin current flows along the \hat{x} direction. In other words, the spin current in the Py strip flows parallel to the YIG film and can therefore not enter it to excite magnons. However, one can tilt the magnetic field slightly off-axis, i.e. off the \hat{z} -axis, as depicted in Fig. 3.2. The spin current induced by the ASHE then gains an out-of-plane component and is able to excite magnons in the YIG [115]. At the detectors the opposite process, the inverse ASHE, converts a spin current in a measurable charge current.

3.3 METHOD

In this section we consider the microscopic Hamiltonian for a thin film of YIG and derive the equations of motion for the spin density. The formalism that we use, however, is completely general and can be applied to any bosonic Hamiltonian with anomalous coefficients.

We consider a thin film of YIG, with N layers, of thickness $d = Na$, with a magnetic field perpendicular to the film. We include both the dipole-dipole and exchange interaction, which gives us a full description of the spin wave dynamics. We apply a Holstein-Primakoff transformation to the Hamiltonian, retain terms up to second order, and Fourier-transform along the x, y directions. We can then write the quadratic part of the Hamiltonian as

$$\mathcal{H}_k = \sum_{\mathbf{k}} \begin{pmatrix} b_{\mathbf{k}}^{\dagger} & b_{\mathbf{k}} \end{pmatrix} \begin{pmatrix} A_{\mathbf{k}} & B_{\mathbf{k}} \\ B_{\mathbf{k}}^{\dagger} & A_{\mathbf{k}} \end{pmatrix} \begin{pmatrix} b_{\mathbf{k}} \\ b_{-\mathbf{k}}^{\dagger} \end{pmatrix}, \quad (3.1)$$

where $b_{\mathbf{k}}^{\dagger} = (b_{\mathbf{k}}^{\dagger}(z_1), \dots, b_{\mathbf{k}}^{\dagger}(z_N))$ are the creation operators for magnons with the two-dimensional wave vector \mathbf{k} and $A_{\mathbf{k}}$ and $B_{\mathbf{k}}$ are $N \times N$ matrices with N the number of internal degrees of freedom within a unit cell, which is in our case equivalent to the number of layers. More details are found in Appendix 3.E. We evaluate the dipole-dipole interaction using the Ewald summation method [23]. This allows us to accurately compute the magnon spectrum, even at long wavelengths, where conventional summing methods are slow [116], but where we do expect the Berry curvature to be large [108]. From the anomalous coefficients $B_{\mathbf{k}}$, which are due to the dipole-dipole interaction, it is clear that spin is not conserved. The dipolar interactions couple the magnons to the lattice, which therefore acts as a spin sink and/or source.

We note that the anomalous coefficients in the Hamiltonian create a squeezed magnon state, which is not an eigenstate of the spin in the z -direction [117]. Between a metallic lead and the magnetic system there is thus an interface of a squeezed (the YIG) and a spin state with definite spin in the z -direction (the metallic lead). This leads to corrections to the spin current over the interface, which we show in more detail in Sec. 3.3.1.

In a bosonic system with anomalous coefficients, the Bogoliubov-de Gennes (BdG) Hamiltonian $\mathcal{H}_{\mathbf{k}}$ is diagonalized by a para-unitary transformation [100], such that

$$\mathcal{T}_{\mathbf{k}}^\dagger \mathcal{H}_{\mathbf{k}} \mathcal{T}_{\mathbf{k}} = \mathcal{E}_{\mathbf{k}}; \quad \mathcal{T}_{\mathbf{k}}^\dagger \nu \mathcal{T}_{\mathbf{k}} = \nu, \quad (3.2)$$

where

$$\begin{aligned} \mathcal{E}_{\mathbf{k}} &= \text{diag} \left[E_{\mathbf{k}}^1, \dots, E_{\mathbf{k}}^N, E_{-\mathbf{k}}^1, \dots, E_{-\mathbf{k}}^N \right], \\ \nu &= \text{diag} [1, \dots, 1, -1, \dots, -1], \end{aligned}$$

and $\mathcal{T}_{\mathbf{k}}$ is a para-unitary transformation matrix of size $2N \times 2N$. Note that we only have N distinct bands, since the bands n and $n + N$ are related to each other via the para-unitary structure.

In order to derive the equations of motion we perform the gradient expansion of the Hamiltonian. We first define the Berry connection (suppressing the \mathbf{k} -label from here onwards)

$$A^\alpha = i\nu \mathcal{T}^\dagger \nu (\partial_{k_\alpha} \mathcal{T}), \quad (3.3)$$

where $\alpha \in (x, y)$. Numerically, we calculate the Berry connection using the component-wise form

$$\mathcal{A}_{nm}^\alpha = -i \frac{[\mathcal{T}^\dagger (\partial_{k_\alpha} H) \mathcal{T}]_{nm}}{\mathcal{E}_n - \nu_n \nu_m \mathcal{E}_m}, \quad n \neq m, \quad (3.4)$$

where $n, m = 1, \dots, 2N$. This form also makes it clear that the Berry connection increases close to band crossings.

From the Berry connection we define the Berry curvature for the n -th band as

$$\begin{aligned} \Omega_n^{\alpha\beta} &= \left(\partial_{k_\alpha} A^\beta - \partial_{k_\beta} A^\alpha \right)_{nn} \\ &= i \left(A^\alpha A^\beta - A^\beta A^\alpha \right)_{nn} \end{aligned} \quad (3.5)$$

The Berry curvature satisfies the sum rule $\sum_n \Omega_n^{\alpha\beta} = 0$, where n is summed over all $2N$ bands. We note that these definitions for the Berry phase and curvature are equivalent to those given by Shindou *et al.* [118], who were the first to consider the topology of magnons, and also to those of Lein and Sato [119], who showed rigorously that the concept of the Berry phase can be applied to BdG-type Hamiltonians.

Now we are able to derive the equations of motions for general bosonic systems with non-zero anomalous coefficients. As noted, this is applicable to the magnons described here, but also for other bosonic systems, such as phonons and photons [104, 120], where geometrical effects are also known. We

start from the quantum kinetic equations in the Keldysh formalism, which are derived by performing a Wigner transformation and expanding the gradients up to first order [112]. Moreover, we assume damped quasiparticles in (local) thermal equilibrium. We have relegated the details of this calculation to Appendix 3.A and will only state the equation of motion for the spin density $s^z(\mathbf{r}, t)$ here, which is given by

$$\partial_t s^z + \nabla \cdot \mathbf{J}_s = \Gamma_s \mu_m, \quad (3.6)$$

where we have only kept terms up to first order in the magnon chemical potential μ_m . Here, Γ_s describes the relaxation rate of the magnons. The spin current \mathbf{J}_s is written component-wise as

$$J_s^\alpha = \sigma_s \partial_{r_\alpha} \mu_m + \sigma_s^H \sum_\beta \varepsilon^{\alpha\beta} \partial_{r_\beta} \mu_m, \quad (3.7)$$

where σ_s is the magnon spin conductivity, σ_s^H is the Hall conductivity and $\varepsilon^{\alpha\beta}$ is the two-dimensional Levi-Civita symbol. The Berry curvature only affects the magnon Hall conductivity σ_s^H , and bands with a greater Berry curvature contribute to a larger Hall conductivity. From the Keldysh formalism the coefficients σ_s , σ_s^H and Γ_s can be calculated using the microscopic Hamiltonian, by integrating the relevant quantities over the entire Brillouin zone. We show the details of this calculation in Appendix 3.E. We consider a clean system in the low-temperature limit, such that the dominant damping source is the Gilbert damping [33]. Moreover, we disregard heat transport, since long-range magnon transport is dominated by the magnon chemical potential [29].

The complete magnon dynamics are thus given by Eq. (3.6), where we calculate the transport coefficients using the microscopic Hamiltonian. We therefore do not have to rely on fitting parameters, but only on experimentally measurable quantities.

3.3.1 Metallic lead

In order to model the electrical detection and injection, we consider a metallic lead interfaced with the YIG film, as shown in Fig. 3.2. As a result of this interface the equations of motion have to be modified, such that we have at the interface between the magnet and the metallic lead that

$$\partial_t s^z(\mathbf{r}, t) + \nabla \cdot \mathbf{J}_s = \Gamma_s \mu_m + A \mu_m + B \mu_e + C, \quad (3.8)$$

where μ_e is the electron spin accumulation in the lead. We show the detailed derivation of this correction and the coefficients A , B and C in Appendix 3.C. The correction $A \mu_m$, with $A > 0$, describes the relaxation of the magnons into the metallic lead. $B \mu_e$ is the injection of spin driven by the chemical potential in the metallic lead.

The constant C is related to the fact that the magnons are squeezed, whereas the spins in the metallic lead are not squeezed. The main correction is a constant injection of angular momentum into the YIG, even with zero chemical potential in the Py lead, which is a characteristic feature of elliptic magnonic systems [121]. The source of this spin current is the lattice, which couples to the magnons via the dipole-dipole interaction. The constant C is therefore zero in the absence of dipolar interactions. There are also corrections due to dipolar interactions to the constants A and B , which are of less importance. In absence of these corrections we would have $A = -B$, such that the spin current is zero when $\mu_e = \mu_m$ [29]. With the metallic lead modelled, we now have all the necessary parts for a full description of the dynamics of magnons in a Hall bar.

3.3.2 Diffusion-relaxation

We now write down the full diffusion-relaxation equation, which we solve numerically to give the full description of the Hall bar, including electrical injection and detection. Since the Hall conductivities enter through antisymmetric terms in the current, see Eq. (3.7), these drop out in the final diffusion-relaxation equation, which becomes

$$\sigma_s \nabla^2 \mu_m = \Gamma_s \mu_m. \quad (3.9)$$

The Hall conductivities only appear in the expressions for the boundary conditions, where we require that the normal component of the current vanishes, i.e. that $\mathbf{J}_s \cdot \hat{\mathbf{n}} = 0$ at the edges of the film if there is no metallic lead present, where $\hat{\mathbf{n}}$ is the normal vector to the boundary. To measure a finite Hall response we consider a Hall bar setup, as shown in Fig. 3.1. The Hall response can then be measured between terminals 2 and 4. As far as we are aware, there are no analytical solutions for such a geometry. We therefore numerically solve the diffusion-relaxation equation, Eq. (3.9).

Specifically, we solve the diffusion-relaxation equation on the square $0 \leq x \leq M$ and $0 \leq y \leq M$, where the diffusion is given by Eq. (3.9). We use a Finite Element Method, with a symmetric square grid, implemented in the FreeFEM++ software [122]. At the open boundaries we require that $\mathbf{J}_s \cdot \hat{\mathbf{n}} = 0$. At the injector and detectors we have the boundary condition $\mathbf{J}_s \cdot \hat{\mathbf{n}} = J_s^{\text{int}}(\mu_m)$, where the interface current J_s^{int} is a function of the magnon chemical potential at the interface μ_m^{int} and includes the contributions A, B and C as discussed in Sec. 3.3.1. We give the full form of J_s^{int} in Appendix 3.D. We then define the total spin current injected or detected at Py strip i as $I_i = \int_{\partial S_i} \mathbf{J}_s \cdot \hat{\mathbf{n}} ds$, where ∂S_i is the interface between the Py and the YIG.

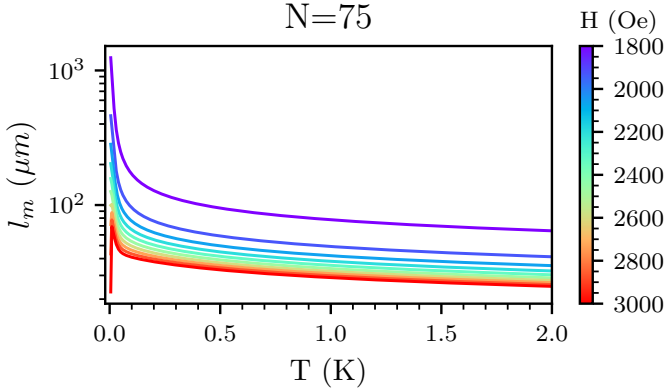


Figure 3.3: The spin diffusion length l_m for a thin film of YIG with thickness $N=75$, for varying magnetic field strength. The corresponding Hall angle is shown in Fig. 3.4a.

3.4 HALL ANGLE AND DIFFUSION LENGTH

With the full description of the transport coefficients complete, we now numerically evaluate these using the microscopic Hamiltonian. We have relegated the derivation of these coefficients to Appendix 3.B. The parameters used in this chapter are shown in Table 3.1. We only consider the low-temperature regime $T < 2$ K, since at higher temperatures we expect other damping mechanisms besides the Gilbert damping to play a role. Moreover, one might expect the ferrimagnetic branches in the YIG dispersion relation to be relevant at room temperature [123], which are not captured in our model.

First, we show the results for the spin diffusion length, $\ell_m = \sqrt{\sigma_s/\Gamma_s}$, for a film of thickness $N = 75$ in Fig. 3.3. The diffusion length peaks for low temperatures, and converges to a constant value in the high temperature regime. This can be explained by the energy dependence of the Gilbert damping: for low temperature only the lowest energy bands contribute, which have the lowest Gilbert damping, since the damping is proportional to energy. The drop-off of the diffusion length at low temperature and high magnetic field is explained by the fact that the temperature is not high enough to occupy the first band, and there is thus no transport possible. At elevated temperatures we compare the spin diffusion length to a simple model that only considers the lowest exchange band of YIG, from which the spin diffusion length is estimated as $l_m \approx 4\sqrt{J/3k_B T M_s \alpha_G^2}$ [29]. We expect this approximation to be only valid for relatively high temperatures, where the higher exchange bands

Table 3.1: Parameters for YIG used in the numerical calculations in this chapter. Note that S follows from $S = M_s a^3 / \mu$, where $\mu = 2\mu_B$ is the magnetic moment of the spins, with μ_B the Bohr magneton. We are not aware of any values of the parameters μ_e and α_{IF} for a YIG|Py interface and have therefore assumed values that are equivalent to the YIG|Platinum interface. Since the injection and detection is described in linear response, their exact values do not affect the final results.

Quantity	Value
a	12.376 Å [93]
S	14.2
$4\pi M_s$	1750 G [94]
J	1.60 K [23]
α_G	10^{-4} [18]
α_{IF}	10^{-2} [18]
μ_e	8 μ V [29]

are occupied, and for thicker films. We therefore compare this approximation with our calculations at $T = 2$ K and find that $l_m \approx 35 \mu\text{m}$, whereas our numerical model found $l_m = 55 \mu\text{m}$ for $N = 150$ and $H = 1800$ Oe. Moreover, as is evident from Fig. 3.3, our numerically calculated diffusion length also scales as $1/\sqrt{T}$. For different thicknesses (not shown here) the behaviour and order of magnitude of the spin diffusion length is similar.

Next, we consider the Hall angle, $\theta_H = \sigma_s^H / \sigma_s$. We compare two films with thicknesses $N = 75$ and $N = 150$ in Fig. 3.4. It is clear that the Hall angle peaks for small temperature, and tends to a lower constant value for higher temperature. The complete drop-off at $T = 0$ is explained by the fact that there are no magnons thermally excited at zero temperature. In order to further explain these results we first need to focus on the Berry curvature for these thin films, since the Berry curvature is directly related to the Hall conductivity in this system. We therefore show the Berry curvature Ω_n^{yz} of the n -th band in Fig. 3.5 for these two films. We can see that the Berry curvature is largest for the lowest band, which we therefore expect to dominate transport. Furthermore, in the dipolar regime, at small wavevectors, the Berry curvature is largest. This explains the temperature dependence of θ_H we observe in Fig. 3.4. At low temperatures the dipolar magnons dominate transport, and they have a large Berry curvature. Furthermore, the exchange bands naturally have a larger contribution to transport than the dipolar magnons (not shown here). As the temperature increases, the ratio between the exchange and dipolar

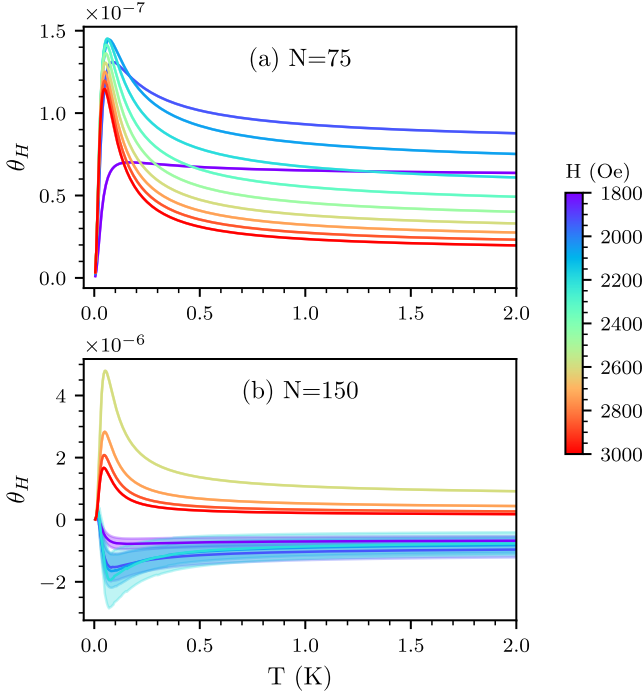


Figure 3.4: The Hall angle $\theta_H = \sigma_s^H / \sigma_s$ for two different film thicknesses, (a) $N = 75$ and (b) $N = 150$. The shaded area indicates the error, which results from a slowly converging integral over the Brillouin zone.

magnons shift towards the exchange magnons, increasing the magnon spin conductivity, but not the Hall conductivity.

For the film with thickness $N = 150$, shown in Fig. 3.4b, the Hall angle is negative for low magnetic field. Here the shaded region indicates the error from integrating the Berry curvature Ω_n over the Brillouin zone. The larger errors can be explained from the behaviour of the Berry curvature close to band crossings, as shown in Fig. 3.5b. The Berry curvatures grows at band crossings—but never diverges, since none of the bands are ever degenerate. This can also be seen from Eq. (3.4), where it is clear that the Berry connection matrix and therefore the Berry curvature of the band n is inversely proportional to the energy gap. Integrating such a function is numerically very costly, and we only reach the precision as indicated by the shaded region. The avoided band crossings in the dispersion, which lead to an increased Berry curvature, are only present for thicker films ($N \gtrsim 150$). The results for the Berry curvature can directly be compared to the Berry curvature as obtained by Okamoto and Murakami [124], who showed the same behaviour as we

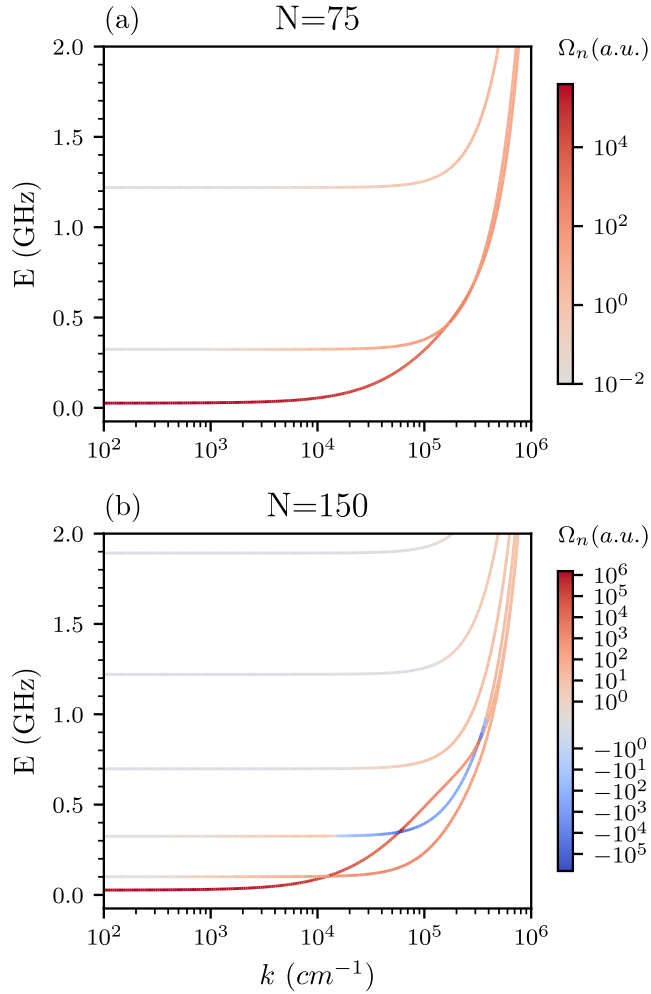


Figure 3.5: The Berry curvature Ω_n^{yz} per band for the forward-volume modes of a thin film with (a) $N = 75$ and (b) $N = 150$ layers, and a magnetic field strength $H = 1800$ Oe. Note the more complicated Berry curvature structure for $N = 150$, which is not present for the $N = 75$ thin film and is due to the band crossings. We also note that the Berry curvature is negative for certain bands for $N = 150$, but for none for $N = 75$.

have shown for the $N = 150$ film, with an enhanced Berry curvature at the band crossings and a negative Berry curvature for some of the higher bands.

The negative Hall angle can be explained from the negative Berry curvature, which is present for $N = 150$, but not for $N = 75$, as was shown in Fig. 3.5. This sign switch of the Hall angle is similar to what was observed by Hirschberger *et al.* [125] in measuring the thermal Hall effect in a Kagome magnet.

For the forward volume modes, the magnetic field acts as a way to introduce a finite energy shift of the bands. This can be used to explain the behaviour of the spin diffusion length as shown in Fig. 3.3. A higher magnetic field reduces the diffusion length, since by shifting all the bands the magnetic field changes which bands are occupied and therefore contribute. For the Hall angle, θ_H , the magnetic field dependence is more complicated, at least for smaller magnetic fields. As a function of magnetic field strength, the Hall angle rises rapidly, until it peaks for a field of strength ~ 2400 Oe, after which it drops again. For higher fields, the magnetic field essentially shifts the ratio between which type of magnons contribute at a given energy: the exchange or the dipolar magnons. This does not explain the low magnetic field behaviour though, since we expect this behaviour to be (roughly) linear. Further research is needed to understand this in more detail.

Since we have determined that thickness plays a role in the Hall effect of YIG, we also show the results for a fixed magnetic field, with increasing thickness in Fig. 3.6. It can clearly be observed that the Hall angle increases for thicker films. However, one should be aware that this is still assuming that there is no diffusive transport along the film normal, i.e. the spin diffusion length is larger than the film thickness. The spin diffusion length for YIG thin films at the temperature range considered here has not yet been measured, but for $T = 30$ K it is roughly $5 \mu\text{m}$ [126], which would make our description valid for thin films up to $N = 5000$.

We have now calculated the transport coefficients σ_s, σ_s^H and Γ_s . Not discussed in the main text are the coefficients A, B and C that govern spin injection at the metallic lead interface, which we show in App. 3.C. Next, we solve the diffusion-relaxation equation, in order to determine if the magnon Hall effect can be measured electrically.

3.5 DIFFUSION IN THE HALL BAR

Experimentally, the main observable is the difference between the spin currents detected by terminals 2 and 4. We define a Hall coefficient as the signal difference between detectors 2 and 4,

$$\Delta I = \frac{I_2 - I_4}{I_2 + I_4}. \quad (3.10)$$

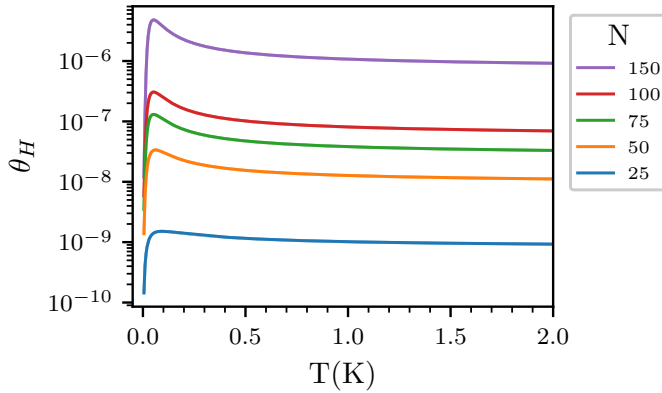


Figure 3.6: The Hall angle θ_H for $H = 2600$ Oe, as a function of temperature and for varying thicknesses. We were not able to numerically calculate θ_H for thicker films, so it is not clear if the Hall angle will continue to increase.

In order to confirm that a non-zero Hall angle θ_H results in a finite ΔI we numerically solve the diffusion-relaxation equation. We choose $M = 8 \mu\text{m}$, $L_a = 3 \mu\text{m}$ and $L_b = 0.1 \mu\text{m}$, which are the same dimensions used by Das *et al.* [115] to measure the planar Hall effect in YIG. The distribution of the chemical potential for a typical system is shown in Fig. 3.1. The chemical potential diffuses through the film and gets picked up by the three detectors. Note that the difference between the currents picked up by detectors 2 and 4, i.e. ΔI , is too small to be visible on the color scale of Fig. 3.1.

We then calculate the Hall coefficient ΔI for $N = 75$ and show the results in Fig. 3.7. These results can be compared to the Hall angle, θ_H , in Fig. 3.4a. From this comparison it is clear that the Hall angle θ_H is directly related to the Hall coefficient ΔI . We see little to no effect from the magnon relaxation, since the spin diffusion length is much longer than the size of the Hall bar. Most importantly, there are no (large) corrections from interface effects due to the electrical injection and detection. This is also the case for different thicknesses. We therefore conclude that the magnon Hall effect can in principle be measured electrically in a Hall bar geometry.

3.6 CONCLUSION AND DISCUSSION

We have derived and calculated the anomalous Hall conductivity for magnons in a thin film of YIG, using a microscopic model. Furthermore, we have shown that a non-zero anomalous Hall conductivity results in a measurable signal in a Hall bar setup and can be measured electrically. The magnon Hall effect has

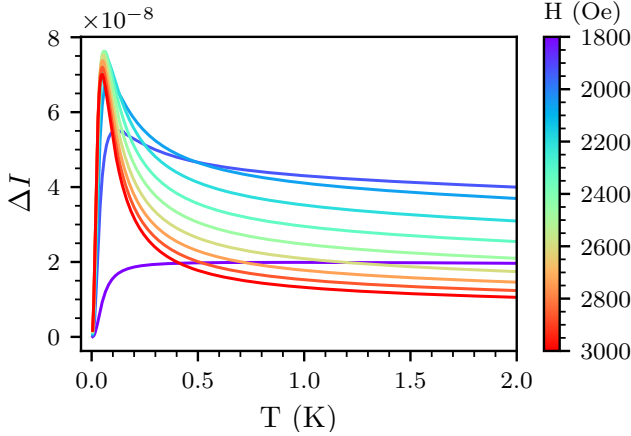


Figure 3.7: The Hall coefficient ΔI , which follows from the numerical solution to the diffusion-relaxation equation for a Hall bar geometry. The thickness of the film is $N = 75$ and this can therefore be directly compared to the Hall angle θ_H in Fig. 3.4a. From this comparison it is clear that a Hall response can be measured, and that θ_H is a direct predictor of ΔI .

previously only been measured thermally in materials with a Dzyaloshinskii-Moriya spin-orbit interaction [105], but with a Hall bar setup as discussed here this magnon Hall effect could also be measured electrically in YIG.

Using realistic parameters we have calculated the size of the expected Hall angle, and its dependency on temperature and magnetic field. Moreover, we have shown that for thicker films of YIG, there is a sign change in the Hall angle as a function of the magnetic field, which would be a strong experimental indicator of the magnon Hall effect.

The presented method can be applied to any bosonic system with anomalous coefficients to determine anomalous transport properties. In fact, the physical origin of the anomalous transport properties discussed here are the dipole-dipole interactions, which are universally present in any magnetic system. As such, this method can be applied to a wide range of magnetic materials.

In order to measure this effect it is possible to use the fact that the sign of the Hall angle switches as the field is reversed. Therefore, by comparing measurements with opposite field, the anomalous contributions can be isolated. This is especially useful since the spin diffusion and relaxation means that the distance between the injector at lead 1 and the detectors at leads 2 and 4 is critical.

As was shown by Takahashi and Nagaosa [127] and Okamoto *et al.* [128], for magnetoelastic waves the Berry curvature is enhanced at the crossing of the magnon and phonon branches. This could therefore serve to further enhance

the magnon Hall effect discussed here. The inclusion of magnon-phonon coupling on our formalism is left for future chapter.

3.A QUANTUM KINETIC EQUATIONS

In this appendix we derive the equation of motion for the spin density of a bosonic Hamiltonian. We start from the quantum kinetic equations:

$$(\hat{\varepsilon} - \nu \hat{H}) \hat{G}^K = \nu \hat{\Sigma}^K \hat{G}^A + \nu \hat{\Sigma}^R \hat{G}^K; \quad (3.11)$$

$$\hat{G}^K (\hat{\varepsilon} - \hat{H} \nu) = \hat{G}^R \hat{\Sigma}^K \nu + \hat{G}^K \hat{\Sigma}^A \nu, \quad (3.12)$$

where $\hat{\varepsilon} = \delta(\mathbf{r} - \mathbf{r}') \delta(t - t') i\hbar \partial_{\mu}$, $\hat{\Sigma}^{R/A/K}$ and $\hat{G}^{R/A/K}$ are the retarded, advanced and Keldysh self-energies and Green's functions, hats indicate matrices in space and time and $\nu = \text{diag}[1, \dots, 1, -1, \dots, -1]$. We apply a Wigner transformation, defined as

$$A(\mathbf{r}, t; \mathbf{p}, \varepsilon) = \int d\mathbf{r}' \int dt' \hat{A} \left(\mathbf{r} + \frac{\mathbf{r}'}{2}, t + \frac{t'}{2}; \mathbf{r} - \frac{\mathbf{r}'}{2}, t - \frac{t'}{2} \right) e^{-i(\mathbf{k} \cdot \mathbf{r}' - \omega t')}$$

and expand up to first order in \hbar , such that we have (suppressing all labels from here on)

$$\left(\varepsilon - \nu H - \nu \Sigma^R + \frac{i\hbar}{2} \partial_t + \frac{i}{2} \nu (\nabla_p H) \cdot \nabla_r \right) G^K = \nu \Sigma^K G^A; \quad (3.13)$$

$$G^K \left(\varepsilon - H \nu - \Sigma^A \nu - \frac{i\hbar}{2} \overleftarrow{\partial}_t - \frac{i}{2} \overleftarrow{\nabla}_r \cdot (\nabla_p H) \nu \right) = G^R \Sigma^K \nu, \quad (3.14)$$

where we assume that the Hamiltonian does not depend explicitly on position or time, i.e. $H(\mathbf{r}, t; \mathbf{k}, \omega) = H(\mathbf{k})$ and have used arrows to indicate to which function the derivative applies, if there are ambiguities.

Furthermore, we define a covariant derivative as

$$D_{k_\alpha} \mathcal{E} \equiv \mathcal{T}^\dagger (\partial_{k_\alpha} \mathcal{H}) \mathcal{T} = \partial_{k_\alpha} \mathcal{E} + i\mathcal{E} A^\alpha - i\nu \mathcal{E} \nu A^\alpha. \quad (3.15)$$

We introduce the transformed Green's functions and self-energies

$$g^{R/A/K} = \mathcal{T}^{-1} G^{R/A/K} (\mathcal{T}^\dagger)^{-1}; \quad \sigma^{R/A/K} = \mathcal{T}^\dagger \Sigma^{R/A/K} \mathcal{T},$$

and assume damped quasiparticles in (local) thermal equilibrium, such that

$$\sigma^{R/A}(\mathbf{k}, \omega) = \mp i\nu [\Gamma^{\text{mm}}(\mathbf{k}, \omega) + \Gamma^{\text{mr}}(\mathbf{k}, \omega)]; \quad (3.16)$$

$$\begin{aligned} \sigma^K(\mathbf{r}; \mathbf{k}, \omega) &= -2i\Gamma^{\text{mm}}(\mathbf{k}, \omega) F_n(\mathbf{r}, \omega) \\ &\quad - 2i\Gamma^{\text{mr}}(\mathbf{k}, \omega) F_n^{\mu m=0}(\mathbf{r}, \omega), \end{aligned} \quad (3.17)$$

where

$$\Gamma_{mn}^\eta(\mathbf{k}, \omega) = \delta_{mn} \times \begin{cases} \gamma^\eta(\mathbf{k}, \omega) & 1 \leq n \leq N, \\ \gamma^\eta(-\mathbf{k}, -\omega) & N+1 \leq n \leq 2N, \end{cases}$$

with $\eta \in \{\text{mr}, \text{mm}\}$ representing the magnon relaxation processes (which do not conserve spin) and magnon-magnon interactions (which conserve spin) respectively. The distribution function is defined as

$$F_{mn}(\mathbf{r}, \omega) = \delta_{mn} \times \begin{cases} f_B(\mathbf{r}, \omega) & 1 \leq n \leq N, \\ f_B(\mathbf{r}, -\omega) & N+1 \leq n \leq 2N, \end{cases}$$

where $f_B = \coth\left(\frac{\hbar\omega - \mu_m}{2k_B T}\right)$ is the symmetrized Bose-Einstein distribution. The distribution function $F_n^{\mu_m=0}(\mathbf{r}, \omega)$ describes the relaxation of magnons to the lattice. For brevity, we write $\Gamma_n(\mathbf{k}, \omega) = \Gamma_n^{\text{mr}}(\mathbf{k}, \omega) + \Gamma_n^{\text{mm}}(\mathbf{k}, \omega)$.

The retarded and advanced Green's functions are then given by

$$g^{R/A} = \frac{\delta_{nm}}{\nu_n(\hbar\omega \pm i\Gamma_n) - \mathcal{E}_n}. \quad (3.18)$$

For the Keldysh Green function we first solve the diagonal component of the distribution function, $f_n \equiv \frac{i\hbar}{2} g_{nn}^K$, using the difference between Eqs. (3.11) and (3.12), such that

$$\begin{aligned} \partial_t f_n + \sum_\alpha \partial_{r_\alpha} j_n^\alpha &= -2 \frac{\Gamma_n^{\text{mr}}}{\hbar} \left[f_n - \frac{\hbar\Gamma_n}{(\hbar\omega - \nu_n \mathcal{E}_n)^2 + \Gamma_n^2} F_n^{\mu_m=0} \right] \\ &\quad - 2 \frac{\Gamma_n^{\text{mm}}}{\hbar} \left[f_n - \frac{\hbar\Gamma_n}{(\hbar\omega - \nu_n \mathcal{E}_n)^2 + \Gamma_n^2} F_n \right], \end{aligned} \quad (3.19)$$

where the current density

$$j_n^\alpha = \frac{\nu_n}{\hbar} (\partial_{k_\alpha} \mathcal{E}_n) f_n + \nu_n \frac{i}{4} \sum_{m \neq n} \left[(D_{k_\alpha} \mathcal{E})_{nm} g_{mn}^K + g_{nm}^K (D_{k_\alpha} \mathcal{E})_{mn} \right], \quad (3.20)$$

has contributions from the off-diagonal components.

We now assume that there is local thermal equilibrium, and thus that the local distribution function f_n can be described by small corrections δf_n on top of the thermal equilibrium. This is possible because the spin conserving processes (represented by Γ^{mm}) are much faster than the non-spin-conserving processes (represented by Γ^{mr}). Thus, we disregard the $F_n^{\mu_m=0}$ term in Eq. (3.19) and make the ansatz

$$f_n = \frac{\hbar\Gamma_n}{(\hbar\omega - \nu_n \mathcal{E}_n)^2 + \Gamma_n^2} F_n + \delta f_n, \quad (3.21)$$

where δf_n is at least one order higher in gradients. In a steady state (such that $\partial_t f_n = 0$) we further note that from Eq. (3.19) it is clear that

$$\sum_{\alpha} \partial_{r_{\alpha}} j_n^{\alpha} = -2 \frac{\Gamma_n}{\hbar} \left(\delta f_n + \frac{\Gamma_n^{\text{mr}}}{(\hbar\omega - \nu_n \mathcal{E}_n)^2 + \Gamma_n^2} (F_n - F_n^{\mu_m=0}) \right). \quad (3.22)$$

This can then be solved up to first order in gradients by inserting the ansatz, Eq. (3.21), into the current density, Eq. (3.20), and using the fact that g_{nm}^K is one order higher in gradients and can thus be discarded. Then we find

$$\delta f_n = -\frac{\nu_n \hbar}{2} (\partial_{k_{\alpha}} \mathcal{E}_n) \frac{1}{(\hbar\omega - \nu_n \mathcal{E}_n)^2 + \Gamma_n^2} (\partial_{r_{\alpha}} F_n) - \frac{\hbar \Gamma_n^{\text{mr}}}{(\hbar\omega - \nu_n \mathcal{E}_n)^2 + \Gamma_n^2} (F_n - F_n^{\mu_m=0}). \quad (3.23)$$

In order to find g_{nm}^K we consider the sum of Eqs. (3.11) and (3.12) and find for $m \neq n$ that

$$\begin{aligned} [2\hbar\omega - \nu_n \mathcal{E}_n - \nu_m \mathcal{E}_m + i(\Gamma_n - \Gamma_m)] g_{nm}^K = \\ -\frac{i}{2} \sum_{\alpha} \sum_l \left[\nu_n (D_{k_{\alpha}} \mathcal{E})_{nl} (\partial_{r_{\alpha}} g_{lm}^K) - \nu_m (\partial_{r_{\alpha}} g_{nl}^K) (D_{k_{\alpha}} \mathcal{E})_{lm} \right]. \end{aligned} \quad (3.24)$$

It is convenient to proceed in the quasiparticle limit ($\lim_{\Gamma_n \rightarrow 0^+}$), where

$$\lim_{\Gamma \rightarrow 0^+} f_n = \pi \delta(\omega - \nu_n \mathcal{E}_n / \hbar) F_n(\omega) + \delta f_n. \quad (3.25)$$

We now use the fact that g_{nm}^K is one order higher in gradients than f_n , and as such for $m \neq n$ can write

$$\begin{aligned} g_{nm}^K = \frac{1}{\hbar} \frac{i\pi}{\nu_m \mathcal{E}_n - \nu_n \mathcal{E}_m} \sum_{\alpha} \partial_{r_{\alpha}} (D_{k_{\alpha}} \mathcal{E})_{nm} \times \\ \left[\nu_m \delta(\omega - \nu_n \mathcal{E}_n / \hbar) F_n(\omega) + \nu_n \delta(\omega - \nu_m \mathcal{E}_m / \hbar) F_m(\omega) \right], \end{aligned} \quad (3.26)$$

where we have used the diagonal components f_n to rewrite Eq. (3.24), only keeping terms up to first order in gradients. Using the definition of the covariant derivative in Eq. (3.15) we now write the current as

$$\begin{aligned} j_n^{\alpha} = \nu_n (\partial_{k_{\alpha}} \mathcal{E}_n) \pi \delta(\omega - \nu_n \mathcal{E}_n / \hbar) \left[F_n - \frac{\Gamma_n^{\text{mr}}}{\Gamma_n} (F_n - F_n^{\mu_m=0}) \right] \\ - \frac{1}{2\Gamma_n \hbar} \sum_{\beta} (\partial_{k_{\alpha}} \mathcal{E}_n) (\partial_{k_{\beta}} \mathcal{E}_n) \pi \delta(\omega - \nu_n \mathcal{E}_n / \hbar) \partial_{r_{\beta}} F_n \\ + \frac{i\pi}{4} \sum_{m \neq n} \sum_{\beta} (\nu_n \nu_m \mathcal{E}_m - \mathcal{E}_n) (A_{mn}^{\alpha} A_{nm}^{\beta} - A_{mn}^{\beta} A_{nm}^{\alpha}) \times \\ \partial_{r_{\beta}} [\nu_n \delta(\omega - \nu_m \mathcal{E}_m / \hbar) F_m + \nu_m \delta(\omega - \nu_n \mathcal{E}_n / \hbar) F_n], \end{aligned} \quad (3.27)$$

such that we now have a full description of the equation of motion, Eq. (3.19) for the distribution function of the magnons. Note that the first term in Eq. (3.27) will be zero if integrated over, due to inversion symmetry.

We continue with the spin density, which is defined as

$$\begin{aligned} s^z(\mathbf{r}, t) &= -\frac{i\hbar}{4} \text{Tr} [\hat{G}^K], \\ &= -\frac{i\hbar}{4} \int \frac{d^d k}{(2\pi)^d} \int \frac{d\omega}{2\pi} \text{Tr} [\mathcal{T}^\dagger \mathcal{T} g^K], \end{aligned} \quad (3.28)$$

such that

$$\begin{aligned} \partial_t s^z(\mathbf{r}, t) &= \frac{1}{2} \int \frac{d^d k}{(2\pi)^d} \int \frac{d\omega}{2\pi} \sum_n (\mathcal{T}^\dagger \mathcal{T})_{nn} \times \\ &\quad \left[\sum_\alpha \partial_{r_\alpha} j_n^\alpha + 2 \frac{\Gamma_n^{\text{mr}}}{\hbar} \left(f_n - \frac{\hbar \Gamma_n}{(\hbar\omega - v_n \mathcal{E}_n)^2 + \Gamma_n^2} F_n^{\mu_m=0} \right) \right], \end{aligned} \quad (3.29)$$

where we have only kept terms up to first order in gradients. Since the processes described by Γ^{mm} always conserve spin and because we assume them to approximately conserve momentum, we furthermore disregard all terms related to Γ^{mm} , such that $\Gamma_n = \Gamma_n^{\text{mr}}$. Its inclusion up to this point was however necessary, since without it a local thermal equilibrium cannot be properly defined and a current density cannot be expressed in terms of the magnon chemical potential.

3.B COEFFICIENTS

From here on, we assume Gilbert damping for the magnon relaxation process, such that $\gamma^{\text{mr}}(\mathbf{k}, \omega) = 2\alpha_G \hbar \omega$ [33], where α_G is the bulk Gilbert damping parameter. With the generic equation of motion, Eq. (3.29), we now derive the equation of motion up to linear order in the magnon chemical potential, giving

$$\partial_t s^z(\mathbf{r}, t) + \sum_\alpha \partial_{r_\alpha} J_s^\alpha = \Gamma_s \mu_m, \quad (3.30)$$

where $J_s^\alpha = \sigma^{\alpha\alpha} \partial_{r_\alpha} \mu_m + \sum_\beta \sigma^{\alpha\beta} \partial_{r_\beta} \mu_m$, with

$$\begin{aligned} \sigma^{\alpha\alpha} &= -\frac{1}{32\hbar\alpha_G k_B T} \int \frac{d^2 k}{(2\pi)^2} \sum_n (\mathcal{T}^\dagger \mathcal{T})_{nn} \frac{(\partial_{k_\alpha} \mathcal{E}_n)^2}{\mathcal{E}_n} \text{csch} \left[\frac{\mathcal{E}_n}{2k_B T} \right]^2, \\ \sigma^{\alpha\beta} &= \frac{1}{32k_B T \hbar} \int \frac{d^2 k}{(2\pi)^2} \sum_{\substack{n,m; \\ m \neq n}} (v_n (\mathcal{T}^\dagger \mathcal{T})_{nn} + v_m (\mathcal{T}^\dagger \mathcal{T})_{mm}) \times \end{aligned} \quad (3.31)$$

$$(v_n v_m \mathcal{E}_m - \mathcal{E}_n) \Omega_m^{\alpha\beta} \operatorname{csch} \left[\frac{\mathcal{E}_n}{2k_B T} \right]^2, \quad (3.32)$$

$$\Gamma_s = -\frac{1}{2k_B T} \int \frac{d^2 k}{(2\pi)^2} \int \frac{d\omega}{2\pi} \sum_n \left(\mathcal{T}^\dagger \mathcal{T} \right)_{nn} \times \frac{(2\alpha_G \hbar \omega)^2}{(\hbar \omega - v_n \mathcal{E}_n)^2 + (2\alpha_G \hbar \omega)^2} \operatorname{csch} \left[\frac{v_n \hbar \omega}{2k_B T} \right]^2. \quad (3.33)$$

Here we have disregarded the Γ^{mm} term, since magnon-magnon scattering preserves momentum and should therefore not contribute to the magnon spin conductivity $\sigma^{\alpha\alpha}$. We then have $\sigma_s = \sigma^{xx} = \sigma^{yy}$ and $\sigma_s^H = \sigma^{xy}$, since the system is rotationally invariant.

In order to calculate these coefficients we diagonalize the Hamiltonian H with a paraunitary matrix \mathcal{T} , which also gives the energies \mathcal{E} . Moreover, we construct $\partial_{k_\alpha} H$, such that we calculate the Berry phase and subsequently the Berry curvature using Eq. (3.4). These terms are further shown in Appendix 3.E. We can then integrate the coefficients σ_s^H, σ_s and Γ_s over the entire Brillouin zone, where we use the translation invariance to employ the one-dimensional Gauss-Kronrod quadrature formula, which also gives an error estimate. These results are shown in Sec. 3.4.

3.C METALLIC LEAD

We now consider how the equation of motion for the spin density has to be modified if a metallic lead is interfaced to the ferromagnet. Attaching a metallic lead, the self-energies are modified such that $\Sigma^{R/A/K} = \Sigma_{\text{bulk}}^{R/A/K} + \Sigma_{\text{IF}}^{R/A/K}$, with

$$\Sigma_{\text{IF}}^{R/A}(\mathbf{r}, t; \mathbf{k}, \omega) = \mp i \alpha_{\text{IF}} (\hbar \omega - \nu \mu_e), \quad (3.34)$$

$$\Sigma_{\text{IF}}^K(\mathbf{r}, t; \mathbf{k}, \omega) = 2 \Sigma_{\text{IF}}^R F_e(\omega), \quad (3.35)$$

where

$$F_e(\mathbf{r}, \omega) = \delta_{nm} \times \begin{cases} \coth \left[\frac{\hbar \omega - \mu_e}{2k_B T} \right] & 1 \leq n \leq N, \\ \coth \left[\frac{-\hbar \omega - \mu_e}{2k_B T} \right] & N+1 \leq n \leq 2N, \end{cases} \quad (3.36)$$

and α_{IF} is the interfacial Gilbert damping. The equation of motion for the spin density, Eq. (3.29), is then modified to $\partial_t s^z + \nabla \cdot \mathbf{J}^s = \Gamma_s + \Gamma_s^{\text{IF}}$, where

$$\Gamma_s^{\text{IF}} = -\frac{1}{4} \int \frac{d^d k}{(2\pi)^d} \int \frac{d\omega}{2\pi} \operatorname{Tr} \left[\mathcal{T}^\dagger \nu \Sigma_{\text{IF}}^K \mathcal{T} g^A - \mathcal{T}^\dagger \nu \Sigma_{\text{IF}}^K \mathcal{T} g^R + \mathcal{T}^\dagger \nu \Sigma_{\text{IF}}^R \mathcal{T} g^K - \mathcal{T}^\dagger \nu \Sigma_{\text{IF}}^A \mathcal{T} g^K \right]. \quad (3.37)$$

Noting that, up to lowest order in the interfacial coupling, the Green's functions $g^{R/A/K}$ are unchanged by the interfacial self-energies, we can further write this as (in the quasiparticle limit)

$$\Gamma_s^{\text{IF}} = \frac{\alpha_{\text{IF}}}{2\hbar} \int \frac{d^d k}{(2\pi)^d} \text{Tr} \left[\mathcal{T}^\dagger (\mathcal{E} - \mu_e) \mathcal{T} F(\nu \mathcal{E}) - \mathcal{T}^\dagger \nu (\mathcal{E} - \mu_e) F_e(\nu \mathcal{E}) \mathcal{T} \nu \right]. \quad (3.38)$$

We again keep only terms linear in μ_m and μ_e , such that we can write $\Gamma_s^{\text{IF}} = A\mu_m + B\mu_e + C$, with

$$A = \frac{\alpha_{\text{IF}}}{4\hbar k_B T} \int \frac{d^2 k}{(2\pi)^2} \text{Tr} \left[\mathcal{T}^\dagger \mathcal{E} \mathcal{T} \text{csch} \left[\frac{\mathcal{E}}{2k_B T} \right]^2 \right]; \quad (3.39)$$

$$B = -\frac{\alpha_{\text{IF}}}{2\hbar} \int \frac{d^2 k}{(2\pi)^2} \text{Tr} \left[\mathcal{T}^\dagger \mathcal{T} \coth \left[\frac{\mathcal{E}}{2k_B T} \right] - \frac{1}{2k_B T} \mathcal{E} \text{csch} \left[\frac{\mathcal{E}}{2k_B T} \right]^2 + \coth \left[\frac{\mathcal{E}}{2k_B T} \right] \right]; \quad (3.40)$$

$$C = \frac{\alpha_{\text{IF}}}{2\hbar} \int \frac{d^2 k}{(2\pi)^2} \text{Tr} \left[(\mathcal{T}^\dagger \mathcal{E} \mathcal{T} - \mathcal{E}) \coth \left[\frac{\mathcal{E}}{2k_B T} \right] \right]. \quad (3.41)$$

3.D BOUNDARY CONDITIONS

With the equation of motion for the spin density completely determined, we can now consider the boundary condition for the spin density in the Hall bar geometry. For the metal strips we assume a thin strip, where $L_a \ll L_b$ and the long side L_b interfaces the Hall bar, as shown in Fig. 3.1. Then the detector can be described by Eq. (3.8), with the boundary condition that the current at its interface with the main region is continuous. Thus we have,

$$\int_{\partial S_i} ds \mathbf{J}_s \cdot \hat{\mathbf{n}} = \int_{S_i} dS [(\Gamma_s + A)\mu_m + B\mu_e + C], \quad (3.42)$$

where S_i is the area of detector i . Note that for the detectors $\mu_e = 0$. We now Taylor expand the chemical potential in the detector strip perpendicular to the interface, and integrate over the short side of the strip, keeping only terms linear in L_a , which gives the boundary condition

$$\int_{\partial S_i} ds \mathbf{J}_s \cdot \hat{\mathbf{n}} = L_a \int_{\partial S_i} ds [(\Gamma_s + A)\mu_m + B\mu_e + C], \quad (3.43)$$

where we have required that $\mathbf{J}_s \cdot \hat{\mathbf{n}} = 0$ at the other three sides of the detector. The boundary condition can now be identified as

$$\mathbf{J}_s \cdot \hat{\mathbf{n}} = J_s^{\text{int}}(\mu_m), \quad (3.44)$$

where

$$J_s^{\text{int}}(\mu_m) = L_a [(\Gamma_s + A) \mu_m + B\mu_e + C]. \quad (3.45)$$

3.E HAMILTONIAN

In order to determine the dynamics of the magnons in the YIG, we describe this system using the Heisenberg spin Hamiltonian [91]

$$\begin{aligned} \mathcal{H} = & -\frac{1}{2} \sum_{ij} J_{ij} \mathbf{S}_i \cdot \mathbf{S}_j - \mu \mathbf{H}_e \cdot \sum_i \mathbf{S}_i \\ & - \frac{1}{2} \sum_{ij, i \neq j} \frac{\mu^2}{|\mathbf{R}_{ij}|^3} [3 (\mathbf{S}_i \cdot \hat{\mathbf{R}}_{ij}) (\mathbf{S}_j \cdot \hat{\mathbf{R}}_{ij}) - \mathbf{S}_i \cdot \mathbf{S}_j], \end{aligned} \quad (3.46)$$

where the sums are over the lattice sites \mathbf{R}_i , with $\mathbf{R}_{ij} = \mathbf{R}_i - \mathbf{R}_j$ and $\hat{\mathbf{R}}_{ij} = \mathbf{R}_{ij}/|\mathbf{R}_{ij}|$. We only consider nearest neighbour exchange interactions, so $J_{ij} = J$ for nearest neighbours and 0 otherwise. Here $\mu = 2\mu_B$ is the magnetic moment of the spins, with $\mu_B = e\hbar/(2m_e c)$ the Bohr magneton. \mathbf{H}_e is the external magnetic field, which we take strong enough to fully saturate the ferromagnet.

We apply the Holstein Primakoff transformation up to quadratic order,

$$S_i^+ = \sqrt{2S} b_i; \quad S_i^- = \sqrt{2S} b_i^\dagger; \quad S_i^z = S - b_i^\dagger b_i \quad (3.47)$$

to the Heisenberg spin Hamiltonian, Eq. (3.46), and apply the Fourier transformation in the xy -plane, introducing $\mathbf{k} = (k_x, k_y)$. The coordinate system used is summarized in Fig. 3.2 in the main text. We can now write the quadratic part of the Hamiltonian in the basis $(b_{\mathbf{k}}(z_1), \dots, b_{\mathbf{k}}(z_N), b_{-\mathbf{k}}^\dagger(z_1), \dots, b_{-\mathbf{k}}^\dagger(z_N))^T$ as

$$\mathcal{H}_{\mathbf{k}} = \begin{pmatrix} \mathbf{A}_{\mathbf{k}} & \mathbf{B}_{\mathbf{k}} \\ \mathbf{B}_{\mathbf{k}}^\dagger & \mathbf{A}_{\mathbf{k}} \end{pmatrix}, \quad (3.48)$$

where the amplitude factors are

$$\begin{aligned} A_{\mathbf{k}}(z_{ij}) &= \sum_{\mathbf{r}_{ij}} e^{-i\mathbf{k}\cdot\mathbf{r}} A(z_i - z_j, \mathbf{r}), \\ &= \delta_{ij} \left[h + S \sum_n D_0^{zz}(z_{in}) \right] \\ &\quad - \frac{S}{2} \left[D_{\mathbf{k}}^{yy}(z_{ij}) + D_{\mathbf{k}}^{xx}(z_{ij}) \right] + SJ_{\mathbf{k}}(z_{ij}), \end{aligned} \quad (3.49)$$

$$\begin{aligned} B_{\mathbf{k}}(z_{ij}) &= \sum_{\mathbf{r}_{ij}} e^{-i\mathbf{k}\cdot\mathbf{r}} B(z_i - z_j, \mathbf{r}), \\ &= -\frac{S}{2} \left[D_{\mathbf{k}}^{xx}(z_{ij}) - D_{\mathbf{k}}^{yy}(z_{ij}) + iD_{\mathbf{k}}^{xy}(z_{ij}) \right], \end{aligned} \quad (3.50)$$

where

$$J_{\mathbf{k}}(z_{ij}) = J[\delta_{ij}(6 - \delta_{j1} - \delta_{jN} - 2\cos(k_x a) - 2\cos(k_y a)) - \delta_{ij+1} - \delta_{ij-1}], \quad (3.51)$$

$\mathbf{r}_{ij} = (x_{ij}, y_{ij})$ and $D_{\mathbf{k}}^{\alpha\beta}(z_{ij})$ describes the dipole-dipole interaction.

For the Berry curvature we need to calculate $\partial_{k_\alpha} \mathcal{H}_{\mathbf{k}}$, where $\alpha \in (x, y)$. This is given by

$$\partial_{k_\alpha} \mathcal{H}_{\mathbf{k}} = \begin{pmatrix} \partial_{k_\alpha} A_{\mathbf{k}} & \partial_{k_\alpha} B_{\mathbf{k}} \\ \partial_{k_\alpha} B_{\mathbf{k}}^\dagger & \partial_{k_\alpha} A_{\mathbf{k}} \end{pmatrix}, \quad (3.52)$$

where

$$\partial_{k_\alpha} A_{\mathbf{k}}(z_{ij}) = -\frac{S}{2} \left[\partial_{k_\alpha} D_{\mathbf{k}}^{yy}(z_{ij}) + \partial_{k_\alpha} D_{\mathbf{k}}^{xx}(z_{ij}) \right] + 2SJ_a \sin(k_\gamma a), \quad (3.53)$$

$$\partial_{k_\alpha} B_{\mathbf{k}}(z_{ij}) = -\frac{S}{2} \left[\partial_{k_\alpha} D_{\mathbf{k}}^{xx}(z_{ij}) - \partial_{k_\alpha} D_{\mathbf{k}}^{yy}(z_{ij}) + i\partial_{k_\alpha} D_{\mathbf{k}}^{xy}(z_{ij}) \right], \quad (3.54)$$

For the dipolar sums we apply the Ewald summation method, as previously developed by Kreisel *et al.* [23], and find

$$D_{\mathbf{k}}^{zz}(z_{ij}) = \frac{\pi\mu^2}{a^2} \sum_{\mathbf{g}} \left(\frac{8\sqrt{\varepsilon}}{3\sqrt{\pi}} e^{-p^2 - q^2} - |\mathbf{k} + \mathbf{g}| f(p, q) \right) \quad (3.55)$$

$$- \frac{4\mu^2}{3} \sqrt{\frac{\varepsilon^5}{\pi}} \sum_{\mathbf{r}} \left(|\mathbf{r}_{ij}|^2 - 3z_{ij}^2 \right) \cos(k_x x_{ij}) \cos(k_y y_{ij}) \varphi_{3/2}(|\mathbf{r}_{ij}|^2 \varepsilon);$$

$$D_{\mathbf{k}}^{yy}(z_{ij}) = \frac{\pi\mu^2}{a^2} \sum_{\mathbf{g}} \left(\frac{4\sqrt{\varepsilon}}{3\sqrt{\pi}} e^{-p^2 - q^2} - \frac{(k_y + g_y)^2}{|\mathbf{k} + \mathbf{g}|} f(p, q) \right) \quad (3.56)$$

$$- \frac{4\mu^2}{3} \sqrt{\frac{\varepsilon^5}{\pi}} \sum_{\mathbf{r}} \left(|\mathbf{r}_{ij}|^2 - 3y_{ij}^2 \right) \cos(k_x x_{ij}) \cos(k_y y_{ij}) \varphi_{3/2}(|\mathbf{r}_{ij}|^2 \varepsilon);$$

$$D_{\mathbf{k}}^{xy}(z_{ij}) = -\frac{\pi\mu^2}{a^2} \sum_{\mathbf{g}} \frac{(k_y + g_y)(k_x + g_x)}{|\mathbf{k} + \mathbf{g}|} f(p, q) \quad (3.57)$$

$$-4 \frac{\varepsilon^{5/2} \mu^2}{\sqrt{\pi}} \sum_{\mathbf{r}} y_{ij} x_{ij} \sin(k_x x_{ij}) \sin(k_y y_{ij}) \varphi_{3/2}(|\mathbf{r}_{ij}|^2 \varepsilon),$$

where

$$\varphi_{3/2}(x) = e^{-x} \frac{3+2x}{2x^2} + \frac{3\sqrt{\pi} \operatorname{Erfc}(\sqrt{x})}{4x^{5/2}} \quad (3.58)$$

and $q = z_{ij}\sqrt{\varepsilon}$, $p = |\mathbf{k} + \mathbf{g}|/(2\sqrt{\varepsilon})$ and $f(p, q) = e^{-2pq} \operatorname{Erfc}(p-q) + e^{2pq} \operatorname{Erfc}(p+q)$. The sums are either over the real space lattice or the reciprocal lattice, where the reciprocal lattice vectors are $g_x = 2\pi m$, $g_y = 2\pi n$, $\{m, n\} \in \mathbb{Z}$. ε determines the ratio between the reciprocal and real sums. We choose $\varepsilon = a^{-2}$, such that $2pq \approx 1$ and $\exp[\pm 2pq]$ converges quickly. Note that $D_{\mathbf{k}}^{xx}$ from the symmetry $D_{\mathbf{k}}^{yy} = D_{\mathbf{k}}^{xx}(k_x \rightarrow k_y, k_y \rightarrow k_x)$. Taking the derivatives w.r.t. k_x and k_y we find

$$\begin{aligned} \partial_{k_y} D_{\mathbf{k}}^{zz}(z_{ij}) &= \frac{\pi \mu^2}{a^2} \sum_{\mathbf{g}} \left(\frac{16p\sqrt{\varepsilon}}{3\sqrt{\pi}} e^{-p^2-q^2} \frac{\partial p}{\partial k_y} + p2\sqrt{\varepsilon} \frac{\partial f}{\partial k_y} + \frac{k_y + g_y}{2\sqrt{\varepsilon} p} f(p, q) \right) \\ &\quad + \frac{4\mu^2}{3} \sqrt{\frac{\varepsilon^5}{\pi}} \sum_{\mathbf{r}} y_{ij} (|\mathbf{r}_{ij}|^2 - 3z_{ij}^2) \cos(k_x x_{ij}) \sin(k_y y_{ij}) \varphi_{3/2}(|\mathbf{r}_{ij}|^2 \varepsilon); \\ \partial_{k_y} D_{\mathbf{k}}^{yy}(z_{ij}) &= -\frac{\pi \mu^2}{a^2} \sum_{\mathbf{g}} \left(\frac{8p\sqrt{\varepsilon}}{3\sqrt{\pi}} e^{-p^2-q^2} \frac{\partial p}{\partial k_y} + \frac{(k_y + g_y)^2}{|\mathbf{k} + \mathbf{g}|} \frac{\partial f}{\partial k_y} \right. \\ &\quad \left. + \frac{2(k_y + g_y)|\mathbf{k} + \mathbf{g}|^2 - (k_y + g_y)^3}{|\mathbf{k} + \mathbf{g}|^3} f(p, q) \right) \\ &\quad + \frac{4\mu^2}{3} \sqrt{\frac{\varepsilon^5}{\pi}} \sum_{\mathbf{r}} y_{ij} (|\mathbf{r}_{ij}|^2 - 3y_{ij}^2) \cos(k_x x_{ij}) \sin(k_y y_{ij}) \varphi_{3/2}(|\mathbf{r}_{ij}|^2 \varepsilon); \\ \partial_{k_x} D_{\mathbf{k}}^{yy}(z_{ij}) &= -\frac{\pi \mu^2}{a^2} \sum_{\mathbf{g}} \left(\frac{8p\sqrt{\varepsilon}}{3\sqrt{\pi}} e^{-p^2-q^2} \frac{\partial p}{\partial k_x} - \frac{(k_y + g_y)^2}{|\mathbf{k} + \mathbf{g}|} \frac{\partial f}{\partial k_x} \right. \\ &\quad \left. + \frac{(k_y + g_y)^2(k_x + g_x)}{|\mathbf{k} + \mathbf{g}|^3} f(p, q) \right) \\ &\quad + \frac{4\mu^2}{3} \sqrt{\frac{\varepsilon^5}{\pi}} \sum_{\mathbf{r}} z_{ij} (|\mathbf{r}_{ij}|^2 - 3y_{ij}^2) \cos(k_y y_{ij}) \sin(k_x z_{ij}) \varphi_{3/2}(|\mathbf{r}_{ij}|^2 \varepsilon); \\ \partial_{k_y} D_{\mathbf{k}}^{xy}(z_{ij}) &= -\frac{\pi \mu^2}{a^2} \sum_{\mathbf{g}} \left(\frac{(k_x + g_x)|\mathbf{k} + \mathbf{g}|^2 - (k_y + g_y)^2(k_x + g_x)}{|\mathbf{k} + \mathbf{g}|^3} f(p, q) \right. \\ &\quad \left. + \frac{(k_y + g_y)(k_x + g_x)}{|\mathbf{k} + \mathbf{g}|} \frac{\partial f}{\partial k_y} \right) \\ &\quad - 4 \frac{\varepsilon^{5/2} \mu^2}{\sqrt{\pi}} \sum_{\mathbf{r}} y_{ij}^2 x_{ij} \sin(k_x x_{ij}) \cos(k_y y_{ij}) \varphi_{3/2}(|\mathbf{r}_{ij}|^2 \varepsilon), \end{aligned}$$

where

$$\frac{\partial p}{\partial k_\alpha} = \frac{k_\alpha + g_\alpha}{4\varepsilon p};$$

$$\frac{\partial f}{\partial k_\alpha} = \frac{k_\alpha + g_\alpha}{4p\varepsilon} \left(2qe^{2pq} \operatorname{Erfc}(p+q) - 2qe^{-2pq} \operatorname{Erfc}(p-q) - \frac{4}{\sqrt{\pi}} e^{-p^2-q^2} \right)$$

and the remaining terms follow from symmetry, by swapping $k_y \leftrightarrow k_x$.

ZERO-FREQUENCY CHIRAL MAGNONIC EDGE STATES PROTECTED BY NON-EQUILIBRIUM TOPOLOGY

Topological bosonic excitations must, in contrast to their fermionic counterparts, appear at finite energies. This is a key challenge for magnons, as it prevents straightforward excitation and detection of topologically-protected magnonic edge states and their use in magnonic devices. In this work, we show that in a non-equilibrium state, in which the magnetization is pointing against the external magnetic field, the topologically-protected chiral edge states in a magnon Chern insulator can be lowered to zero frequency, making them directly accessible by existing experimental techniques. We discuss the spin-orbit torque required to stabilize this non-equilibrium state, and show explicitly using numerical Landau-Lifshitz-Gilbert simulations that the edge states can be excited with a microwave field. Finally, we consider a propagating spin wave spectroscopy experiment, and demonstrate that the edge states can be directly detected.¹

4.1 INTRODUCTION

Over the past decade, it has become clear that the concepts of topological band theory cannot only be applied to electrons [39, 42], but also to a whole range of other (quasi)-particles, encompassing photons [129, 130] and collective bosonic modes in quantum condensed matter systems like phonons [131], plasmons [132, 133], and magnons [64]. Among the latter, topological magnon systems, such as magnon Chern insulators [12, 43, 44, 47–49, 118, 134], magnon spin Hall insulators [53–55], magnon Dirac semimetals [56, 57], magnon Weyl semimetals [58, 59], and higher-order topological magnon insulators [60–62] are especially of interest because they couple to external magnetic fields providing an exceptional handle for control. Arguably, the most fundamental of these phases is the magnon Chern insulator, which supports chiral edge states that could be used as fault-tolerant spin-wave current splitters and interferometers [63, 118] and for highly efficient spin

¹ This chapter is based on P. M. Gunnink, J. S. Harms, R. A. Duine, and A. Mook, *Zero-frequency chiral magnonic edge states protected by non-equilibrium topology*, (Feb. 13, 2023) arXiv:2302.06597. A.M. conceived the project, R.A.D. and J.S.H. introduced the non-equilibrium states and P.M.G. performed the calculations and prepared the manuscript. All authors contributed to the manuscript.

transport robust against backscattering at moderate disorder [135, 136]. Multiple magnetic materials have been predicted to be magnon Chern insulators from their bulk band structure obtained by inelastic neutron scattering experiments [50–52, 137]. However, the hallmark chiral edge states have to date not been directly observed. Alternatively, as a direct probe of bulk band topology Raman scattering has been proposed [138].

This lack of evidence for chiral bosonic edge states is strongly tied to the fundamental difference between fermion topological insulators and their bosonic analogs. Since bosonic collective excitations do not obey a particle number conservation law, their mathematical description relies on the Bogoliubov-de Gennes formalism, which comes with a doubled particle space. As a result, the topologically-protected edge states have to appear at finite frequencies above the first bulk band [118, 139, 140]. For magnon Chern insulators, this means the edge states have energies set by the magnetic exchange energy scale, which is typically meV [51, 141]. The corresponding frequency is in the THz-range, which is beyond the reach of experimental tools, such as Brillouin Light Scattering or microwave excitation and detection.

In this work we propose a method to lower the topologically-protected chiral edge states in magnon Chern insulators to zero frequency, such that they are easily accessible by microwave techniques. This is achieved by considering magnon excitations on top of a uniform magnetization that is pointing *against* the applied external magnetic field, as opposed to considering excitations on top of a magnetization parallel to the magnetic field, as shown in Fig. 4.1(a-b). In such a *non-equilibrium* setup, the magnon excitations decrease the energy of the system, allowing us to tune the frequency of the edge modes to zero frequency. Since the non-equilibrium state is energetically unstable, it has to be rendered dynamically stable, which is achieved by an appropriate spin-orbit torque. Using numerical Landau-Lifshitz-Gilbert simulations we show that the edge modes can be excited at low frequencies, and are topologically protected against backscattering. Finally, we consider a propagating spin-wave spectroscopy (PSWS) experiment with two antennas, and demonstrate that the edge modes can be directly detected at gigahertz frequencies, even in the presence of disorder.

4.2 MODEL

We consider a two-dimensional magnetic system of localized spins S_i with length S on two sublattices (denoted \mathcal{A} and \mathcal{B}), subject to an external magnetic field \mathbf{H} with strength H_0 and orientated along the z -axis, such that $\mathbf{H} = H_{\pm} \hat{z}$, where we have introduced $H_{\pm} \equiv \pm H_0$. After linearizing the spin Hamiltonian \mathcal{H} in fluctuations around a uniform state we find a two-band spin-wave Hamiltonian. We assume the spin-wave Hamiltonian to realize a

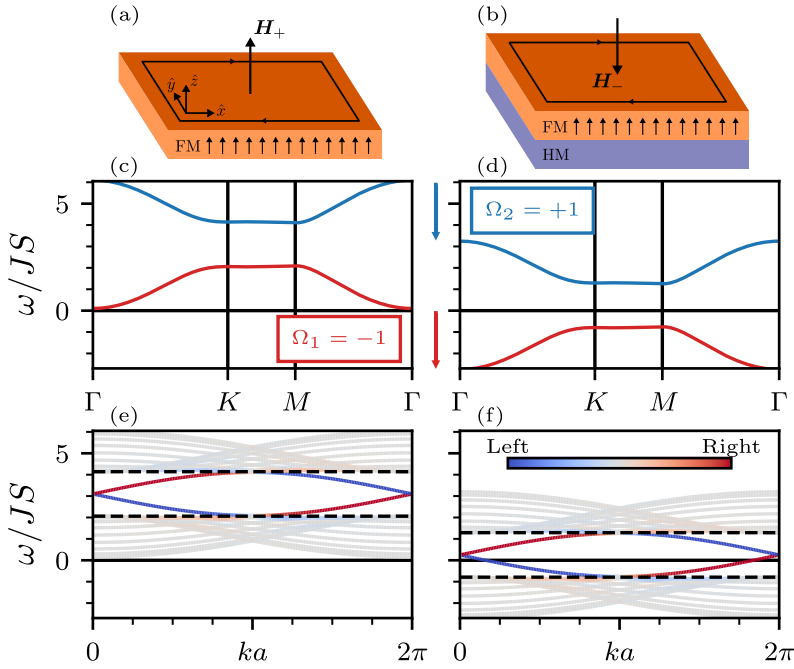


Figure 4.1: Strategy for generating zero-frequency chiral magnonic edge states in a magnon Chern insulator ferromagnet (FM), comparing the equilibrium (a,c,e) with the non-equilibrium (b,d,f) situation, with the uniform magnetization (see arrows) and magnetic field H_{\pm} aligned parallel and anti-parallel, respectively. In the non-equilibrium case, the magnetization is stabilized by spin-orbit torques originating from the adjacent heavy metal (HM) layer. (c,d) Bulk magnon band structure with indicated Chern numbers, $\Omega_{1,2}$. (e,f) Magnon band structure of an armchair edge ribbon. The colorscale of the eigenfrequencies indicates the edge localization and dashed lines denote the bulk band gap. In equilibrium, $H_+/(JS) = 0.1$, the edge states lie at high frequencies, but they are lowered down to zero frequency in non-equilibrium, $H_-/(JS) = -2.75$.

magnon Chern insulator, exhibiting topologically non-trivial magnon bands, and topologically-protected chiral edge states whose dispersion run across the bulk band gap. The edge states therefore have a finite energy, which cannot be lower than that of the first bulk band [118, 139, 140].

The central thesis of this work is that we can use a non-equilibrium state with the magnetization pointing against the external magnetic field to lower the edge states down to zero frequency. We thus consider the state $\mathbf{S}_i = S\hat{z}$, whilst $\mathbf{H} = H_- \hat{z}$. We refer to the case of $H = H_+$ as the equilibrium, and $H = H_-$ as the non-equilibrium. The non-equilibrium state is unstable and will thus relax to the equilibrium state in the presence of dissipation—such as Gilbert damping—with the magnetization parallel to the applied magnetic field. A spin-orbit torque is therefore necessary to render the energetically-unstable situation dynamically stable. Experimentally, this could be accomplished by interfacing the ferromagnetic insulator (FM) with a heavy metal (HM), as indicated in Fig. 4.1(b), such that the spin Hall effect generates a transverse spin current in the HM, injecting spin into the FM¹.

The spin dynamics are governed by the semiclassical Landau-Lifshitz-Gilbert (LLG) equation

$$\partial_t \mathbf{S}_i = \mathbf{S}_i \times \left(-\frac{\partial \mathcal{H}}{\partial \mathbf{S}_i} + \frac{\alpha}{S} \partial_t \mathbf{S}_i + \frac{J_s}{S} \mathbf{S}_i \times \hat{z} \right), \quad (4.1)$$

where α is the Gilbert damping and we allow for the system to be driven by a spin-orbit torque, J_s . We now expand the LLG Eq. (4.1) in deviations $m_{\mathcal{A}/\mathcal{B},i}^\pm = (S_{\mathcal{A}/\mathcal{B},i}^x \mp iS_{\mathcal{A}/\mathcal{B},i}^y) / \sqrt{2S}$ around the uniform state, $\mathbf{S}_{\mathcal{A}/\mathcal{B},i} = S\hat{z}$, where $m_{\mathcal{A}/\mathcal{B},i}^\pm$ refer to excitations for the equilibrium state, $H = H_+$, and non-equilibrium state, $H = H_-$, on the sublattices \mathcal{A}/\mathcal{B} . After introducing the Fourier transform of the spin-wave operators, $m_{\mathcal{A}/\mathcal{B},i}^\pm = \sqrt{2/N} \sum_{\mathbf{k}} e^{i\mathbf{k} \cdot \mathbf{R}_i} m_{\mathcal{A}/\mathcal{B},\mathbf{k}}^\pm$, the LLG Eq. (4.1) can be written as a Bogoliubov-de-Gennes (BdG) like equation in momentum space,

$$i(\tau_0 + i\alpha\tau_z)\partial_t \Psi_{\mathbf{k}}^\pm = (\tau_z \mathcal{H}_{\mathbf{k}}^\pm + iJ_s\tau_0) \Psi_{\mathbf{k}}^\pm, \quad (4.2)$$

where τ_j are the Pauli matrices in particle-hole space and we have introduced the magnon state vector $\Psi_{\mathbf{k}}^\pm = (m_{\mathcal{A},\mathbf{k}}^\pm, m_{\mathcal{B},\mathbf{k}}^\pm, m_{\mathcal{A},-\mathbf{k}}^{\pm*}, m_{\mathcal{B},-\mathbf{k}}^{\pm*})^T$ in particle-hole space.

We first determine the stability criterion for the non-equilibrium state, which can be found by solving the BdG-like Eq. (4.2) up to zeroth order in \mathbf{k} and up to first order in the dissipative terms, α and J_s . We then find that $\omega_{0,\pm} = H_\pm - i(\alpha H_\pm - J_s)$. For stability, we require that $\text{Im}[\omega_{0,\pm}] < 0$, which in equilibrium, where $H = H_+ > 0$, means that the system is stable in the

¹ Because of the specific geometry considered here, where the magnetization is perpendicular to the plane, one would need to make use of the anomalous spin Hall effect in a ferromagnetic heavy metal, such as permalloy [114].

absence of spin-orbit torque. In non-equilibrium, where $H = H_- < 0$, we require that $J_s \geq \alpha H$ and thus the non-equilibrium state can be rendered dynamically stable with a sufficiently large spin-orbit torque.

Although our general method is valid for any magnon Chern insulator, we now explicitly consider the well-known magnon Haldane model [43, 44], the details of which we review in Appendix 4.A. In the magnon Haldane model, the Dzyaloshinskii-Moriya interaction (DMI) opens the topological gap.

In the absence of dissipation, $\alpha = J_s = 0$, we obtain two sets of two spin wave solutions to Eq. (4.2), as a result of the particle-hole symmetry. However, this doubling is not a physical effect and merely the result of the fact that we represent the spin waves using complex scalar fields [142]. We can thus choose to only work with one branch of the solutions and we then obtain two bands with dispersion relations

$$\omega_{\mathbf{k},1}^{\pm} = H_{\pm} + 3JS + |\mathbf{h}_{\mathbf{k}}|, \quad \omega_{\mathbf{k},2}^{\pm} = H_{\pm} + 3JS - |\mathbf{h}_{\mathbf{k}}|, \quad (4.3)$$

where J is the exchange constant and $\mathbf{h}_{\mathbf{k}}$ comprises the details of the magnon Haldane model, further discussed in Appendix 4.A. We show this bulk dispersion in Fig. 4.1(c-d), comparing equilibrium and non-equilibrium. In equilibrium, we obtain only states with positive frequencies, whereas in non-equilibrium, where $H = H_- < 0$, the bands are shifted down in frequency, and we now obtain states with negative frequencies. The negative frequency modes have opposite handedness compared to the positive frequency modes, and thus rotate counterclockwise, whereas the positive frequency modes rotate clockwise. They also carry opposite angular momentum. The shift down in frequency can be explained from the fact that in non-equilibrium the effective magnetic field $\delta\mathcal{H}/\delta\mathbf{S}_i$ is pointing against the magnetization, thus lowering the frequency of the modes. We refer the reader to a full discussion about the particle-hole symmetry and its implications to Appendix 4.C, where we also discuss the stability and band structure in the presence of magnetic anisotropy.

The topological invariant for this system, the Chern number of the band n , is now defined as $2\pi\Omega_n = \sum_{\mathbf{k}} \varepsilon_{ij} \partial_{k_i} \mathcal{A}_j^n$, where $\mathcal{A}_j^n = i \langle \Psi_{\mathbf{k}}^n | \sigma_3 | \partial_{k_j} \Psi_{\mathbf{k}}^n \rangle$ is the Berry connection [2, 118, 119] and $\Psi_{\mathbf{k}}^n$ is the n -th eigenstate. In the bulk band structure, Fig. 4.1(c-d), we have indicated the Chern number, ± 1 , for the two bands. In equilibrium, the two bands have opposite Chern number and therefore there are topologically-protected chiral edge modes connecting the two bands. In non-equilibrium, the Chern number of the bands is preserved, and since one band is shifted down to negative frequency, we therefore expect the edge modes connecting the two bulk modes to cross zero frequency.

To further illustrate the topological nature of the edge states, we show the bandstructure of a ribbon, 16 unit cells wide, with armchair edges in Fig. 4.1(e-f), and indicate the edge localization in the colorscale. We have chosen compensated boundaries, such that the edge coordination number, i.e.,

the number of nearest neighbors, is equal to the bulk coordination number, and discuss the case of uncompensated boundaries in the Appendix 4.D. In equilibrium, we obtain topologically-protected edge states, as can be seen from their localization and their dispersion crossing the bulk band gap, and they thus have a finite frequency. In non-equilibrium the edge states remain, but are lowered in frequency and in fact cross zero frequency. We still have one forward-moving mode localized on one side of the ribbon, and a backward-moving mode on the other side. However, there are forward- and backward-moving edge modes with both positive and negative frequencies, and thus opposite handedness.

4.3 NUMERICAL VERIFICATION OF THE EDGE MODES

To verify the existence of the edge states at low frequencies, we numerically solve the LLG Eq. (4.1), including Gilbert damping and the spin-orbit torque needed to stabilize the non-equilibrium setup. This allows us to capture the full dynamics, in particular nonlinearities that are not included in linear spin-wave theory. We describe the specifics of the simulations used in Appendix 4.E and show the resulting dynamics in Fig. 4.2. We focus on the non-equilibrium dynamics, and use the same parameters used to calculate the bandstructure in Fig. 4.1(c,f), and set $\alpha = 10^{-3}$ and $J_s = \alpha H_-$. A spin wave is excited with positive frequency $\omega_0/J_S = 0.7$, Fig. 4.2(a-c), and negative frequency $\omega_0/J_S = -0.7$, Fig. 4.2(d-f), at one single edge site using a transversely oscillating magnetic field with frequency ω_0 . We show the spin-wave amplitude, defined as the deviation of the spins from the z-axis, $\mathcal{M}_i(t) \equiv 1 - S_i^z(t)$.

For both positive and negative excitation frequency, an edge mode is excited, which travels clockwise around the system. Its topological stability due to the absence of backscattering is proven by its bypassing of the defect in the upper left corner, where three edge spins are missing. Importantly, the excitations with opposite frequency have an opposite handedness, i.e., the individual spins rotate in the opposite direction in the (x, y) -plane and thus carry opposite angular momentum. This is in sharp contrast to the equilibrium situation, in which all magnons have the same chirality and carry the same angular momentum. Experimentally, this difference could be accessed by means of time-resolved spin pumping [35], because the pumped spin current $I_s(t) \propto \hat{z} \cdot (\mathbf{S}_i(t) \times \dot{\mathbf{S}}_i(t))$ [123] and the resulting spin-Hall voltage are a direct probe of handedness and, hence, of the topological negative-frequency excitations. To illustrate this, we show the pumped spin current, $I_s(t)$, for a site on the edge in Fig. 4.2(g). $I_s(t)$ is opposite between positive and negative excitation frequencies, showing that the excitations carry opposite angular momentum. Moreover, the arrival times of opposite excitation frequencies differ, which we attribute to the different group velocity of the excited modes.

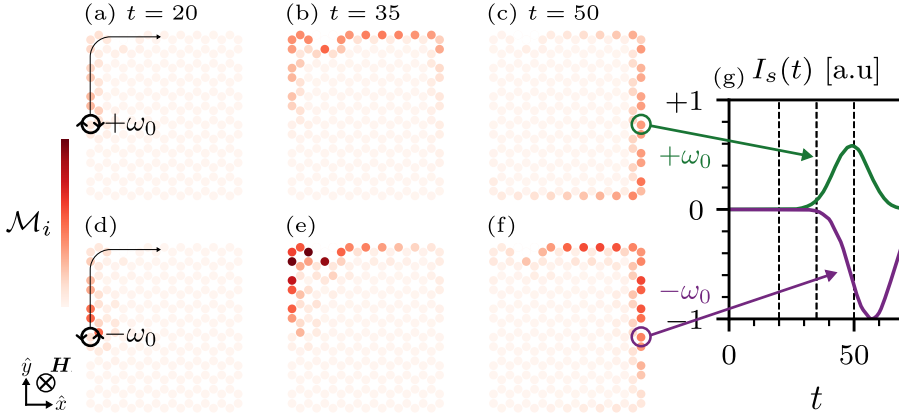


Figure 4.2: Spin dynamics simulation of a finite-size system in non-equilibrium, revealing the time evolution under a local excitation pulse with (a-c) positive and (d-f) negative frequency at $\pm\omega_0$, respectively. The chiral propagation direction of the edge modes is indicated by the arrow. The system starts in a uniform state, $\mathbf{S} = S\hat{z}$, and is continuously excited at one single site at the left edge, circled in (a,d). (a-c) Snapshots of the time evolution of the spin-wave amplitude $\mathcal{M}_i(t)$ for a positive excitation frequency, $+\omega_0$. (d-f) Same as (a-c) but for a negative excitation frequency, $-\omega_0$. (g) The pumped spin current $I_s(t)$ for a site on the edge. The dashed vertical lines correspond to the times at which the snapshots in (a-f) are taken.

This difference in group velocity can also be seen from the asymmetry of the band structure with respect to $\omega = 0$, Fig. 4.1(f), and is tuneable by varying the magnetic field. Finally, we observe that the absolute magnitude of $I_s(t)$ is larger for negative-frequency excitations. This is explained by the Gilbert damping, $\alpha\omega$, having the opposite sign for negative frequency modes compared to their positive frequency counterparts.

4.4 PROPAGATING SPIN WAVE SPECTROSCOPY

A central goal in the field of magnon topology is the transport of angular momentum by topologically protected edge states in magnonic devices [89]. Since usual frequencies of the edge states are in the THz range, these cannot be excited using conventional microwave antennas. However, in the non-equilibrium setup, the edge states extend to zero frequency, and are therefore easily accessible. We thus consider a propagating spin wave spectroscopy (PSWS) experiment [143], where two antennas are placed a distance d from each other. One antenna excites spin waves, which are picked up by the

second antenna after traveling through the film (see the inset of Fig. 4.3 for a device illustration). We consider a nanoribbon 10 unit cells wide, with length d , orientated such that the edges are of the armchair type, which corresponds to the dispersion shown in Fig. 4.1(e,f).

In the excitation antenna, the Oersted field oscillating with frequency ω excites all possible spin waves with the frequencies $\pm\omega$. Specifically, we model the excitation field by adding a local magnetic field term, $\partial_t \mathbf{S}_i|_{\text{exc}} = \mathbf{S}_i \times \mathbf{h}_i$, to the LLG Eq. (4.1), expand in deviations m_i^\pm , and numerically solve the resulting equation of motion to lowest nontrivial order in m_i^\pm in position and frequency space. The second antenna is sensitive to the total microwave power, which we define as the transmission $S(\omega) \equiv \sum_{i \in \mathbb{R}_p} |m_i(\omega)|^2$, where \mathbb{R}_p are the sites connected to the pickup antenna. We also model a concentration w of defects by removing spins, in order to capture the topological protection of the edge modes. The details of this calculation are discussed in Appendix 4.F. We also consider three additional types of disorder in Appendix 4.G in order to show that the robustness of the zero-frequency edge states is not dependent on the specific disorder considered in the main text.

We show the resulting transmission in Fig. 4.3(a-b), comparing the equilibrium and non-equilibrium states, and the topologically trivial state, $D = 0$, and non-trivial state $D/J = -0.2$, where D is the strength of the DMI. We choose $\alpha = 10^{-2}$ and stabilize the non-equilibrium state with a spin-orbit torque, $J_s = \alpha H$. We first focus on the equilibrium state, $H_+/JS = 0.1$, and simulate finite disorder, $w = 0.05$, i.e., 5% of all sites have a defect. In Fig. 4.3(a), we observe a broad peak in transmission at frequencies in the topologically nontrivial bulk band gap for $D/J = -0.2$. This feature is absent for $D = 0$, proving that it is an effect of the non-trivial topology because the backscattering-immune edge states enable transmission while the bulk state transmission is suppressed.

Turning now to the topologically nontrivial non-equilibrium state, $H_-/JS = -2.75$ and $D/J = -0.2$, where the edge state lies around zero frequency [cf. Fig. 4.1(f)], we see that transmission instead peaks around zero frequency. Again, we find a clear distinction with the topologically trivial case, $D = 0$, where transmission is suppressed at low frequencies at finite disorder. An important feature of the zero-frequency edge states is their higher transmission compared to the equilibrium edge states. This we attribute to the Gilbert damping, $\alpha\omega$, being proportional to frequency and thus lower for the zero-frequency edge states.

The transmission follows an exponential decay as a function of distance, i.e., $S(d, \omega) \propto \exp(-d/\lambda(\omega))$, where the decay length $\lambda(\omega)$ is a function of the excitation frequency. We therefore fit the transmission over a range of separation distances $20a < d < 200a$ (a lattice constant) and obtain an estimate for the the decay length, $\lambda(\omega)$, which we show as a function of excitation

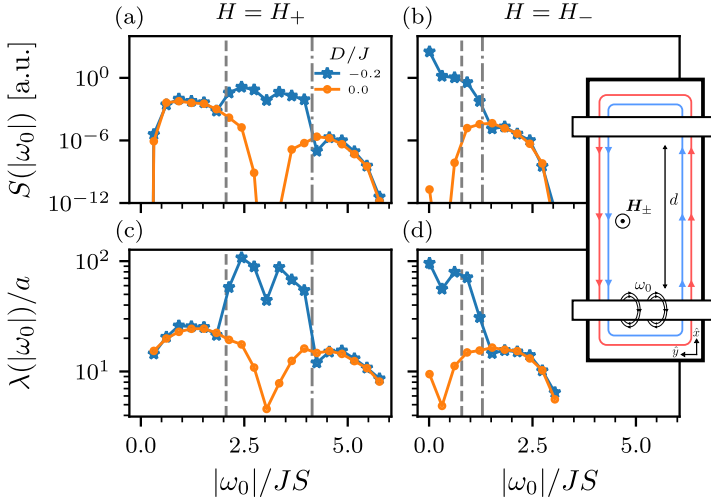


Figure 4.3: Propagating spin wave spectroscopy experiment as sketched in the inset, with edge modes excited by one antenna traveling through the film and picked up by the second antenna. (a-b) The transmission at finite disorder, $w = 0.05$, and a fixed distance $d = 200a$, as a function of excitation frequency ω , for the equilibrium state ($H = H_+$) and the non-equilibrium state ($H = H_-$) for the topologically trivial state, $D = 0$ and non-trivial state $D/J = -0.2$. Transmission is calculated with a finite Gilbert damping and a stabilizing spin-orbit torque for the non-equilibrium state. (c-d) The corresponding decay length of the transmission. The dashed and dashed-dotted lines indicate the bottom and top of the bulk band gap.

frequency, ω , in Fig. 4.3(c-d). We observe that the decay length reflects the topological protection of the edge states, peaking when the edge states are excited. Furthermore, the decay lengths are much larger for $D/J = -0.2$ compared to $D = 0$, reflecting the robustness against disorder of the edge states. Most importantly, in non-equilibrium, in the limit $\omega \rightarrow 0$ the decay length increases, which is in stark contrast with the equilibrium state, where the finite gap induced by the magnetic field blocks transmission.

4.5 DISCUSSION AND CONCLUSION

We have shown that by considering the magnetic excitations on top of a non-equilibrium state, stabilized by spin-orbit torques, we can effectively lower the frequency of topologically-protected chiral magnon edge modes. We obtain edge states with negative and positive frequency and we have confirmed

their existence by numerically solving the Landau-Lifshitz-Gilbert equation, showing their stability and robustness against defects. Furthermore, we have shown that in a propagating spin wave spectroscopy experiment, the edge modes can be directly detected.

In Appendix 4.H we provide estimates for the required strength of the external magnetic field and spin-orbit torque for specific material choices. Here we note that in general the magnetic fields and spin-orbit torque, αH_- , are proportional to the frequency of the edge mode in equilibrium. It would therefore be beneficial to consider this non-equilibrium state in a topological magnon crystal, where the frequencies of the edge modes is set by dipolar interaction, which is in the range of GHz [118, 144]. An alternative approach would be to look at the transient regime, by first aligning to system to an external magnetic field, and then reversing the direction of the applied field. For a short transient period one would then observe the same features as discussed here, but after some time the system would relax to equilibrium.

Our strategy can be used to lower other topological magnon excitations to zero frequency. Specifically, magnon Weyl semimetals would be an interesting prospect because zero-frequency Weyl points and associated topological surface states could come with the same transport anomalies as their finite-frequency counterparts [54, 145, 146]. Beyond magnons, it will be exciting to explore similar ideas for other bosonic Chern insulators, such as those formed by photons [129] or phonons [147, 148]. In these bosonic systems, non-equilibrium is accessible through external pumping, analogous to the spin-orbit torque used in this work. Finally, we note that non-equilibrium incoherent Hall-type transport [105, 149, 150] could be of interest because low-frequency edge states could potentially dominate transport.

4.A HALDANE MODEL

In this work we consider the magnon Haldane model [43, 44], described by the two-dimensional Hamiltonian

$$\mathcal{H} = -\frac{1}{2} \sum_{ij} [J_{ij} \mathbf{S}_i \cdot \mathbf{S}_j - D_{ij} \hat{z} \cdot (\mathbf{S}_i \times \mathbf{S}_j)] - \sum_i [H_{\pm} S_i^z - K_y (S_i^y)^2], \quad (4.4)$$

where \mathbf{S}_i are spins of length S located on lattice sites \mathbf{R}_i of a honeycomb lattice, as indicated in Fig. 4.4. Nearest neighbors experience an exchange coupling, $J_{ij} = J$, and next-nearest neighbors are coupled through the Dzyaloshinskii-Moriya interaction (DMI), $D_{ij} = -D_{ji} = D$. The spins are aligned to an external magnetic field, H_{\pm} , applied in the z direction, contributing a Zeeman energy. We also consider an anisotropy with strength K_y , which will lead to elliptical precessions.

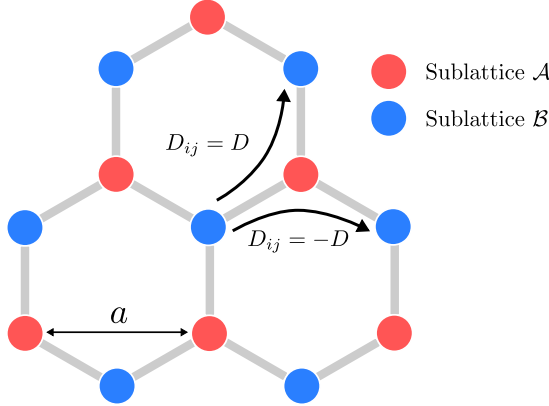


Figure 4.4: The honeycomb lattice of the Haldane model considered here. The relative sign of the Dzyaloshinskii-Moriya interaction is indicated.

Furthermore, because we require a spin-orbit torque to stabilize the non-equilibrium state, there will be a current flowing in-plane in the heavy metal. This current will induce an Oersted field, affecting the spin dynamics. Assuming the current to flow along the x -direction, we have an additional torque in the LLG-equation (4.1):

$$\partial_t \mathbf{S}_i|_{\text{Oe}} = -\mathbf{S}_i \times H_{\text{Oe}} \hat{\mathbf{y}}, \quad (4.5)$$

where H_{Oe} is the strength of the Oersted field. After linearization—which we will perform next—this torque can be included in the effective spin-wave Hamiltonian.

We introduce the deviations $m_{\pm}^i = (S_i^x \mp iS_i^y)/\sqrt{2S}$ around the uniform state, $\mathbf{S}_i = S\hat{\mathbf{z}}$, where m_{\pm}^i refer to excitations for the equilibrium state ($H = H_+$) and non-equilibrium state ($H = H_-$). We expand the Hamiltonian, Eq. (4.4), up to the first nontrivial order in m_{\pm}^i , and obtain the quadratic spin-wave Hamiltonian

$$\mathcal{H}_2 = \sum_{ij} \left[A_{ij} m_i^{\pm*} m_j^{\pm} + \frac{1}{2} B_{ij} (m_i^{\pm} m_j^{\pm} + m_i^{\pm*} m_j^{\pm*}) \right], \quad (4.6)$$

where

$$A_{ij} = \delta_{ij} \left(H_{\pm} + H_{\text{Oe}} + KS + S \sum_n J_{in} \right) - S(J_{ij} + iD_{ij}); \quad (4.7)$$

$$B_{ij} = \delta_{ij}(H_{\text{Oe}} + K_y S), \quad (4.8)$$

and we have included the current-induced Oersted contribution to the spin-wave dynamics.

We introduce the Fourier transform of the spin-wave operators, $m_{\mathcal{A}/\mathcal{B},i}^{\pm} = \sqrt{2/N} \sum_{\mathbf{k}} e^{i\mathbf{k} \cdot \mathbf{R}_i} m_{\mathcal{A}/\mathcal{B},\mathbf{k}}^{\pm}$ for the sublattices \mathcal{A}/\mathcal{B} respectively, and obtain the Hamiltonian

$$\mathcal{H}_{\mathbf{k}} = \sum_{\mathbf{k}} \mathbf{\Psi}_{\mathbf{k}}^{\pm\dagger} \left[(H_{\pm} + H_{\text{Oe}} + K_y S + 3JS) \sigma_0 \tau_0 + (H_{\text{Oe}} + K_y S) \sigma_0 \tau_1 + (\mathbf{h}_{\mathbf{k}} \cdot \boldsymbol{\sigma}) \tau_0 \right] \mathbf{\Psi}_{\mathbf{k}}^{\pm}, \quad (4.9)$$

where $\mathbf{\Psi}_{\mathbf{k}}^{\pm} = (m_{\mathcal{A},\mathbf{k}}^{\pm}, m_{\mathcal{B},\mathbf{k}}^{\pm}, m_{\mathcal{A},-\mathbf{k}}^{\pm*}, m_{\mathcal{B},-\mathbf{k}}^{\pm*})^T$ is the magnon state vector, σ_{η} are the Pauli matrices in the sublattice space, τ_{η} are the Pauli matrices in particle-hole space, $\boldsymbol{\sigma}$ is a pseudovector of Pauli matrices and

$$\mathbf{h}_{\mathbf{k}} = S \sum_i \begin{pmatrix} -J \cos(\mathbf{k} \cdot \boldsymbol{\delta}_i) \\ J \sin(\mathbf{k} \cdot \boldsymbol{\delta}_i) \\ 2D \sin(\mathbf{k} \cdot \boldsymbol{\rho}_i) \end{pmatrix}, \quad (4.10)$$

where $\boldsymbol{\delta}_i$ and $\boldsymbol{\rho}_i$ are the vectors connecting nearest and next nearest neighbors,

$$\boldsymbol{\delta} = [(0, -a/\sqrt{3}), (a/2, a/\sqrt{3}), (-a/2, a/\sqrt{3})]^T, \quad (4.11)$$

$$\boldsymbol{\rho} = [(a, 0), (-a/2, \sqrt{3}a/2), (-a/2, -\sqrt{3}a/2)]^T. \quad (4.12)$$

The spin dynamics are now described by the LLG-equation (4.1) in the main text, and after linearization we obtain the BdG-like equation, which has two sets of solutions. Choosing the solutions with positive norm, we find that (disregarding anisotropy and the Oersted field)

$$\omega_{\mathbf{k},1}^{\pm} = H_{\pm} + 3JS + |\mathbf{h}_{\mathbf{k}}|, \quad \omega_{\mathbf{k},2}^{\pm} = H_{\pm} + 3JS - |\mathbf{h}_{\mathbf{k}}|. \quad (4.13)$$

In absence of DMI, the two bands touch at the Dirac points ($\mathbf{K} = (4\pi/3a)$, $\mathbf{K}' = (2\pi/3a, 2\pi/\sqrt{3}a)$), but a non-zero DMI opens up a gap at these points. The dispersion at the Dirac points is given by $\omega_{\mathbf{K},1}^{\pm} = \omega_{\mathbf{K}',1}^{\pm} = H_{\pm} + 3JS + 3\sqrt{3}DS$ and $\omega_{\mathbf{K},2}^{\pm} = \omega_{\mathbf{K}',2}^{\pm} = H_{\pm} + 3JS - 3\sqrt{3}DS$. The opening of the gap implies a non-trivial topology, as can be shown by calculating the Chern number of the bands [45]. This gap remains topological in non-equilibrium, as discussed in the main text.

4.B ANISOTROPY

We now briefly discuss the effect of the effective anisotropy, $K \equiv H_{\text{Oe}} + K_y S$, on the results obtained in the main text, where we have incorporated the effects of the current-induced Oersted field into the effective anisotropy. The anisotropy we consider yields elliptical precession, as can also be seen from

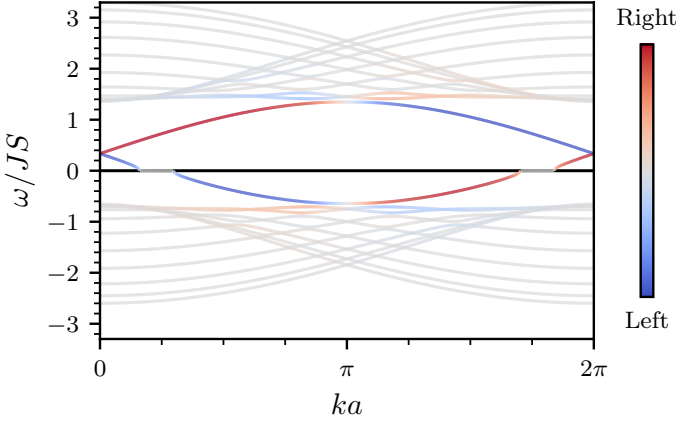


Figure 4.5: The magnon bandstructure in the presence of anisotropy, $K/J_S = 0.1$. Where the edge states cross zero frequency we obtain an exceptional line.

the Hamiltonian, Eq. (4.4). Firstly, this has implications for the spin wave solutions up to first order in the dissipative terms, α and J_s , and up to zeroth order in \mathbf{k} , which now become

$$\omega_{0,\pm} = \sqrt{(H_{\pm} + K)^2 - K^2} - i[\alpha(H_{\pm} + K) - J_s]. \quad (4.14)$$

Therefore, the stability criterion is also changed and in order to have $\text{Im}[\omega_{0,-}] < 0$ in non-equilibrium, we require that

$$-J_s \geq \max[-\alpha(H_- + K), K]. \quad (4.15)$$

There are thus now two requirements: the spin-orbit torque has to overcome the Gilbert damping and the instability created by the anisotropy (giving elliptical precession). We note that in the Haldane model we consider here the magnetic field is orientated perpendicular to the plane, and there is therefore no ellipticity induced by the shape anisotropy. The only possible source of anisotropy is therefore the magnetocrystalline anisotropy, in addition to the anisotropy resulting from the current-induced Oersted field.

In the presence of anisotropy, we also observe the existence of an exceptional line where the edge states cross zero frequency, as shown in Fig. 4.5. This exceptional line, a region in \mathbf{k} -space where $\text{Im}[\omega_{\mathbf{k}}] \neq 0$ and $\text{Re}[\omega_{\mathbf{k}}] = 0$, is related to the same instability induced by anisotropy in the bulk system. It is thus present even in the absence of dissipation. However, it is a local instability at the edges of the system, and will therefore only lead to a local canting of the spins, which we have confirmed to be small with numerical LLG simulations. This canting will be counteracted by the applied spin-orbit

torque, and therefore the system could always be stabilized with a strong enough spin-orbit torque. However, because the instability occurs at finite \mathbf{k} , it is not straight-forward to accurately determine the strength of the spin-orbit torque required. Finally, because of this canting the linearization procedure we apply is technically no longer valid, because we assume a uniform state to introduce the fluctuations. However, because we expect the canting to be small, we also expect the errors introduced by linearizing around a uniform state to be small. We therefore disregard the effects of anisotropy in the main text.

4.C PARTICLE-HOLE SYMMETRY

As discussed in the main text, there are two sets of solutions to the BdG-like equation (4.2), due to the particle-hole symmetry (PHS), which implies that $\tau_x(H^\pm + i\alpha\omega^*\tau_z + iJ_s\tau_0)\tau_x = -(H^\pm - i\alpha\omega\tau_z + iJ_s\tau_0)^*$. This implies that if ω is an eigenfrequency of H^\pm with eigenvector $\Psi = (u \ v)^T$ then $-\omega^*$ is an eigenfrequency with eigenvector $(v^* \ u^*)^T$. These two modes have opposite norm, defined as $\|\Psi\| = \langle \Psi | \sigma_z | \Psi \rangle$ [142]. Note that we have chosen the orientation of the deviations, m_i^\pm , dependent on the sign of the magnetic field in order to obtain this definition of the norm.

Because of the doubling, it is sufficient to only consider one set of solutions. In the main text, we choose to only consider the set of solutions with positive norm, which means that out of equilibrium we naturally obtain negative frequencies. Alternatively, one can also choose to work with only positive frequencies, and both positive and negative norms. One can even include both positive and negative norms as well as frequencies, and take care of the double counting with a factor $\frac{1}{2}$.

In equilibrium, one set of solutions has positive norm and only positive frequencies, and the second set with negative norm has only negative frequencies. Therefore, only considering the positive-norm modes in equilibrium is equivalent to only considering positive frequencies, as is common practice. However, when we consider spin-wave excitations on top of the non-equilibrium state, there may be positive-norm states with negative frequency, and negative-norm states with positive frequency. Here we therefore have to consider the full frequency range, including negative frequencies.

Upon quantization of the excitations, one naturally obtains magnons and antimagnons, defined as having respectively a positive and negative product of frequency and norm. Similar to particles and holes, the antimagnons also carry opposite spin compared to the magnons. This thus implies that the negative frequency excitations as shown in the main text become antimagnons upon quantization, and carry negative angular momentum. Classically, which is what we consider in the main text, this corresponds to excitations having

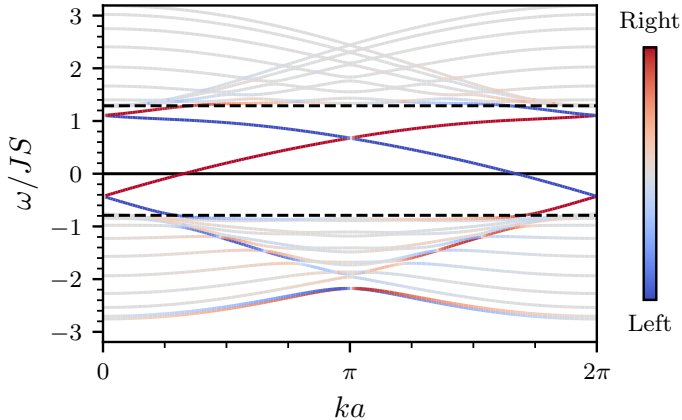


Figure 4.6: The nanoribbon bandstructure for uncompensated boundaries.

opposite chirality. For a further discussion on the magnon and antimagnons we refer the reader to Harms *et al.* [142].

4.D UNCOMPENSATED BOUNDARIES

In this work, we have always considered compensated boundaries, such that the edge coordination number, i.e., the number of nearest neighbors, is equal to the bulk coordination number. This is implemented through substituting

$$S \sum_n J_{in} \rightarrow 3SJ \quad (4.16)$$

in the linearized Hamiltonian, Eq. (4.8). In a real system this is not the case, and the effective field acting on edge sites will be lower. The edge excitations are thus lowered in frequency, but this does not affect the topological character of the edge modes. For completeness, we also show here the main results with uncompensated boundaries: the bandstructure for an armchair nanoribbon and the transmission and decay length, in Figs. 4.6 and 4.7. From the bandstructure we observe that the features as discussed in the main text are still present, with the edge modes crossing zero frequency. There are however small modifications to the specific dispersion of the edge mode, but from the transmission and decay length results we can conclude that these are insignificant. Furthermore, the main difference between the compensated and uncompensated boundaries appears for the equilibrium state, and the non-equilibrium state is barely affected, as can be seen from comparing Fig. 4.3 in the main text and Fig. 4.7 in this supplementary material.

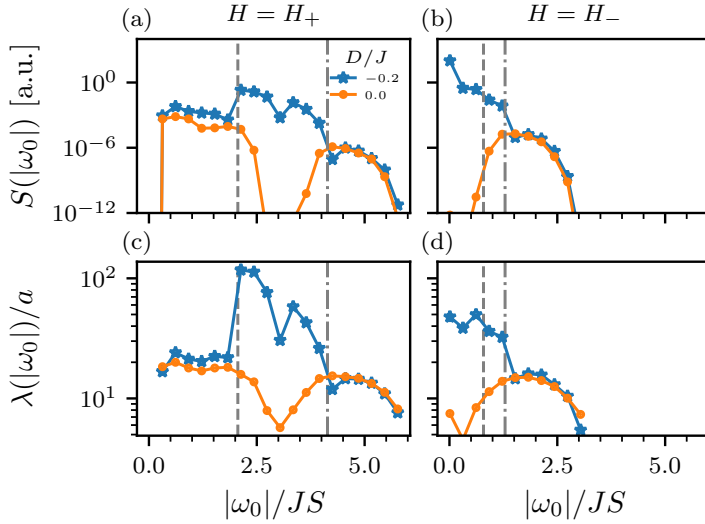


Figure 4.7: The transmission and decay length for uncompensated boundaries. Compare to Fig. 4.3 in the main text.

4.E LANDAU-LIFSHITZ-GILBERT SIMULATIONS

We consider a 10×10 unit cell structure and solve the Landau-Lifshitz-Gilbert (LLG) equation (4.1) in the main text, and include a transverse magnetic field, $\partial_t \mathbf{S}_i|_{\text{exc}} = -\delta_{in} \mathbf{S}_i \times \mathbf{h}_i(t)$, where

$$\mathbf{h}_i(t) = f_e(t) h_0 (\cos(\omega_0 t), \sin(\omega_0 t), 0)^T \quad (4.17)$$

at one edge site n , with strength $h_0/S = 10^{-6}$ and frequency $\omega_0/JS = 0.7$. Here $f_e(t) = \exp(-(t-b)^2/2c^2)$ is an envelope function which slowly turns the pulse on and off, since turning on the excitation pulse instantaneously will excite a range of spurious frequencies. We choose $b = 25$ and $c = 10$. We thus excite only a specific frequency ω_0 and only one edge mode with a specific handedness. At $t = 0$ the system is in the uniform state, $\mathbf{S}_i = S\hat{z}$. We set $D/J = -0.2$, such that we are in the topologically non-trivial regime. In non-equilibrium, there are edge modes close to zero frequency, and we thus expect to excite one of those edge modes. We also choose to work with compensated boundaries, and therefore apply a magnetic field of strength JS to all edge sites with only two neighbors.

Since we also want to determine the stability of the system, we consider both Gilbert damping, $\alpha = 10^{-3}$ and the spin-orbit torque $J_s = \alpha H_-$ needed to render this state stable. The snapshots in the main text, Fig. 4.2, show

the spin-wave amplitude, defined as the deviation of the spins from the z -axis, $\mathcal{M}_i(t) \equiv 1 - S_i^z(t)$. The three missing atoms in the top-left corner are modeled by applying a large on-site magnetic field, rendering them effectively inaccessible to spin-waves.

4.F TRANSMISSION

We model the excitation field induced the nanoantenna by adding to the LLG equation (4.1) in the main text, a local Oersted field oscillating with frequency ω parallel to the propagation direction, $\partial_t \mathbf{S}_i|_{\text{exc}} = \delta_{in} \mathbf{S}_i \times \mathbf{h}_{\text{exc}}$, where $\mathbf{h}_{\text{exc}} = b_0 \cos \omega t \hat{x}$. We expand in deviations $m_{\pm}^i = (S_i^x \mp iS_i^y)/\sqrt{2S}$ and after Fourier transforming to frequency space we obtain the following equation of motion in position space,

$$\mathbf{G}^{-1}(\omega) \mathbf{\Psi}(\omega) = \mathbf{h}(\omega). \quad (4.18)$$

Here $\mathbf{\Psi}(\omega) = [m_1, \dots, m_N, m_1^*, \dots, m_N^*]^T$ is the spin wave state vector, $\mathbf{h}(\omega) = [h_1(\omega), \dots, h_N(\omega), h_1^*(\omega), \dots, h_N^*(\omega)]$ is the Fourier transform of the circular components $h_i(\omega) = (h_i^x \mp ih_i^y) \delta_{i \in \mathbb{R}_a}$ of the excitation field, which is only non-zero for the sites \mathbb{R}_a connected to the antenna. The inverse magnon propagator is given by [135]

$$\mathbf{G}^{-1}(\omega) = \tau_z \sigma_0 \omega + \tau_0 \sigma_0 (\alpha \omega - J_s) - \tau_z \mathbf{A}, \quad (4.19)$$

where σ and τ are the Pauli matrices defined in the sublattice and magnon/antimagnon space respectively, and \mathbf{A} was defined in Eq. (4.8). Note here that the transmission is calculated after linearization in deviation from a uniform state, and therefore anisotropy has to be excluded, since this will lead to a finite canting of the spins, as discussed in Sec. 4.B. However, we expect that after linearization around this canted state the inverse magnon propagator will be close to the one obtained after linearization around a uniform state, and thus only a small error is introduced.

Specifically, we are interested in the signal generated by the pickup antenna, which is sensitive to the total microwave power $S(\omega) = \sum_{i \in \mathbb{R}_p} |m_i(\omega)|^2$ of the sites \mathbb{R}_p connected to the pick-up antenna. By using the solution of the linearized LLG (4.18), $m_i(\omega) = \sum_j \mathbf{G}_{ij}(\omega) h_j(\omega)$, we can write this as

$$S(\omega) = \text{Tr}_{i \in \mathbb{R}_p} \left[\mathbf{G}(\omega) \mathbf{H}(\omega) \mathbf{G}^\dagger(\omega) \right], \quad (4.20)$$

where $\mathbf{H}(\omega) = \text{diag}[|\mathbf{h}(\omega)|^2]$ and the trace is performed over the sites \mathbb{R}_p which are connected to the pick-up antenna. Here it is important to note that the antenna is placed perpendicularly to the propagation direction, as shown in the inset of Fig. 4.3 in the main text. The Oersted field generated by

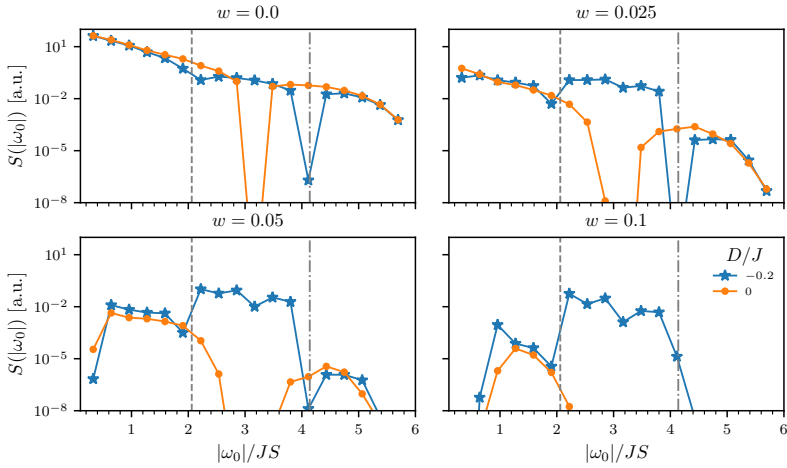


Figure 4.8: The transmission for increasing disorder w , as a function of excitation frequency, in equilibrium ($H_+/JS = 0.1$), comparing the topologically trivial ($D = 0$) and non-trivial ($D \neq 0$) phases. The bottom and top of the bulk band gap is indicated by the dashed and dashed-dotted gray lines. The sharp dips in transmission, which are most prominent for zero disorder, are the result of the absence of modes with that specific frequency.

the antenna will induce a transverse magnetic field, $\cos \omega t \hat{x}$, and thus will excite both positive and negative frequencies, as can be readily seen by taking the Fourier transform of this excitation field. Therefore, both positive and negative frequency spin waves are excited. In order to account for this, we have summed over both positive- and negative-norm solutions by tracing over the entire particle-hole space, for only positive frequency. This is equivalent to considering both positive and negative frequencies, and only the positive norm, as was also explained in Sec. 4.C, and is done for numerical simplicity. Because both positive and negative frequencies are excited, we show the absolute frequency of the bulk band throughout this work. For excitation frequencies below the bottom of the absolute bulk gap two edge modes with positive and negative frequency can be excited, whilst between the bottom and top of the absolute bulk gap only one edge mode with positive frequency exists.

We add a large on-site magnetic field to wN randomly chosen lattice sites, where N is the total number of lattice sites and $w \in [0, 1]$ is the disorder concentration. This large magnetic field makes these sites effectively inaccessible

for the spin waves. We average over multiple realizations of the disorder until we reach convergence.

We will discuss here the transmission for the equilibrium state, in order to show that this formalism captures the topological protection of the edge modes. We show the transmission for increasing disorder in Fig. 4.8. We can clearly see that for increasing disorder levels, the bulk modes are suppressed, while the edge modes, which lie in the bulk band gap, are unaffected. This can also be seen by comparing to the topologically trivial phase, where $D = 0$, which does not contain such edge states, to the topologically non-trivial phase, $D/J = -0.2$. From the magnitude of the transmission of the edge states in the bulk band gap for increasing disorder, we also observe that the edge modes are barely affected by the increasing disorder level. This we can thus attribute to the topological protection of the edge modes, which disallows backscattering. We can therefore conclude that the transmission of spin waves in the bulk band gap, in presence of a finite disorder level, is a good indication of topologically protected edge modes.

We observe that there are fluctuations in the transmission signal as a function of frequency inside the gap in Fig. 4.3. We propose that these fluctuations are related to a combination of the Gilbert damping and variations in the group velocity of the edge modes, combined with the presence of defects. The topological protection implies that the edge modes will travel around the defects, similar to the effect shown in Fig. 4.2. Therefore, the total path traveled and thus the passage time of the modes increases also, which causes them to be damped out further by the Gilbert damping. There are further variations because the group velocity is not constant across the gap and therefore modes with different frequencies have different passage times. The dip in transmission in the middle of the band gap is most likely the result of the disorder creating a mid-gap impurity band in Chern insulators [151]. We also note that the Gilbert damping scales as $\alpha\omega_0$, which reduces the signal for larger frequencies. We have furthermore confirmed that the results as shown in Fig. 4.3 have converged as a function of disorder ensemble size, and they are therefore not artifacts of the disorder sampling.

4.G ADDITIONAL SOURCES OF DISORDER

In any real system there can be a wide variety of disorder. We therefore consider here three further sources of disorder, in addition to the defects as described in the main text: a random on-site magnetic potential, drawn from the uniform distribution $[-\frac{\beta}{2}, +\frac{\beta}{2}]$; fluctuating bond strengths, such that $J \rightarrow J + \delta J$, where δJ is drawn from the uniform distribution $[-\frac{\Delta J}{2}, +\frac{\Delta J}{2}]$; and non-uniformity in the heavy metal | ferromagnet interface, modeled by adding

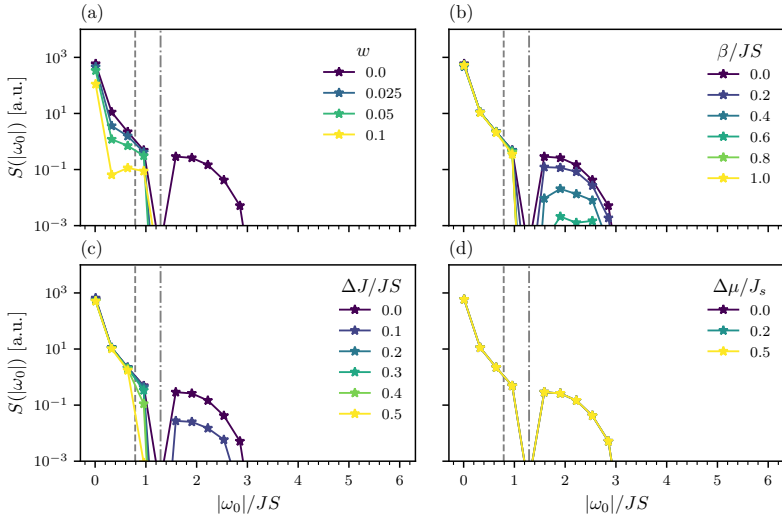


Figure 4.9: Transmission in the non-equilibrium state for four types of disorder: (a) defects with concentration w , (b) random on-site magnetic fields parameterized by the distribution width β , (c) fluctuating bonds parameterized by the distribution width ΔJ and (d) non-uniform spin-orbit torque, parameterized by the distribution width $\Delta\mu$. The dashed and dashed-dotted lines indicate the bottom and top of the bulk band gap.

local fluctuations $\delta\mu$ to the applied spin-orbit torque drawn from the uniform distribution $[-\frac{\Delta\mu}{2}, +\frac{\Delta\mu}{2}]$, such that $J_s \rightarrow J_s + \delta\mu$.

We show the results for all four kinds of disorder in Fig. 4.9 for the non-equilibrium state. A full study of the effects of disorder is beyond the scope of this Supplementary Material, but we can draw the important conclusion that the zero-frequency edge states in non-equilibrium can be measured through a propagating spin wave spectroscopy experiment, at moderate levels of disorder.

4.H ESTIMATION OF ENERGY SCALES

It is useful to consider here the energy scales of real materials, in order to determine what strength of magnetic field would be required to lower the frequency to an accessible level. In order to push the edge modes down to zero energy, we need to apply an opposite magnetic field equal to the bulk gap in the absence of a magnetic field. As a rule of thumb, a magnetic field of strength

$H = 1$ T corresponds to an energy $g\mu_B H$ of approximately $0.1 \text{ meV} \approx 0.1 \text{ THz}$ (assuming a g -factor of 2).

The edge states in CrI_3 , a prominent topological magnon insulator candidate, have energies $\sim 10 \text{ meV}$ [51], and would therefore require very large magnetic fields (100 T), making it not the best candidate to realize the zero-energy edge state as proposed here. Alternative candidates would be the kagome lattice ferromagnet $\text{Cu}(1,3\text{-bdc})$, where the topological excitations have energies $\sim 1 \text{ THz}$ [50] or the YIG|Fe magnonic crystal as proposed by Shindou *et al.* [118], where (depending on the specific implementation), the edge modes have energies $\sim 35 \text{ GHz}$. Even though these two systems are not realizations of the honeycomb Haldane model, the non-equilibrium state should still exhibit low energy topological edge modes, although the specific dispersion of the edge modes might be different.

The spin-orbit torque strength required to stabilize the non-equilibrium state is $J_s = \alpha H_-$. Therefore, when a strong magnetic field is required to lower the edge states to zero energy, the spin-orbit torque required is also large. The specific strength of the spin-orbit torque in real systems will depend on the specifics of the heavy metal|ferromagnet bilayer system, such as the interface roughness, the spin Hall angle of the heavy metal used and the Gilbert damping of the ferromagnet. It is however clear that here it would also be beneficial to have as small a spin-orbit torque as possible, to prevent unwanted side-effects such as heating and structural deformations.

NONLINEAR DYNAMICS OF THE NON-HERMITIAN SU-SCHRIEFFER-HEEGER MODEL

We numerically determine the robustness of the lasing edge modes in a spin-torque oscillator array that realizes the non-Hermitian Su-Schrieffer-Heeger model. Previous studies found that the linearized dynamics can enter a topological regime in which the edge mode is driven into auto-oscillation, while the bulk dynamics are suppressed. Here we investigate the full non-linear and finite-temperature dynamics, whose understanding is essential for spin-torque oscillators-based applications. Our analysis shows that the lasing edge mode dynamics persist in the non-linear domain for a broad range of parameters and temperatures. We investigate the effects of perturbations relevant to experimental implementations and discuss which ones might be detrimental to the stability of the lasing edge mode. Finally, we map our model onto a photonic model. Our analysis has the potential to shed light onto the dynamics of a plethora of non-Hermitian systems with non-linearities.¹

5.1 INTRODUCTION

The application of topology to condensed matter systems has been profoundly fruitful on both theoretical and experimental fronts and has led to the discovery of a wide range of new phenomena and materials [39]. Recently, considerable effort has been devoted towards the exploration of non-Hermitian systems [152, 153] with active gain and loss. A framework for addressing non-Hermitian topological phases has been provided by the growing field of topological theories of non-Hermitian systems [154–157].

Recent works have shown that the bulk-boundary correspondence [158], which is the cornerstone of topology in Hermitian systems, also holds for specific non-Hermitian systems [159], although not in general [160–162]. Some systems also exhibit a non-Hermitian skin effect, where even the bulk modes can be very sensitive to boundary conditions [68]. Nevertheless, the existence

¹ This chapter is based on P. M. Gunnink, B. Flebus, H. M. Hurst, and R. A. Duine, “Nonlinear dynamics of the non-Hermitian Su-Schrieffer-Heeger model,” *Physical Review B* **105**, 104433 (2022). R.A.D. conceived the project and P.M.G. performed the calculations and prepared the manuscript. All authors contributed to the manuscript.

of non-Hermitian edge modes has been shown in a variety of systems, such as microring resonators [70, 71, 163] and electrical circuits [164–166].

One of the most striking properties of non-Hermitian topological phases is the co-existence of lasing edge modes, i.e. edge states with gain-like dynamics, with a purely real bulk spectrum. Most importantly, these modes are topologically protected [155] and can therefore be useful in applications, since they are robust against disorder. In photonics these lasing modes have been used to build a single-mode laser stable against perturbations [167].

The majority of developments in non-Hermitian topological insulators have been in the field of photonics [168–171], where gain and dissipation can be readily tuned. Recent works have also unveiled non-Hermitian topological phases in mechanical [172, 173], electrical [164–166, 174] and magnetic systems [175–177]. Here we focus on magnetic systems, in which the loss is inherently present due to coupling of the magnonic excitations to the lattice and whose dynamics can be driven using spin-transfer torques. Due to the tunability of gain and loss, magnetic systems might represent a nearly ideal system to explore non-Hermitian phenomena.

Specifically, we consider the topology of the one-dimensional (1D) array of spin-torque oscillators (STOs) as shown in Fig. 5.1, building on the work of Flebus *et al.* [66]. Spin-torque oscillators are current-driven magnetic nanopillars, whose magnetization dynamics are determined by the balance of spin current injection and intrinsic (Gilbert-like) dissipation [178]. It has been experimentally shown that the coupling between STOs arranged in an array can be tuned [179, 180]. Flebus *et al.* [66] have shown that, by modulating the coupling between STOs and the local spin injection, the array can be driven into the topological phase of the non-Hermitian Su-Schrieffer-Heeger (SSH) model [65], known to host lasing edge states [72, 73]. However, STOs also exhibit strong non-linear effects, such as a non-linear frequency shift [178]. Furthermore, thermal fluctuations have also been shown to introduce significant noise into these systems [181]. In this chapter, we aim to investigate in detail how non-linearities and thermal fluctuations affect the topological character of a 1D array of STOs, in order to assess the experimental feasibility of this setup. Our results can be straightforwardly generalized to the realization of this model in photonic systems, which also exhibit non-linear and stochastic dynamics, making our work of interest to a broader audience.

This chapter is organized as follows: in Sec. 5.2 we start by introducing our model and we analyze its topological properties. In Sec. 5.3, we discuss in detail the numerical simulations deployed to investigate the non-linear dynamics at finite temperatures. We present the results of our simulations for a wide range of parameters in Sec. 5.4 and we identify the parameter regions where the lasing edge mode is realized. In Sec. 5.5 we show how our model is similar to previous implementations of the non-Hermitian SSH model in

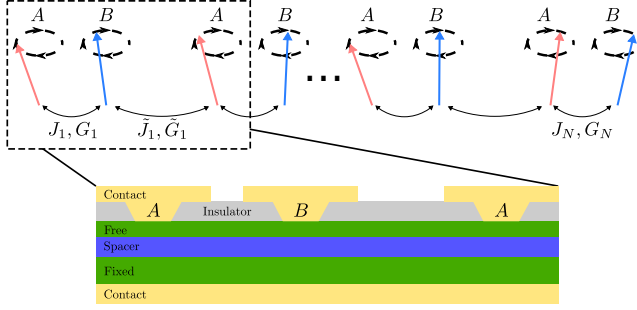


Figure 5.1: Schematic illustration of the model considered in this chapter. The array of STOs is represented as a 1D lattice with a two-sublattice (A and B) unit cell. The STOs are connected via a metallic spacer that mediates an intra-cell (J_i, G_i) and inter-cell (\tilde{J}_i, \tilde{G}_i) complex nearest-neighbor hopping. The inset shows a possible experimental realization of the STOs array, with the stacking of contact | fixed layer | spacer | free layer | contact. The magnetic layers extend throughout the array, and spin waves excited by one STO can reach and dissipatively couple the neighboring STOs.

photonic systems. A summary and conclusion are given in Sec. 5.6. Finally, we discuss the details of our numerical and analytical calculations in, respectively, Appendix 5.A and 5.B.

5.2 SYSTEM

We consider an array of $2N$ STOs that realize the non-Hermitian SSH model, as shown in Fig. 5.1. A STO consists of a magnetic polarizing layer separated from a magnetic free layer by a thin spacer. An external magnetic field $\mathbf{H} = H_0 \hat{z}$ sets the equilibrium direction of the magnetic order parameter \mathbf{m} of the free layer. The polarizing layer converts a DC current into a spin current J_s , which, in turn, exerts a spin-transfer torque on the magnetic order parameter \mathbf{m} . The loss and gain dynamics of the ferromagnetic order parameter \mathbf{m} associated with each nanopillar is described by the Landau-Lifshitz-Gilbert (LLG) equation as [178]

$$\partial_t \mathbf{m}_{\eta,i}|_0 = \omega_{\eta,i} \hat{z} \times \mathbf{m}_{\eta,i} + \alpha_{\eta,i} \mathbf{m}_{\eta,i} \times \partial_t \mathbf{m}_{\eta,i} + J_{s\eta,i} \mathbf{m}_{\eta,i} \times (\mathbf{m}_{\eta,i} \times \hat{z}), \quad (5.1)$$

where i labels the unit cells and $\eta = A, B$. Here, $\omega_{\eta,i} = \gamma_{\eta,i}(H_0 - 4\pi m_{z,\eta,i})$ is the ferromagnetic resonance frequency, $\gamma_{\eta,i}$ is the gyromagnetic ratio and $M_{\eta,i}$ the saturation magnetization. $\alpha_{\eta,i} \ll 1$ is the Gilbert damping parameter that captures the relaxation of the macrospin Kittel mode. The last term is the

spin-transfer torque exerted by the spin current $J_{s\eta,i}$ on the magnetic order parameter.

We consider three kinds of intra (inter)-cell couplings between the STOs. Firstly, we account for the Ruderman-Kittel-Kasuya-Yosida (RKKY)-type exchange, parameterized by the frequencies J_i (\tilde{J}_i). Secondly, there is a dissipative coupling G_i (\tilde{G}_i), which is mediated by spin pumping through the spacer layers [75]. The exchange and dissipative couplings only couple the nearest neighbors, as indicated in Fig. 5.1. These two couplings were already introduced in Ref. [66]. Additionally, in this chapter we also introduce the dipolar couplings between the STOs, which affect the non-linear dynamics [182, 183].

The dynamics of the coupled array are then described by

$$\begin{aligned} \partial_t \mathbf{m}_{A,i}|_{\text{coup}} = & -\mathbf{m}_{A,i} \times (J_i \mathbf{m}_{B,i} + \tilde{J}_{i-1} \mathbf{m}_{B,i-1}) \\ & - G_i \mathbf{m}_{B,i} \times \partial_t \mathbf{m}_{B,i} - \tilde{G}_{i-1} \mathbf{m}_{B,i-1} \times \partial_t \mathbf{m}_{B,i-1} \\ & - \Omega_d \mathbf{m}_{A,i} \times \sum'_{\eta,j} \frac{3\hat{\mathbf{x}} (\hat{\mathbf{x}} \cdot \mathbf{m}_{\eta,j}) - \mathbf{m}_{\eta,j}}{r_{A\eta,j}^3}, \end{aligned} \quad (5.2)$$

$$\begin{aligned} \partial_t \mathbf{m}_{B,i}|_{\text{coup}} = & -\mathbf{m}_{B,i} \times (J_i \mathbf{m}_{A,i} + \tilde{J}_i \mathbf{m}_{A,i+1}) \\ & - G_i \mathbf{m}_{A,i} \times \partial_t \mathbf{m}_{A,i} - \tilde{G}_i \mathbf{m}_{A,i+1} \times \partial_t \mathbf{m}_{A,i+1} \\ & - \Omega_d \mathbf{m}_{B,i} \times \sum'_{\eta,j} \frac{3\hat{\mathbf{x}} (\hat{\mathbf{x}} \cdot \mathbf{m}_{\eta,j}) - \mathbf{m}_{\eta,j}}{r_{B\eta,j}^3}, \end{aligned} \quad (5.3)$$

where \sum' indicates that the sum excludes the self-interaction. The dipolar interaction is parametrized by $\Omega_d = \gamma_{\eta,i} V_{\text{eff}\eta,i} / a^3$, where $V_{\text{eff}\eta,i}$ is the effective volume of a STO and a is the separation distance between STOs, which we assume to be constant. $r_{\eta\eta',i'j} = R_{\eta\eta',i'j} / a$ is the normalized distance between $\text{STO}_{\eta i}$ and $\text{STO}_{\eta' j}$. Here we have incorporated terms proportional to the Gilbert-like on-site damping of the G_i, \tilde{G}_i couplings into the Gilbert damping, i.e. $\alpha_{A,i} = \alpha_{\eta,i} + G_i + \tilde{G}_i$ and $\alpha_{B,i} = \alpha_{\eta,i} + G_i + \tilde{G}_{i-1}$. In what follows we assume identical unit cells and drop the dependency on the unit cell index i , unless stated otherwise, such that $\omega_{\eta,i} = \omega$, $\alpha_{\eta,i} = \alpha + G + \tilde{G}$, $J_i = J$, $\tilde{J}_i = \tilde{J}$, $G_i = G$ and $\tilde{G}_i = \tilde{G}$. Furthermore, we assume spin-current injection only on sublattice A, i.e. $J_{s,B} = 0$, $J_{s,A} = J_s$.

The equations of motion for this system are then given by Eqs. (5.1-5.3), which can be linearized around the equilibrium direction of the magnetic order parameter. We write $\mathbf{m}_{\eta,i} = (m_{\eta,i}^x, m_{\eta,i}^y, 1)$ and neglect terms that are second order in the fluctuations from equilibrium. We then introduce the complex variable $2m_{\eta,i} = m_{\eta,i}^x - im_{\eta,i}^y$ and invoke the Holstein-Primakoff transformation [19] $m_{\eta,i}(t) = \langle \eta_i \rangle e^{-i\omega t}$, where $\eta_i = a_i, b_i$ are second-quantized operators annihilating magnons at sublattice η and obeying bosonic commutation relations. From the corresponding Heisenberg equation of motion we

can identify the effective quadratic magnon Hamiltonian, which we will use next for topological classification.

The non-linear character of the equations of motion means that the Hamiltonian should also contain higher order interactions. The on-site dynamics, i.e. Eq. (5.1), would introduce on-site interaction terms, and the exchange interaction would result in quartic and higher order interactions terms between neighboring spins. How these interaction terms affect the topology is still an unanswered question [184, 185]. We therefore only consider the quadratic Hamiltonian to determine the topological properties. However, in our numerical simulations we do take into account the non-linearities of the equations of motion, thus capturing the full dynamics resulting from the higher order interaction terms.

Our starting point is the \mathcal{PT} (parity-time) symmetric case, analyzed as well by Flebus *et al.* [66]. Here $J_s = 2\alpha\omega$ and $\Omega_d = G = \tilde{G} = 0$. In this regime, the system hosts two edge modes with energies $\text{Re } E - \omega = 0$ and $\text{Im } E \neq 0$ for $|J| < |\tilde{J}|$. The \mathcal{PT} -symmetry indicates the system is invariant under combined parity (swapping site A with B and vice versa) and time reversal ($t \rightarrow -t$) operations [152, 153]. We assume the strength of the dissipative coupling and the dipole-dipole interactions to be small compared to ω , and treat them as perturbations. We note here that we do have access to the full (including non-linear) dynamics that result from the dissipative and dipolar coupling and only treat them as perturbations in the topological analysis. In the simulations that follow we describe the full dynamics of the system, including dissipative and dipolar couplings.

The Hamiltonian of the \mathcal{PT} -symmetric model is

$$\begin{aligned} H_i = \omega & \left[a_i^\dagger a_i + b_i^\dagger b_i \right] + i (J_{sA} - \alpha\omega) a_i^\dagger a_i \\ & - i\alpha\omega b_i^\dagger b_i - J \left[a_i^\dagger b_i + \text{h.c.} \right] \\ & - \tilde{J} \left[a_i^\dagger b_{i-1} + \text{h.c.} \right], \end{aligned} \quad (5.4)$$

for $i \neq 1, N$, with open boundary conditions

$$\begin{aligned} H_j = \omega & \left[a_j^\dagger a_j + b_j^\dagger b_j \right] + i (J_{sA} - \alpha\omega) a_j^\dagger a_j \\ & - i\alpha\omega b_j^\dagger b_j - J \left[a_j^\dagger b_j + \text{h.c.} \right] \\ & - \tilde{J} \left[b_j^\dagger a_l + \text{h.c.} \right], \end{aligned} \quad (5.5)$$

where $j = 1, N$ and $l = 2, N - 1$. The full Hamiltonian, including the dissipative and dipole-dipole coupling, is given in Appendix 5.B.

We first briefly discuss the phase diagram, which captures the linear dynamics. For a full discussion the reader is referred to the earlier work of Flebus

et al. [66]. The topological nature of the edge modes can be characterized by a global complex Berry phase [72], i.e., an integer that predicts the number of pairs of edge modes. The complex Berry phase can be found to be one for $|J| < |\tilde{J}|$, signaling the presence of topologically protected edge states.

Furthermore, the system has an exceptional point at $|\tilde{J} \pm \alpha\omega| = |J|$, where the system transitions from the \mathcal{PT} -unbroken into the \mathcal{PT} -broken regime [72]. In the \mathcal{PT} -unbroken regime the edge state spectra come as complex-conjugated pairs, while the bulk spectrum is purely real. Thus, the edge mode with positive imaginary energy starts lasing, while the bulk modes remain inactive. In the \mathcal{PT} -broken regime the bulk modes also become complex valued, such that they also will start lasing spontaneously. In order to isolate the dynamics of the lasing edge mode we therefore require $|J| < |\tilde{J} - \alpha\omega|$, i.e. to be in the \mathcal{PT} -unbroken regime.

When dissipative couplings G, \tilde{G} are present, all bulk modes will have a non-zero imaginary component, since the system is no longer \mathcal{PT} -symmetric. The edge mode is still well defined and separated in energy from the bulk modes. However, because all bulk modes have a non-zero imaginary component, these modes can start lasing as well, as was also noted by Flebus *et al.* [66]. We note that chiral-inversion (CI) symmetry protects the stability of the edge states [186], such that the topologically protected edge modes are now present for $|J - iG\omega| < |\tilde{J} - i\tilde{G}\omega|$. Since in almost all experimental realizations of the setup discussed here the dissipative coupling will be much weaker than the RKKY-type coupling, the system will most likely still be in the topologically non-trivial regime.

For the dipole-dipole interactions we note that the dipolar fields are \mathcal{PT} -invariant, and thus the bulk spectrum will remain real. However, long-range interactions are typically not captured by topological classifications [187], and it is unclear from the linearized model alone how the long-range dipolar interaction will affect the lasing edge modes. This will be investigated numerically in the next section.

As was noted before, the phase diagram only captures the linear behavior of the STO array. In the STO array considered here, the STOs are easily driven into the non-linear regime [66, 188]. Non-linearities therefore need to be taken into account when describing this topological array. Thus, we proceed to investigate the full non-linear dynamics numerically.

5.3 SIMULATIONS

We numerically simulate the system described by Eqs. (5.1-5.3), using the parametrization outlined in Appendix 5.A. This parametrization maps the magnetic order parameter $m_{\eta,i}$ to the microwave power $p_{\eta,i}$ (which is experimentally measurable) and the azimuthal angle $\phi_{\eta,i}$. The thermal fluctuations

are taken into account by using a stochastic field, the strength of which is chosen such that an isolated STO reaches thermal equilibrium [181]. We note that this noise will equilibrate the whole array to $2N$ individual STOs in thermal equilibrium, since the couplings between STOs are not taken into account in the equilibration. However, we assume couplings to be weak compared to the on-site dynamics (i.e. $J, \tilde{J} \ll \omega$), making this a valid approximation. The noise is thus chosen to have zero mean and a second-order correlator

$$\begin{aligned} \langle f_{\eta,i}(t) f_{\eta',j}(t') \rangle &= 0; \\ \langle f_{\eta,i}(t) f_{\eta',j}^*(t') \rangle &= 2\delta_{i,j} \delta_{\eta,\eta'} D_{\eta,i}(p_{\eta,i}) \delta(t-t'), \end{aligned} \quad (5.6)$$

where $D_{\eta,i}(p)$ is a diffusion coefficient that characterizes the noise amplitude, which has to be taken to be dependent on $p_{\eta,i}$ in order to correctly describe the stochastic dynamics of a non-linear oscillator. The explicit form of $D_{\eta,i}(p)$ is reported in Appendix 5.A.

In order to integrate the resulting stochastic differential equation we use the Euler-Heun algorithm as implemented in the DifferentialEquations.jl package [189]. As initial conditions we take the phase $\phi_{\eta,i}$ to be uniformly and randomly distributed between 0 and 2π and the power $p_{\eta,i}$ to be distributed according to the equilibrium Boltzmann distribution

$$P_{eq} \propto \exp \left[-\frac{2\lambda_{\eta,i}}{k_B T} p_{\eta,i} \right], \quad (5.7)$$

where $\lambda_{\eta,i}$ is a scale factor relating the dimensionless oscillator power p and the oscillator energy.

Since this system is inherently stochastic, both from the initial conditions and the thermal fluctuations, we collect statistics by running every configuration of parameters N_R times. The main observable we are interested in is the number of lasing modes, where a lasing mode is defined as any mode that has power $p_{\eta,i} \geq \epsilon p_0$, where p_0 is the steady-state power of a single oscillator [178]. We let the system run for a time t_{end} and choose $\epsilon = 0.9$ to account for the fluctuations around the equilibrium power of a STO. Our stochastic simulations may not capture all possible processes, such as rare low probability events, in a single run. However, by running multiple ‘trajectories’ we can gather statistics and gain insight into the behavior of the system. This is also true of experimental runs, where the number of lasing modes will vary in any one realization of the experiment. We will discuss this problem in greater detail in Sec. 5.4.2, where we also show how the experimental observation times should be chosen.

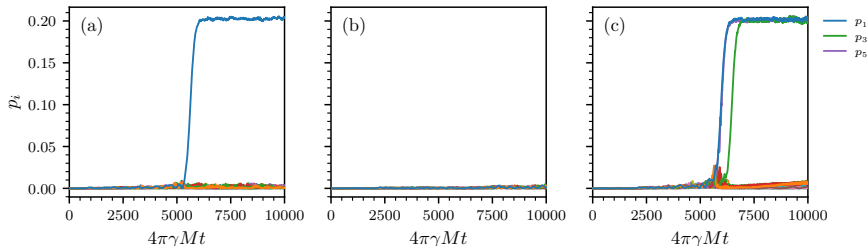


Figure 5.2: Three types of behavior of the system, with $\tilde{J} = -0.025/4\pi\gamma M$, $J/\tilde{J} = 0.5$, $k_B T/\lambda = 10^{-5}$ and $G = \Omega_d = 0$. (a) Only the edge mode starts lasing, while all the bulk modes are suppressed. (b) No modes start lasing within the specified time frame. (c) Both the edge modes and bulk modes start lasing. The simulation is run for $4\pi\gamma M t = 10^5$, which for a typical STO with $4\pi\gamma M = 10$ GHz is equal to $10 \mu\text{s}$.

5.4 RESULTS

In this section, we present the results from the simulations described in Sec. 5.3. Unless stated otherwise, we set $\alpha = 10^{-2}$, $\omega/4\pi\gamma M = 0.5$, $J_{s,A} = 2\alpha\omega$, $J_{s,B} = 0$ and $G = \Omega_d = 0$, such that we are in the \mathcal{PT} -symmetric regime and work with an array of $N = 10$ unit cells. We run the simulations of Eqs. (5.1-5.3) for $4\pi\gamma M t = 10^5$, which for a typical STO with $4\pi\gamma M = 10$ GHz corresponds to $10 \mu\text{s}$ and collect statistics over $N_R = 100$ runs. We are interested in two main observables: whether the edge mode starts lasing, and how many bulk modes also start lasing. It is worth noting that since the B-sites dynamics are suppressed because they are not directly driven, we only have N possible lasing modes. We choose $k_B T/\lambda$ in the range 10^{-6} to 10^{-4} , with the latter corresponding to room temperature for a typical STO [178].

In Fig. 5.2 we show three typical examples of the system dynamics. The system is initially in thermal equilibrium, and at $t = 0$ the spin-torque current is turned on for all A-sites. Fig. 5.2a show the case where after some time the left-most mode starts lasing at the steady-state power for a single oscillator, whilst the dynamics of the bulk modes are suppressed. Alternatively, no modes can start lasing at all (Fig. 5.2b), which we will discuss further in Sec. 5.4.2. We also observed the lasing of bulk modes together with the edge mode, as shown in Fig. 5.2c. In this specific example the bulk mode starts lasing shortly after the edge mode. We have not investigated this timing further, but it seems likely that a lasing edge mode could also excite bulk modes close to the edge. Moreover, we also observed cases where bulk modes start lasing later in time, seemingly independent of the lasing of the edge mode.

Since all three cases are possible, we further explore the parameter space, and focus on the amount of lasing modes as an observable. We note that in all of the cases discussed here we never observed a lasing bulk mode without a lasing edge mode. This is a direct result of the topology of the array.

As discussed before, the system hosts a lasing topological edge state for $-1 < J/|\tilde{J}| < 1$. We thus show the average number of lasing bulk (dashed line) and edge (solid line) modes as a function of $J/|\tilde{J}|$ for different temperatures in Fig. 5.3. The transition from the topological to the trivial regime at $J/|\tilde{J}| = -1$ is affected by the temperature. For low temperatures the transition is sharper than for high temperatures. However, at high temperatures the system still exhibits signs of a non-Hermitian topological insulator (suppressing of the bulk modes, with only a single lasing edge mode), even if the system is in the trivial phase, i.e. if $|J| > |\tilde{J}|$.

As was previously discussed, the system has broken \mathcal{PT} -symmetry when $|\tilde{J} - \alpha\omega| < |J| < |\tilde{J} + \alpha\omega|$, where multiple modes will start to lase. In Fig. 5.3 the \mathcal{PT} -broken regime is indicated by the shaded area and it is easy to see that more bulk modes start lasing. For higher temperatures more bulk modes will start to lase. We remark here that these simulations were only run for a fixed time t_{end} , and therefore not all modes might have started lasing yet. We return to this issue in Sec. 5.4.2.

The number of lasing bulk modes also increases as a function of temperature. Instead of a sharp transition at the exceptional point (EP), there is a transitional regime, due to the non-linear and stochastic effects. This indicates that, depending on the operating temperature, it is necessary to stay further away from the EP than one might initially expect. Specifically for this parameter set it would mean choosing $|J| \ll |\tilde{J} + \alpha\omega|$, such that there are no unwanted bulk contributions from the \mathcal{PT} -broken regime. The fact that the \mathcal{PT} -broken regime extends further than expected might also have implications for applications using the exceptional point, such as enhanced sensing [190, 191] and encircling the exceptional point [192].

5.4.1 Sensitivity to perturbations

We now consider three main perturbations present in any experimental realization of the system: (1) the dissipative coupling modulated by spin-waves traveling in the metallic spacer layer, (2) the dipole-dipole coupling between the macrospins of the STOs and (3) variations in the parameters of the individual STOs.

We first consider the inter (intra)-layer dissipative coupling G (\tilde{G}), induced by the metallic spacer layer. This coupling is known to synchronize STOs [183]. Since it is modulated by the metallic spacer layer it can be tuned to an extent, e.g. by choosing a spacer layer with a certain spin relaxation. It is also possible

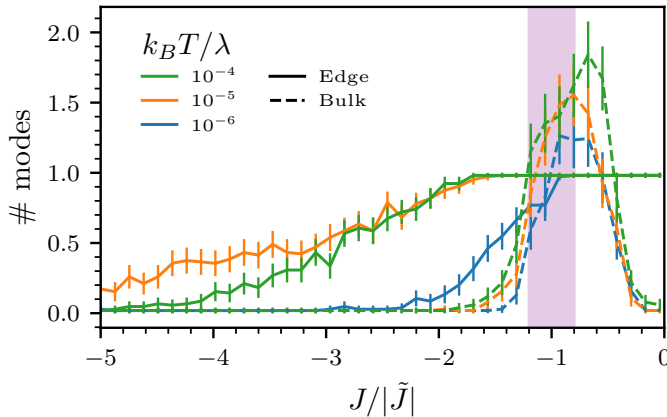


Figure 5.3: Average number of lasing bulk (dashed line) and edge (solid line) modes as a function of $|J|$, for different temperatures. The \mathcal{PT} -broken regime is indicated by the shaded region. Note that these simulations were only run for $4\pi\gamma Mt = 10^5$ and this is therefore only a snapshot of the number of lasing modes. The error bars show the 95% confidence interval.

to choose a STO nano-pillar geometry in which the metallic spacer layer does not extend in-between the STOs and therefore no spin waves can propagate, thus suppressing the dissipative coupling [178].

We vary the dissipative coupling $G = G_i = \tilde{G}_i$, the results of which are shown in Fig. 5.4a. We note here that even though the dissipative coupling breaks the \mathcal{PT} -symmetry, the edge modes are still protected by CI-symmetry. When $G/|\tilde{J}| > 10^{-3}$, first the bulk modes are suppressed. This can be attributed to the increased overall dissipation in the system, suppressing the bulk excitations. When $G/|\tilde{J}| > 0.05$ the edge modes are also suppressed, which again can be attributed to the increased overall dissipation. This result thus suggests that it is desirable to design a system where the dissipative coupling is weak, such as by using the nano-pillar geometry. However, a small dissipative coupling might be beneficial, effectively suppressing the bulk excitations, while allowing the edge modes to lase.

Next, we discuss the dipole-dipole coupling, which is present in any magnetic system. It has also been known to synchronize the precession in STOs [183]. The dipolar coupling strength can be controlled by the spacing between the STOs. We vary the dipolar coupling strength $\Omega_d/4\pi\gamma M$ for different temperatures, as shown in Fig. 5.4b. For small Ω_d we see no changes, and only for $\Omega_d/4\pi\gamma M > 10^{-3}$ the bulk modes will start to lase. For STOs of typical dimensions $10 \times 10 \times 10$ nm and a separation distance 10 nm, $\Omega_d/4\pi\gamma M \approx 10^{-3}$.

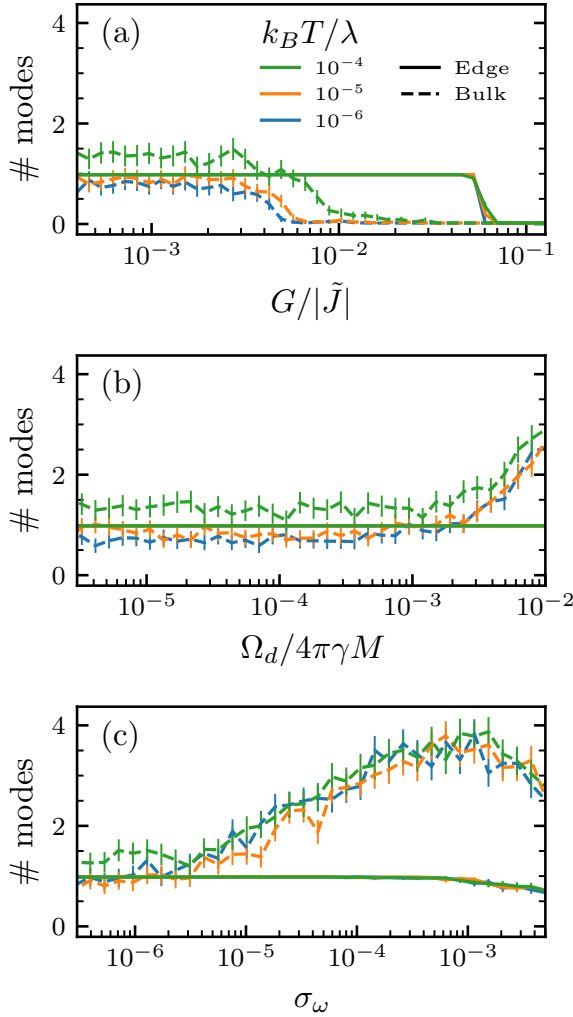


Figure 5.4: Average number of lasing bulk (dashed line) and edge (solid line) modes for different perturbations that will always be present in any realistic system. The error bars show the 95% confidence interval. Here $\tilde{J} = -0.025/4\pi\gamma M$, $J/\tilde{J} = 0.5$. (a) As a function of the strength of the dissipative coupling $G = G_i = \tilde{G}_i$, which is mediated by the spacer layers between the STOs. (b) As a function of the dipole-dipole coupling strength $\Omega_d/4\pi\gamma M$, which can be tuned by the spacing between the STOs (c) As function of the variation of the individual FMR-frequency $\omega_{\eta,i}$, chosen from a normal distribution with mean $\omega/4\pi\gamma M = 0.5$ and standard deviation σ_ω .

Our results indicate a lower bound on the spacing between STOs in order to avoid activation of the bulk lasing modes due to the dipole-dipole interaction.

In any experimental setup there will be small variations between the individual STOs. Since the system considered here is only \mathcal{P} -symmetric if the dissipation is balanced with the driving, even small variations in any parts of the STO array involved in the driving and dissipation processes will break the \mathcal{PT} -symmetry. Since the topological classification of this system is based on the \mathcal{PT} -symmetry, it is useful to consider the effect of breaking this symmetry.

In order to model spatial disorder we consider an array with small variations in the individual frequencies ω_i , by assuming they are normally distributed with standard deviation σ_ω and mean ω . If the local spin-transfer torque is kept constant at $J_s = 2\alpha\omega$ throughout the array, the system is no longer \mathcal{PT} -symmetric. This spin-injection model corresponds to setup in which a single current source, rather than individual ones, are used to inject spin angular momentum into the STOs. The number of lasing modes is shown in Fig. 5.4c, where it is clear that as the variance is increased, more bulk modes start lasing. The disorder we introduce breaks the \mathcal{PT} -symmetry, and the edge states are no longer topologically protected. The bulk modes are therefore no longer suppressed and can start lasing. We have also modeled the case where $J_{s,i} = 2\alpha\omega_i$, i.e. where the STOs are individually driven. This did not affect the results, indicating that it is not just the \mathcal{PT} -symmetry within one unit cell, but rather the \mathcal{PT} -symmetry of the complete array that protects the edge states. The robustness of non-Hermitian topological states against disorder is still poorly understood. From the linear dynamics we know that if a variance σ_ω is introduced the bulk modes also gain a non-zero imaginary component and will therefore start lasing or be suppressed. This is thus in essence not a non-linear or stochastic effect, in contrast to the other effects discussed previously.

We thus conclude that the non-Hermitian SSH chain can be experimentally realized using STOs, but care needs to be taken to control the dissipative coupling, dipolar interactions and the variations between STOs.

5.4.2 Nucleation

The processes that we consider in this chapter are fully stochastic, and so is the lasing of the edge mode: there is a finite probability that the edge mode will start lasing. It is therefore possible that even in the topological phase, the edge mode might only start lasing at time scales longer than the experimental observation time. Motivated by this consideration, we thus investigate here the nucleation times of the lasing edge modes.

As before, we prepare our system in thermal equilibrium, and turn on the spin current at $t = 0$. We only consider the RKKY-type coupling, and set

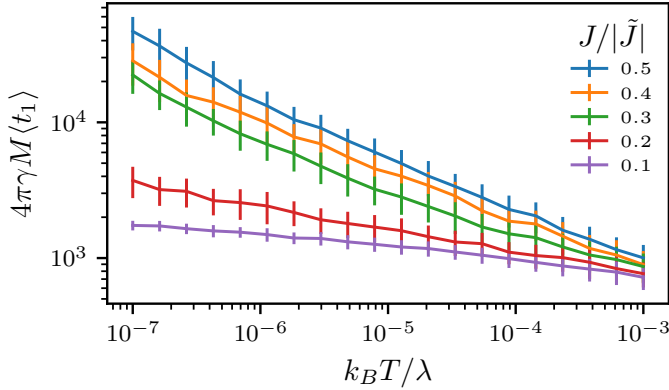


Figure 5.5: The average time for the edge mode to start lasing, for different ratios $J/|\tilde{J}|$. These simulations are all in the unbroken \mathcal{PT} -regime. For a typical FMR frequency $4\pi\gamma M = 10$ GHz these times are in the order of 0.01 ms to 1 ms. The error bars show one standard deviation.

$G = \tilde{G} = \Omega_d = 0$. In Fig. 5.5 we show the temperature dependence of the time at which the edge mode starts lasing, for different ratios $J/|\tilde{J}|$. We have chosen the ratio $J/|\tilde{J}|$ such that we are in the unbroken \mathcal{PT} regime and we only expect the edge state to start lasing.

It is clear that the time until the edge mode starts lasing follows an exponential distribution as a function of temperature. Moreover, for lower intra-cell coupling J , the average time decreases. This observation can be explained in terms of overcoming an energy barrier. The probability of the edge mode to start lasing is

$$P_1 \propto \exp\left[-\frac{\Delta E}{k_B T}\right], \quad (5.8)$$

where ΔE is the energy difference between the state with no modes lasing and the state with a lasing edge mode, which is directly related to the coupling strength J .

The nucleation problem also illustrates that the finite runtimes inherent with numerical simulations might not be representative of experiments. Since the nucleation is a stochastic process, it is possible that for longer runtimes, such as seconds, all modes will start lasing. In order to have robust isolated edge modes, these devices might therefore be limited to shorter runtimes (on the order of μ s), especially at higher temperatures. The opposite problem of course also exist, where one has to wait a long time for the edge mode to start lasing. The nucleation time can however be tuned with the exchange coupling, as is shown in Fig. 5.5. The inherent stochastic nature of this device

could make it useful for stochastic computing, which relies on systems with inherent randomness [193, 194].

5.5 COMPARISON TO PHOTONIC SYSTEMS

The array of STOs considered here shares many similarities with the photonic microring resonators experimentally realized in Ref. [163]. The linear dynamics of the magnetic excitations considered in this model are closely related to the dynamics of the photonic excitations in the microring resonators. Both models realize the non-Hermitian SSH model as described by Eq. (5.4). Moreover, their non-linear dynamics are similar, as we show next.

The dynamics of the microring resonator array are, up to second order in the (normalized) electric modal field amplitudes a_n^η , described by [195]

$$\begin{aligned}\partial_t a_n^A &= -i\Omega a_n^A - \gamma - \sigma_A \left(1 - |a_n^A|^2\right) + i\kappa_1 a_n^B + i\kappa_2 a_{n-1}^B, \\ \partial_t a_n^B &= -i\Omega a_n^B - \gamma - \sigma_B \left(1 - |a_n^B|^2\right) + i\kappa_1 a_n^A + i\kappa_2 a_{n+1}^A,\end{aligned}\tag{5.9}$$

where Ω is the lasing mode frequency, γ is the mode loss, σ_η is the mode gain and $\kappa_{1,2}$ are the coupling constants. Thus, we can draw a direct analogue between the two systems, by identifying γ as the constant part of the Gilbert damping ($\gamma = \alpha\omega$), the lasing mode frequency Ω as the precession frequency ($\Omega = \omega$) and the mode gain as the spin current contribution ($\sigma_\eta = J_{s,\eta}$). One distinction is the linear coupling $\kappa_{1,2}$, whereas the RKKY coupling between the STOs is non-linear. However, we note that up to first order in p_i the RKKY coupling is linear as well. In order to fully describe the dynamics of the microring resonators the carrier density also has to be taken into account. However, for timescales longer than the time-response of the laser, typically a few nanoseconds [196], the carrier dynamics can be disregarded and one obtains Eq. (5.9).

Most importantly, both systems have saturated gain. This feature is inherent to many driven non-Hermitian system, if the driving is limited in some way. We do note that the non-linear contributions to the precession and Gilbert damping that are present in STO systems are not present in photonics. The phase diagram, as presented in Fig. 5.3, might thus be different for the photonic system.

In this chapter we have considered three perturbations: dissipative couplings, dipole-dipole interactions and variations in the FMR-frequency, as shown in Fig. 5.4. Dissipative coupling can also be present in photonic systems, but when employing evanescent coupling is usually negligible [197], indicating that it is less relevant for photonic implementations of the non-Hermitian SSH chain. The long-range dipole-dipole interaction has no photonic analogue, but variations in the parameters are inevitably present in photonic systems.

Non-linear effects are a common feature of many experimental realizations of non-Hermitian systems. Our results are therefore applicable beyond STO arrays to other non-Hermitian topological phases.

5.6 CONCLUSION AND DISCUSSION

In conclusion, we have shown that the lasing topological edge states can be successfully accessed using STOs in a realistic non-Hermitian SSH array. We have considered both non-linear and stochastic dynamics, to determine if an experimental implementation of this model is feasible. Firstly, we found that the lasing edge mode is robust in the presence of a wide range of temperatures and perturbations, provided that we are in the topological regime. This occurs despite various perturbations breaking the \mathcal{PT} -symmetry of the original Hamiltonian such that topological protection is not guaranteed. Our result is important for ensuring that the lasing edge mode can be probed in an experiment. Secondly, we found that even though the system is topological in the linear regime, in which no bulk modes should start to lase, non-linear and stochastic effects can still access these bulk modes, reducing the usefulness of the topologically protected edge modes. We have explored the transition between the \mathcal{PT} -unbroken and \mathcal{PT} -broken regimes, which is not a sharp transition. Instead, we find a regime around the exceptional point where more bulk modes will start to lase.

Moreover, we have considered three kinds of perturbations that can naturally be present in this array and have shown in which regime the topology of the system is unaffected. We hope that these results can be used to guide future experiments. We find that at a given temperature and for equal strength of the perturbative term, the perturbation that mostly affects the dynamics of bulk modes is the variation in the parameters of the individual STOs. This might complicate the experimental realization of the STO array, and will be an inherent complication in any physical realization of a non-Hermitian SSH model, where variations are more likely. Finally, we have shown that there is a finite nucleation time, after which the edge state will start lasing.

Interactions between STOs as considered here are not easily tunable, since they depend on the spacing between the STOs [183]. Moreover, STOs cannot be brought arbitrarily close together because of Joule heating [198]. To circumvent this problem, one could couple the STOs using strip-line antennas above each STO, controlled by the microwave current generated at the adjacent STO [199]. This more direct method has the advantage that the signal could be electrically amplified, thus allowing control over the coupling strength. Even though this coupling has a different physical origin, the conclusions as presented in this chapter will still hold.

5.A NUMERICAL IMPLEMENTATION

A single STO η in unit cell i can be parametrized with the complex amplitude $c_{\eta,i}(t)$ [178]

$$\mathbf{m}_{\eta,i} = M_{\eta,i} \begin{pmatrix} \sqrt{1-p_{\eta,i}} (c_{\eta,i} + c_{\eta,i}^*) \\ \sqrt{1-p_{\eta,i}} (ic_{\eta,i} - ic_{\eta,i}^*) \\ 1 - 2p_{\eta,i} \end{pmatrix}, \quad (5.10)$$

where $p_{\eta,i} = |c_{\eta,i}|^2$ and $M_{\eta,i}$ is the magnetization length. The Langevin equation of motion then becomes

$$\frac{dc_{\eta,i}}{dt} + i\omega_{\eta,i}(p_{\eta,i}) c_{\eta,i} + \Gamma_{\eta,i}^+(p_{\eta,i}) c_{\eta,i} - \Gamma_{\eta,i}^-(p_{\eta,i}) c_{\eta,i} = f_{\eta,i}(t), \quad (5.11)$$

where

$$\omega_{\eta,i}(p) = \omega + 2p, \quad (5.12)$$

$$\Gamma_{\eta,i}^+(p) = \omega_{\eta,i} \alpha_{\eta,i} (1 + (2/\omega_{\eta,i} - 1)p), \quad (5.13)$$

$$\Gamma_{\eta,i}^-(p) = J_{s;\eta,i} (1 - p), \quad (5.14)$$

where the superscript \pm indicates loss/gain and $f_{\eta,i}(t)$ is a complex field, representing the thermal fluctuations. The stochastic field is a phenomenological description of all thermal processes and chosen to have zero mean and a second-order correlator

$$\begin{aligned} \langle f_{\eta,i}(t) f_{\eta',j}(t') \rangle &= 0, \\ \langle f_{\eta,i}(t) f_{\eta',j}^*(t') \rangle &= 2\delta_{i,j} \delta_{\eta,\eta'} D_{\eta,i}(p_{\eta,i}) \delta(t - t'), \end{aligned} \quad (5.15)$$

The diffusion coefficient $D_{\eta,i}(p)$ has to be taken dependent on p such that the system tends to thermal equilibrium. This is done by deriving the Fokker-Planck equation from the Langevin Eq. (5.11) and finding a physically-consistent solution [181]. For a single STO this is

$$D_{\eta,i}(p) = \Gamma_{\eta,i}^+(p) \frac{k_B T}{\lambda_{\eta,i} \omega_{\eta,i}(p)}, \quad (5.16)$$

where $\lambda_{\eta,i}$ is a scale factor relating the dimensionless oscillator power p and the oscillator energy, which is $\lambda_{\eta,i} = V_{\text{eff},i} M_{\eta,i} / \gamma_{\eta,i}$ for our choice of parametrization.

As initial conditions we choose $c_{\eta,i} = \sqrt{p_0} e^{i\phi}$, where ϕ is randomly chosen between 0 and 2π and p_0 is drawn from a thermal equilibrium distribution P_{eq} for an ensemble of isolated STOs

$$P_{\text{eq}} \propto \exp \left[-\frac{2\lambda_{\eta,i}}{k_B T} p_{\eta,i} \right]. \quad (5.17)$$

For the array as considered in the main text, the equation of motion is given by

$$\begin{aligned}
\partial_t c_{A,i} &= f_{\text{STO}}(c_{A,i})c_{A,i} \\
&+ J_i f_J(c_{A,i}, c_{B,i}) + \tilde{J}_{i-1} f_J(c_{A,i}, c_{i-1,B}) \\
&+ G_i f_G(c_{A,i}, c_{B,i}) + \tilde{G}_{i-1} f_G(c_{A,i}, c_{i-1,B}) \\
&+ \Omega_d \sum_{\eta,j} \frac{f_{\text{dip}}(c_{A,i}, c_{\eta,j})}{r_{Ai,\eta j}^3}, \tag{5.18}
\end{aligned}$$

$$\begin{aligned}
\partial_t c_{B,i} &= f_{\text{STO}}(c_{B,i})c_{B,i} \\
&+ J_i f_J(c_{B,i}, c_{A,i}) + \tilde{J}_i f_J(c_{B,i}, c_{i+1,A}) \\
&+ G_i f_G(c_{B,i}, c_{A,i}) + \tilde{G}_{i-1} f_G(c_{B,i}, c_{i+1,A}), \\
&+ \Omega_d \sum_{\eta,j} \frac{f_{\text{dip}}(c_{B,i}, c_{\eta,j})}{r_{Bi,\eta j}^3}, \tag{5.19}
\end{aligned}$$

where $f_J(c_{\eta,i}, c_{\eta',j})$, $f_G(c_{\eta,i}, c_{\eta',j})$ and $f_{\text{dip}}(c_{B,i}, c_{\eta,j})$ are the RRKY, dissipative and dipolar couplings between $\text{STO}_{\eta,i}$ and $\text{STO}_{\eta',j}$. These are given by

$$\begin{aligned}
f_{\text{STO}} &= -i(\omega_{\eta,i} + 2p_{\eta,i}) + J_{s,\eta,i}(1 - p_{\eta,i}) - \alpha_{\eta,i}\omega_{\eta,i}(1 + (2/\omega_{\eta,i} - 1)p_{\eta,i}), \\
f_J &= \frac{i}{2\sqrt{1 - p_{\eta,i}}} \left\{ c_{\eta',j}(2 - 3p_{\eta,i})\sqrt{1 - p_{\eta',j}} - 2c_{\eta,i}\sqrt{1 - p_{\eta,i}} \right. \\
&\quad \left. + c_{\eta,i}c_{\eta',j}^*(4c_{\eta',j}\sqrt{1 - p_{\eta,i}} - c_{\eta,i}\sqrt{1 - p_{\eta',j}}) \right\}, \\
f_G &= \frac{c_{\eta',j}\omega_{\eta',j}}{1 - p_{\eta,i}} \left\{ -\sqrt{1 - p_{\eta',j}}\sqrt{1 - p_{\eta,i}} + c_{\eta',j}^*(2c_{\eta',j}\sqrt{1 - p_{\eta',j}}\sqrt{1 - p_{\eta,i}} - c_{\eta,i}) \right. \\
&\quad \left. - 2c_{\eta',j}p_{\eta',j}(\sqrt{1 - p_{\eta',j}}\sqrt{1 - p_{\eta,i}} + c_{\eta,i}c_{\eta',j}^*) \right\}, \\
f_{\text{dip}} &= \frac{i}{\sqrt{1 - p_{\eta,i}}} \left\{ c_{\eta,i}(1 - 2p_{\eta',j})\sqrt{1 - p_{\eta,i}} + 2c_{\eta,i}^2c_{\eta',j}^*\sqrt{1 - p_{\eta',j}} \right. \\
&\quad \left. - \sqrt{1 - p_{\eta',j}}(1 - 3c_{\eta,i}\text{Re}[c_{\eta,i}]) (c_{\eta',j} - 3\text{Re}[c_{\eta',j}]) \right\}.
\end{aligned}$$

5.B HAMILTONIAN

The full Hamiltonian is given by $H = \sum_i H_i + H_i^G + H_i^{\text{dip}}$, where H_i is given in Eq. (5.4) and

$$H_i^G = iG\omega \left[a_i^\dagger b_i + \text{h.c.} \right] + i\tilde{G}\omega \left[a_i^\dagger b_{i-1} + \text{h.c.} \right], \quad (5.20)$$

$$H_i^{\text{dip}} = \Omega_d \sum_\eta \left[\eta_i^\dagger \eta_i + \sum_{\eta', j} \frac{\eta_i^\dagger \eta'_j + 3\eta_i^\dagger \eta'_j{}^\dagger + 3\eta_i \eta'_j}{2r_{\eta_i, \eta'_j}^3} \right], \quad (5.21)$$

with $\eta, \eta' = a, b$ and the \sum' indicates that the sum excludes self-interactions (i.e. $i = j, \nu = \eta$). The boundary conditions are then given by Eq. (5.5) and

$$H_j^G = iG\omega \left[a_j^\dagger b_j + \text{h.c.} \right] + i\tilde{G}\omega \left[b_j^\dagger a_l + \text{h.c.} \right]. \quad (5.22)$$

ELECTRICAL CONTROL OF CHIRAL EDGE STATES IN THE NON-HERMITIAN MAGNON CHERN INSULATOR

Non-Hermitian topological phases offer an enticing framework to further engineer and manipulate robust edge modes, building on the already extensive field of Hermitian topology. In this chapter we show that the chiral edge states in the magnon Haldane model can be electrically manipulated by including a sublattice-dependent spin-orbit torque. This creates an effective non-Hermitian magnon Chern insulator, which exhibits the hybrid skin-effect, where the edge modes are localized on one side of the sample. We discuss its implications under periodic boundary conditions and demonstrate that this effect leads to an amplification or damping of the edge modes in a finite-size system through numerical Landau-Lifshitz-Gilbert simulations. Finally, we consider a transport setup where spin waves are excited with a microwave field and detected with a normal metal lead, and show that the amplification is robust against disorder.¹

6.1 INTRODUCTION

Non-Hermitian Hamiltonians are an effective description of a system that is open to the environment, forming a convenient and simple framework to treat environmental effects [200]. In general, non-Hermitian Hamiltonians possess complex eigenvalues and biorthogonal eigenmodes, both of which are not found in Hermitian systems. From a practical standpoint, non-Hermitian systems also offer additional handles for control [201]. Recently, non-Hermitian extensions of topological systems have come under much investigation, where topological phases are realized in non-Hermitian systems, which can have profound effects on the topological properties [154–156]. Two of the most notable of these effects are the topological non-Hermitian skin-effect, where the eigenmodes are extremely sensitive to boundary effects [68, 69], and the existence of lasing edge modes [163, 167]. These effects are not just interesting for fundamental reasons, but could also be of use in applications [202].

Magnon systems offer an attractive platform to realize non-Hermitian topological phases, since a wide variety of environmental couplings can be engi-

¹ R.A.D. and P.M.G. conceived the project and P.M.G. prepared the manuscript. Both authors contributed to the manuscript.

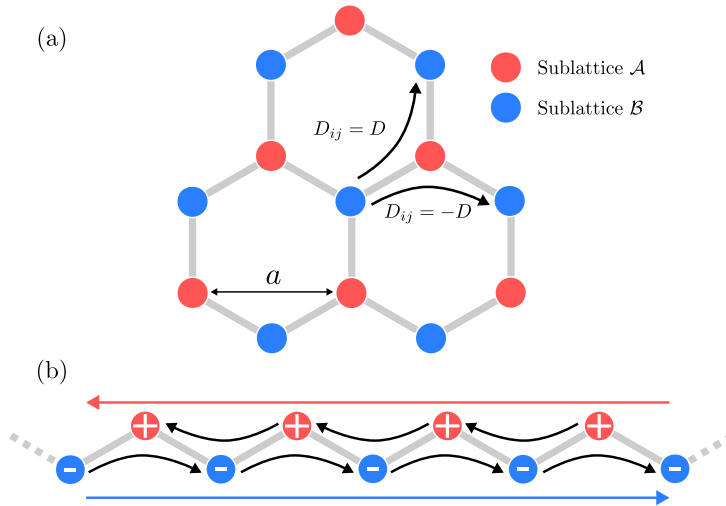


Figure 6.1: (a) The spins on a honeycomb lattice realizing the magnon Haldane model through the next-nearest neighbor Dzyaloshinskii-Moriya interaction (DMI). The spin-orbit torque is chosen such that it has the opposite sign between sublattices \mathcal{A} and \mathcal{B} . (b) The zigzag edge as a one-dimensional chain, with the direction of the DMI and the gain and loss indicated. The amplified \mathcal{A} -sites in combination with the DMI result in a hybrid skin-effect, where the edge modes pile up at the left boundary.

needed in magnon systems, such as (non-)local dissipation [32, 34, 75, 201, 203], non-reciprocal couplings [74] and local pumping through a spin-orbit [204–206] and spin-transfer torque [207, 208]. Furthermore, various topological magnon phases have been proposed, such as magnon Chern insulators [12, 43, 44, 47–49, 118, 134], magnon spin Hall insulators [53–55], magnon Dirac [56, 57] and Weyl [58, 59] systems. Of these, central to the field of magnon topology is the magnon Chern insulator, because it requires no additional symmetries [38], and its one-dimensional chiral edge modes could enable highly efficient spin transport [135, 136].

In this chapter we expand on the topological properties of the magnon Chern insulator by considering a sublattice-dependent spin-orbit torque. This extends the magnon Chern insulator to an effective non-Hermitian system, resulting in a topological amplification of the chiral edge states for a specific edge geometry. This paves the way forward for further on-chip manipulation of spin waves, offering an efficient scheme for the direct electrical control of propagating spin waves.

The remainder of this chapter is organized as follows. We first discuss the non-Hermitian magnon Haldane model in Section 6.2, demonstrating the effect of the spin-orbit torque on the linear spin-wave spectrum. In Section 6.3

we show that the magnon density in a finite-size system can be controlled through the spin-orbit torque. Next, in Section 6.4 we show using numerical Landau-Lifshitz-Gilbert simulations how an excited magnon mode can be amplified or damped. Finally, we consider a transport setup including disorder in Section 6.5 and we end with a conclusion and outlook in Section 6.6.

6.2 NON-HERMITIAN MAGNON CHERN INSULATOR

We consider the well-known magnon Haldane model [43, 44] as shown in Fig. 6.1(a), which is a prototypical model of the magnon Chern insulator. We consider the addition of a spin-orbit torque, which we take to be sublattice-dependent. The spin dynamics are then described by the Landau-Lifshitz-Gilbert equation

$$\partial_t \mathbf{S}_i = \mathbf{S}_i \times \left(-\frac{\partial \mathcal{H}}{\partial \mathbf{S}_i} - \frac{\alpha}{S} \partial_t \mathbf{S}_i + \frac{\alpha_{\text{sp}}}{S} \mathbf{S}_i \times \boldsymbol{\mu}_i \right), \quad (6.1)$$

where $\alpha = \alpha_0 + \alpha_{\text{sp}}$ is the sum of the Gilbert damping α_0 and the interface Gilbert damping enhancement α_{sp} [34]. The Hamiltonian is

$$\mathcal{H} = -\frac{1}{2} \sum_{ij} [J_{ij} \mathbf{S}_i \cdot \mathbf{S}_j - D_{ij} \hat{\mathbf{z}} \cdot (\mathbf{S}_i \times \mathbf{S}_j)] - H_0 \sum_i S_i^z, \quad (6.2)$$

where nearest neighbors experience an exchange coupling, $J_{ij} = J$, and next-nearest neighbors are coupled through the Dzyaloshinskii-Moriya interaction (DMI), $D_{ij} = -D_{ji} = D$. The spins are aligned to an external magnetic field applied in the z direction, contributing a Zeeman energy H_0 . Furthermore, $\boldsymbol{\mu}_i = \mu_i \hat{\mathbf{z}}$ is the spin accumulation in the normal metal attached to site i , taken such that

$$\mu_i = \begin{cases} +\mu & i \in \mathcal{A} \\ -\mu & i \in \mathcal{B} \end{cases} \quad (6.3)$$

changes sign between sublattices \mathcal{A} and \mathcal{B} . We refer to μ as the spin bias throughout this chapter. Since in the specific magnon Haldane model we consider the spins are orientated perpendicular to the plane, the spin Hall effect would not lead to a transverse spin current and a spin accumulation at the normal metal | ferromagnet interface. Instead, the anomalous spin Hall effect has to be used [114, 115]. We note here that one could also choose a spin-orbit torque that only affects one of the sublattice sites, which would result in the same topological features as we will discuss in this chapter. For completeness, we discuss this setup in App. 6.A, and continue in this chapter with the symmetric spin-orbit torque as shown in Eq. (6.3).

We linearize the LLG Equation (6.1) in deviations $m_i = (S_i^x + iS_i^y)/\sqrt{2S}$ from the uniform state $S_i = S\hat{z}$, apply the Fourier transform of the spin-wave operators, $m_{A/B,i} = \sqrt{2/N} \sum_{\mathbf{k}} e^{i\mathbf{k}\cdot\mathbf{R}_i} m_{A/B,\mathbf{k}}$ and obtain the following equation of motion,

$$i(1 + i\alpha)\partial_t \Psi_{\mathbf{k}} = \mathcal{H}_{\mathbf{k}} \Psi_{\mathbf{k}}, \quad (6.4)$$

where we have introduced the effective non-Hermitian Hamiltonian

$$\mathcal{H}_{\mathbf{k}} = (H + 3JS)\sigma_0 + \mathbf{h}_{\mathbf{k}} \cdot \boldsymbol{\sigma} + i\gamma\sigma_z. \quad (6.5)$$

Here $\Psi_{\mathbf{k}} = (m_{A,\mathbf{k}}, m_{B,\mathbf{k}})^T$ is the magnon state vector, $\boldsymbol{\sigma}$ is a pseudovector of Pauli matrices σ_η and

$$\mathbf{h}_{\mathbf{k}} = S \sum_i \begin{pmatrix} -J \cos(\mathbf{k} \cdot \boldsymbol{\delta}_i) \\ J \sin(\mathbf{k} \cdot \boldsymbol{\delta}_i) \\ 2D \sin(\mathbf{k} \cdot \boldsymbol{\rho}_i) \end{pmatrix}, \quad (6.6)$$

where $\boldsymbol{\delta}_i$ and $\boldsymbol{\rho}_i$ are the vectors connecting nearest and next nearest neighbors. We have incorporated the spin-orbit torque in the Hamiltonian, resulting in an effective imaginary mass $i\gamma\sigma_z$, where $\gamma \equiv \alpha_{\text{sp}}\mu$, which renders the Hamiltonian non-Hermitian.

The stability of this system can be determined by solving Eq. (6.4) for $\mathbf{k} = 0$ and up to first order in the dissipative terms, α and γ . We then find that $\omega_{\mathbf{k}=0} = H + 3JS - i\alpha H - \sqrt{9J^2S^2 - \gamma^2}$, and thus the system is stable if $\gamma^2 < 9J^2S^2$. At $\gamma^2 = 9J^2S^2$ there is an exceptional point, signaling a phase transition [209]. We focus in this chapter on the stable regime, and choose $\gamma < 3JS$. Furthermore, we will work with compensated boundaries, such that the edge coordination number, i.e., the number of nearest neighbors, is equal to the bulk coordination number.

The Chern number \mathcal{C}_n of the n -th band is still well-defined in the presence of the imaginary mass γ , and we find $\mathcal{C}_1 = -1$ and $\mathcal{C}_2 = 1$, if $D \neq 0$ and $|\gamma|/JS < 1$ [210]. Therefore, from the bulk-boundary correspondence we expect that in the topologically non-trivial phase there exist chiral edge modes for open boundary conditions. However, the finite imaginary mass γ plays an important role in the character of the chiral edge modes, resulting in an enhanced lifetime and localizing the modes on one side of the sample [211]. This can be seen by considering the zigzag edge as a one-dimensional chain, as shown in Fig. 6.1(b). We have indicated the direction of the DMI and the gain and loss on the \mathcal{A} and \mathcal{B} sites. The left-moving modes are mainly formed on the \mathcal{A} -sites, as can be seen from the direction of the DMI, which is also where the gain is applied. Under open boundary conditions, this will thus lead to a hybrid skin-effect, due to imbalance of gain and loss in combination with the DMI, and the edge modes are localized on one side of the sample [212,

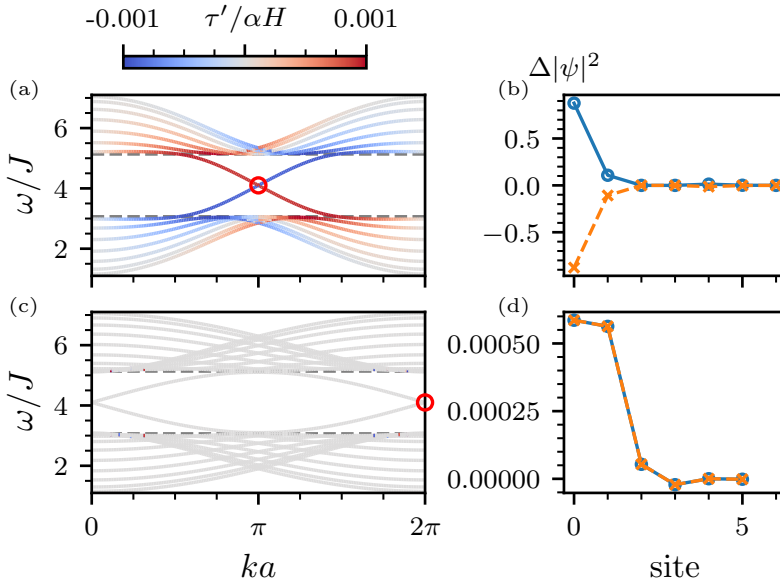


Figure 6.2: The bandstructure for a zigzag (a) and armchair nanoribbon (c) and the corresponding spatially asymmetric part of the eigenmodes $\Delta|\psi|^2$ circled in red (b, d). The colorscale indicates the lifetime correction τ' induced by the spin bias $\mu/J = 1$. The lifetimes of the left- and right-moving edge mode in the zigzag nanoribbon are enhanced and reduced respectively, whereas in the armchair nanoribbon the edge modes exhibit the hybrid skin-effect. There are bulk lifetime corrections for both the zigzag and armchair edges, but the latter are too small to be visible on the colorscale.

213]. Under periodic boundary conditions, there is no skin-effect, but instead the left-moving modes are amplified compared to the right-moving modes. The skin-effect here is hybrid, since it only occurs for the edge modes, while the bulk modes are not localized, a variation on the higher-order skin-effect [214, 215]. The hybrid character can be explained from the fact that the DMI cancels in the bulk, but it does not for the edge. We stress here that both the hybrid skin-effect and the lasing are two sides of the same coin and simply manifest differently under open and periodic boundary conditions.

The effects as discussed here are fundamentally due to the fact that the DMI does not cancel at the zigzag edge, which is not the case for the armchair case and thus there are no amplified states for the armchair edges. To show the difference between zigzag and armchair edges we consider a nanoribbon with either zigzag or armchair edges under periodic boundary conditions in Fig. 6.2. We show the lifetime correction, $\tau' \equiv \text{Im}[\epsilon] - \alpha\omega$, defined as the difference between the actual lifetime, $\text{Im}[\epsilon]$, and the Gilbert damping contribution, $\alpha\omega$,

where ϵ is the complex energy obtained from diagonalizing the effective non-Hermitian Hamiltonian and $\omega = \text{Re}[\epsilon]$. We show both the dispersion, with the corrected lifetime as the colorscale, and the localization of the edge modes. We choose $S = 1$, $D/J = 0.2$, $\alpha_0 = 5 \times 10^{-3}$ and $\alpha_{\text{sp}} = 5 \times 10^{-3}$.

For the zigzag edges, Fig. 6.2(a), the left-moving modes have an increased lifetime, while the right-moving modes have a reduced lifetime. This therefore indicates that a left-moving mode is amplified relative to a right-moving mode. The bulk modes also have lifetime corrections and therefore in the limit of zero Gilbert damping, the edge modes will not start lasing spontaneously, in contrast to parity-time symmetric non-Hermitian topological insulators [216]. However, the edge states are topologically protected and are thus robust against disorder, whilst the bulk modes do not enjoy such protection. We therefore expect that in any system with a realistic disorder the bulk mode lifetime correction will be reduced, whilst the edge modes remain protected. We will show the effects of disorder in more detail in Section 6.5.

We show the spatially asymmetric part of the eigenmodes, defined as $\Delta|\psi|^2 \equiv |\psi_t|^2 - |\psi_b|^2$, where $\psi_{t,b}$ are the top and bottom parts of the eigenmodes, corresponding to the energies indicated by the red dot in Fig. 6.2(b). The eigenmodes are localized symmetrically on either the top or the bottom of the nanoribbon, which is unchanged from the Hermitian case. There is therefore no skin-effect for the zigzag nanoribbon, which is to be expected since we have imposed period boundary conditions along the zigzag edge and thus there is no imbalance of gain and loss.

In contrast, the left- and right-moving modes of the armchair nanoribbon, Fig. 6.2(c) are not amplified or damped. There are small lifetime corrections to the bulk modes—too small to be visible in this color scale—but again we do not expect these corrections to be robust against disorder. However, the eigenmodes, Fig. 6.2(d), are both localized asymmetrically on the top of the ribbon. Not shown here are the bulk modes, but we have confirmed that these do not exhibit this asymmetric localization. This is therefore a hybrid skin-effect, which can be explained from the geometry of the nanoribbon, since now the zigzag edge is oriented along the open boundary direction. Therefore, the same reasoning as applied before to the 1D zigzag chain hold, and a hybrid skin-effect appears for the edge modes.

6.3 FINITE-SIZE SYSTEM

Having established the hybrid skin-effect and lasing under periodic boundary conditions in the non-Hermitian magnon Chern insulator, we now turn our attention to a finite-size system. We first demonstrate that the hybrid skin-effect can be measured in a finite-size system at finite temperature, by probing the magnon density $\langle n_i(\omega) \rangle \equiv \langle m_i(\omega) m_i^*(\omega) \rangle$. Specifically, we add

to the LLG equation (6.1) a stochastic magnetic field h_i , modeling thermal fluctuations, which will be fixed by the fluctuation-dissipation theorem (FDT). After performing the same linearization as before, we obtain for a finite-size system

$$\sum_j \mathbf{G}_{ij}^{-1}(\omega) m_j(\omega) = h_i^0(\omega) + h_i^{\text{SP}}(\omega), \quad (6.7)$$

where $h_i^{0/\text{SP}}(\omega)$ is the Fourier transform of the circular components $h_i^{0/\text{SP}} = h_i^x + ih_i^y$ of the stochastic magnetic field, where we take into account the fluctuations related to the bulk Gilbert damping (h_i^0) and to the interfacial spin-pumping (h_i^{SP}). The inverse magnon propagator is given by

$$\mathbf{G}_{ij}^{-1}(\omega) = -\delta_{ij}(1 + i\alpha)\omega + H_{ij}, \quad (6.8)$$

where H_{ij} is the effective non-Hermitian Hamiltonian in real space. At finite temperatures, the stochastic magnetic field $h_i(\omega)$ has to be chosen such that $\langle h_i(\omega) \rangle = 0$ and $\langle h_i^{0/\text{SP}}(\omega) h_j^{0/\text{SP}}(\omega')^* \rangle = 2\pi\delta(\omega - \omega') \mathbb{R}_{ij}^{0/\text{SP}}(\omega)$, where

$$\mathbb{R}_{ij}^0(\omega) = \delta_{ij} \frac{4\alpha_0\omega/S}{e^{\omega/k_B T} - 1}; \quad \mathbb{R}_{ij}^{\text{SP}}(\omega) = \delta_{ij} \frac{4\alpha_{\text{sp}}(\omega - \mu_i)/S}{e^{(\omega - \mu_i)/k_B T} - 1} \quad (6.9)$$

are covariance matrices determined by the quantum-mechanical FDT to ensure agreement with the quantum-mechanical linear spin-wave theory for magnons [92, 217, 218]. This allows us to accurately incorporate the thermal population of the magnons, including the fluctuations stemming from the interface of the ferromagnet with the normal metal inducing the spin-orbit torque. Here it is important to note that in order for the system to be stable in the presence of fluctuations we require that $\mu_i < H$, i.e., the spin accumulation in the attached normal metal cannot be larger than the lowest magnon band. In order to maximize the effects for the small systems as considered here we choose $\mu/J = \pm 1$, but in real systems we expect the effects to also be sufficiently large for smaller spin bias.

We show the magnon density,

$$\langle n_i(\omega) \rangle = \left\{ \mathbf{G}(\omega) \left[\mathbb{R}^0(\omega) + \mathbb{R}^{\text{SP}}(\omega) \right] \mathbf{G}^\dagger(\omega) \right\}_{ii}, \quad (6.10)$$

for a frequency in the gap in Fig. 6.3(d-f), at a temperature $T/J = 0.8$, comparing the Hermitian ($\mu = 0$) and the non-Hermitian case ($\mu \neq 0$) and the effect of switching the sign of spin bias μ . Choosing the frequency in the gap ensures that we only get contributions from the edge modes. This firstly manifests itself in the localization on the edges for both the Hermitian and non-Hermitian case. Secondly, the imaginary mass induces a hybrid skin-effect, increasing the magnon density on one side of the system, as can be seen by comparing the magnon density between $\mu/J = \pm 1$. This localization can be switched

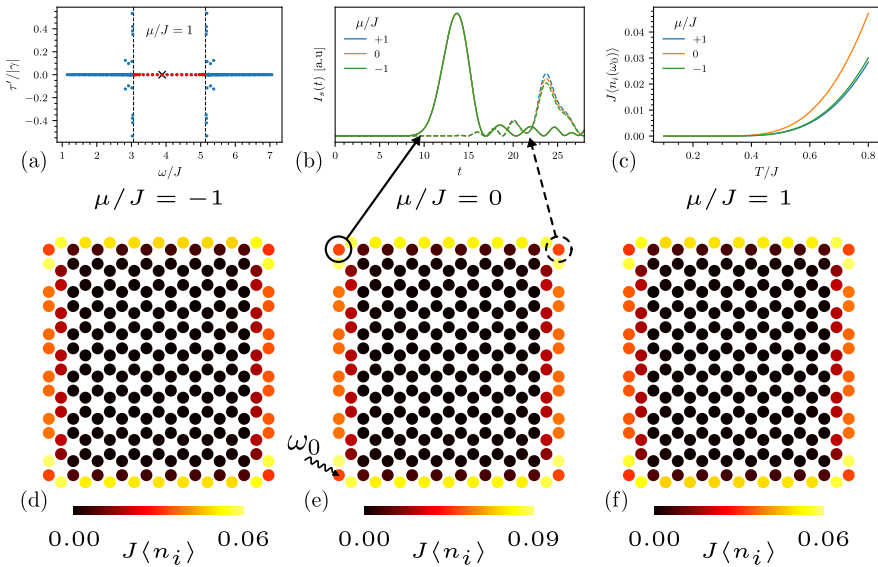


Figure 6.3: For a finite-size system: (a) The eigenfrequencies ω and the lifetime correction τ' . The edge modes are shown in red and the excitation frequency $\omega_0/J = 3.9$ used in (b-f) is indicated by a cross. (b) The injected spin current at the top left corner (solid line) and the top right corner (dashed line), after injection of a pulse at frequency ω_0 at the bottom left corner. (c) The magnon density, $\langle n_i(\omega_0) \rangle$, at the top left corner site for increasing temperature, showing the hybrid skin-effect. (d-f) The magnon density at finite temperature $T/J = 0.8$ for $\mu/J = -1, 0$ and $+1$ respectively.

with the sign of μ , as shown here, or the sign of the DMI. Since the latter is not easily experimentally accessible, we focus in this chapter on the spin bias, which can be directly electrically controlled.

The temperature dependence of the hybrid skin-effect is shown in Fig. 6.3(c), where we show the magnon density of the top left corner site, as a function of temperature. The difference in magnon density for different values of the spin bias μ , which is a measure of the hybrid skin-effect, is more prominent for higher temperature. This can be attributed to the larger occupation of the high-frequency edge states at higher temperatures, making the hybrid skin-effect more pronounced.

In Fig. 6.3(a) we show the eigenvalues of this system, with the edge modes indicated in red. We do not observe the enhanced lifetime of the chiral edge modes, since we have two zigzag edges of the same length, but oppositely oriented. Therefore, any mode which is amplified on the top zigzag edge, will be damped on the bottom zigzag edge, thus nullifying each other. Instead,

as we have discussed before, the topology induced by the imaginary mass is reflected in the hybrid skin-effect.

6.4 NUMERICAL LLG SIMULATIONS

The magnon density as shown in Fig. 6.3(d-f) is calculated within linear spin-wave theory, and thus does not take into account the full non-linear dynamics. Since for finite μ the magnon density increases (compare the colorbar scalings in Fig. 6.3(d-f)), we expect the non-linear effects to be significant. We therefore also perform numerical LLG simulations on the same finite-size system, exciting an edge mode at $t = 0$ at the bottom left site with a frequency ω_0 in the gap, such that an edge magnon is excited. The excitation is performed using a local transversely oscillating magnetic field $\mathbf{h}_e = b_0 \cos \omega_0 t \hat{x}$, which is pulsed for one period. In Fig. 6.3(b) we show the pumped spin current, $I_s(t) \propto \mathbf{S} \times \partial_t \mathbf{S}$ at the indicated corner sites, representing the angular momentum injected in a (fictitious) normal metal lead. We initialize the system in the uniform state $\mathbf{S}_i = S \hat{z}$, and solve the LLG equation (6.1) numerically at $T = 0$.

After excitation, the edge mode travels around the system, arriving at the first detector after some characteristic time which is set by the group velocity of the excited mode. At the first detector, the edge mode has only traveled through an armchair edge, and is therefore not amplified, and the signal strength is unaffected by the spin-orbit torque and neither is the arrival time.

However, at the second detector the edge mode has now traveled through a zigzag edge, and therefore it is amplified. This amplification is clearly reflected in the signal strength I_s , which is increased for $\mu > 0$ and is decreased for $\mu < 0$ relative to the reference signal with $\mu = 0$. This shows that the amplification or damping is dependent on the sign of μ , reflecting the lifetime enhancement we observed under periodic boundary conditions, shown in Fig. 6.2, and the hybrid skin-effect, shown in Fig. 6.3(d-f). The arrival times are unaffected, since the group velocity is unchanged by the finite imaginary mass.

6.5 TRANSPORT

The chiral edge states in the magnon Chern insulator are particularly interesting, because they can be utilized for highly efficient spin transport [135]. We therefore consider here a setup where spin transport through the zigzag edges can be electrically controlled, even in the presence of disorder. We consider a setup as shown in Fig. 6.4, where magnons are excited with a microwave antenna on the left, and detected with a normal metal strip on the right. We thus add an excitation field, $\mathbf{h}_i^{\text{exc}} = h(\cos(\omega_0 t), \sin(\omega_0 t), 0)$ to the sites in contact with the microwave antenna, with strength h and frequency ω_0 . The

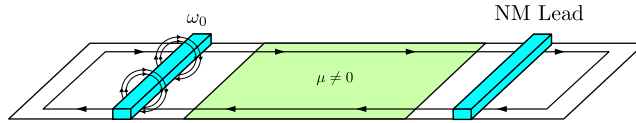


Figure 6.4: The transport setup considered in Section 6.5, where magnons are excited at the left antenna, and are detected through spin pumping into a normal metal lead on the right.

excited spin waves travel through the system, and are picked up by a normal metal lead. The imaginary mass is only non-zero in the middle of the film, such that the detection and excitation is performed in the Hermitian phase of the magnon Chern insulator.

The observable in this system is the total spin injected in the right lead, which can be obtained from the continuity equation $\partial_t \langle S_i^z \rangle = 0$ [135]. At finite temperature there will also be spin injected in the lead because of the thermal population of the magnons, but this effect can easily be subtracted experimentally. We thus focus on the zero temperature limit, $T = 0$, where the current injected into the right lead is given by

$$I(\omega_0) = \alpha_{IF} \int \frac{d\omega}{2\pi} \sum_{i \in \text{IF}} \left\{ \omega \mathbf{G}(\omega) \mathbf{H}(\omega) \mathbf{G}^\dagger(\omega) \right\}_{ii}, \quad (6.11)$$

where $[\mathbf{H}(\omega)]_{ij} = h_i^{\text{exc}}(\omega) h_j^{\text{exc}}(\omega) = h^2 \delta(\omega - \omega_0) \delta_{i \in \text{antenna}}$, the summation is over all lattice sites in contact with the right lead and α_{IF} is the interfacial Gilbert damping enhancement of the normal metal lead. We set $\alpha_{IF} = 1$ in order to minimize the reflection of spin waves.

One key feature of topological edge modes is their robustness against disorder. We therefore implement disorder in our discrete lattice model, by adding a large on-site magnetic field to randomly chosen lattice sites, which makes them effectively inaccessible to the magnons. We select randomly a set of wN lattice sites, where N is the total number of lattice sites and $0 < w < 1$ is the disorder concentration, and we average over multiple realizations, thus modeling disorder. These wN sites do not have an applied spin-orbit torque, i.e., $\mu_i = 0$, such that these sites behave like defects. This kind of disorder represents a specific defect concentration w . We calculate transport through a zigzag nanoribbon of length $d/a = 200$, since for the zigzag edges we have observed the amplification of the edge modes in Section 6.4. In the calculations that follow, we always consider a finite disorder level of $w = 0.05$, in order to illustrate the topological protection of the edge modes.

We show the resulting spin current injected in the right lead in Fig. 6.5 for $\mu/J = \pm 1$ and $\mu = 0$, for the topological trivial ($D = 0$) and non-trivial ($D/J = 0.2$) system. In the topologically trivial case, $D = 0$, there is no

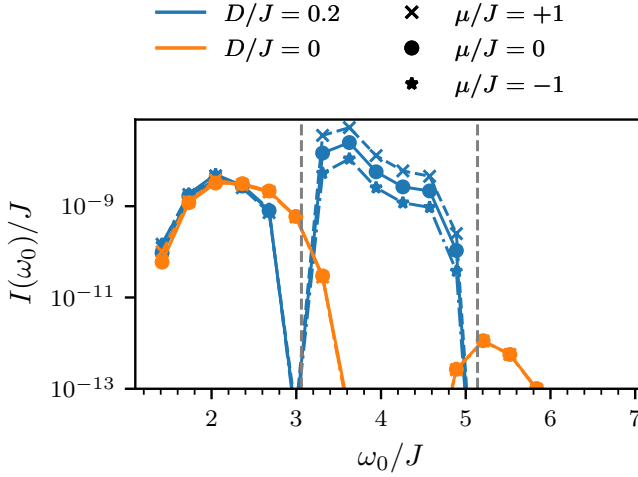


Figure 6.5: The injected spin current in the right lead, $I(\omega_0)$, as a function of excitation frequency ω_0 , at a fixed distance $d/a = 200$, comparing the topologically trivial ($D = 0$) and topologically non-trivial ($D/J = -0.2$) case and the effects of μ .

notable amplification of the signal for $\mu/J = \pm 1$ compared to $\mu = 0$. However, for the non-trivial case, $D \neq 0$, we observe an amplification or damping, depending on the sign of the spin bias, μ , in direct agreement with the numerical Landau-Lifshitz-Gilbert simulations as shown in Fig. 6.3(b). This amplification or damping is strongest for excitation frequencies in the gap and we thus attribute this to amplification or damping of the topologically-protected edge modes. In turn, this can be related to the lasing of the edge modes under periodic boundary conditions and the resulting hybrid skin-effect under open boundary conditions. Moreover, since we have included a finite disorder level, we draw the conclusion that the amplification is robust against disorder. As can be seen from comparing the bulk and edge transport, at a finite disorder level the amplification or damping of the bulk modes is strongly suppressed, and can be effectively ignored.

We now investigate the distance dependence of the amplified signal in Fig. 6.6 by defining an amplification factor $\Delta I \equiv I^{+\mu} - I^{-\mu}$ as the difference in signal between opposite signs of μ . We first observe that the signal carries much farther for excitation frequencies in the gap, as is to be expected from the topological protection of these modes, since the finite disorder suppresses the transport of the bulk modes. The amplification is furthermore strongest for the excitation frequencies low in the band gap, which can be

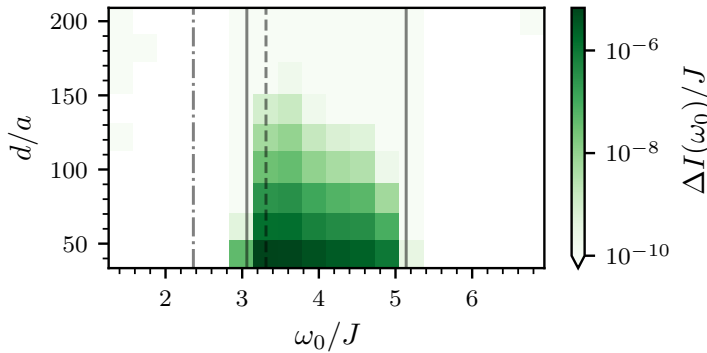


Figure 6.6: For $D/J = 0.2$ and $\mu/J = 1$, the current $I(\omega_0)$ as a function of distance, d , and excitation frequency, ω_0 . The solid lines indicate the bulk band gap, and the dashed and dotted-dashed lines indicate the edge and bulk frequency for which we show the amplification in Fig. 6.7.

explained from the fact that the damping rate within the Gilbert damping description is proportional to frequency, thus suppressing the transport at higher frequencies.

Having thus identified that at finite disorder the edge modes are amplified, whilst the bulk modes are suppressed, we now turn our attention to the effect of increasing the spin bias on an excitation frequency low in the band gap, compared to a bulk frequency. We choose $\omega_0/J = 3.3$ as edge frequency and $\omega_0/J = 2.4$ as bulk frequency, as also indicated by the dashed and dotted-dashed line respectively in Fig. 6.6, and show the injected spin current as a function of distance for increasing values of μ , in Fig. 6.7. The decay of the signal is exponential, but is reduced as a function of μ . Furthermore, this reduction is constant as a function of distance, which can be explained from the fact that the normal metal is attached throughout the entire film. Furthermore, the signal for a bulk frequency excitation follows a much stronger decay compared to the edge excitation, even for $\mu = 0$. This is a result of the topological protection, which renders the edge modes robust against the applied disorder. Furthermore, the bulk mode is amplified much more weakly compared to the edge mode, which can also be seen from Fig. 6.6.

6.6 CONCLUSION AND DISCUSSION

In conclusion, we have shown in this chapter that the chiral edge states in the magnon Haldane model can be electrically controlled through applying a

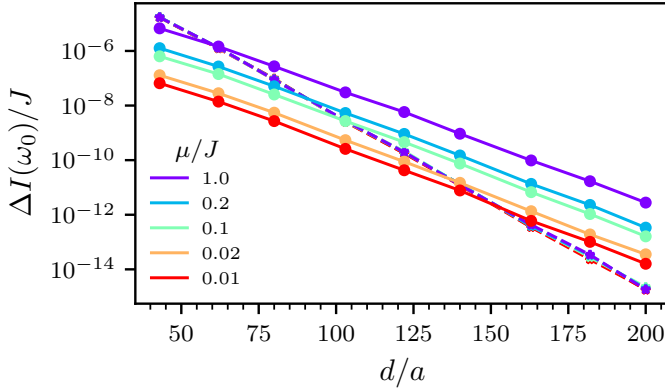


Figure 6.7: The amplification factor $\Delta I(\omega_0) \equiv I^{+\mu} - I^{-\mu}$, for varying strengths of μ as a function of distance d . We compare a frequency $\omega_0/J = 3.3$ in the gap (solid lines) and a bulk frequency $\omega_0/J = 2.4$ (dashed lines). These frequencies are also indicated by respectively the dashed and dotted-dashed line in Fig. 6.6. The amplification of the bulk modes is negligible, and therefore only the $\mu/J = 1$ result is visible.

spin-orbit torque. For the zigzag edge geometry this results in an amplification of the edge modes and the hybrid skin-effect, which we have confirmed using numerical Landau-Lifshitz-Gilbert simulations. Furthermore, we have shown this enhanced transport to be robust against disorder within the linear spin-wave theory formalism, indicating that amplification over large distances is a possibility.

Throughout this chapter we have chosen $\mu_i < H$ in order to ensure stability of the fluctuations. Increasing the spin accumulation beyond the energy of the lowest band causes an accumulation of magnons, which is not described by the linear spin-wave theory considered in this chapter. In the presence of certain non-linear effects this can lead to large-amplitude precessions or Bose-Einstein condensation [33]. The non-linear interaction between the edge and bulk magnons remains however an open question and it is therefore not clear what the effects of $\mu_i > H$ would be.

In order to realize the sublattice-dependent spin-orbit torque as considered in this chapter, we propose to make use of the buckled honeycomb structure of certain ferromagnetic Van der Waals materials [219]. Because of the buckling, the \mathcal{A} -sites will couple more strongly to a normal metal layer above the ferromagnet, while the \mathcal{B} -sites will couple more strongly to the layer below. Through the applied voltage on the top and bottom metal layers the setup as discussed in this work can be realized.

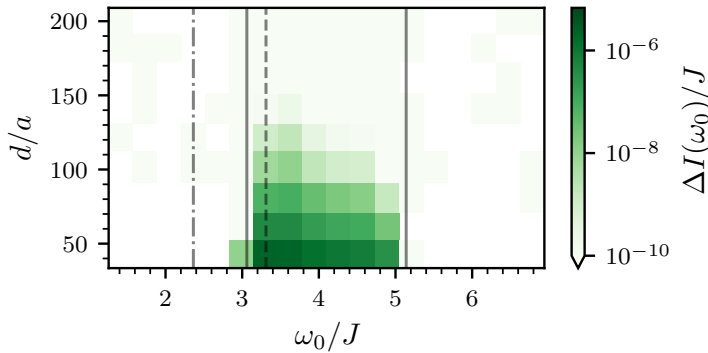


Figure 6.8: The amplification for the asymmetric spin-orbit torque only applied on the \mathcal{A} -sites, with $\mu/J = 1$. We have chosen the color-scaling identical to Fig. 6.6, showing that the amplification is weaker with the asymmetric spin-orbit torque.

The excitation frequencies required to access the chiral edge modes in most of the proposed realizations of the magnon Chern insulator are in the THz-range [51, 141], which cannot be accessed with conventional microwave antennas. This problem might be circumvented by employing the recently proposed antiferromagnetic spin-torque oscillator [220]. These spin-torque oscillators can be driven into the THz regime, and have the right geometry to excite magnons in the Haldane model we consider.

In this chapter, we have explicitly considered the magnon Haldane model, and more work is needed to fully understand if the results obtained here are general for any magnon Chern insulator. Specifically, it would be of interest if the same amplification can be obtained in the proposed topological magnonic crystals [118, 144], since these would offer exquisite control over the edge geometry.

6.A ASYMMETRIC SPIN-ORBIT TORQUE

In this Appendix we consider the case where the spin accumulation is non-zero on the \mathcal{A} -sites only,

$$\mu_i = \begin{cases} \mu & i \in \mathcal{A} \\ 0 & i \in \mathcal{B} \end{cases}, \quad (6.12)$$

which might be experimentally more feasible, since it only requires a single normal metal layer. In what follows, we assume for simplicity that the Gilbert damping enhancement α_{sp} is still present on all sites—such that $\alpha = \alpha_0 + \alpha_{\text{sp}}$ is constant throughout the system—but this is not a necessary requirement. After linearization, we obtain the same equation of motion (6.4), but with $i\gamma\sigma_z \rightarrow i\gamma\delta_{\mathcal{A}\mathcal{A}}$, such that there is only an imaginary mass on the \mathcal{A} -sites. The long-wavelength excitations are then, up to first order in the dissipative terms, $\omega_{\mathbf{k}=0} = H - i(\alpha H - \gamma/2)$ and thus the system is only stable if $\gamma/2 < \alpha H$. There are therefore now two stability requirements: $\alpha_{\text{sp}}\mu/2 < \alpha H$ and $\mu < H$.

We choose $\mu/J = 1$, which fulfills both stability requirements since $H/J = 1.1$, and show the amplification of the spin current for the asymmetric setup in Fig. 6.8. We can clearly observe the same amplification of the topological edge states. Thus, the same robust amplification of the chiral edge modes can be achieved. Furthermore, by comparing Figs. 6.6 and 6.8, which share the same color-scaling, we can conclude that the amplification is weaker for the asymmetric setup.

CONCLUSION AND OUTLOOK

The central purpose of this Thesis has been to further the study of topology in magnonic systems. To this end, we have considered a range of magnonic systems in which topology plays a central role. We first considered the symmetry breaking at the interface of a ferromagnetic thin film in Chapter 2. The carrier of this symmetry breaking is the long-ranged dipole-dipole interaction. Intuitively, this can be understood from the demagnetization field arising from the dipole-dipole interaction, which minimizes the magnetic field lines outside of the thin film. Since the magnetic dipoles are pushed out of the plane by the external magnetic field, extra external fields are formed at the interface of the thin film and the vacuum, breaking the symmetry. Using microscopic calculations we have shown that there is a transverse spin current associated with the symmetry breaking, which can be measured with a heavy-metal lead.

The dipole-dipole interaction can lead to a magnon Hall effect if the magnetic field is applied perpendicular to the plane of a ferromagnetic thin film, which we studied in Chapter 3. Again, the dipole-dipole interaction breaks the symmetry, equipping the magnons with a finite Berry curvature. At the edges of the sample there is therefore a magnon edge current, which circulates around the sample. We have shown that therefore there is a magnon Hall effect that can be measured using electrical injection and detection.

If in a system with the magnon Hall effect a gap is opened a magnon Chern insulator may be realized. Here the magnon edge modes cross the bulk gap, and are topologically protected. However, they typically have high frequencies, making them inaccessible to experiment. To solve this problem we have proposed a general strategy to lower the edge modes to zero frequency in Chapter 4, by using a non-equilibrium state. In this state the bulk modes are gapped out, whereas the edge modes have zero frequency.

Magnonic systems can also be used for the realization of a non-Hermitian topological insulator, the subject of Chapters 5 and 6. In Chapter 5 we considered the non-Hermitian Su-Schrieffer-Heeger model, realized by coupling spin-torque oscillators. In this chapter we showed that the lasing edge mode dynamics persist in the non-linear domain. This model also serves as a clear

example as to how non-Hermitian topology and magnonic systems are a natural fit.

Finally, in Chapter 6 we explored a non-Hermitian extension of the Chern insulator, showing that the chiral edge states can be robustly electrically controlled using a spin-orbit torque. This manifested itself in two effects: (1) edge states can be localized on one side of the sample, leading to a hybrid skin-effect and (2) the transport through these modes can be amplified or damped. Both the sign and the magnitude of these effects can be controlled through the spin-orbit torque.

In this Thesis we have therefore shown how topology plays a central role in magnonic systems and can be studied through various out-of-equilibrium techniques. This can in part be attributed to the dipole-dipole interaction, which is ubiquitous in ferromagnets and will therefore introduce topological effects in a wide range of magnonic systems. Furthermore, we have shown that magnetic systems offer an ideal platform to engineer an impressive variety of magnonic topological phases, including non-Hermitian topological phases.

OUTLOOK

Topology in magnonic systems remains relatively unexplored, which can in part be attributed to the high frequencies of the edge modes. The non-equilibrium state we have proposed in Chapter 4 is one possible solution, and the results obtained for the magnon Chern insulator can be easily generalized to other topological magnon phases. Of particular interest would be a magnon Weyl semimetal [54, 145, 146], since zero-frequency Weyl points would dominate the transport response. Moreover, it would be of interest to consider these non-equilibrium states in non-Hermitian topological phases, essentially combining Chapters 4 and 6. In such a setup one would obtain zero-frequency edge modes which can be electrically controlled. Especially the incoherent transport response in this system would be well worth exploring.

The strategy used in Chapter 4 to obtain zero-frequency edge modes is general for any bosonic system and could perhaps be generalized to other bosonic Chern insulators, such as those realized by photons [129]. Even though these photonic systems do not suffer from the problem of the inaccessibility of the edge modes, they might be an ideal platform to further investigate the novel physics associated with the low-frequency edge modes, such as the concurrent existence of positive and negative frequency edge modes.

An alternative solution to the problem of the high frequency of the edge modes could come from magnetic meta-materials, where the magnetization is artificially created through modern fabrication techniques such as patterning [118, 144]. The energy scales of these magnetic meta-materials is set by the dipole-dipole interaction instead of the exchange interaction, and thus the

edge states sit at easily accessible GHz-frequencies. There are still many open questions regarding the topology in these meta-materials and it remains unclear if they can actually be experimentally realized. Specifically, a complete microscopic description of the dipole-dipole interactions—including the short-wavelength limit—is lacking, which could be remedied by employing the same Ewald summation technique as in Chapters 2 and 3. This would also be useful to explicitly verify the Chern number, which requires an integration over the entire Brillouin zone and thus over all wave numbers.

The field of non-Hermitian topological insulators has grown considerably in the past decade, uncovering novel topological phases [154]. These phases are not only protected by non-Hermitian symmetries [155], but also exhibit a wide range of previously unknown phenomena, such as the non-Hermitian skin effect and lasing edge modes. Magnon systems might be a perfect candidate to realize much of these non-Hermitian phases, since the magnons couple naturally to the environment. Gain is easily introduced through spin-transfer and spin-orbit torques, which are now a standard part of the magnetic toolbox, and loss is always present, as parameterized by the Gilbert damping. Through engineering the gain and loss, magnonic systems can be made parity-time (PT) symmetric [175, 221], and thus have a purely real spectrum, although the Hamiltonian is non-Hermitian [153]. The PT-symmetry in magnetic systems has been studied in Chapter 5 and gave rise to topologically protected lasing edge modes in a one-dimensional chain. Here it remains an open question how the PT symmetry can be generalized to higher dimensions [216], where the lasing edge modes can be used for transport without spurious bulk contributions.

By tuning the gain and loss one also naturally obtains an exceptional point (EP) in PT-symmetric systems, where both the eigenvectors and eigenmodes coalesce into a single point on the Riemann surface [222]. At an EP the spectrum is extremely sensitive to perturbations, which would make it an ideal sensor [190]. However, this would require keeping the system precisely at the EP, which might prove difficult under real world conditions, since the system has to be protected against unwanted perturbations, such as thermal fluctuations. If an EP could be harnessed as a magnetic sensor, it might be possible to accurately detect a single magnon, similar to how photomultiplier tubes can detect a single photon.

Another potential application is to encircle an EP in parameter space by varying two parameters, such that after a full rotation the system returns to the same parameter state. Because of the topological structure of the Riemann surface at the EP the system ends up on a different eigenmode and eigenvalue branch [192, 223], which can be harnessed for asymmetric mode switching [224]. The encircling of the parameter space would require close control over the Hamiltonian, something which is readily available in magnetic materials.

For example, the external magnetic field and the local spin-orbit torque can be electrically controlled, the anisotropy can be varied through experimental techniques [225, 226] and the coupling between two magnetic systems can be modulated through the thickness of the Ruderman-Kittel-Kasuya-Yosida coupling layer [227–229]. With these techniques, an exceptional point can be encircled by a magnon wave-packet moving through a spatially modulated Hamiltonian in a waveguide setup [224].

The existence of the PT-symmetry also naturally leads to the question if this PT-symmetry can be broken. In fact, in a simple two-mode setup the PT-symmetry breaks when the system goes through the EP [175], signaling a dynamical phase transition. Beyond the EP we then obtain unstable dynamics, which can be stabilized by the non-linear interactions, leading to novel dynamical phases [209, 230]. These phases are particularly interesting to engineer magnetic nano-oscillators with large-amplitude oscillations and a large frequency range [178, 231, 232], but are also of interest for more fundamental reasons, uncovering the relations between non-linearities and EPs [233]. Magnetic systems might offer here an ideal platform to realize and investigate these relations.

Beyond gain and loss, various non-local environmental couplings have been proposed in magnetic materials, such as unidirectional [74] and dissipative couplings [32, 34, 75, 201, 203]. These couplings could be used to engineer a wide range of non-Hermitian topological phases [155]. From an application perspective these phases are particularly interesting, since they can be used to further manipulate and control the topologically protected edge modes, as shown in Chapter 6.

Topology in magnetic systems thus has a large potential, not just for fundamental reasons, but also for application purposes. By considering also non-Hermitian systems the topological features can be further extended and controlled. The possibilities have most certainly not been exhausted and many more avenues remain to be explored.

TOPOLOGISCHE SPINGOLVEN RAKEN UIT EVENWICHT

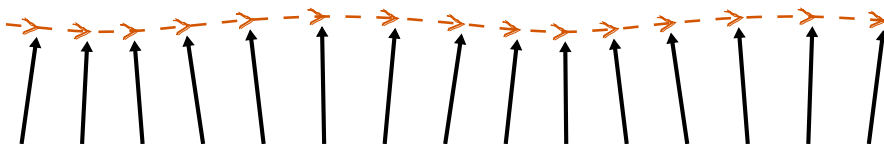
In dit hoofdstuk wordt een Nederlandse samenvatting gegeven van de belangrijkste resultaten van het Proefschrift.

Iedere computerchip produceert warmte. Iedereen die wel eens een laptop voor langere tijd op schoot heeft gehad, weet dat maar al te goed. De warmteproductie functioneert effectief als een begrenzer, want als de computerchip de warmte niet kwijt kan, wordt de rekensnelheid teruggeschroefd. Een computerchip die minder warmte produceert is dus gelijk een snellere en energiezuinigere computerchip. En energiezuinigere computers zijn hard nodig, want computers en datacenters zijn verantwoordelijk voor minstens 5% van het globale energieverbruik.

ALTERNATIEVE COMPUTERS

Er is daarom veel interesse in alternatieven voor de conventionele computerchip. Een van de mogelijkheden is het gebruik van spingolven, ook wel magnonen genoemd. Dit zijn uitwijkingen van de microscopische magnetische momenten—de spins—in een magnetisch materiaal, die zich als golven voortbewegen, zoals schematisch weergegeven in figuur 1. Een spingolf kan worden gebruikt om informatie mee te transporteren en is dus geschikt om een computer mee te verwezenlijken. Met een belangrijk voordeel: spingolven vereisen geen elektrische stroom en zijn daarom significant energiezuiniger.

Maar hier lopen we tegen een nieuw probleem aan, want spingolven zijn geen behouden deeltjes en dus na een tijd is de spingolf uitgedoofd. Dit komt omdat als de spingolf botst, bijvoorbeeld op een imperfectie, een roostertrilling of een andere spingolf, er impulsmoment wordt overgedragen aan het kristalrooster. Dit zorgt ervoor dat de spin golven uitdoven, wat het ontwerpen van een spingolfcomputer vermoelijk.



Figuur 1: Een spingolf bestaat uit afwijkingen van de individuele spins (zwarte pijlen) in een magneet, die zich als een golf door het materiaal bewegen.

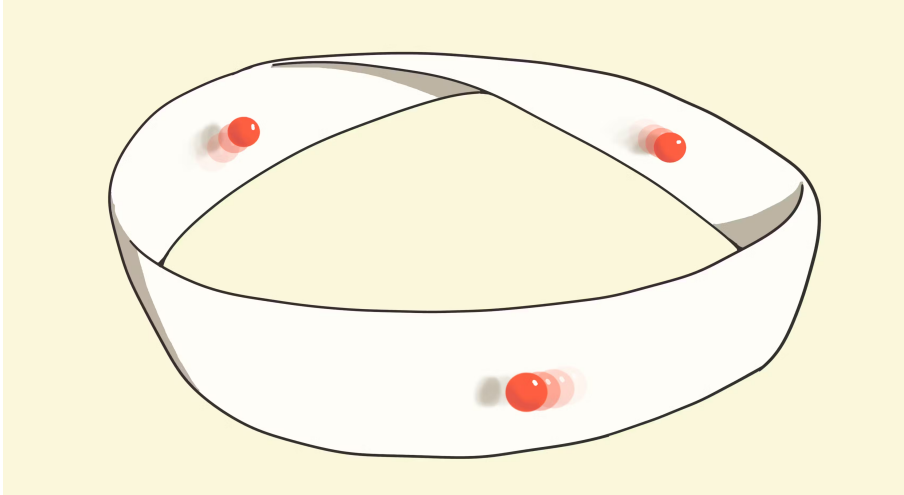
Kader 1: Magnonics

Het gebruik van spingolven om informatie te verwerken wordt *Magnonics* genoemd [234]. Hierbij zijn spingolven de informatiedragers. Het is dan mogelijk om de klassieke elektronische computer één-op-één na te bouwen, waarbij de spingolven de rol van bits spelen—een 1 of 0. De uitdaging is dan om de spingolven zo te manipuleren zodat er berekeningen mee kunnen worden uitgevoerd. De tweede mogelijkheid is om gebruik te maken van het golfkarakter van de spingolven. Hiermee representeren de spingolven geen bits meer, maar is de informatie opgeslagen in de structuur van de golf. Bepaalde wiskundige computeroperaties zijn hiermee zeer efficiënt uit te voeren, zoals de Fouriertransformatie. Ook is het mogelijk om spingolven in te zetten voor *neuromorfische* computers—waarmee het brein wordt nagebootst. Hiermee zijn op een efficiënte manier neurale netwerken mee door te rekenen. Met de huidige revolutie in kunstmatige intelligentie, die mede mogelijk is gemaakt door grote neurale netwerken, heeft deze onderzoeksrichting natuurlijk een boost gekregen. Deze alternatieve invalshoeken worden ook wel *onconventioneel* rekenen genoemd, omdat er geen bits meer aan te pas komen zoals in conventionele computerchips. Ook al is deze techniek flink sneller voor bepaalde operaties zoals een neuraal netwerk of een Fouriertransformatie, het is wel moeilijker om alle functies van een computer na te bootsen. Onconventionele rekenmethodes zullen dus waarschijnlijk altijd moeten worden gebruikt in combinatie met een elektronisch computercircuit. Is de snelheidswinst echter voldoende dan is het gebruik natuurlijk interessant.

Een mogelijke oplossing hiervoor is het gebruiken van spingolven die een topologisch karakter hebben, analoog aan de Möbiusband in figuur 2. De topologische objecten zijn nu de banen door het materiaal die de spingolven kunnen volgen. In bepaalde kristalroosters vormen deze banen eenzelfde Möbiusband [235]. Deze spingolven noemen we dan ook “topologisch”. Ze hebben de bijzondere eigenschap dat bepaalde botsingen niet meer zijn toegestaan en kunnen dus over langere afstanden bewegen zonder uit te doven. Dat maakt topologische spingolven erg interessant om te gebruiken in een mogelijke spingolfcomputer.

TOPOLOGISCHE TRANSPORTEFFECTEN

Topologische effecten zijn meetbaar door het systeem uit evenwicht te brengen en te kijken naar de resulterende respons. Iets minder ingewikkeld gezegd: door een transportexperiment. De magneet begint in evenwicht en nu slaan

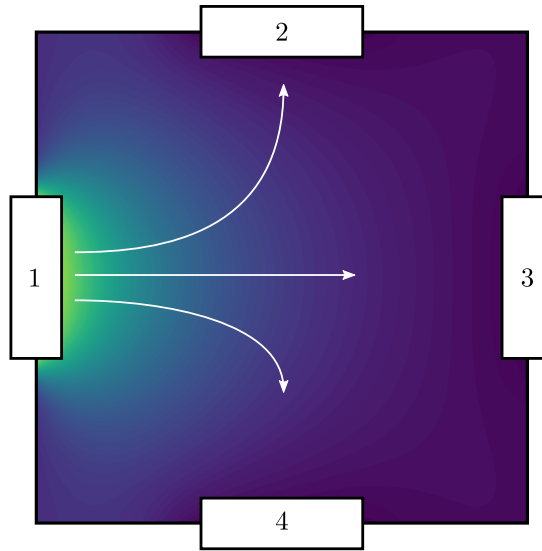


Figuur 2: Een Möbiusband, die je maakt door een papieren strip 180 graden te draaien en aan elkaar te plakken. De Möbiusband heeft maar één zijde: een balletje dat begint te rollen over de band komt vanzelf terug op zijn beginpositie, maar heeft wel alle kanten van het papier geraakt. Bij een gewone papieren strip is dit niet mogelijk en dus zijn deze twee voorwerpen topologisch gezien verschillend. *Figuur gebaseerd op Sketchplanations.com.*

we aan één zijde de magneet aan, waardoor spingolven ontstaan die zich door de magneet gaan bewegen.

Het topologische effect vertaalt zich erin dat de spingolf die wordt aangeslagen, niet recht op zijn doel af gaat, maar een rotatie meekrijgt. Intuïtief kan dit worden vergeleken met een tafeltennisspeler, die met een goede backhand het balletje kan laten spinnen. Het balletje beschrijft nu niet meer een rechte baan, maar wijkt af naar links of rechts. Analoog hieraan heeft een topologische spingolf een afwijking naar links of rechts. Een eenvoudig experiment—tenminste, eenvoudig theoretisch te beschrijven—om de topologische eigenschappen te meten is door een vierpuntsmeting te doen, zoals weergegeven in figuur 3. Links worden spingolven aangeslagen en het verschil tussen de bovenste en de onderste detector is dan het resultaat van de topologische afwijking. De rechter detector functioneert hier als referentiesignaal.

Het experiment zoals hierboven beschreven klinkt wellicht simpel, maar is niet eenvoudig uit te voeren. Dit komt omdat de spingolven continue botsen. Al deze botsingen zorgen ervoor dat de aangeslagen spingolf verstrooid raakt en zo wordt ook de afwijking uitgesmeerd. Om een topologisch effect te zien moeten de spingolven dus worden gemeten na een zeer korte afstand, omdat ze dan nog maar weinig botsingen hebben ondergaan.



Figuur 3: Een vierpuntsmeting, waarmee de topologische afwijking van de spingolven te meten is. Op plek 1 worden spingolven geïnjecteerd, waarna deze gemeten worden op plekken 2, 3 en 4. Als er een verschil tussen 2 en 4 wordt gemeten dan komt dat door de topologische afwijking van de spingolven. De detectie op plek 3 functioneert als een referentiesignaal. De kleurschaal geeft de lokale concentratie spingolven weer en de kleurschakeling betekent dus dat er diffusie plaats vindt. Gebaseerd op Figuur 3.1 uit Hoofdstuk 3.

Het is echter ook mogelijk om de diffusie van spingolven te meten—zie kader 2. In deze situatie kijken we juist naar wat er gebeurt na heel veel botsingen. Tussen die botsingen in bewegen de topologische spingolven zich zoals we hebben beschreven en hebben dus een afwijking naar links of rechts. We kunnen ons daarom het volgende experiment voorstellen. Eerst wordt lokaal de concentratie spingolven verhoogd. Door diffusie verspreidt deze verhoging zich als een olievlek uit over de rest van het systeem, en kan worden gemeten in een vierpuntopstelling. Wij hebben laten zien in Hoofdstuk 3 dat als de spingolven een topologisch karakter hebben, dit zich vertaalt in een te meten verschil tussen de bovenste en onderste detector.

Kader 2: Spingolfdiffusie

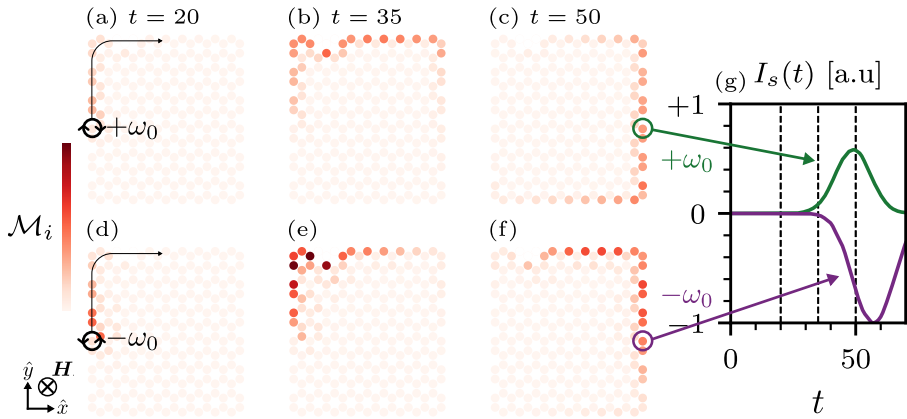
Voor typische spingolfsystemen zijn de meest voorkomende botsingen juist die botsingen met andere spingolven, waarbij het totale aantal spingolven behouden blijft, maar wel energie wordt uitgewisseld [29]. Dat betekent dat een spingolf heel vaak botst met een groot aantal andere

spingolven, voordat het botst op iets anders. Vanuit de statistische thermodynamica weten we dat hierbij de spingolven zich op deze manier verdelen volgens een thermische distributie. Op een korte tijdschaal wordt de energie dus constant genivelleerd. Maar omdat het totaal aantal spingolven behouden blijft, kan er wel diffusie plaatsvinden. Een lokaal hoge concentratie spingolven kan zich zo verspreiden over het systeem. De diffusie kan over lange afstanden plaatsvinden en wordt niet gelimiteerd door de botsingen van de spingolven, wat een groot voordeel is.

NIET-EVENWICHTSTOESTAND

Er is nog een verbazingwekkend effect geassocieerd met de topologische spingolven, naast de rotatie zoals hierboven beschreven. Dit topologische effect—dat voor het eerst ontdekt werd in elektronensystemen—heeft een nogal contra-intuïtieve uitwerking: het zorgt ervoor dat er op de randen van het systeem extra toestanden ontstaan. Deze randtoestanden hebben een bijzondere eigenschap, want het is niet mogelijk ze te vernietigen door op de rand een stukje materiaal weg te halen. Dit is in schril contrast met de gewone spingolftoestanden die zich midden in het materiaal bevinden, want deze worden verstrooid door een missend stukje materiaal of andere onzuiverheden. Een topologische randtoestand beweegt zich er echter gewoon omheen en is dus zeer robuust. We noemen dit ook wel de *topologische bescherming*.

Er is echter een probleem: in de meeste materialen die mogelijk topologische spingolvmaterialen zijn, bevinden de topologische spingolven zich op te hoge frequenties, rond de terrahertz. Dat maakt het erg moeilijk om met ze te werken en topologische spingolven zijn dus ook nog niet direct gemeten. In Hoofdstuk 4 hebben we een mogelijke strategie voorgesteld om toch de topologische spingolven te kunnen gebruiken, door ze te verlagen in frequentie. Hier kunnen we gebruik maken van een handige eigenschap van spingolfsystemen: ze zijn makkelijk extern te beïnvloeden. Dat maakt het mogelijk om een niet-evenwichtstoestand te ontwerpen, waarbij de spins recht tegenover een extern magneetveld staan. Normaal gesproken zouden in zo'n situatie de spins zich omdraaien om parallel aan het externe veld te staan. Door middel van een extern krachtmoment op de spins—in dit geval uitgeoefend door een metallische laag—is het echter mogelijk om deze situatie te stabiliseren, resulterend in lage-frequentie topologische spingolven. Dit is exemplarisch voor spingolfsystemen: deze bijzondere niet-evenwichtstoestanden zijn relatief gemakkelijk te realiseren omdat spingolfsystemen eenvoudig te manipuleren zijn.



Figuur 4: Het aanslaan van een spingolf met positieve (a-c) en negatieve (d-f) frequentie ω_0 . De kleurschaal in de panelen geeft de lokale sterkte van de spingolf weer op drie opeenvolgende tijden. Het laatste paneel (g) geeft de rotatierichting van een spin op de rand weer, die wisselt van richting afhankelijk van of we een positieve of negatieve frequentie gebruiken. *Figuur 4.2 uit Hoofdstuk 4.*

De niet-evenwichtstoestand leidt tot nog een ander opvallend resultaat. Het blijkt dat er nu in één systeem topologische spingolven met een positieve en een negatieve frequentie simultaan kunnen bestaan. Een negatieve frequentie betekent hier dat de individuele spins tegen de klok in draaien, in plaats van met de klok mee zoals bij een positieve frequentie. Beide spingolven hebben nog steeds dezelfde topologische eigenschappen, dus ze bewegen allebei over de rand en zijn topologisch beschermd. We laten dit zien in figuur 4, met een simulatie van twee spingolven met positieve (bovenste rij) en negatieve (onderste rij) frequentie. Een mogelijke toepassing van deze positieve en negatieve frequentie spingolven zou als bits in een spingolfcomputer kunnen zijn, waarbij de positieve en negatieve frequentie een 1 en een 0 representeren.

TOEKOMST

Het veld van topologische spingolven staat feitelijk nog maar in de kinderschoenen. Een belangrijke stap is het experimenteel realiseren van een spingolfsysteem met topologische randtoestanden. Met een dergelijk systeem zou het mogelijk zijn om een aantal belangrijke voorspellingen van de theorie te toetsen, zoals de topologische bescherming. Is er een topologisch spingolfsysteem gevonden, dan is de volgende stap het realiseren van nieuwe niet-evenwichtstoestanden. In dit artikel hebben we een voorbeeld gegeven van wat mogelijk is, maar er zijn nog veel meer niet-evenwichtstoestanden met

interessante effecten. Hierdoor kunnen we ook meer leren over het samenspel tussen topologie en niet-evenwichtseffecten, iets wat maar beperkt mogelijk is in andere systemen. En al deze kennis zou zich uiteindelijk kunnen vertalen in een praktische toepassing: de energiezuinige spingolfcomputer, mede mogelijk gemaakt door topologische spingolven.

ACKNOWLEDGMENTS

First of all, I want to thank my promotor **Rembert**. When I started four years ago I had no real idea what I was getting myself into, but you were always a very supportive supervisor, letting me figure out what I was interested in. You also infected me with the road cycling virus, which led to me buying a road bike and riding more than 10.000 kilometers to distract myself during Corona times. And if I ever felt anxious about cycling and not working instead, I just had to look up your Strava activity to see that I was still not cycling as frequently as my own supervisor.

I would like to thank **Alexander Mook** for being my co-promotor. We met almost a year ago during a conference, and we ended up working together on the work in Chapter 4, which was based on your ideas. I always enjoyed our discussions and you were always willing to help me with any problems I was stuck on. You subsequently also offered me a post-doc position in your group in Mainz, and I am looking forward to working closer with you.

Here I would also like to thank **Alexander Brinkman**: when I mentioned to you that I would maybe be interested in a theoretical PhD position you started enthusiastically emailing your contacts in the Dutch physics community, which eventually resulted in Rembert offering me this position. There is a certain satisfaction that you will now also be able to assess if your enthusiasm about me was justified by being part of my reading and defense committee.

Joren, we started almost simultaneously, and should also finish around the same time (provided you finish your own Thesis in time). I think our approaches to physics could not be any more different and perhaps that is why we have also never actually collaborated on anything tangible. During the conferences we visited together I have come to know you better, since we often had to share a room. You were always good company and it was always fun to find dinner that was pleasing to both my own (perhaps slightly too critical) taste and your gluten-intolerance, especially in Japan—where they apparently put gluten in anything. Since you will also go do a post-doc, I wish you good luck on your further academic path!

Even though you would not know it from the contents of this Thesis, **Tim**, I think you were actually the one who I worked together with the most. Although I guess that it is exemplary of our usually meandering discussions that this has not yet resulted in a publication,¹ but I hope that this will soon be remedied. I always enjoyed our discussions about a wide variety of physics

¹ Whose fault this is, is probably better left unsaid.

and physics-adjacent subjects and was always impressed with your wide interest. I wish you the best of luck in your endeavor as a philosopher/physicist/freelance educator!

I would also like to thank the current and former members of the Duinegroup I have shared some time with. A special thanks to **Mithuss** for allowing me to supervise your Bachelor's thesis. This is also the right point to thank the lunch table at ITF for creating the necessary distraction with non-research related discussions during lunch.

Als laatste kan ik natuurlijk ook **Jantine** niet onvermeld laten. Ik weet ook wel dat ik vroeger altijd zei dat *een PhD doen echt niets voor mij was*, wat langzaam veranderde naar *misschien wil ik er even over nadenken* en uiteindelijk toch *ik ga de positie in Utrecht aannemen* werd. Hetzelfde riedeltje herhaalde zich daarna nog een keer, maar nu met het mogelijk doen van een post-doc. Gelukkig prikte je er altijd wel doorheen en wist je meestal beter dan ik wat ik eigenlijk wil. Ik weet dat het soms als een grote stap aanvoelt om te verhuizen richting Mainz, maar met zijn drieën komen we er vast uit.

CURRICULUM VITAE

Pieter Gunnink completed his pre-university secondary education (VWO) at Johannes Fontanus College, Barneveld, after which he started the study Applied Physics at the University of Twente in 2013. He graduated in 2019 with a master's thesis on *Engineering a topological insulator* under supervision of Prof. Alexander Brinkman. Thereafter he continued as a PhD student under the supervision of Prof. Rembert Duine, which has led to this Thesis. He will continue his research into topological magnonics as a post-doc at the Johannes Gutenberg University in Mainz, under supervision of Dr. Alexander Mook.

BIBLIOGRAPHY

- [1] P. M. Gunnink, R. A. Duine, and A. Rückriegel, "Electrical detection of unconventional transverse spin currents in obliquely magnetized thin films," *Physical Review B* **101**, 220407(R) (2020).
- [2] P. M. Gunnink, R. A. Duine, and A. Rückriegel, "Theory for electrical detection of the magnon Hall effect induced by dipolar interactions," *Physical Review B* **103**, 214426 (2021).
- [3] P. M. Gunnink, J. S. Harms, R. A. Duine, and A. Mook, *Zero-frequency chiral magnonic edge states protected by non-equilibrium topology*, (Feb. 13, 2023) arXiv:2302.06597.
- [4] P. M. Gunnink, B. Flebus, H. M. Hurst, and R. A. Duine, "Nonlinear dynamics of the non-Hermitian Su-Schrieffer-Heeger model," *Physical Review B* **105**, 104433 (2022).
- [5] P. M. Gunnink, R. L. Bouwmeester, and A. Brinkman, "Artificial oxide heterostructures with non-trivial topology," *Journal of Physics: Condensed Matter* **33**, 085601 (2020).
- [6] W. Van Heddeghem, S. Lambert, B. Lannoo, D. Colle, M. Pickavet, and P. Demeester, "Trends in worldwide ICT electricity consumption from 2007 to 2012," *Computer Communications, Green Networking* **50**, 64–76 (2014).
- [7] C. Freitag, M. Berners-Lee, K. Widdicks, B. Knowles, G. S. Blair, and A. Friday, "The real climate and transformative impact of ICT: A critique of estimates, trends, and regulations," *Patterns* **2**, 100340 (2021).
- [8] G. E. Moore, "Cramming more components onto integrated circuits, Reprinted from *Electronics*, volume 38, number 8, April 19, 1965, pp.114 ff.," *IEEE Solid-State Circuits Society Newsletter* **11**, 33–35 (2006).
- [9] C. A. Mack, "Fifty Years of Moore's Law," *IEEE Transactions on Semiconductor Manufacturing* **24**, 202–207 (2011).
- [10] T. N. Theis and H.-S. P. Wong, "The End of Moore's Law: A New Beginning for Information Technology," *Computing in Science & Engineering* **19**, 41–50 (2017).
- [11] S.-M. Kang, Y. Leblebici, and C. W. Kim, *CMOS Digital Integrated Circuits Analysis & Design*, 3rd (McGraw-Hill, New York, 2003).

- [12] H. Katsura, N. Nagaosa, and P. A. Lee, "Theory of the Thermal Hall Effect in Quantum Magnets," *Physical Review Letters* **104**, 066403 (2010).
- [13] N. W. Ashcroft and N. D. Mermin, *Solid State Physics* (Saunders College Publishing, 1976).
- [14] J. M. Radcliffe, "Some properties of coherent spin states," *Journal of Physics A: General Physics* **4**, 313 (1971).
- [15] L. Landau and E. Lifshitz, "On the theory of the dispersion of magnetic permeability in ferromagnetic bodies," *Phys. Zeitsch. der Sow.* **8**, 153–169 (1935).
- [16] W. F. Brown, "Thermal Fluctuations of a Single-Domain Particle," *Physical Review* **130**, 1677–1686 (1963).
- [17] T. Gilbert, "A phenomenological theory of damping in ferromagnetic materials," *IEEE Transactions on Magnetics* **40**, 3443–3449 (2004).
- [18] M. Haertinger, C. H. Back, J. Lotze, M. Weiler, S. Geprägs, H. Huebl, S. T. B. Goennenwein, and G. Woltersdorf, "Spin pumping in YIG/Pt bilayers as a function of layer thickness," *Physical Review B* **92**, 054437 (2015).
- [19] T. Holstein and H. Primakoff, "Field Dependence of the Intrinsic Domain Magnetization of a Ferromagnet," *Physical Review* **58**, 1098–1113 (1940).
- [20] H. Y. Yuan, Y. Cao, A. Kamra, R. A. Duine, and P. Yan, "Quantum magnonics: When magnon spintronics meets quantum information science," *Physics Reports* **965**, 1–74 (2022).
- [21] B. A. Kalinikos and A. N. Slavin, "Theory of dipole-exchange spin wave spectrum for ferromagnetic films with mixed exchange boundary conditions," *Journal of Physics C: Solid State Physics* **19**, 7013–7033 (1986).
- [22] B. A. Kalinikos, M. P. Kostylev, N. V. Kozhus, and A. N. Slavin, "The dipole-exchange spin wave spectrum for anisotropic ferromagnetic films with mixed exchange boundary conditions," *Journal of Physics: Condensed Matter* **2**, 9861–9877 (1990).
- [23] A. Kreisel, F. Sauli, L. Bartosch, and P. Kopietz, "Microscopic spin-wave theory for yttrium-iron garnet films," *The European Physical Journal B* **71**, 59 (2009).

- [24] L. Fallarino, M. Madami, G. Duerr, D. Grundler, G. Gubbiotti, S. Tacchi, and G. Carlotti, "Propagation of Spin Waves Excited in a Permalloy Film by a Finite-Ground Coplanar Waveguide: A Combined Phase-Sensitive Micro-Focused Brillouin Light Scattering and Micromagnetic Study," *IEEE Transactions on Magnetics* **49**, 1033–1036 (2013).
- [25] M. P. Marder, *Condensed matter physics*, 2nd ed (Wiley, Hoboken, N.J, 2010).
- [26] G. Sundaram and Q. Niu, "Wave-packet dynamics in slowly perturbed crystals: Gradient corrections and Berry-phase effects," *Physical Review B* **59**, 14915–14925 (1999).
- [27] D. Xiao, Y. Yao, Z. Fang, and Q. Niu, "Berry-Phase Effect in Anomalous Thermoelectric Transport," *Physical Review Letters* **97**, 026603 (2006).
- [28] A. Jünger, *Transport equations for semiconductors*, Lecture Notes in Physics 773 (Springer, Berlin, 2009).
- [29] L. J. Cornelissen, K. J. H. Peters, G. E. W. Bauer, R. A. Duine, and B. J. van Wees, "Magnon spin transport driven by the magnon chemical potential in a magnetic insulator," *Physical Review B* **94**, 014412 (2016).
- [30] J. Sinova, S. O. Valenzuela, J. Wunderlich, C. H. Back, and T. Jungwirth, "Spin Hall effects," *Reviews of Modern Physics* **87**, 1213–1260 (2015).
- [31] R. A. Duine, A. Brataas, S. A. Bender, and Y. Tserkovnyak, "Spintronics and Magnon Bose-Einstein Condensation," in *Universal Themes of Bose-Einstein Condensation*, edited by D. W. Snoke, N. P. Proukakis, and P. B. Littlewood (Cambridge University Press, Cambridge, 2017), pages 505–524.
- [32] Y. Tserkovnyak, A. Brataas, and G. E. W. Bauer, "Spin pumping and magnetization dynamics in metallic multilayers," *Physical Review B* **66**, 224403 (2002).
- [33] S. A. Bender, R. A. Duine, A. Brataas, and Y. Tserkovnyak, "Dynamic phase diagram of dc-pumped magnon condensates," *Physical Review B* **90**, 094409 (2014).
- [34] Y. Tserkovnyak, A. Brataas, and G. E. W. Bauer, "Enhanced Gilbert Damping in Thin Ferromagnetic Films," *Physical Review Letters* **88**, 117601 (2002).
- [35] A. V. Chumak, A. A. Serga, M. B. Jungfleisch, R. Neb, D. A. Bozhko, V. S. Tiberkevich, and B. Hillebrands, "Direct detection of magnon spin transport by the inverse spin Hall effect," *Applied Physics Letters* **100**, 082405 (2012).

- [36] S. A. Bender, R. A. Duine, and Y. Tserkovnyak, "Electronic Pumping of Quasiequilibrium Bose-Einstein-Condensed Magnons," *Physical Review Letters* **108**, 246601 (2012).
- [37] S. A. Bender and Y. Tserkovnyak, "Interfacial spin and heat transfer between metals and magnetic insulators," *Physical Review B* **91**, 140402 (2015).
- [38] D. Xiao, M.-C. Chang, and Q. Niu, "Berry Phase Effects on Electronic Properties," *Reviews of Modern Physics* **82**, 1959–2007 (2010).
- [39] M. Z. Hasan and C. L. Kane, "Colloquium: Topological insulators," *Reviews of Modern Physics* **82**, 3045–3067 (2010).
- [40] X.-L. Qi and S.-C. Zhang, "Topological insulators and superconductors," *Reviews of Modern Physics* **83**, 1057–1110 (2011).
- [41] A. Bansil, H. Lin, and T. Das, "Colloquium: Topological band theory," *Reviews of Modern Physics* **88**, 021004 (2016).
- [42] F. D. M. Haldane, "Model for a Quantum Hall Effect without Landau Levels: Condensed-Matter Realization of the "Parity Anomaly"," *Physical Review Letters* **61**, 2015–2018 (1988).
- [43] S. A. Owerre, "A first theoretical realization of honeycomb topological magnon insulator," *Journal of Physics: Condensed Matter* **28**, 386001 (2016).
- [44] S. K. Kim, H. Ochoa, R. Zarzuela, and Y. Tserkovnyak, "Realization of the Haldane-Kane-Mele Model in a System of Localized Spins," *Physical Review Letters* **117**, 227201 (2016).
- [45] T. Fukui, Y. Hatsugai, and H. Suzuki, "Chern Numbers in Discretized Brillouin Zone: Efficient Method of Computing (Spin) Hall Conductances," *Journal of the Physical Society of Japan* **74**, 1674–1677 (2005).
- [46] K. von Klitzing, "Developments in the quantum Hall effect," *Philosophical Transactions of the Royal Society A: Mathematical, Physical and Engineering Sciences* **363**, 2203–2219 (2005).
- [47] K. A. van Hoogdalem, Y. Tserkovnyak, and D. Loss, "Magnetic texture-induced thermal Hall effects," *Physical Review B* **87**, 024402 (2013).
- [48] L. Zhang, J. Ren, J.-S. Wang, and B. Li, "Topological magnon insulator in insulating ferromagnet," *Physical Review B* **87**, 144101 (2013).
- [49] A. Mook, J. Henk, and I. Mertig, "Edge states in topological magnon insulators," *Physical Review B* **90**, 024412 (2014).
- [50] R. Chisnell, J. S. Helton, D. E. Freedman, D. K. Singh, R. I. Bewley, D. G. Nocera, and Y. S. Lee, "Topological Magnon Bands in a Kagome Lattice Ferromagnet," *Physical Review Letters* **115**, 147201 (2015).

- [51] L. Chen, J.-H. Chung, B. Gao, T. Chen, M. B. Stone, A. I. Kolesnikov, Q. Huang, and P. Dai, "Topological Spin Excitations in Honeycomb Ferromagnet CrI_3 ," *Physical Review X* **8**, 041028 (2018).
- [52] F. Zhu, L. Zhang, X. Wang, F. J. dos Santos, J. Song, T. Mueller, K. Schmalzl, W. F. Schmidt, A. Ivanov, J. T. Park, J. Xu, J. Ma, S. Lounis, S. Blügel, Y. Mokrousov, Y. Su, and T. Brückel, "Topological magnon insulators in two-dimensional van der Waals ferromagnets CrSiTe_3 and CrGeTe_3 : Toward intrinsic gap-tunability," *Science Advances* **7**, eabi7532 (2021).
- [53] K. Nakata, S. K. Kim, J. Klinovaja, and D. Loss, "Magnonic topological insulators in antiferromagnets," *Physical Review B* **96**, 224414 (2017).
- [54] A. Mook, B. Göbel, J. Henk, and I. Mertig, "Taking an electron-magnon duality shortcut from electron to magnon transport," *Physical Review B* **97**, 140401 (2018).
- [55] H. Kondo, Y. Akagi, and H. Katsura, " \mathbb{Z}_2 Topological Invariant for Magnon Spin Hall Systems," *Physical Review B* **99**, 041110 (2019).
- [56] J. Fransson, A. M. Black-Schaffer, and A. V. Balatsky, "Magnon Dirac materials," *Physical Review B* **94**, 075401 (2016).
- [57] S. S. Pershoguba, S. Banerjee, J. C. Lashley, J. Park, H. Ågren, G. Aeppli, and A. V. Balatsky, "Dirac Magnons in Honeycomb Ferromagnets," *Physical Review X* **8**, 011010 (2018).
- [58] F.-Y. Li, Y.-D. Li, Y. B. Kim, L. Balents, Y. Yu, and G. Chen, "Weyl magnons in breathing pyrochlore antiferromagnets," *Nature Communications* **7**, 12691 (2016).
- [59] A. Mook, J. Henk, and I. Mertig, "Tunable Magnon Weyl Points in Ferromagnetic Pyrochlores," *Physical Review Letters* **117**, 157204 (2016).
- [60] Z. Li, Y. Cao, P. Yan, and X. Wang, "Higher-order topological solitonic insulators," *npj Computational Materials* **5**, 1–7 (2019).
- [61] T. Hirose, S. A. Díaz, J. Klinovaja, and D. Loss, "Magnonic Quadrupole Topological Insulator in Antiskyrmion Crystals," *Physical Review Letters* **125**, 207204 (2020).
- [62] A. Mook, S. A. Díaz, J. Klinovaja, and D. Loss, "Chiral hinge magnons in second-order topological magnon insulators," *Physical Review B* **104**, 024406 (2021).
- [63] X. S. Wang, H. W. Zhang, and X. R. Wang, "Topological Magnonics: A Paradigm for Spin-Wave Manipulation and Device Design," *Physical Review Applied* **9**, 024029 (2018).
- [64] P. A. McClarty, "Topological Magnons: A Review," *Annual Review of Condensed Matter Physics* **13**, 171–190 (2022).

- [65] W. P. Su, J. R. Schrieffer, and A. J. Heeger, "Solitons in Polyacetylene," *Physical Review Letters* **42**, 1698–1701 (1979).
- [66] B. Flebus, R. A. Duine, and H. M. Hurst, "Non-Hermitian topology of one-dimensional spin-torque oscillator arrays," *Physical Review B* **102**, 180408 (2020).
- [67] H. M. Hurst and B. Flebus, "Non-Hermitian physics in magnetic systems," *Journal of Applied Physics* **132**, 220902 (2022).
- [68] F. K. Kunst, E. Edvardsson, J. C. Budich, and E. J. Bergholtz, "Biorthogonal Bulk-Boundary Correspondence in Non-Hermitian Systems," *Physical Review Letters* **121**, 026808 (2018).
- [69] N. Okuma, K. Kawabata, K. Shiozaki, and M. Sato, "Topological Origin of Non-Hermitian Skin Effects," *Physical Review Letters* **124**, 086801 (2020).
- [70] M. A. Bandres, S. Wittek, G. Harari, M. Parto, J. Ren, M. Segev, D. N. Christodoulides, and M. Khajavikhan, "Topological insulator laser: Experiments," *Science* **359**, eaar4005 (2018).
- [71] G. Harari, M. A. Bandres, Y. Lumer, M. C. Rechtsman, Y. D. Chong, M. Khajavikhan, D. N. Christodoulides, and M. Segev, "Topological insulator laser: Theory," *Science* **359**, eaar4003 (2018).
- [72] S. Lieu, "Topological phases in the non-Hermitian Su-Schrieffer-Heeger model," *Physical Review B* **97**, 045106 (2018).
- [73] K. Yokomizo and S. Murakami, "Non-Bloch Band Theory of Non-Hermitian Systems," *Physical Review Letters* **123**, 066404 (2019).
- [74] H. Y. Yuan, R. Lavrijsen, and R. A. Duine, "Unidirectional magnetic coupling induced by chiral interaction and nonlocal damping," *Physical Review B* **107**, 024418 (2023).
- [75] A. Houshang, E. Iacocca, P. Dürrenfeld, S. R. Sani, J. Åkerman, and R. K. Dumas, "Spin-wave-beam driven synchronization of nanocontact spin-torque oscillators," *Nature Nanotechnology* **11**, 280–286 (2016).
- [76] D. A. Bozhko, H. Y. Musiienko-Shmarova, V. S. Tiberkevich, A. N. Slavin, I. I. Syvorotka, B. Hillebrands, and A. A. Serga, "Unconventional spin currents in magnetic films," *Physical Review Research* **2**, 023324 (2020).
- [77] L. J. Cornelissen, J. Liu, R. A. Duine, J. B. Youssef, and B. J. van Wees, "Long-distance transport of magnon spin information in a magnetic insulator at room temperature," *Nature Physics* **11**, 1022–1026 (2015).
- [78] B. L. Giles, Z. Yang, J. S. Jamison, and R. C. Myers, "Long-range pure magnon spin diffusion observed in a nonlocal spin-Seebeck geometry," *Physical Review B* **92**, 224415 (2015).

- [79] R. L. Stamps, S. Breitzkreutz, J. L. Akerman, A. V. Chumak, Y. Otani, G. E. W. Bauer, J.-U. Thiele, M. Bowen, S. A. Majetich, M. Kläui, I. L. Prejbeanu, B. Dieny, N. M. Dempsey, and B. Hillebrands, "The 2014 Magnetism Roadmap," *Journal of Physics D: Applied Physics* **47**, 333001 (2014).
- [80] G. Csaba, Á. Papp, and W. Porod, "Perspectives of using spin waves for computing and signal processing," *Physics Letters A* **381**, 1471–1476 (2017).
- [81] S. Klingler, P. Pirro, T. Brächer, B. Leven, B. Hillebrands, and A. V. Chumak, "Spin-wave logic devices based on isotropic forward volume magnetostatic waves," *Applied Physics Letters* **106**, 212406 (2015).
- [82] A. Khitun, M. Bao, and K. L. Wang, "Magnonic logic circuits," *Journal of Physics D: Applied Physics* **43**, 264005 (2010).
- [83] A. Khitun and K. L. Wang, "Non-volatile magnonic logic circuits engineering," *Journal of Applied Physics* **110**, 034306 (2011).
- [84] A. V. Chumak, A. A. Serga, and B. Hillebrands, "Magnon transistor for all-magnon data processing," *Nature Communications* **5**, 4700 (2014).
- [85] T. Schneider, A. A. Serga, B. Leven, B. Hillebrands, R. L. Stamps, and M. P. Kostylev, "Realization of spin-wave logic gates," *Applied Physics Letters* **92**, 022505 (2008).
- [86] T. Fischer, M. Kewenig, D. A. Bozhko, A. A. Serga, I. I. Syvorotka, F. Ciubotaru, C. Adelmann, B. Hillebrands, and A. V. Chumak, "Experimental prototype of a spin-wave majority gate," *Applied Physics Letters* **110**, 152401 (2017).
- [87] G. A. Melkov, A. A. Serga, V. S. Tiberkevich, A. N. Oliynyk, and A. N. Slavin, "Wave Front Reversal of a Dipolar Spin Wave Pulse in a Nonstationary Three-Wave Parametric Interaction," *Physical Review Letters* **84**, 3438–3441 (2000).
- [88] A. V. Sadovnikov, S. A. Odintsov, E. N. Beginin, S. E. Sheshukova, Yu. P. Sharaevskii, and S. A. Nikitov, "Toward nonlinear magnonics: Intensity-dependent spin-wave switching in insulating side-coupled magnetic stripes," *Physical Review B* **96**, 144428 (2017).
- [89] A. V. Chumak, V. I. Vasyuchka, A. A. Serga, and B. Hillebrands, "Magnon spintronics," *Nature Physics* **11**, 453–461 (2015).
- [90] E. Saitoh, M. Ueda, H. Miyajima, and G. Tatara, "Conversion of spin current into charge current at room temperature: Inverse spin-Hall effect," *Applied Physics Letters* **88**, 182509 (2006).

- [91] V. Cherepanov, I. Kolokolov, and V. L'vov, "The saga of YIG: Spectra, thermodynamics, interaction and relaxation of magnons in a complex magnet," *Physics Reports* **229**, 81–144 (1993).
- [92] J. Zheng, S. Bender, J. Armaitis, R. E. Troncoso, and R. A. Duine, "Green's function formalism for spin transport in metal-insulator-metal heterostructures," *Physical Review B* **96**, 174422 (2017).
- [93] S. Geller and M. A. Gilleo, "The crystal structure and ferrimagnetism of yttrium-iron garnet, $Y_3Fe_2(FeO_4)_3$," *Journal of Physics and Chemistry of Solids* **3**, 30–36 (1957).
- [94] B. R. Tittmann, "Possible identification of magnetostatic surface spin wave modes in ferromagnetic resonance on epitaxial yttrium-iron-garnet films," *Solid State Communications* **13**, 463–466 (1973).
- [95] V. Sharma and B. K. Kuanr, "Magnetic and crystallographic properties of rare-earth substituted yttrium-iron garnet," *Journal of Alloys and Compounds* **748**, 591–600 (2018).
- [96] K. Harii, Y.-J. Seo, Y. Tsutsumi, H. Chudo, K. Oyanagi, M. Matsuo, Y. Shiomi, T. Ono, S. Maekawa, and E. Saitoh, "Spin Seebeck mechanical force," *Nature Communications* **10**, 1–5 (2019).
- [97] S. Vonsovskii and M. Svirskii, "Phonon Spin," *Soviet Physics, Solid State* **3**, 1568 (1962).
- [98] A. T. Levine, "A note concerning the spin of the phonon," *Il Nuovo Cimento* **26**, 190–193 (1962).
- [99] L. Zhang and Q. Niu, "Angular Momentum of Phonons and the Einstein–de Haas Effect," *Physical Review Letters* **112**, 085503 (2014).
- [100] J. H. P. Colpa, "Diagonalization of the quadratic boson hamiltonian," *Physica A: Statistical Mechanics and its Applications* **93**, 327–353 (1978).
- [101] N. Nagaosa, J. Sinova, S. Onoda, A. H. MacDonald, and N. P. Ong, "Anomalous Hall effect," *Reviews of Modern Physics* **82**, 1539–1592 (2010).
- [102] T. Qin, J. Zhou, and J. Shi, "Berry curvature and the phonon Hall effect," *Physical Review B* **86**, 104305 (2012).
- [103] C. Strohm, G. L. J. A. Rikken, and P. Wyder, "Phenomenological Evidence for the Phonon Hall Effect," *Physical Review Letters* **95**, 155901 (2005).
- [104] M. Onoda, S. Murakami, and N. Nagaosa, "Hall Effect of Light," *Physical Review Letters* **93**, 083901 (2004).
- [105] Y. Onose, T. Ideue, H. Katsura, Y. Shiomi, N. Nagaosa, and Y. Tokura, "Observation of the Magnon Hall Effect," *Science* **329**, 297–299 (2010).

- [106] T. Ideue, Y. Onose, H. Katsura, Y. Shiomi, S. Ishiwata, N. Nagaosa, and Y. Tokura, "Effect of lattice geometry on magnon Hall effect in ferromagnetic insulators," *Physical Review B* **85**, 134411 (2012).
- [107] R. Matsumoto and S. Murakami, "Theoretical Prediction of a Rotating Magnon Wave Packet in Ferromagnets," *Physical Review Letters* **106**, 197202 (2011).
- [108] R. Matsumoto and S. Murakami, "Rotational motion of magnons and the thermal Hall effect," *Physical Review B* **84**, 184406 (2011).
- [109] R. Matsumoto, R. Shindou, and S. Murakami, "Thermal Hall effect of magnons in magnets with dipolar interaction," *Physical Review B* **89**, 054420 (2014).
- [110] K. Tanabe, R. Matsumoto, J.-I. Ohe, S. Murakami, T. Moriyama, D. Chiba, K. Kobayashi, and T. Ono, "Observation of magnon Hall-like effect for sample-edge scattering in unsaturated YIG," *Physica Status Solidi B* **253**, 783–787 (2016).
- [111] L. J. Cornelissen, J. Liu, B. J. van Wees, and R. A. Duine, "Spin-Current-Controlled Modulation of the Magnon Spin Conductance in a Three-Terminal Magnon Transistor," *Physical Review Letters* **120**, 097702 (2018).
- [112] A. Kamenev and A. Levchenko, "Keldysh technique and non-linear sigma-model: basic principles and applications," *Advances in Physics* **58**, 197–319 (2009).
- [113] J. E. Hirsch, "Spin Hall Effect," *Physical Review Letters* **83**, 1834–1837 (1999).
- [114] K. S. Das, W. Y. Schoemaker, B. J. van Wees, and I. J. Vera-Marun, "Spin injection and detection via the anomalous spin Hall effect of a ferromagnetic metal," *Physical Review B* **96**, 220408(R) (2017).
- [115] K. S. Das, J. Liu, B. J. van Wees, and I. J. Vera-Marun, "Efficient Injection and Detection of Out-of-Plane Spins via the Anomalous Spin Hall Effect in Permalloy Nanowires," *Nano Letters* **18**, 5633–5639 (2018).
- [116] R. N. Costa Filho, M. G. Cottam, and G. A. Farias, "Microscopic theory of dipole-exchange spin waves in ferromagnetic films: Linear and nonlinear processes," *Physical Review B* **62**, 6545–6560 (2000).
- [117] A. Kamra, W. Belzig, and A. Brataas, "Magnon-squeezing as a niche of quantum magnonics," *Applied Physics Letters* **117**, 090501 (2020).
- [118] R. Shindou, R. Matsumoto, S. Murakami, and J.-i. Ohe, "Topological chiral magnonic edge mode in a magnonic crystal," *Physical Review B* **87**, 174427 (2013).

- [119] M. Lein and K. Sato, "Krein-Schrödinger formalism of bosonic Bogoliubov-de Gennes and certain classical systems and their topological classification," *Physical Review B* **100**, 075414 (2019).
- [120] L. Lu, J. D. Joannopoulos, and M. Soljačić, "Topological photonics," *Nature Photonics* **8**, 821–829 (2014).
- [121] A. Rückriegel and R. A. Duine, "Hannay Angles in Magnetic Dynamics," *Annals of Physics* **412**, 168010 (2020).
- [122] F. Hecht, "New development in FreeFem++," *Journal of Numerical Mathematics* **20**, 251–266 (2012).
- [123] J. Barker and G. E. W. Bauer, "Thermal Spin Dynamics of Yttrium Iron Garnet," *Physical Review Letters* **117**, 217201 (2016).
- [124] A. Okamoto and S. Murakami, "Berry curvature for magnons in ferromagnetic films with dipole-exchange interactions," *Physical Review B* **96**, 174437 (2017).
- [125] M. Hirschberger, R. Chisnell, Y. S. Lee, and N. P. Ong, "Thermal Hall Effect of Spin Excitations in a Kagome Magnet," *Physical Review Letters* **115**, 106603 (2015).
- [126] L. J. Cornelissen, J. Shan, and B. J. van Wees, "Temperature dependence of the magnon spin diffusion length and magnon spin conductivity in the magnetic insulator yttrium iron garnet," *Physical Review B* **94**, 180402(R) (2016).
- [127] R. Takahashi and N. Nagaosa, "Berry Curvature in Magnon-Phonon Hybrid Systems," *Physical Review Letters* **117**, 217205 (2016).
- [128] A. Okamoto, S. Murakami, and K. Everschor-Sitte, "Berry curvature for magnetoelastic waves," *Physical Review B* **101**, 064424 (2020).
- [129] F. D. M. Haldane and S. Raghu, "Possible Realization of Directional Optical Waveguides in Photonic Crystals with Broken Time-Reversal Symmetry," *Physical Review Letters* **100**, 013904 (2008).
- [130] T. Ozawa, H. M. Price, A. Amo, N. Goldman, M. Hafezi, L. Lu, M. C. Rechtsman, D. Schuster, J. Simon, O. Zilberberg, and I. Carusotto, "Topological photonics," *Reviews of Modern Physics* **91**, 015006 (2019).
- [131] G. Ma, M. Xiao, and C. T. Chan, "Topological phases in acoustic and mechanical systems," *Nature Reviews Physics* **1**, 281–294 (2019).
- [132] D. Jin, L. Lu, Z. Wang, C. Fang, J. D. Joannopoulos, M. Soljačić, L. Fu, and N. X. Fang, "Topological magnetoplasmon," *Nature Communications* **7**, 13486 (2016).
- [133] D. Jin, T. Christensen, M. Soljačić, N. X. Fang, L. Lu, and X. Zhang, "Infrared Topological Plasmons in Graphene," *Physical Review Letters* **118**, 245301 (2017).

- [134] A. Mook, K. Plekhanov, J. Klinovaja, and D. Loss, "Interaction-Stabilized Topological Magnon Insulator in Ferromagnets," *Physical Review X* **11**, 021061 (2021).
- [135] A. Rückriegel, A. Brataas, and R. A. Duine, "Bulk and edge spin transport in topological magnon insulators," *Physical Review B* **97**, 081106 (2018).
- [136] X. S. Wang, A. Brataas, and R. E. Troncoso, "Bosonic Bott Index and Disorder-Induced Topological Transitions of Magnons," *Physical Review Letters* **125**, 217202 (2020).
- [137] T. Weber, D. M. Fobes, J. Waizner, P. Steffens, G. S. Tucker, M. Böhm, L. Beddrich, C. Franz, H. Gabold, R. Bewley, D. Voneshen, M. Skoulatos, R. Georgii, G. Ehlers, A. Bauer, C. Pfleiderer, P. Böni, M. Janoschek, and M. Garst, "Topological magnon band structure of emergent Landau levels in a skyrmion lattice," *Science* **375**, 1025–1030 (2022).
- [138] E. Viñas Boström, T. S. Parvini, J. W. McIver, A. Rubio, S. V. Kusminskiy, and M. A. Sentef, "Direct Optical Probe of Magnon Topology in Two-Dimensional Quantum Magnets," *Physical Review Letters* **130**, 026701 (2023).
- [139] F. Lu and Y.-M. Lu, *Magnon band topology in spin-orbital coupled magnets: classification and application to α - ruiCl_3* , (July 26, 2018) arXiv:1807.05232.
- [140] Q.-R. Xu, V. P. Flynn, A. Alase, E. Cobanera, L. Viola, and G. Ortiz, "Squaring the fermion: The threefold way and the fate of zero modes," *Physical Review B* **102**, 125127 (2020).
- [141] M. Mena, R. S. Perry, T. G. Perring, M. D. Le, S. Guerrero, M. Storni, D. T. Adroja, Ch. Rüegg, and D. F. McMorrow, "Spin-Wave Spectrum of the Quantum Ferromagnet on the Pyrochlore Lattice $\text{Lu}_2\text{V}_2\text{O}_7$," *Physical Review Letters* **113**, 047202 (2014).
- [142] J. S. Harms, H. Y. Yuan, and R. A. Duine, *Antimagnonics*, (Oct. 29, 2022) arXiv:2210.16698.
- [143] V. Vlaminck and M. Bailleul, "Spin-wave transduction at the submicrometer scale: Experiment and modeling," *Physical Review B* **81**, 014425 (2010).
- [144] R. Shindou, J.-i. Ohe, R. Matsumoto, S. Murakami, and E. Saitoh, "Chiral spin-wave edge modes in dipolar magnetic thin films," *Physical Review B* **87**, 174402 (2013).
- [145] Y. Su and X. R. Wang, "Chiral anomaly of Weyl magnons in stacked honeycomb ferromagnets," *Physical Review B* **96**, 104437 (2017).
- [146] T. Liu and Z. Shi, "Magnon quantum anomalies in Weyl ferromagnets," *Physical Review B* **99**, 214413 (2019).

- [147] Z. Yang, F. Gao, X. Shi, X. Lin, Z. Gao, Y. Chong, and B. Zhang, "Topological Acoustics," *Physical Review Letters* **114**, 114301 (2015).
- [148] P. Wang, L. Lu, and K. Bertoldi, "Topological Phononic Crystals with One-Way Elastic Edge Waves," *Physical Review Letters* **115**, 104302 (2015).
- [149] S. Murakami and A. Okamoto, "Thermal Hall Effect of Magnons," *Journal of the Physical Society of Japan* **86**, 011010 (2017).
- [150] A. A. Kovalev and V. Zyuzin, "Spin torque and Nernst effects in Dzyaloshinskii-Moriya ferromagnets," *Physical Review B* **93**, 161106 (2016).
- [151] E. V. Castro, M. P. López-Sancho, and M. A. H. Vozmediano, "Anderson localization and topological transition in Chern insulators," *Physical Review B* **92**, 085410 (2015).
- [152] C. M. Bender, D. C. Brody, and H. F. Jones, "Complex Extension of Quantum Mechanics," *Physical Review Letters* **89**, 270401 (2002).
- [153] C. M. Bender and S. Boettcher, "Real Spectra in Non-Hermitian Hamiltonians Having \mathcal{PT} Symmetry," *Physical Review Letters* **80**, 5243–5246 (1998).
- [154] E. J. Bergholtz, J. C. Budich, and F. K. Kunst, "Exceptional topology of non-Hermitian systems," *Reviews of Modern Physics* **93**, 015005 (2021).
- [155] K. Kawabata, K. Shiozaki, M. Ueda, and M. Sato, "Symmetry and Topology in Non-Hermitian Physics," *Physical Review X* **9**, 041015 (2019).
- [156] Z. Gong, Y. Ashida, K. Kawabata, K. Takasan, S. Higashikawa, and M. Ueda, "Topological Phases of Non-Hermitian Systems," *Physical Review X* **8**, 031079 (2018).
- [157] H. Shen, B. Zhen, and L. Fu, "Topological Band Theory for Non-Hermitian Hamiltonians," *Physical Review Letters* **120**, 146402 (2018).
- [158] C.-K. Chiu, J. C. Y. Teo, A. P. Schnyder, and S. Ryu, "Classification of topological quantum matter with symmetries," *Reviews of Modern Physics* **88**, 035005 (2016).
- [159] K. Kawabata, K. Shiozaki, and M. Ueda, "Anomalous helical edge states in a non-Hermitian Chern insulator," *Physical Review B* **98**, 165148 (2018).
- [160] V. M. Martinez Alvarez, J. E. Barrios Vargas, and L. E. F. Foa Torres, "Non-Hermitian robust edge states in one dimension: Anomalous localization and eigenspace condensation at exceptional points," *Physical Review B* **97**, 121401 (2018).

- [161] D. S. Borgnia, A. J. Kruchkov, and R.-J. Slager, "Non-Hermitian Boundary Modes and Topology," *Physical Review Letters* **124**, 056802 (2020).
- [162] S. Yao and Z. Wang, "Edge States and Topological Invariants of Non-Hermitian Systems," *Physical Review Letters* **121**, 086803 (2018).
- [163] M. Parto, S. Wittek, H. Hodaei, G. Harari, M. A. Bandres, J. Ren, M. C. Rechtsman, M. Segev, D. N. Christodoulides, and M. Khajavikhan, "Edge-Mode Lasing in 1D Topological Active Arrays," *Physical Review Letters* **120**, 113901 (2018).
- [164] V. V. Albert, L. I. Glazman, and L. Jiang, "Topological Properties of Linear Circuit Lattices," *Physical Review Letters* **114**, 173902 (2015).
- [165] M. Ezawa, "Non-Hermitian higher-order topological states in nonreciprocal and reciprocal systems with their electric-circuit realization," *Physical Review B* **99**, 201411 (2019).
- [166] S. Liu, S. Ma, C. Yang, L. Zhang, W. Gao, Y. J. Xiang, T. J. Cui, and S. Zhang, "Gain- and Loss-Induced Topological Insulating Phase in a Non-Hermitian Electrical Circuit," *Physical Review Applied* **13**, 014047 (2020).
- [167] H. Zhao, P. Miao, M. H. Teimourpour, S. Malzard, R. El-Ganainy, H. Schomerus, and L. Feng, "Topological hybrid silicon microlasers," *Nature Communications* **9**, 981 (2018).
- [168] T. Ozawa, H. M. Price, A. Amo, N. Goldman, M. Hafezi, L. Lu, M. C. Rechtsman, D. Schuster, J. Simon, O. Zilberberg, and I. Carusotto, "Topological photonics," *Reviews of Modern Physics* **91**, 015006 (2019).
- [169] V. M. Martinez Alvarez, J. E. Barrios Vargas, M. Berdakin, and L. E. F. Foa Torres, "Topological states of non-Hermitian systems," *The European Physical Journal Special Topics* **227**, 1295–1308 (2018).
- [170] Ş. K. Özdemir, S. Rotter, F. Nori, and L. Yang, "Parity–time symmetry and exceptional points in photonics," *Nature Materials* **18**, 783–798 (2019).
- [171] R. Su, E. Estrecho, D. Biegańska, Y. Huang, M. Wurdack, M. Pieczarka, A. G. Truscott, T. C. H. Liew, E. A. Ostrovskaya, and Q. Xiong, "Direct measurement of a non-Hermitian topological invariant in a hybrid light-matter system," *Science Advances* **7**, eabj8905 (2021).
- [172] A. Ghatak, M. Brandenbourger, J. van Wezel, and C. Coulais, "Observation of non-Hermitian topology and its bulk–edge correspondence in an active mechanical metamaterial," *Proceedings of the National Academy of Sciences* **117**, 29561–29568 (2020).

- [173] C. Scheibner, W. T. M. Irvine, and V. Vitelli, "Non-Hermitian Band Topology and Skin Modes in Active Elastic Media," *Physical Review Letters* **125**, 118001 (2020).
- [174] T. Helbig, T. Hofmann, S. Imhof, M. Abdelghany, T. Kiessling, L. W. Molenkamp, C. H. Lee, A. Szameit, M. Greiter, and R. Thomale, "Generalized bulk–boundary correspondence in non-Hermitian topoelectrical circuits," *Nature Physics* **16**, 747–750 (2020).
- [175] J. M. Lee, T. Kottos, and B. Shapiro, "Macroscopic magnetic structures with balanced gain and loss," *Physical Review B* **91**, 094416 (2015).
- [176] P. A. McClarty and J. G. Rau, "Non-Hermitian topology of spontaneous magnon decay," *Physical Review B* **100**, 100405 (2019).
- [177] K. Deng and B. Flebus, "Non-Hermitian skin effect in magnetic systems," *Physical Review B* **105**, L180406 (2022).
- [178] A. Slavin and V. Tiberkevich, "Nonlinear Auto-Oscillator Theory of Microwave Generation by Spin-Polarized Current," *IEEE Transactions on Magnetics* **45**, 1875–1918 (2009).
- [179] S. Kaka, M. R. Pufall, W. H. Rippard, T. J. Silva, S. E. Russek, and J. A. Katine, "Mutual phase-locking of microwave spin torque nano-oscillators," *Nature* **437**, 389–392 (2005).
- [180] F. B. Mancoff, N. D. Rizzo, B. N. Engel, and S. Tehrani, "Phase-locking in double-point-contact spin-transfer devices," *Nature* **437**, 393–395 (2005).
- [181] V. Tiberkevich, A. Slavin, and J.-V. Kim, "Microwave power generated by a spin-torque oscillator in the presence of noise," *Applied Physics Letters* **91**, 192506 (2007).
- [182] N. Locatelli, A. Hamadeh, F. Abreu Araujo, A. D. Belanovsky, P. N. Skirdkov, R. Lebrun, V. V. Naletov, K. A. Zvezdin, M. Muñoz, J. Grollier, O. Klein, V. Cros, and G. de Loubens, "Efficient Synchronization of Dipolarly Coupled Vortex-Based Spin Transfer Nano-Oscillators," *Scientific Reports* **5**, 17039 (2015).
- [183] A. N. Slavin and V. S. Tiberkevich, "Theory of mutual phase locking of spin-torque nanosized oscillators," *Physical Review B* **74**, 104401 (2006).
- [184] M. Ezawa, "Nonlinearity-induced transition in the nonlinear Su-Schrieffer-Heeger model and a nonlinear higher-order topological system," *Physical Review B* **104**, 235420 (2021).
- [185] M. Ezawa, "Nonlinear non-Hermitian higher-order topological laser," *Physical Review Research* **4**, 013195 (2022).

- [186] L. Jin and Z. Song, "Bulk-boundary correspondence in a non-Hermitian system in one dimension with chiral inversion symmetry," *Physical Review B* **99**, 081103 (2019).
- [187] Z.-X. Gong, M. F. Maghrebi, A. Hu, M. L. Wall, M. Foss-Feig, and A. V. Gorshkov, "Topological phases with long-range interactions," *Physical Review B* **93**, 041102 (2016).
- [188] J.-V. Kim, Q. Mistral, C. Chappert, V. S. Tiberkevich, and A. N. Slavin, "Line Shape Distortion in a Nonlinear Auto-Oscillator Near Generation Threshold: Application to Spin-Torque Nano-Oscillators," *Physical Review Letters* **100**, 167201 (2008).
- [189] C. Rackauckas and Q. Nie, "DifferentialEquations.jl – A Performant and Feature-Rich Ecosystem for Solving Differential Equations in Julia," *Journal of Open Research Software* **5**, 15 (2017).
- [190] W. Chen, Ş. Kaya Özdemir, G. Zhao, J. Wiersig, and L. Yang, "Exceptional points enhance sensing in an optical microcavity," *Nature* **548**, 192–196 (2017).
- [191] M.-A. Miri and A. Alù, "Exceptional points in optics and photonics," *Science* **363**, eaar7709 (2019).
- [192] C. Dembowski, B. Dietz, H.-D. Gräf, H. L. Harney, A. Heine, W. D. Heiss, and A. Richter, "Encircling an exceptional point," *Physical Review E* **69**, 056216 (2004).
- [193] A. F. Vincent, J. Larroque, N. Locatelli, N. Ben Romdhane, O. Bichler, C. Gamrat, W. S. Zhao, J.-O. Klein, S. Galdin-Retailleau, and D. Querlioz, "Spin-Transfer Torque Magnetic Memory as a Stochastic Memristive Synapse for Neuromorphic Systems," *IEEE Transactions on Biomedical Circuits and Systems* **9**, 166–174 (2015).
- [194] J. Grollier, D. Querlioz, K. Y. Camsari, K. Everschor-Sitte, S. Fukami, and M. D. Stiles, "Neuromorphic spintronics," *Nature Electronics* **3**, 360–370 (2020).
- [195] A. U. Hassan, H. Hodaei, M.-A. Miri, M. Khajavikhan, and D. N. Christodoulides, "Nonlinear reversal of the \mathcal{PT} -symmetric phase transition in a system of coupled semiconductor microring resonators," *Physical Review A* **92**, 063807 (2015).
- [196] G. P. Agrawal and N. K. Dutta, *Semiconductor Lasers* (Springer US, Boston, MA, 1995).
- [197] J. Ding and M.-A. Miri, "Mode discrimination in dissipatively coupled laser arrays," *Optics Letters* **44**, 5021–5024 (2019).
- [198] A. Slavin, "Spin-torque oscillators get in phase," *Nature Nanotechnology* **4**, 479–480 (2009).

- [199] S. Wittrock, S. Perna, R. Lebrun, R. Dutra, R. Ferreira, P. Bortolotti, C. Serpico, and V. Cros, *Exceptional points controlling oscillation death in coupled spintronic nano-oscillators*, (Aug. 10, 2021) arXiv:2108.04804.
- [200] C. M. Bender, "Making Sense of Non-Hermitian Hamiltonians," *Reports on Progress in Physics* **70**, 947–1018 (2007).
- [201] Y. Tserkovnyak, "Exceptional points in dissipatively coupled spin dynamics," *Physical Review Research* **2**, 013031 (2020).
- [202] H. Zhao, X. Qiao, T. Wu, B. Midya, S. Longhi, and L. Feng, "Non-Hermitian topological light steering," *Science* **365**, 1163–1166 (2019).
- [203] Y. Tserkovnyak, A. Brataas, G. E. W. Bauer, and B. I. Halperin, "Non-local magnetization dynamics in ferromagnetic heterostructures," *Reviews of Modern Physics* **77**, 1375–1421 (2005).
- [204] A. Manchon and S. Zhang, "Theory of nonequilibrium intrinsic spin torque in a single nanomagnet," *Physical Review B* **78**, 212405 (2008).
- [205] A. Manchon and S. Zhang, "Theory of spin torque due to spin-orbit coupling," *Physical Review B* **79**, 094422 (2009).
- [206] A. Chernyshov, M. Overby, X. Liu, J. K. Furdyna, Y. Lyanda-Geller, and L. P. Rokhinson, "Evidence for reversible control of magnetization in a ferromagnetic material by means of spin-orbit magnetic field," *Nature Physics* **5**, 656–659 (2009).
- [207] J. C. Slonczewski, "Current-driven excitation of magnetic multilayers," *Journal of Magnetism and Magnetic Materials* **159**, L1–L7 (1996).
- [208] L. Berger, "Emission of spin waves by a magnetic multilayer traversed by a current," *Physical Review B* **54**, 9353–9358 (1996).
- [209] K. Deng, X. Li, and B. Flebus, "Exceptional points as signatures of dynamical magnetic phase transitions," *Physical Review B* **107**, L100402 (2023).
- [210] Y. Li, C. Liang, C. Wang, C. Lu, and Y.-C. Liu, "Gain-Loss-Induced Hybrid Skin-Topological Effect," *Physical Review Letters* **128**, 223903 (2022).
- [211] W. Zhu and J. Gong, "Hybrid skin-topological modes without asymmetric couplings," *Physical Review B* **106**, 035425 (2022).
- [212] C. H. Lee, L. Li, and J. Gong, "Hybrid Higher-Order Skin-Topological Modes in Nonreciprocal Systems," *Physical Review Letters* **123**, 016805 (2019).
- [213] X. Zhang, Y. Tian, J.-H. Jiang, M.-H. Lu, and Y.-F. Chen, "Observation of higher-order non-Hermitian skin effect," *Nature Communications* **12**, 5377 (2021).

- [214] K. Kawabata, M. Sato, and K. Shiozaki, "Higher-order non-Hermitian skin effect," *Physical Review B* **102**, 205118 (2020).
- [215] R. Okugawa, R. Takahashi, and K. Yokomizo, "Second-order topological non-Hermitian skin effects," *Physical Review B* **102**, 241202 (2020).
- [216] A. Y. Song, X.-Q. Sun, A. Dutt, M. Minkov, C. Wojcik, H. Wang, I. A. D. Williamson, M. Orenstein, and S. Fan, " \mathcal{PT} -Symmetric Topological Edge-Gain Effect," *Physical Review Letters* **125**, 033603 (2020).
- [217] A. Brataas, H. Skarsvåg, E. G. Tveten, and E. Løhaugen Fjærbu, "Heat transport between antiferromagnetic insulators and normal metals," *Physical Review B* **92**, 180414 (2015).
- [218] S. A. Bender, H. Skarsvåg, A. Brataas, and R. A. Duine, "Enhanced Spin Conductance of a Thin-Film Insulating Antiferromagnet," *Physical Review Letters* **119**, 056804 (2017).
- [219] C. Gong, L. Li, Z. Li, H. Ji, A. Stern, Y. Xia, T. Cao, W. Bao, C. Wang, Y. Wang, Z. Q. Qiu, R. J. Cava, S. G. Louie, J. Xia, and X. Zhang, "Discovery of intrinsic ferromagnetism in two-dimensional van der Waals crystals," *Nature* **546**, 265–269 (2017).
- [220] R. E. Troncoso, K. Rode, P. Stamenov, J. M. D. Coey, and A. Brataas, "Antiferromagnetic single-layer spin-orbit torque oscillators," *Physical Review B* **99**, 054433 (2019).
- [221] T. Yu, H. Yang, L. Song, P. Yan, and Y. Cao, "Higher-order exceptional points in ferromagnetic trilayers," *Physical Review B* **101**, 144414 (2020).
- [222] W. D. Heiss, "The physics of exceptional points," *Journal of Physics A: Mathematical and Theoretical* **45**, 444016 (2012).
- [223] A. A. Mailybaev, O. N. Kirillov, and A. P. Seyranian, "Geometric phase around exceptional points," *Physical Review A* **72**, 014104 (2005).
- [224] J. Doppler, A. A. Mailybaev, J. Böhm, U. Kuhl, A. Girschik, F. Libisch, T. J. Milburn, P. Rabl, N. Moiseyev, and S. Rotter, "Dynamically encircling an exceptional point for asymmetric mode switching," *Nature* **537**, 76–79 (2016).
- [225] R. Lavrijsen, J. H. Franken, J. T. Kohlhepp, H. J. M. Swagten, and B. Koopmans, "Controlled domain-wall injection in perpendicularly magnetized strips," *Applied Physics Letters* **96**, 222502 (2010).
- [226] J. H. Franken, M. Hoeijmakers, R. Lavrijsen, J. T. Kohlhepp, H. J. M. Swagten, B. Koopmans, E. van Veldhoven, and D. J. Maas, "Precise control of domain wall injection and pinning using helium and gallium focused ion beams," *Journal of Applied Physics* **109**, 07D504 (2011).

- [227] M. A. Ruderman and C. Kittel, "Indirect Exchange Coupling of Nuclear Magnetic Moments by Conduction Electrons," *Physical Review* **96**, 99–102 (1954).
- [228] T. Kasuya, "A Theory of Metallic Ferro- and Antiferromagnetism on Zener's Model," *Progress of Theoretical Physics* **16**, 45–57 (1956).
- [229] K. Yosida, "Magnetic Properties of Cu-Mn Alloys," *Physical Review* **106**, 893–898 (1957).
- [230] H. Yang, C. Wang, T. Yu, Y. Cao, and P. Yan, "Antiferromagnetism Emerging in a Ferromagnet with Gain," *Physical Review Letters* **121**, 197201 (2018).
- [231] V. E. Demidov, S. Urazhdin, A. Zholud, A. V. Sadovnikov, and S. O. Demokritov, "Nanoconstriction-based spin-Hall nano-oscillator," *Applied Physics Letters* **105**, 172410 (2014).
- [232] R. Cheng, D. Xiao, and A. Brataas, "Terahertz Antiferromagnetic Spin Hall Nano-Oscillator," *Physical Review Letters* **116**, 207603 (2016).
- [233] R. A. Duine, V. Errani, and J. S. Harms, *Non-linear dynamics near exceptional points of synthetic antiferromagnetic spin-torque oscillators*, (Feb. 15, 2023) arXiv:2302.07607.
- [234] A. V. Chumak *et al.*, "Advances in Magnetism Roadmap on Spin-Wave Computing," *IEEE Transactions on Magnetism* **58**, 1–72 (2022).
- [235] X. S. Wang and X. R. Wang, "Topological magnonics," *Journal of Applied Physics* **129**, 151101 (2021).